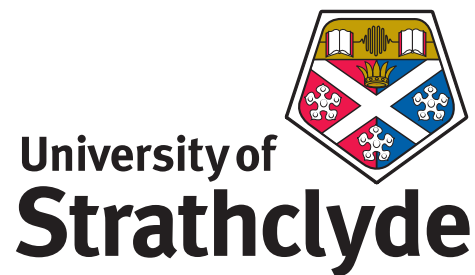**UNIVERSITY OF STRATHCLYDE**

Department of Physics

Novel optical communications and imaging enabled by CMOS interfaced LED technology

by

Alexander D. Griffiths

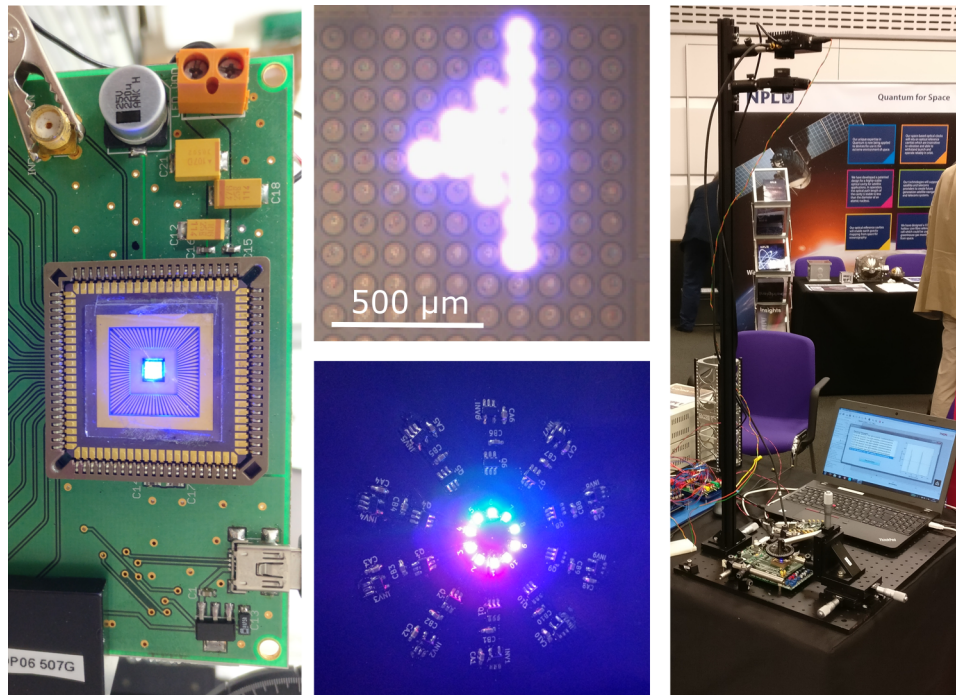A thesis submitted for the degree of Doctor of Philosophy

May 2018

Frontispiece

CMOS controlled micro-LED arrays (left, upper middle), commercial LEDs exhibiting pulsed emission across the visible spectrum (lower middle) and the few photon satellite communication link demonstrated at the 2017 Quantum Technology Showcase (right).

Abstract

Arrays of micron sized light-emitting diodes (micro-LEDs) allow high-frequency spatial and temporal modulation of an optical signal. Contacting micro-LED arrays to complementary metal-oxide-semiconductor (CMOS) electronics provides a mm-chip-scale device with a high level of control over the optical emission through digital input. Such devices enable novel forms of optical communication and imaging to be investigated.

This thesis first demonstrates the use of CMOS controlled micro-LEDs in multi-level intensity modulated optical communications. By generating signals in a discrete fashion with weighted groups of pixels in an array, the non-linearity issues of single LED elements can be avoided and the device functions as a digital-to-light converter. Pulse amplitude modulation and discrete orthogonal frequency division multiplexing were performed, yielding data rates up to 200 Mb/s, and spectral efficiencies up to 3.96 bits/s/Hz.

A novel form of optical communications is introduced where data is sent through modulation of the temporal correlation of a pulsed optical signal. Utilising single-photon detection at the receiver enables transmission at low received power levels, on the order of picowatts. While data rates prove to be modest, the scheme is robust to both constant and modulated background signals. Additionally, the implementation requires only simple semiconductor components, exhibits low electrical power consumption, and has been demonstrated under power from a nanosatellite simulation testbed.

The pulse correlation approach also presents opportunities in imaging. Received signals are dependent on optical power; therefore, if relative emitted power from multiple transmitters is known, information on the reflectance or absorption of an intermediate material can be obtained. This potentially enables colour or hyperspectral imaging with single-photon detectors by temporally structuring light sources. Proof-of-principle experiments have been performed using commercially available LEDs of 10 different wavelengths and printed colour targets.

Acknowledgements

Contents

Contents

Contents

Contents

List of Figures

List of Figures

List of Figures

List of Figures

List of Figures

List of Figures

List of Tables

List of Tables

Abbreviations

AC	Alternating current
APD	Avalanche photodiode
BER	Bit error ratio
CMOS	Complementary metal-oxide-semiconductor
DAC	Digital-to-analogue converter
DC	Direct current
dSiPM	Digital silicon photomultiplier
FEC	Forward error correction
FET	Field effect transistor
FPGA	Field programmable gate array
FWHM	Full width at half maximum
GaN	Gallium nitride
I-V	Current - voltage relationship
L-I	Luminosity - current relationship
LED	Light-emitting diode
Micro-LED	Micron-sized Light-emitting diode
MOSFET	Metal-oxide-semiconductor field effect transistor
MQW	Multiple quantum well
ND	Neutral density
NMOS	N-type metal-oxide-semiconductor

PMOS	P-type metal-oxide-semiconductor
OFDM	Orthogonal frequency division multiplexing
OOK	On-off keying
OWC	Optical wireless communications
PAM	Pulse amplitude modulation
PCB	Printed circuit board
PDP	Photon detection probability
PPM	Pulse position modulation
PRBS	Pseudorandom bit sequence
QAM	Quadrature amplitude modulation
RF	Radio frequency
RMS	Root mean square
SMA	Subminiature version A
SNR	Signal-to-noise ratio
SPAD	Single photon avalanche diode
USB	Universal serial bus
VLC	Visible light communications

Symbols

c	Speed of light
h	Planck's constant
λ	Wavelength
$P(t)$	Probability
$f(t)$	Probability distribution
η_{PDP}	Photon detection probability
Φ	Photon flux
R_{dark}	Dark count rate
τ_d	Detector dead time
f_{bg}	Probability distribution under constant flux
ρ	Photon number
$\delta(t)$	Dirac delta function
$g(\tau)$	Autocorrelation of $f(t)$
τ	Correlation time
$g(\tau_j)$	Discrete autocorrelation function
T	Temporal pulse separation
R_{rep}	Repetition rate
N_{slots}	Number of slots used in pulse position modulation
t_p	Temporal pulse width
N_r	Number repetitions

R_s Sampling rate

n_{av} Average photon number

$f_d(t)$ Probability of a SPAD being in recovery mode

R_{data} Data rate

R_{sig} Signal count rate

σ Spectrum

$\bar{x}, \bar{y}, \bar{z}$ CIE colour matching functions

x, y CIE chromaticity coordinates

Chapter 1

Introduction

The content of this thesis discusses novel forms of optical communications and imaging enabled by micron sized light-emitting diode (micro-LED) arrays integrated with electronic control systems. Indium gallium nitride (InGaN) LEDs bonded to complementary metal-oxide-semiconductor (CMOS) control electronics provide a compact, mm-chip-scale device with a high degree of control over the optical emission. This introductory chapter first covers a general background on LEDs, followed by a description of relevant optical wireless communications and transmission schemes. The remainder of the chapter focusses on the CMOS-controlled micro-LED arrays, including the characteristics of micro-LEDs, bonding methods, and the capabilities of the complete devices.

Following the introduction, Chapter 2 describes use of the CMOS integrated micro-LED array to generate discrete multi-level signals suitable for visible light communications. Operated in this way, the device provides a digital-to-light converter, allowing an increase in spectral efficiency. Chapter 3 introduces the mathematical framework to a novel form of data transmission, utilising temporal correlations in an optical signal and single-photon detectors. Chapter 4 discusses the practical implementation of such a system, using a single CMOS-controlled micro-LED pixel to generate the optical signals, and a commercial single-photon avalanche diode as a receiver. The system is

characterised, with particular focus on performance in the presence of background signals. In Chapter 5, the system and scheme are demonstrated for different application scenarios, and improvements from arrayed receivers are discussed. Chapter 6 broadens the temporal correlation approach to a method for colour or hyperspectral imaging, where signals from temporally structured light sources can be identified through their correlation patterns. Finally, Chapter 7 summarises the findings of this thesis, and presents some avenues for further research and development.

1.1 Light-Emitting Diodes

Electroluminescence, the process by which LEDs produce light, was first observed in 1907 by Henry Joseph Round [1]. Crystals of silicon carbide (SiC), or carborundum, emitted a "yellowish light" when under electrical bias of 10 - 110 V, though no further investigation followed. In the 1920s, LEDs were first developed by Oleg Losev, also using SiC [2]. Since this discovery, developments in light emission from semiconductors have resulted in the availability of LEDs covering the majority of the visible spectrum. The III-V compound semiconductor group of binary, ternary and quaternary alloys, proposed in the ealy 1950s, provides band gap energies spanning from 0.17 eV for indium antimonide (InSb) to 6.2 eV for aluminium nitride (AlN) [3]. In principle, this allows LED emission at wavelengths from 200 nm (ultraviolet) to 7 μm (infrared).

LEDs in the infrared [4] and red [5] regions were developed in the 1960s using gallium arsenide (GaAs) and aluminium gallium arsenide (AlGaAs). More recently, these kinds of LEDs have been typically used as infrared transmitters for remote control systems, such as TV remotes [3]. However, red-emitting gallium arsenide phosphide (GaAsP) LEDs [6, 7] became the first mass-produced solid state light source, manufactured by the Monsanto Corporation in 1968 [3]. Additionally, green emission was achieved using nitrogen-doped GaAsP [8] and gallium phosphide (GaP) [9], leading to the familiar LED applications as indicator lights and seven-segment numerical displays.

While efficient red and green LEDs have existed since the 1960s, the availability of blue LEDs was limited to inefficient SiC devices. It was not until the 1990s that efficient blue-emitting LEDs were developed, due to difficulties in producing p-doped gallium nitride (GaN), and poor GaN crystal quality [10,11]. The key steps in resolving these issues were growing low temperature GaN buffer layers on a sapphire substrate, new growth techniques, and p-type GaN formed using low energy electron beam irradiation or thermal annealing [12]. Isamu Akasaki, Hiroshi Amano and Shuji Nakamura were awarded the Nobel prize in physics in 2014 for producing efficient blue LEDs [13]. Blue LEDs are significant as they complete the set of primary colours, and also allow the efficient generation of white light, a key element in the Nobel prize citation. The majority of modern LED light fittings consist of a blue GaN based LED with a phosphor coating, to convert some of the blue light to longer yellow wavelengths. An alternative method is to use a set of red, green and blue LEDs together, to create a multichip white LED [14].

LEDs are now ubiquitous in the modern world, appearing in many application scenarios where efficient optical sources are required. Figure 1.1 shows some examples. The most familiar is in solid-state lighting, where LEDs are expected to dramatically improve efficiency and reduce energy costs for in-home and public lighting [19]. LEDs also see use as headlamps, indicator lights, display systems and backlighting for LCD screens. More recently, "smart lighting" systems have become of interest, where LED lighting can be be used to provide additional functionality, such as data communications [20,21] or object tracking and location [22]. The work in this thesis is primarily focussed on data communications utilising LED systems as optical transmitters.

1.1.1   LED Physics

LEDs are fabricated from semiconductors, which are a class of material in which the electron band structure has a forbidden region or "band gap" which cannot be occupied by charge carriers. Electroluminescence occurs when electrons from the upper

Figure 1.1: Blue-emitting LED (top-left) [15], various LED light fittings (top-right) [16], matrix LED headlights in an Audi TT 8S (bottom-left) [17] and Samsung's "The Wall" micro-LED based TV (bottom-right) [18].

conduction band recombine with holes in the lower valence band, releasing energy as a photon. The energy difference across the band gap dictates the wavelength of the emitted photons, as energy must be conserved.

In order to produce functional devices, the semiconductor materials are doped with donor (n-type) or acceptor (p-type) atoms to increase the number of available carriers. By growing n-type and p-type material together, a p-n junction is formed. Excess carriers and holes diffuse into the opposite material type and recombine, producing a depletion region between n-type and p-type material. A diffusion voltage V_D is formed, giving a potential barrier of energy eV_D, producing the energy band structure shown in Figure 1.2. Under forward bias, carriers are injected into the depletion region where they can recombine and emit photons.

The radiative recombination rate in an LED is dependant on the density of carriers in the active region. However, electrons and holes will propagate through the material
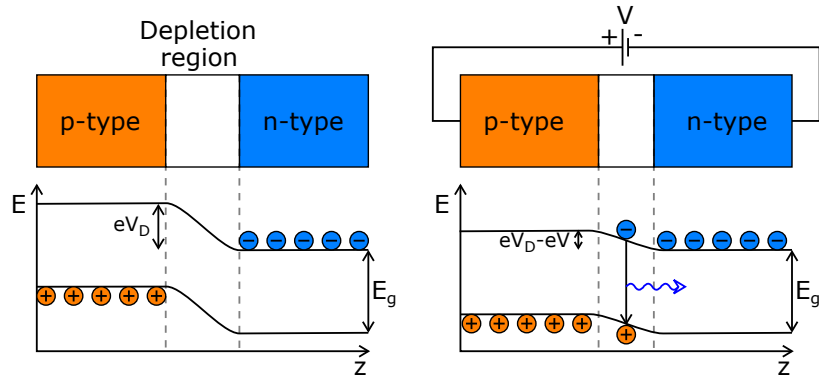
Figure 1.2: Energy levels in a p-n junction in equilibrium (left) and under forward bias (right).

with a characteristic diffusion length. This length can be on the order of several micrometers [3], limiting carrier concentrations. By growing larger band gap materials on either side of a narrow band gap material, potential barriers are formed that confine carriers to a smaller region and thus carrier concentration is increased. If this active region width is comparable to the de Broglie wavelength of the electrons (≈ 10 nm), quantum confinement effects become important. Figure 1.3 shows that quantum well structures discretise the electron energy levels, and raises the lowest energy levels similar to the well-known infinite potential well case [23]. This increases the energy of the emitted photon, as $E_{0,e} - E_{0,h} > E_g$. Careful engineering of the band gap through material choice and width L can therefore control the emission wavelength of an LED.

As current density increases, the quantum well begins to fill up with electrons and holes and carriers will overflow through the device. In order to maximise the number of carriers that undergo radiative recombination, multiple-quantum well (MQW) structures are used, with a repeating series of narrow and wide band gap material [3]. Carriers may still escape by leaking beyond the MQW structures. As electron leakage is usually higher due to larger diffusion constants, an electron blocking layer (EBL) is employed. This additional layer of different material causes an energy barrier in the conduction band that reduces the number of electrons that can escape, forcing them to
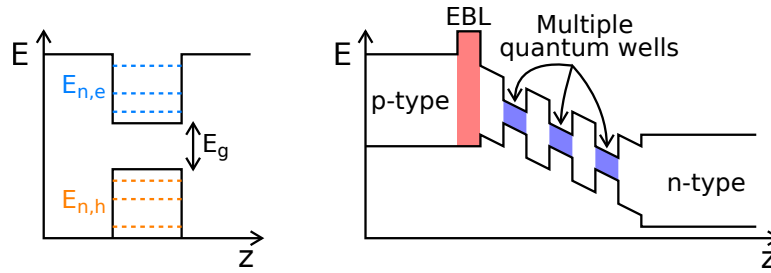
Figure 1.3: Potential well showing discrete electron and hole energy levels (left) and modern LED band diagram, with multiple quantum wells (MQW) and electron blocking layer (EBL).

remain in the active region. Figure 1.3 shows the energy bands of these modern LED structures schematically.

1.1.2 GaN LED Structure

The majority of the devices used in this thesis are based on III-nitride materials. By adjusting the relative compositions of gallium (Ga), indium (In) and aluminium (Al) in a ternary alloy, the band gap of the material can be tuned. The III-nitride system nicely covers the visible spectrum, potentially enabling LEDs to be fabricated with any visible wavelength, and significant extensions into infrared and ultraviolet. In reality, efficient LEDs with wavelengths beyond green are difficult to produce [14]. However, efficient blue-emitting devices fabricated with GaN has enabled white LED lighting. The violet and blue LEDs used in this thesis use an InGaN alloy for their active regions.

Figure 1.4 shows a schematic of a typical GaN wafer used for LED fabrication, with dimensions taken from [24]. Most commercial GaN structures are grown using metal-organic chemical vapour deposition (MOCVD) on c-plane sapphire due to its matching crystal symmetry [10]. However, the lattice mismatch of 16% causes strain within the structure and ultimately dislocations. Growth of an undoped buffer layer on sapphire substrates relaxes the strain and significantly improves crystal quality of the subsequent n-GaN, MQW, EBL and p-GaN layers. A general view of the fabrication process for LEDs is also shown in Figure 1.4. The LED mesa is defined by photolithography and
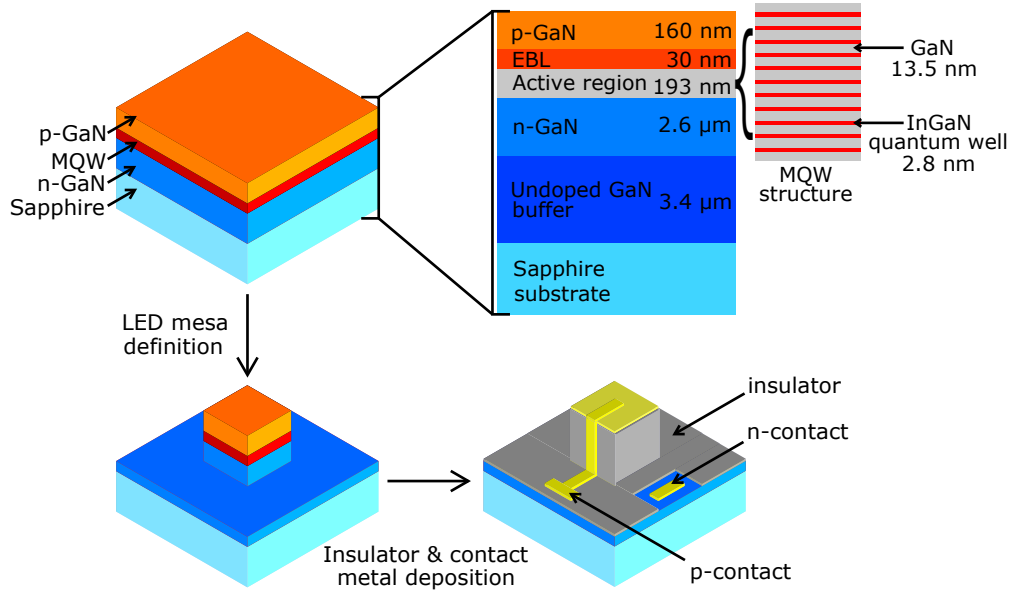
Figure 1.4: Simplified LED fabrication process flow and example GaN wafer structure, not to scale. A semiconductor wafer is selectively etched using photolithography and dry etching methods to form a mesa. Insulation layers and metal contacts are added to form a functional LED. Dimensional values taken from [24].

dry etching techniques. Once the n-GaN is exposed and the LED mesa is defined, a metal current spreading layer is deposited onto the p-GaN to ensure uniform current injection into the highly resistive p-type GaN [3]. Following this process, an insulation layer is deposited and selectively opened to isolate locations for the electrical contact points. Finally, the contacts are deposited through magnetron sputtering or electron-beam evaporation. For the devices used in this thesis, nickel gold and titanium gold alloys are used for p and n-contacts respectively. The device can then be electrically contacted via the contact pads using either a probe setup, or by fixing the chip to a printed circuit board (PCB) and wire bonding the pads to a connection point.

An advantage of the sapphire substrate is that it is optically transparent. This means LEDs can be fabricated in "flip-chip" format, where light extraction is performed through the substrate. In this case the metal deposited on the wafer does not impede

light extraction. The substrate can also be polished to increase the roughness, and reflective contact pads can be used, further increasing extraction efficiencies. This format is especially relevant here, as it allows the devices to be bump-bonded directly to control electronics, as discussed later in Section 1.3.2.

1.2   Optical Wireless Communications

Optical wireless communications (OWC) is the transmission of information using visible, infrared or ultraviolet light. When limited to the visible spectrum, this is often referred to as visible light communications (VLC). Fundamentally, this is not a new concept, as many examples of information transfer with light can found throughout history. Beacon fires and smoke signals are a primitive method for signalling using light, and technological devices such as the heliograph, Claude Chappe's semaphore, and Alexander Graham Bell's photophone were developed in the late 18th and 19th century [25].

Modern OWC is based on the modulation of a light source to send digital information. Commonly, the intensity, frequency, or phase of the light is modulated, though modulation of polarisation, orbital angular momentum and spatial mode is also possible. The modulated light is detected with a photodetector, converting the optical signal to an electrical one, where it can be decoded to reproduce the transmitted data. Data is therefore sent through an optical channel, in contrast to electrical signals through a conductor, or radio frequency (RF) signals using radio waves. A familiar example of OWC for digital communications is in infrared remote controls for consumer electronics. Commands are sent from a remote to an electronic device using an infrared-emitting GaAs LED and photodiode receiver [3]. This transmission is single direction, has a low data rate and can be blocked by objects in the channel, so is being replaced by RF communications such as WiFi and Bluetooth.

Laser based free-space optical communications were developed during the 1960s and

1970s, with kilometre ranges. However, as they were limited by beam divergence and atmospheric effects, fibre optics became the obvious choice for terrestrial long-range optical data transmission [26]. Further research in free-space laser links was driven by military and space applications. More recently, optical links have been demonstrated for Lunar ranges [27] and investigated for communications to Mars [28]. In future, OWC could be deployed on a large scale with satellite and ground platforms to provide backbone communications [29].

The transmission of digital data using the optical spectrum has attracted significant attention in recent years, as a potential alternative to RF communications. With rapid technological advancement, the volume of data traffic is ever increasing. The Cisco Visual Networking Index states that global mobile data traffic grew by 63% in 2016, with global IP traffic expected to reach 278 exabytes (1×10^9 GB) per month by 2021 [30]. Due to the limited frequencies available in RF communications, there is an expected "spectrum crunch", where the demand for data traffic exceeds the supply [25,31]. OWC offers an alternative, where data can be transmitted using the terahertz of licence-free bandwidth in the optical spectrum. Unlike RF, optical signals are constrained by walls and opaque material, reducing security risks and allowing spatial reuse, as multiple data links can be separated optically [32]. In addition, OWC is suitable for use in environments where RF interference is problematic, such as hospitals and aeroplanes.

1.2.1 State of the Art

LEDs in Optical Wireless Communications

OWC and VLC rely upon the modulation of an optical source, and the detection of the emitted light with a photoreceiver. Figure 1.5 shows a simple example of a communication method involving the intensity modulation of an optical source, and the direct detection of the light with a photodiode (so-called IM/DD). Encoded changes in the intensity of light can represent binary data in a number of ways, some of which are
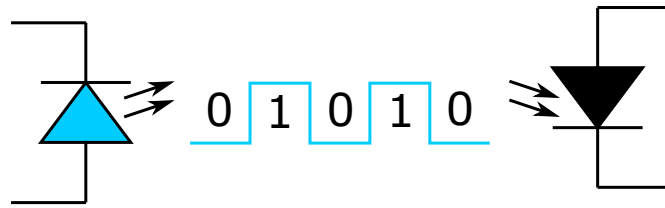
Figure 1.5: Schematic of transmission of data using visible light emission from an LED, detected by a photodiode.

covered in Section 1.2.2. Typically, optical transmitters for OWC and VLC are lasers or LEDs. While laser-based systems can provide highly directional emission and high power, LEDs are attractive due to their simplicity, low cost and robustness. Furthermore, LEDs are rapidly replacing previous lighting technologies, making such optical sources widely available in homes, vehicles and public areas. In principle, every light fitting could the perform dual functionality of illumination and data transmission, enabling "Li-Fi" style systems [33]. Importantly, the emission from an LED is incoherent, in contrast to a laser. This allows the transmitter to provide a degree of coverage over a projected area, or relax the pointing and alignment requirements of a system. However, drawbacks of the incoherent emission are that only intensity modulation methods can be used, and significant amounts of optical power may be wasted in fixed point-to-point communication scenarios.

Commercially available broad area LEDs (0.1-1 mm^2), designed for lighting applications, have limited capability for data transmission. The modulation bandwidth of such devices is typically 10s of MHz, limited by capacitance [32]. In addition, the rare earth phosphor coating often used for white lighting has a long decay time, further limiting modulation bandwidth to only a few MHz. Nevertheless, communication links of over 1 Gb/s have been achieved using phosphor coated [34], and RGB LEDs [35] designed for lighting. Such data rates have been achieved using discrete multitone modulation and wavelength division multiplexing to optimise use of the limited bandwidth. Com-

mercial "Li-Fi" systems are now available, offering bi-directional communication links from light fittings to USB devices with downlink data rates up to 43 Mb/s [36].

Higher data rate systems can be achieved using micro-LEDs (< 100 µm scale) as optical transmitters. For reasons discussed in Section 1.3.1, micro-LEDs have shown modulation bandwidths of 100s of MHz [21], and pushing towards 1 GHz [37]. As the LED bandwidth is typically the limiting factor for the communication system, micro-LEDs permit much higher data rates, with single LED links reaching over 5 Gb/s [37] and wavelength division multiplexing reaching over 10 Gb/s [38].

In both broad area LED and micro-LED systems, the highest data rates are achieved by exploiting advanced modulation schemes, multiplexing and signal processing methods. Pulse amplitude modulation (PAM) and orthogonal frequency division multiplexing (OFDM) make efficient use of the available bandwidth, permitting high data rates [21]. Both schemes are discussed in more detail in Section 1.2.2. Additionally wavelength division multiplexing allows further data rate improvements by transmitting multiple data streams using different wavelength sources. Each stream can then be independently decoded with filtered receivers. This approach also offers the possibility of combining VLC with colour control.

Over recent years, research into LED based VLC has resulted in a rapid increase in achievable data rates. Figure 1.6 shows the annual improvement in reported data rates for VLC using GaN based LED transmitters, based on data in reference [21]. This exponential trend has been enabled by advancements in transmitter hardware, modulation techniques and multiplexing methods, pushing up to 10 Gb/s data rates.

Photon Efficient Optical Communications

In long-range systems, or high-loss environments, the received optical power in a communication system can be very low, requiring highly sensitive receiver systems. An important metric for receiver sensitivity is the number of photons-per-bit required to achieve error-free performance. Conventional optical detectors such as PIN or avalanche
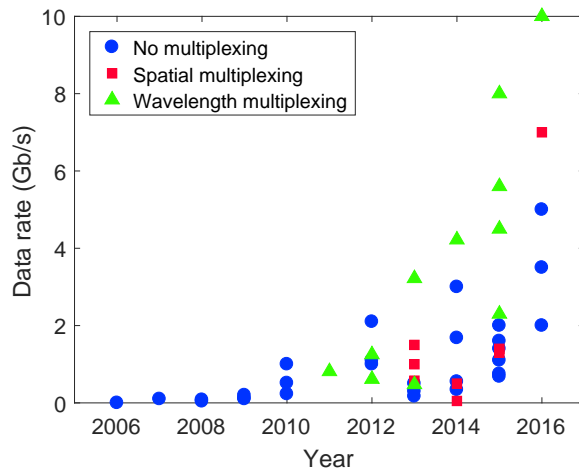
Figure 1.6: Progress in reported data rates for GaN LED based VLC, reproduced from data in [21].

photodiodes have limited sensitivities due to noise, so more advanced methods are required.

Coherent receivers, in which the received signal is interfered with a local oscillator, allows very high sensitivity communications to be performed [39]. By using coherent techniques and methods to account for erroneously transmitted bits, known as forward error correction (FEC) codes, sensitivities of a few photons per bit can be achieved for 100s of Mb/s to almost 10 Gb/s data rates [40, 41].

While coherent communications with powerful FEC provide the highest performance, the systems are complex, requiring local oscillators, balanced photodiodes and optical phase-locked loops. A potentially simpler method to attain high sensitivities is to use intensity modulation and direct detection methods with single-photon counting receivers. Typical technologies for single-photon detection in communications are nanowire superconducting single-photon detectors (SSPDs) [42] or single-photon avalanche diodes (SPADs) [43]. While nanowire SSPDs show higher detection efficiencies at typical telecommunication wavelengths (1.3 - 1.55 µm), SPADs are advantageous due to their semiconductor nature, allowing them to be integrated with receiver electronics and operated in array formats. A detailed discussion of SPAD receivers is
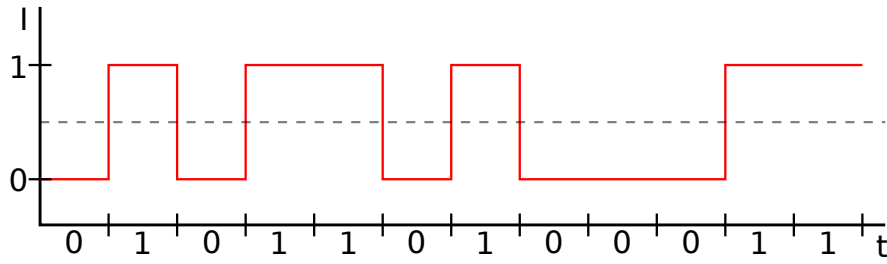
Figure 1.7: Schematic of on-off keying transmission.

presented later in Section 3.2. With single-photon detection and simple on-off keying transmission schemes, data rates of 100s of Mb/s can be achieved with 10s of photons-per-bit [44, 45]. By implementing pulse-position modulation and powerful FEC, efficiencies can be further improved down to 1.5 photons-per-bit, though at a data rate cost due to reduced spectral efficiency [46, 47].

1.2.2 Transmission Schemes

A number of schemes have been established for transmission of digital data by intensity modulation in OWC. Here, the general operating principles of the four transmission schemes that are most relevant to this thesis are discussed.

On-Off Keying

One of the simplest methods of transmitting data is On-off keying (OOK). Here the output intensity of the transmitter modulates between two levels, representing binary values "0" and "1". Often for LEDs the electrical supply is a DC bias combined with the modulated signal through a bias tee. This results in the two intensity levels occurring above and below the DC bias point. Alternatively, an LED can be modulated from an off state to a single on state using a transistor. A schematic representation of OOK transmission is shown in Figure 1.7, where the data sequence [010110100011] is transmitted.

To decode the transmitted data, the receiver will use a threshold level to determine the transmitted bit. Here, the importance of LED bandwidth becomes apparent. As
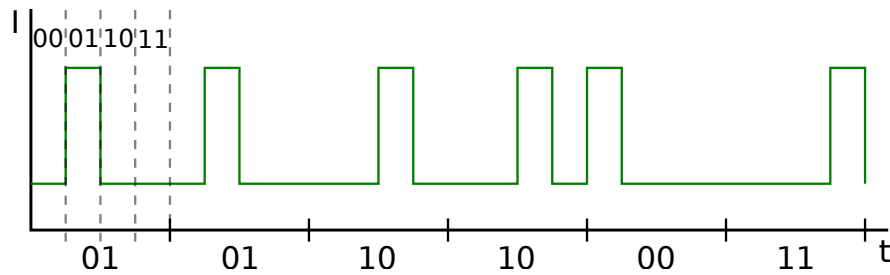
Figure 1.8: Schematic of pulse position modulation.

the modulation rate increases, the two intensity levels will become closer together, as the LED can no longer respond rapidly to the electrical signal. Eventually, the levels will be too close together to reliably distinguish, as noise on the electrical signal will dominate over the OOK stream amplitude. This results in bit errors, where the binary symbols are decoded incorrectly. The bit-error ratio (BER) is a common parameter for characterising communication links, and is defined as the ratio of incorrectly decoded bits to total transmitted bits. A BER as low as possible is desirable, however, BER values on the order of 1×10^{-3} can be corrected for with forward error correction (FEC) algorithms [48].

Pulse Position Modulation

Pulse position modulation (PPM) encodes data in the temporal position of a pulse of light. Each data interval is divided into slots, with each slot representing a binary word. M-PPM transmits $\log_2(M)$ bits per time interval, and requires M time slots to be available. Figure 1.8 shows an example of 4-PPM, where two bits are sent per interval by using one of four pulse positions, where the same binary sequence has been sent as in the previous OOK example.

By comparing Figures 1.8 and 1.7, it can be seen that the PPM case requires sources which can modulate at higher rates to maintain the same data rate. The total time for data transmission is the same, however, the PPM case requires emission of pulses with widths half as wide as that of OOK. Therefore, OOK has higher spectral efficiency,

14
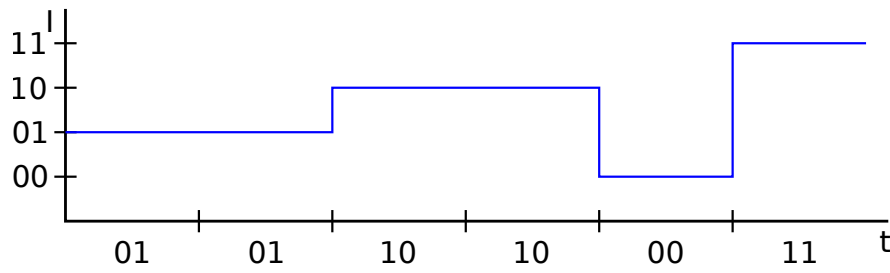
Figure 1.9: Schematic of pulse amplitude modulation.

which is a measure of how much data can be sent for a given bandwidth. As data rate is often the priority in communications, OOK is more widely used, however, PPM is more energy efficient, as higher orders encode many bits to a single pulse of light.

Pulse Amplitude Modulation

When the signal-to-noise ratio (SNR) is high enough, data rates can be increased over OOK by using pulse amplitude modulation (PAM). In this case, multiple (> 2) intensity levels are used to represented binary words. M-PAM transmits $\log_2(M)$ bits per interval, requiring M discrete levels. Figure 1.9 shows the example data stream transmitted using 4-PAM.

In contrast to PPM, it can be seen that PAM requires a lower switching rate from the LED to send the same amount of data as in OOK. It is therefore more spectrally efficient and higher orders of PAM continue to increase the data throughput. However, this puts additional requirements on the LED in terms of power output. The power levels must be distinguishable at the receiver, to avoid the occurrence of bit errors. Furthermore, LED outputs are highly non-linear (see, for example, Figure 1.15(b)), which restricts the power ranges available for such transmission methods.

Orthogonal Frequency Division Multiplexing

As an alternative to the time domain approaches described above, data can instead be encoded in the frequency domain. Orthogonal frequency division multiplexing (OFDM) is the division of data between multiple sinusoidal carrier signals or subcarriers, which
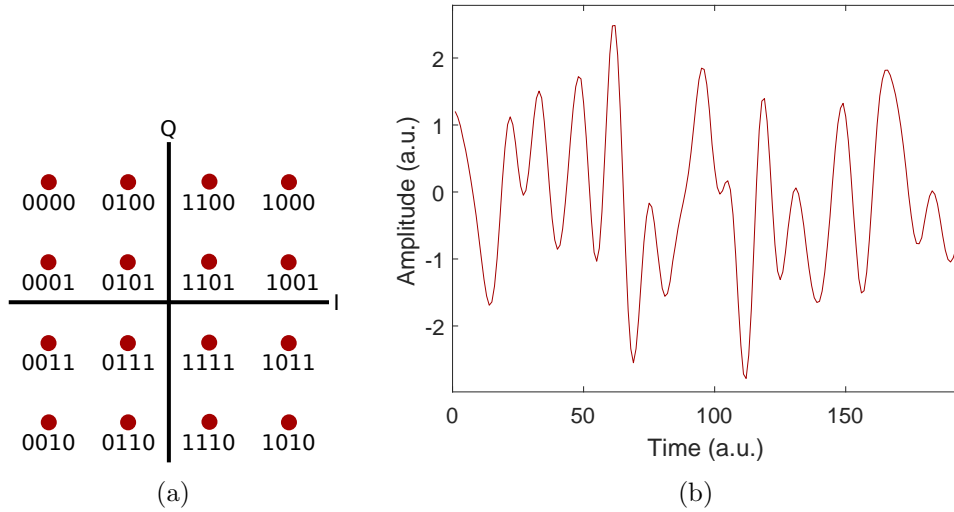
Figure 1.10: (a) 16-QAM constellation diagram. (b) Typical OFDM waveform.

have different, orthogonal frequencies [49]. The technique has been utilised in RF communications for many years, and only applied to optical communications relatively recently. Each subcarrier can be modulated with quadrature amplitude modulation (QAM), where both the amplitude and phase of the carrier wave are modulated to represent binary words. A constellation diagram is a useful visualisation for QAM, as shown in Figure 1.10(a). The amplitude and phase of the carrier wave forms a phasor on the diagram, which will point to a location corresponding to a binary word. Distortions to the signal from noise and interference will mean the received phasor may not exactly match the original location, however it can be decoded through maximum likelihood detection, correcting to the nearest binary word on the constellation diagram.

With each carrier frequency modulated with QAM, the subcarriers are then combined through inverse fast Fourier transform (IFFT) to produce a waveform to be transmitted. As optical transmitters send information through intensity modulation, the OFDM waveform must be real valued and non-negative. Real values are achieved through hermitian symmetry of the OFDM subcarriers. To obtain a non-negative signal, a common approach is to add a DC bias to the signal, referred to as DCO-OFDM [25]. The example waveform in Figure 1.10(b) could be offset by a DC signal

and transmitted by an LED. An alternative is to asymmetrically clip the OFDM wave-form (ACO-OFDM), by setting even subcarriers to zero. This method should result in increased spectral efficiency at low SNR.

Key techniques in OFDM are the use of a cyclic prefix, and adaptive bit and power loading. A cyclic prefix allows the system to account for channel dispersion and reduce inter-symbol and inter-carrier interference. Adaptive bit and power loading is used to optimise OFDM transmission by deciding on the size of the QAM constellations based on the SNR for each carrier. Carriers with high SNR are allocated a higher number of QAM symbols, increasing spectral efficiency.

OFDM has been widely used for optical communications due to its high spectral efficiency, robustness to intersymbol interference and operation in the presence of background lighting. Most record data rates with LEDs have been achieved using OFDM [21], with multi-Gb/s data rates possible with single micro-LEDs [37].

1.3 CMOS Controlled Micro-LED Arrays

Much of the experimental work described in this thesis is enabled by micro-LED arrays bonded to complementary metal-oxide-semiconductor (CMOS) electronics, developed over many years at the Institute of Photonics in collaboration with Prof. Robert K. Henderson's group at the University of Edinburgh. These compact devices provide a high level of digital control over the optical emission of micro-LED arrays. This section describes the background of such devices, their capabilities and performance characteristics.

1.3.1 Micro-LEDs

Conventional, broad area LEDs used for applications such as interior lighting tend to have a single emission area of around 0.1-1 mm^2. These devices are usually intended for DC operation with high light output. In contrast, a micro-LED is simply an LED with

an active area reduced to a smaller scale; typically 100 µm across or less. Naturally, the reduced active area means the output optical power is lower, however, similar fabrication processes can be used to define arrays of micro-LEDs in the same area as a single broad area LED. The first example of micro-LED fabrication was from Kansas State University [50], where circular pixels were defined with a 12 µm diameter. While the output power of 20 µW is modest, the high operational current density of micro-LEDs was immediately recognised, and it was shown that the quantum efficiency per unit area is increased over their broad area counterparts.

A natural advantage of micro-LEDs is the ability to form high-density arrays of individually controllable elements, allowing spatial and temporal control over an optical signal. The first such system consisted of a 10×10 array of 12 µm disks, each with an independent p-contact, and a shared, interconnected n-contact [51]. With individually addressable LED elements, such an array is useful for micro-display systems. However, the array required 100 separate p-contacts arranged around the edge of the LED pixels. This arrangement becomes impractical with higher numbers of LEDs, making packaging the device and controlling each element difficult. An alternative contact method for high-density arrays is discussed in Section 1.3.2, for connecting micro-LED arrays to electronic control chips.

Micro-LED arrays have been fabricated at the Institute of Photonics since 2001 and demonstrated for a variety of applications. Some example devices are shown in Figure 1.11, including: (a) 4×4 groups of individually addressable 39 µm diameter elements for communications, (b) a 16×16 array of tessellated 99×99 µm elements packaged with CMOS electronics, and (c) parallel connected clusters of 40 µm diameter pixels. Images (a) and (c) are taken from the p-GaN side of the device, showing the contact pads and defined mesas of each pixel. Light is extracted through the opposite side. Image (b) is taken from the sapphire side, so the emission area definition can be seen clearly.

Micro-LED arrays are expected to be part of a new generation of display systems

|(a)|(b)|(c)|
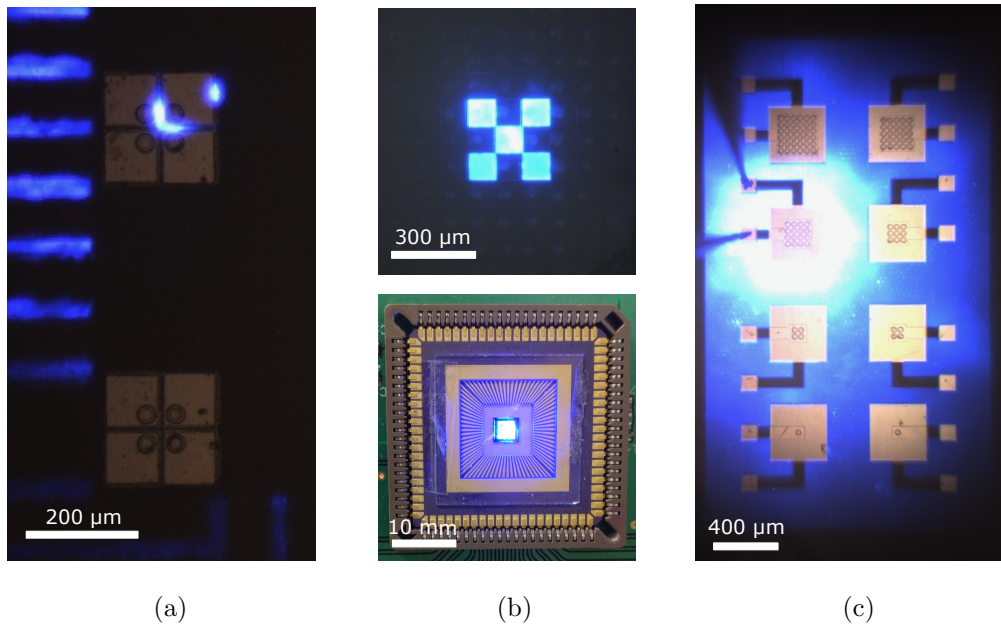
Figure 1.11: Images of micro-LEDs fabricated at the Institute of Photonics: (a) 39 µm diameter pixels in 4×4 groups. (b) CMOS integrated 99×99 µm tessellated device, displaying 5 lit pixels (upper) and the full package (lower). (c) Parallel connected clusters of 40 µm diameter pixels.

due to their advantages over current organic LED (OLED) technology [52]. Displays utilising micro-LEDs show higher brightness, lower power consumption and wider colour gamut. This year (2018), Samsung revealed a 146 inch modular TV, called "The Wall", pictured in Figure 1.1, which uses micro-LEDs to produce an 8K resolution display with high frame rates [18]. The compactness of micro-LED systems also makes them attractive for head-up-displays and augmented (AR) or virtual reality (VR) systems [53]. Recently, a number of micro-LED startups, including mLED Ltd, spun out of the University of Strathclyde, have been acquired by large technology companies such as Facebook-owned Oculus [54], and Apple [52].

The micro-LED characteristic that is most relevant to the work presented in this thesis is the improved performance under modulated driving conditions. The time it takes for an LED to reach a steady state when an applied signal is changed is governed by the capacitance of the device and the carrier lifetime. For larger devices ($>$

200×200 µm), the resistance $\times$ capacitance (RC) time constant is dominant in limiting the switching speed [21]. However, in a micro-LED, the reduced size significantly decreases the capacitance of the device, so the much shorter carrier lifetime is dominant [55]. Furthermore, micro-LEDs operate at very high current densities. As radiative recombination and carrier lifetime are dependent on carrier concentration, this leads to much faster transition speeds. This advantage has been investigated extensively for visible light communication (VLC) (for example: [21,24,37,56,57]). In addition, micro-LEDs are capable of generating extremely short optical pulses, down to 100s of ps [58], which has been demonstrated for fluorescence lifetime measurements [59]. The high speed response of micro-LEDs provides the means to perform the novel communication methods described later in this thesis.

1.3.2 Flip-Chip Bump Bonding

Individually addressing micro-LEDs in an array becomes difficult with hundreds or thousands of individual pixels. One possible solution is to implement a matrix addressing system, where each row of elements shares a common cathode, and each column a common anode [60]. The disadvantage of such an approach is that unwanted pixels may be addressed when specifying the emission patterns. It is therefore more desirable to find a solution where each LED pixel has an individual contact pad and drive electronics. This section discusses micro-LED arrays integrated with complementary metal-oxide semiconductor electronic drivers through flip-chip bump bonding. The result is a mm-scale device capable of independently controlling each pixel in an array. Here, the focus is on a 16×16 array, but the principle extends to larger systems.

To allow a high number of electrical connections from a CMOS driver chip to a micro-LED array, the devices are stacked and bonded with gold bumps between each connection point. By bonding in this way, contact pads can be close to, or on top of the LED mesas, allowing high density arrays without requiring metal tracks to reach the edges.

CMOS chip	Gold bumps deposited	LED array flipped and aligned	Bonded device
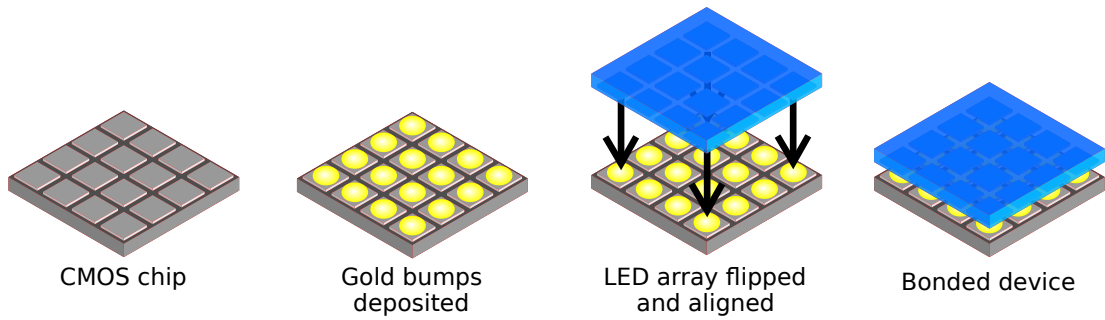
Figure 1.12: Schematic representation of the bump bonding process.

The process of flip-chip bump bonding is shown in Figure 1.12. The two devices to be bonded are fabricated with bond pads that have matching pitch and dimensions. The CMOS chip has metal bumps deposited on each pad using an automatic wire-bonder machine. Thermal, electrical and ultrasonic energy melts gold wire to form a gold ball. Every pad on the device is populated in this way.

The populated chip is then transferred to a flip-chip bonder, along with the LED array. With the LED chip flipped so the contact pads face the CMOS chip, the two devices are aligned and then mechanically pressed together. Application of ultrasonic and thermal energy melts the gold bumps and creates the electrical connections between the pads. A final, optional, step is to underfill the device with an insulating adhesive, to provide mechanical stability.

1.3.3   Device Capability

The CMOS integrated devices used in this thesis, fabricated at the Institute of Photonics, are 16×16 arrays of micro-LED elements with associated drive electronics. These devices were developed in collaboration with Prof. Robert K. Henderson's CMOS Sensors and Systems group at the University of Edinburgh, with several iterative designs [61, 62]. At various stages of development, these devices have been demonstrated for applications in displays [63], fluorescence lifetime experiments [59, 64], optical tweezers [65], mask free lithography [66], and visible light communications [55, 67, 68].

The micro-LED arrays consist of 16×16 arrays of GaN LED elements, with indi-

vidual anodes and a common cathode. Details of fabrication methods can be found in reference [55]. LED elements can be fabricated with a range of different wavelengths, however, the results in this thesis are primarily obtained with emission wavelengths of 405 and 450 nm. Additionally, arrays can be fabricated with a range of dimensions and layouts, with sizes ranging from 14 to 100 µm wide, in circular or square pixels. A PMOS transistor on the control chip functions as the LED driver for each pixel, addressing the individual p-contact for the LED.

The CMOS control chip was implemented in 0.35 µm, 3.3 V CMOS technology by Austria Microsystems. The 16×16 array consists of individual electronic drivers on a 100 µm pitch, each with a 50×50 µm bond pad. The driver is a four-layer device, with the bottom two layers routing the CMOS transistor signals, the third layer forming a protective barrier from the LED voltages, and the upper layer patterned with the bond pads for the LED array. The driver electronics are positioned around the contact pad, as previous devices with electronics directly beneath the pad were damaged during bonding [61]. To further improve mechanical stability, a tungsten column propagates vertically through the entire chip from beneath the pad.

Each individual driver follows the logic circuitry in Figure 1.13. The inputs ROW and COL are used to define the active pixels by row and column respectively. When a pixel is addressed, ROW and COL will be set high, and the output of the flip-flop will match the driver input (DIN) on the rising edge of the clock signal (CLK). DIN is therefore used to set whether or not the driver is active, and the flip-flop maintains the state of DIN even when the pixel is no longer addressed. The output is controlled by $INPUT\_SIG$, which can be sourced in three different ways. It can be tied to a DC signal from the control board, an on-chip voltage controlled oscillator (VCO), or an external logic signal. When the pixel is active, the output will follow the inverse of $INPUT\_SIG$, allowing digital signals to be directly converted into the optical domain. In this thesis, $INPUT\_SIG$ was always an external signal, so details of the VCO are not given here, but can be found in [61].
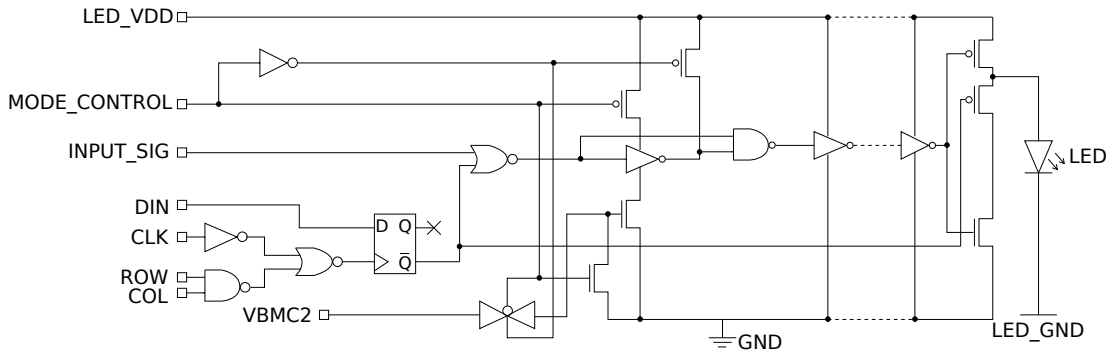
Figure 1.13: Logic circuitry for each individual CMOS driver.

The *MODE_CONTROL* input determines whether the output follows *INPUT_SIG* directly or operates in pulsed mode. If *MODE_CONTROL* is high, the driver operates as above. When *MODE_CONTROL* is set to low, *INPUT_SIG* is also sent through an inverter to introduce a time delay. The delay can be controlled by current starving the inverter with a transistor, allowing it to be set through an external voltage (*VBMC2*). The delayed signal is then sent to a NAND gate, along with the non-delayed *INPUT_SIG*. This results in the generation of a short electrical pulses with repetition rate at the same frequency as *INPUT_SIG*, which can used to drive the LED in short pulse mode [69]. This capability has been used to demonstrate pulse widths as low as 300 ps [58].

The remainder of the circuit diagram in Figure 1.13 is a chain of inverters used to minimise the load capacitance on the input signal and also maximise the drive strength [69]. Finally, an important feature of the driver is that *LED_GND* is physically separated from the main ground of the driver. This allows the LED ground to be shifted by applying a negative bias to *LED_GND*, so that the LED can be driven above 3.3 V without damaging the CMOS electronics.

Driving boards

To operate the CMOS-controlled micro-LED arrays, a control motherboard was developed by the University of Edinburgh, as depicted in Figure 1.14(a). The motherboard

houses a field programmable gate array (FPGA) board, daughtercard, and a series of variable resistors. The FPGA provides a connection between the motherboard and a PC, where the logic signals can be controlled by a graphical user interface (GUI) or MATLAB$^{\text{TM}}$. Power is supplied to the motherboard and CMOS device through the USB connection to the FPGA. The logic signals are transferred to the correct pins on the CMOS device by the daughtercard, which also provides an SMA connector for the external supply of *INPUT_SIG*. The variable resistors allow fine tuning of the supply voltages to the chip, including LED forward bias (*LED_VDD*) and *VBMC2*, for tuning the pulse widths.

A secondary driving board has also been developed, specifically for visible light communications (VLC) applications [62, 67], and is shown in Figure 1.14(b). Access to the VCO and short pulse circuitry, generally unused for VLC, were omitted to reduce complexity. In order to select active pixels, the FPGA was replaced with a USB microcontroller, which was also operated with a PC connection and GUI. Significant effort was made to reduce inductive and capacitive interference when under high speed modulation. In addition, 16 parallel input channels are provided, allowing each column of LEDs to follow a different modulation signal.

1.3.4 Characterisation and Performance

Current, Voltage and Luminescence

An LED's output is typically characterised by the relationships between bias voltage, current draw and output luminescence. Figure 1.15 shows the current to voltage (I-V) and luminescence to current (L-I) relationships of a 99×99 µm pixel in a CMOS-controlled array. The characteristics of this device are summarised in Table 1.1 under "Example 1". The I-V curve shows typical diode behaviour expected of an LED, with a series resistance of $38.67\,\Omega$ and a turn-on voltage of 3.9 V. The L-I curve demonstrates that a single pixel is capable of producing almost 2 mW of optical power before suffering
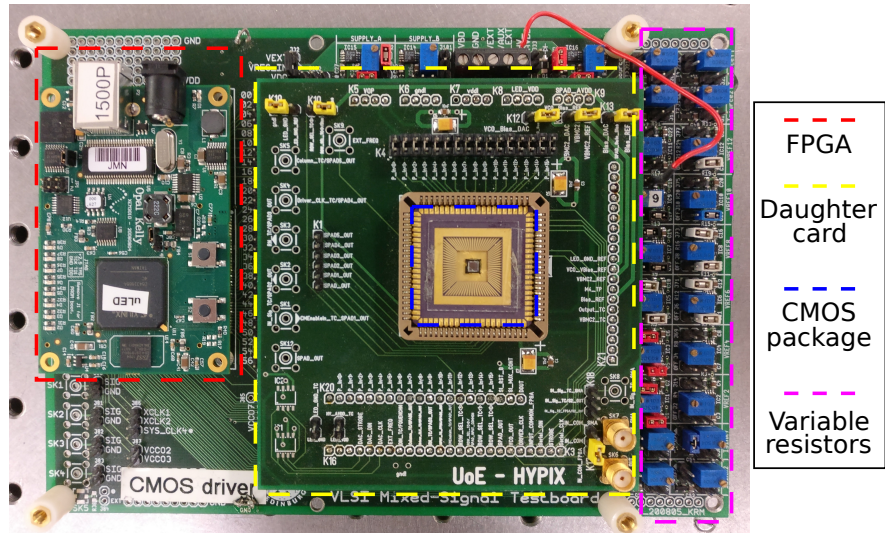
(a)
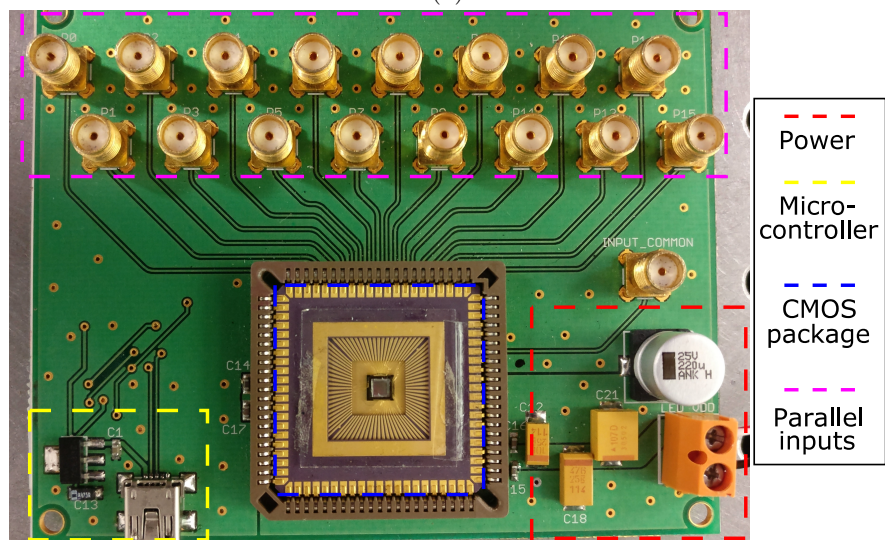
(b)

Figure 1.14: Control boards for CMOS integrated micro-LED arrays. (a) General motherboard. (b) VLC board.

(a)   (b)
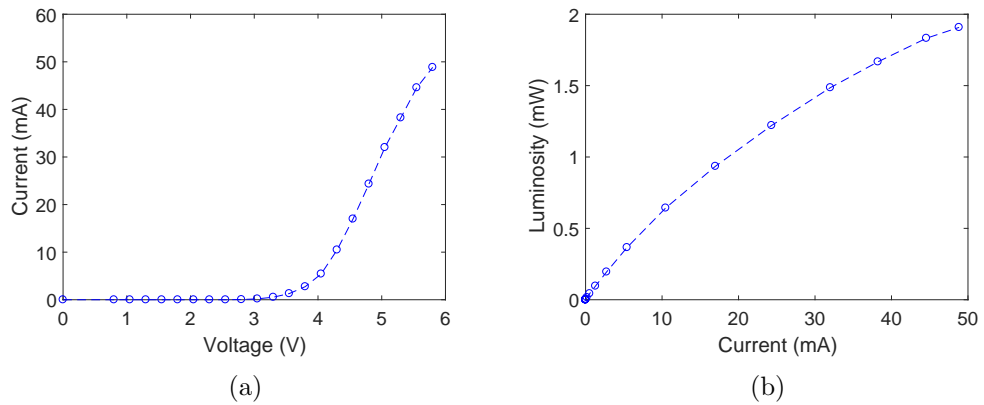
Figure 1.15: (a) I-V and (b) L-I characteristics of a 99 × 99 µm CMOS-controlled micro-LED.
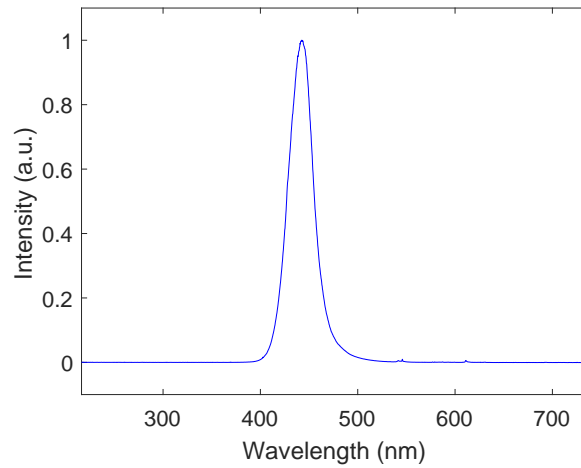
Figure 1.16: Emission spectrum of an LED, taken from the same 99 × 99 µm LED.

from roll-over, caused by self-heating and efficiency droop.

Emission Spectrum

The LED emission wavelength is dictated by the wafer structure used during fabrication, and can be chosen by engineering of the band gap energy and quantum well width, as presented in Section 1.1.1. The micro-LED arrays used in this thesis are fabricated from III-nitride materials, so can be made with a range of visible emission wavelengths.

The emission spectrum from a single 99 × 99 µm CMOS-controlled micro-LED is

shown in Figure 1.16. The measurement was performed with a fibre coupled spectrometer collecting light from the sapphire side of the LED, with the bias at 5 V. The peak wavelength can be identified as 442.2 nm with a FWHM of 28.5 nm, which appears monochromatic to the human eye.

Frequency Response Measurements

The optical output of an LED is strongly dependent on the injected current, therefore, intensity modulated signals are readily produced by controlling the electrical input signal. The primary limitation on data rates for communications using LEDs is the modulation bandwidth of the LED element. This is a measure of the rate at which the device can be switched between different output intensity levels. Broad area LEDs, as used for lighting applications, can be modulated at tens of MHz [32], while micro-LED devices have shown bandwidths approaching 1 GHz [37]. This frequency response is an important measure of the performance of a device, so is described in detail here.

The setup for measuring LED frequency response and the respective LED bias points are shown in Figure 1.17. A network analyser produces an AC electrical signal, that sweeps through a frequency range. This signal is offset by a DC signal from the DC power supply, as the LED will have no output for negative voltages. The LED being measured is modulated with this electrical signal, biasing over the voltage range ΔV, as shown in Figure 1.17(b). As the optical power output depends on the bias voltage, the emitted light level will vary with the sinusoidal signal across the optical power range ΔP. As the modulation frequency increases, ΔP will eventually begin to decrease as the LED cannot respond as rapidly. The output light is collected by an AC coupled avalanche photodiode (APD) and returned to the network analyser, which calculates the frequency response based on the root mean square (RMS) value of the received APD voltage signal.

As the frequency of the AC signal is increased, eventually the LED will no longer be able to respond fast enough to output the correct waveform, and the amplitude of the
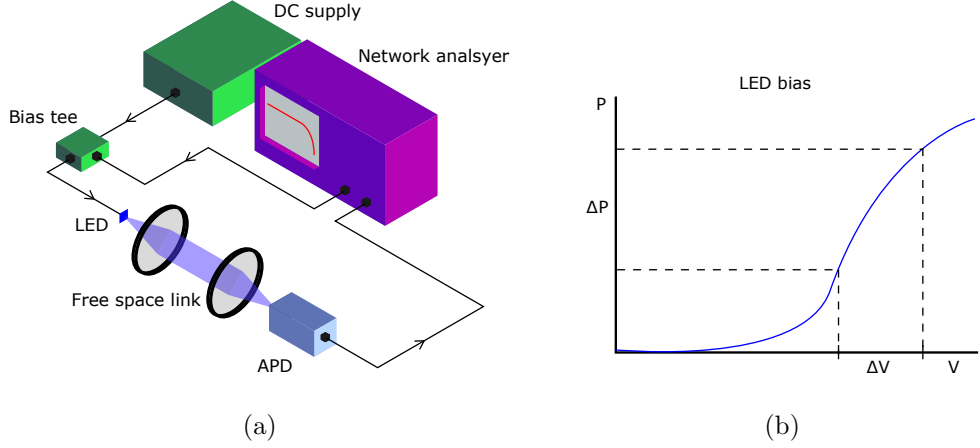
Figure 1.17: (a) Experimental setup for frequency response measurements and LED bias points. (b) Example response curve of a 39 μm diameter LED pixel biased at 80 mA.

sinusoidal optical signal will decrease. The optical bandwidth is defined as the frequency at which the optical power is reduced to 50%, or -3 dB. A photodiode collecting the optical signal converts the optical power to voltage in a linear fashion. However, the network analyser produces a frequency response curve in terms of electrical power, which is proportional to the square of voltage. Therefore, on the electrical response curve, the optical bandwidth corresponds to the -6 dB frequency.

A typical response curve for a micro-LED is shown in Figure 1.18(a). This data is from a 39 μm diameter circular micro-LED pixel biased at 80 mA. A summary of the characteristics of this device can be found in Table 1.1 under "Example 2". The data is interpolated in order to find the frequency values at the desired levels of loss, which in this case corresponds to 201.1 MHz for the optical bandwidth. The optical frequency response ($P(\omega)$) for a micro-LED can be approximated according to:

$$P(\omega) = \frac{1}{1 + (\omega\tau)^2}. \tag{1.1}$$

Here, ω is the angular frequency of the AC signal and τ is the carrier lifetime [3]. The optical bandwidth (f_{bw}) is then given by:
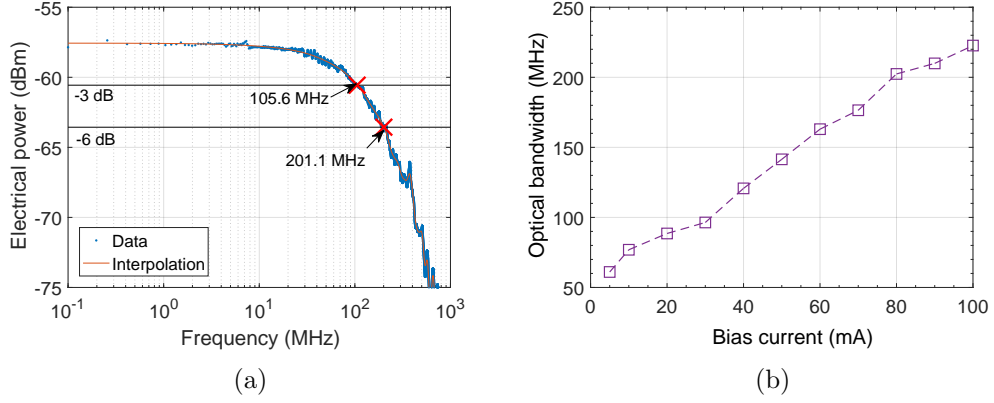
Figure 1.18: (a) Example modulation response curve of a 39 μm diameter GaN LED pixel biased at 80 mA. (b) Bandwidth dependency on bias current for a 39 μm diameter LED pixel.

$$f_{bw} = \frac{1}{2\pi\tau}. \tag{1.2}$$

The bandwidth is strongly dependent on the DC current supplied to the LED, as shown in Figure 1.18(b). As current density in an LED is increased, the density of carriers in the active area of the device increases, which increases the recombination rate, or equivalently decreases the carrier lifetime. Additionally, the device will emit more light, which may become problematic if the receiver is saturated. Equation 1.2 shows that decreased carrier lifetimes directly increase the bandwidth. This is the reason micro-LEDs exhibit high speed modulation characteristics, as they operate at higher current densities, and are not limited by capacitance like broad area devices. Recent research shows that LEDs fabricated using non-polar and semipolar crystal orientation materials show even higher bandwidth capabilities, due to the improved wavefunction overlap in quantum wells [70].

The CMOS-controlled micro-LED arrays used in this thesis show reduced modulation bandwidths when compared to bare micro-LEDs described above. An individual pixel in the 16×16 arrays has a maximum bandwidth of 110 MHz [55]. This limitation is likely due to two factors. Firstly, the CMOS driver itself has a frequency response

and a maximum switching frequency of 555 MHz. Above this, the driver is always in the off state and unable to modulate. Secondly, the modulation method involves full on-off switching of the LEDs, giving a higher modulation depth than the small signal, DC offset modulation used on bare devices. The bandwidth limitations could be lifted by using NMOS transistors as the driver, as they show improved switching speeds [71]. However, this would require the LEDs to be contacted through individual n-contacts, requiring a more complex fabrication method [24, 72].

1.3.5 Device list

As a number of different LED systems are used throughout this thesis, it is useful to summarise some of the key parameters and differences between each device. Table 1.1 shows the details for both micro-LED arrays and commercial devices used.

The "Example" devices were used in the previous subsections and in Chapter 2 to demonstrate characteristics of micro-LEDs. The devices used for multi-level communications in Chapter 2 are given the designation "MLC". The devices used for single photon communications in Chapters 4 and 5 are given the designation "SPC". The commercial devices "Blue LED", "RGB LED" and "Luxeon LED" are the commercially available OSRAM LD CQ7P, OSRAM LE RTDUW S2W and Lumileds LUXEON Z color line respectively.

1.4 Summary

This introductory chapter has covered the relevant background material for the work in this thesis. LEDs are common light sources in the modern world, and can be used as transmitters for OWC and VLC. Basic LED physics and operational principles have been discussed, and a broad description of optical communications has been presented. The state of the art indicates that by reducing LED pixel sizes below $100\,\mu m$, higher modulation bandwidths can be reached enabling higher data rates for communication.

Table 1.1: Summary of the CMOS controlled devices used in this thesis. Pixel dimensions are widths and diameters for square and circular pixels respectively.

Device designation	Device type	Array layout	Pixel shape	Pixel dimensions	Emission wavelength	Modulation bandwidth	Chapter appearance
Example 1	CMOS	16×16	Square	$99\,\mu m$	442 nm	≈ 110 MHz	1 & 2
Example 2	Bare micro-LED	4×4	Circular	$39\,\mu m$	450 nm	201 MHz	1
MLC array A	CMOS	16×16	Circular	$72\,\mu m$	405 nm	≈ 110 MHz	2
MLC array B	CMOS	16×16	Circular	$14\,\mu m$-$84\,\mu m$	405 nm	≈ 110 MHz	2
SPC array A	CMOS	16×16	Square	$99\,\mu m$	405 nm	≈ 110 MHz	4
SPC array B	CMOS	16×16	Square	$99\,\mu m$	450 nm	≈ 110 MHz	4 & 5
Blue LED	Commercial	1×1	Square	1 mm	450 nm	20 MHz	4
RGB LED	Commercial	2×2	Square	1 mm	450/520/632 nm	20 MHz	4 & 6
Luxeon LEDs	Commercial	1×1	Square	1 mm	Various	Unmeasured	6

To date, communication links up to 10 Gb/s have been demonstrated using advanced modulation formats, multiplexing techniques, and micrometer sized devices.

CMOS-controlled micro-LEDs provide a compact device with a high degree of control over optical emission. Such devices have been discussed in detail, including the device structures and assembly methods, system capability and performance characterisation. The CMOS-controlled micro-LEDs enable most of the results in the following chapters of this thesis.

Bibliography

[1] H. Round, "A note on carborundum," *Electrical World*, vol. 19, 1907.

[2] N. Zheludev, "The life and times of the LED - A 100-year history," *Nature Photonics*, vol. 1, pp. 189–192, 2007.

[3] E. F. Schubert, *Light emitting diodes*. Cambridge: Cambridge University Press, 2006.

[4] J. Pankove and J. Berkeyheiser, "A light source modulated at microwave frequencies," *IRE Transactions on Electron Devices*, vol. 9, no. 6, p. 503, 1962.

[5] H. Rupprecht, J. M. Woodall, and G. D. Pettit, "Efficient visible electroluminescence at 300K from $Ga_{1-x}Al_xAs$ p-n junctions grown by liquid-phase epitaxy," *Applied Physics Letters*, vol. 11, no. 3, pp. 81–83, 1967.

[6] A. H. Herzog, W. O. Groves, and M. G. Craford, "Electroluminescence of diffused $GaAs_{1-x}P_x$ Diodes with low donor concentrations," *Journal of Applied Physics*, vol. 40, no. 4, pp. 1830–1838, 1969.

[7] M. G. Craford, R. W. Shaw, A. H. Herzog, and W. O. Groves, "Radiative recombination mechanisms in GaAsP diodes with and without nitrogen doping," *Journal of Applied Physics*, vol. 43, no. 10, pp. 4075–4083, 1972.

Bibliography

[8] W. Groves, A. Herzog, and M. Craford, "The effect of nitrogen doping on GaAs$_{1-x}$P$_x$ electroluminescent diodes," *Applied Physics Letters*, vol. 19, no. 6, pp. 184–186, 1971.

[9] R. A. Logan, H. G. White, and W. Wiegmann, "Efficient green electroluminescence in nitrogen-doped gap p-n junctions," *Applied Physics Letters*, vol. 13, no. 4, pp. 139–141, 1968.

[10] S. Nakamura and S. Chichibu, *Introduction to nitride semiconductor blue lasers and light emitting diodes.* London: CRC Press, 2000.

[11] T. Seong, J. Han, H. Amano, and H. Morkoç, *III-Nitride based light emitting diodes and applications.* Singapore: Springer, 2013.

[12] S. Nakamura, S. Pearton, and G. Fasol, *The blue laser diode: the complete story.* Berlin: Springer, 2000.

[13] ""The 2014 Nobel Prize in Physics - Press Release". *Nobelprize.org.* Nobel Media A B 2014." `https://www.nobelprize.org/nobel_prizes/physics/laureates/2014/press.html`. Accessed 26/02/2018.

[14] M. H. Crawford, "LEDs for solid-state lighting: performance challenges and recent advances," *IEEE Journal on Selected Topics in Quantum Electronics*, vol. 15, no. 4, pp. 1028–1040, 2009.

[15] H. Ko. https://commons.wikimedia.org, January 2007. Reproduced under CC BY-SA 3.0.

[16] G. Landis. https://commons.wikimedia.org, July 2010. Reproduced under CC BY-SA 3.0.

[17] M. von Berg. https://commons.wikimedia.org, March 2014. Reproduced under CC BY-SA 3.0.

Bibliography

[18] "The Future of Display: A First Look at Samsungs 146-inch Modular TV, The Wall." https://news.samsung.com/. Accessed 02/03/2018.

[19] M. D. Al-Amri, M. El-Gomati, and M. S. Zubairy, *Optics in our time*. Cham: Springer International Publishing, 2016.

[20] P. H. Pathak, X. Feng, P. Hu, and P. Mohapatra, "Visible light communication, networking, and sensing: a survey, potential and challenges," *IEEE Communications Surveys & Tutorials*, vol. 17, no. 4, pp. 2047–2077, 2015.

[21] S. Rajbhandari, J. J. D. McKendry, J. Herrnsdorf, H. Chun, G. Faulkner, H. Haas, I. M. Watson, D. O'Brien, and M. D. Dawson, "A review of gallium nitride LEDs for multi-gigabit-per-second visible light data communications," *Semiconductor Science and Technology*, vol. 32, no. 2, pp. 1–44, 2017.

[22] T.-H. Do and M. Yoo, "An in-depth survey of visible light communication based positioning systems," *Sensors*, vol. 16, no. 5, p. 678, 2016.

[23] D. Halliday, R. Resnick, and J. Walker, *Fundamentals of physics*. New York: Wiley, 8th ed., 2008.

[24] E. Xie, M. Stonehouse, R. Ferreira, J. J. McKendry, J. Herrnsdorf, X. He, S. Rajbhandari, H. Chun, A. V. Jalajakumari, O. Almer, G. Faulkner, I. M. Watson, E. Gu, R. K. Henderson, D. C. O'Brien, and M. D. Dawson, "Design, fabrication and application of GaN-based micro-LED arrays with individual addressing by n-electrodes," *IEEE Photonics Journal*, vol. 9, no. 6, 2017.

[25] S. Dimitrov and H. Haas, *Principles of LED light communications*. Cambridge: Cambridge University Press, 2015.

[26] M. Usyal, C. Capsoni, Z. Ghassemlooy, A. Boucouvalas, and E. Udvary, *Optical wireless communications*. Cham: Springer, 2016.

Bibliography

[27] D. M. Boroson and B. S. Robinson, "The lunar laser communication demonstration: NASA's first step toward very high data rate support of science and exploration missions," *Space Science Reviews*, vol. 185, no. 1-4, pp. 115–128, 2014.

[28] J. A. Mendenhall, L. M. Candell, P. I. Hopman, G. Zogbi, D. M. Boroson, D. O. Caplan, C. J. Digenis, D. R. Hearn, and R. C. Shoup, "Design of an optical photon counting array receiver system for deep-space communications," *Proceedings of the IEEE*, vol. 95, no. 10, pp. 2059–2069, 2007.

[29] V. W. S. Chan, "Free-space optical communications," *Journal of Lightwave Technology*, vol. 24, no. 12, pp. 4750–4762, 2006.

[30] "Cisco visual networking index: forecast and methodology, 2016-2021." http://cisco.com/c/en/us/solutions/collateral/service-provider/ip-ngn-ip-next-generation-network/white_paper_c11-481360.pdf. Accessed 05/03/2018.

[31] M. Kavehrad, "Optical wireless applications: a solution to ease the wireless airwaves spectrum crunch," *Proc. of SPIE*, vol. 8645, p. 86450G, 2013.

[32] D. Karunatilaka, F. Zafar, V. Kalavally, and R. Parthiban, "LED based indoor visible light communications: state of the art," *IEEE Communications Surveys & Tutorials*, vol. 17, no. 3, pp. 1649–1678, 2015.

[33] H. Haas, L. Yin, Y. Wang, and C. Chen, "What is LiFi?," *Journal of Lightware Technology*, vol. 34, no. 6, pp. 1533–1544, 2015.

[34] A. M. Khalid, G. Cossu, R. Corsini, P. Choudhury, and E. Ciaramella, "1-Gb/s transmission over a phosphorescent white LED by using rate-adaptive discrete multitone modulation," *IEEE Photonics Journal*, vol. 4, no. 5, pp. 1465–1473, 2012.

[35] C. Kottke, J. Hilt, K. Habel, J. Vučić, and K.-D. Langer, "1.25 Gbit/s Visible Light WDM Link based on DMT Modulation of a Single RGB LED Luminary," *European Conference and Exhibition on Optical Communication*, p. We.3.B.4, 2012.

[36] "Pure LiFi." `https://purelifi.com`. Accessed 30/04/2018.

[37] R. Ferreira, E. Xie, J. McKendry, S. Rajbhandari, H. Chun, G. Faulkner, S. Watson, A. E. Kelly, E. Gu, R. V. Penty, I. H. White, D. C. O'Brien, and D. Dawons, Martin, "High bandwidth GaN-based micro-LEDs for multi-Gbps visible light communications," *IEEE Photonics Technology Letters*, vol. 28, no. 19, p. 1, 2016.

[38] D. Tsonev, D. C. O'Brien, E. Xie, E. Gu, G. Faulkner, H. Haas, H. Chun, J. J. D. McKendry, M. D. Dawson, and S. Rajbhandari, "LED Based Wavelength Division Multiplexed 10 Gb/s Visible Light Communications," *Journal of Lightwave Technology*, vol. 34, no. 13, pp. 3047–3052, 2016.

[39] K. Kikuchi, "Fundamentals of coherent optical fiber communications," *Journal of Lightwave Technology*, vol. 34, no. 1, pp. 157–79, 2015.

[40] M. L. Stevens, D. O. Caplan, B. S. Robinson, D. M. Boroson, and a. L. Kachelmyer, "Optical homodyne PSK demonstration of 1.5 photons per bit at 156 Mbps with rate-(1/2) turbo coding," *Optics Express*, vol. 16, no. 14, pp. 10412–20, 2008.

[41] D. Geisler and T. Yarnall, "Demonstration of 2.1 photon-per-bit sensitivity for BPSK at 9.94-Gb/s with rate- FEC," *Optical Fiber Communication Conference*, pp. 13–15, 2013.

[42] B. S. Robinson, A. J. Kerman, E. A. Dauler, R. J. Barron, D. O. Caplan, M. L. Stevens, J. J. Carney, S. A. Hamilton, J. K. W. Yang, and K. K. Berggren, "781 Mbit/s photon-counting optical communications using a superconducting nanowire detector," *Optics Letters*, vol. 31, no. 4, pp. 444–446, 2006.

[43] E. Fisher, I. Underwood, and R. Henderson, "A reconfigurable single-photon-counting integrating receiver for optical communications," *IEEE Journal of Solid-State Circuits*, vol. 48, no. 7, pp. 1638–1650, 2013.

[44] D. Chitnis, L. Zhang, H. Chun, S. Rajbhandari, G. Faulkner, D. O'Brien, and S. Collins, "A 200 Mb/s VLC demonstration with a SPAD based receiver," *2015 IEEE Summer Topicals Meeting Series, SUM 2015*, vol. 3, pp. 226–227, 2015.

[45] H. Zimmermann, B. Steindl, M. Hofbauer, and R. Enne, "Integrated fiber optical receiver reducing the gap to the quantum limit," *Scientific Reports*, vol. 7, no. 1, p. 2652, 2017.

[46] B. S. Robinson, D. O. Caplan, M. L. Stevens, R. J. Barron, E. A. Dauler, and S. A. Hamilton, "1.5-photons/bit photon-counting optical communications using Geiger-mode avalanche photodiodes," *LEOS summer topical meetings*, 2005.

[47] M. M. Willis, A. J. Kerman, M. E. Grein, J. Kansky, B. R. Romkey, E. A. Dauler, D. Rosenberg, B. S. Robinson, D. V. Murphy, and D. M. Boroson, "Performance of a multimode photon-counting optical receiver for the NASA lunar laser communications demonstration," *Proc. International Conference on Space Optical Systems and Applications (ICSOS)*, 2012.

[48] ITU, Geneva, Switzerland, "Recommendation G.975.1: forward error correction for high bit-rate DWDM submarine systems," 2005.

[49] W. Shieh and I. Djordjevic, *OFDM for optical communications*. London: Elsevier, 2010.

[50] S. X. Jin, J. Li, J. Z. Li, J. Y. Lin, and H. X. Jiang, "GaN microdisk light emitting diodes," *Applied Physics Letters*, vol. 76, no. 5, pp. 631–633, 2000.

[51] H. X. Jiang, S. X. Jin, J. Li, J. Shakya, and J. Y. Lin, "III-nitride blue microdisplays," *Applied Physics Letters*, vol. 78, no. 9, pp. 1303–1305, 2001.

Bibliography

[52] E. Virey, "Is the microLED the next display revolution?," *Compound Semiconductor*, July 2017.

[53] "Plessey demonstrates microLED-based AR and VR HUD Concept to industry leaders during CES 2018." http://www.plesseysemiconductors.com. Accessed 02/03/2018.

[54] "Facebook VR firm buys Strathclyde University spin-out." `http://futurescot.com/facebook-vr-firm-buys-strathclyde-university-spin/`. Accessed 02/03/2018.

[55] J. J. D. McKendry, D. Massoubre, S. Zhang, B. R. Rae, R. P. Green, E. Gu, R. K. Henderson, A. E. Kelly, and M. D. Dawson, "Visible-light communications using a CMOS-controlled micro-light-emitting-diode array," *Journal of Lightwave Technology*, vol. 30, no. 1, pp. 61–67, 2012.

[56] D. Tsonev, H. Chun, S. Rajbhandari, J. J. D. McKendry, S. Videv, E. Gu, M. Haji, S. Watson, A. E. Kelly, G. Faulkner, M. D. Dawson, H. Haas, and D. O'Brien, "A 3-Gb/s single-LED OFDM-based wireless VLC link using a gallium nitride μLED," *IEEE Photonics Technology Letters*, vol. 26, no. 7, pp. 637–640, 2014.

[57] J. J. D. McKendry, R. P. Green, A. E. Kelly, Z. Gong, B. Guilhabert, D. Massoubre, E. Gu, and M. D. Dawson, "High-speed visible light communications using individual pixels in a micro light-emitting diode array," *IEEE Photonics Technology Letters*, vol. 22, no. 18, pp. 1346–1348, 2010.

[58] J. J. D. McKendry, B. R. Rae, Z. Gong, K. R. Muir, B. Guilhabert, D. Massoubre, E. Gu, D. Renshaw, M. D. Dawson, and R. K. Henderson, "Individually addressable AlInGaN micro-LED arrays with CMOS control and subnanosecond output pulses," *IEEE Photonics Technology Letters*, vol. 21, pp. 811–813, Jun 2009.

Bibliography

[59] B. R. Rae, K. R. Muir, Z. Gong, J. McKendry, J. M. Girkin, E. Gu, D. Renshaw, M. D. Dawson, and R. K. Henderson, "A CMOS time-resolved fluorescence lifetime analysis micro-system," *Sensors*, vol. 9, no. 11, pp. 9255–9274, 2009.

[60] Z. Gong, H. X. Zhang, E. Gu, C. Griffin, M. D. Dawson, V. Poher, G. Kennedy, P. M. French, and M. A. Neil, "Matrix-addressable micropixellated InGaN light-emitting diodes with uniform emission and increased light output," *IEEE Transactions on Electron Devices*, vol. 54, no. 10, pp. 2650–2658, 2007.

[61] J. Mckendry, *Micro-pixellated AlInGaN light-emitting diode arrays for optical communications and time-resolved fluorescence lifetime measurements*. PhD thesis, University of Strathclyde, 2011.

[62] S. Zhang, *High performance III-nitride light-emitting diodes for visible light communications and micro-displays*. PhD thesis, University of Strathclyde, 2015.

[63] S. Zhang, Z. Gong, J. J. D. McKendry, S. Watson, A. Cogman, E. Xie, P. Tian, E. Gu, Z. Chen, G. Zhang, A. E. Kelly, R. K. Henderson, and M. D. Dawson, "CMOS-controlled color-tunable smart display," *IEEE Photonics Journal*, vol. 4, pp. 1639–1646, oct 2012.

[64] Y. Wang, B. R. Rae, R. K. Henderson, Z. Gong, J. McKendry, E. Gu, M. D. Dawson, G. A. Turnbull, and I. D. W. Samuel, "Ultra-portable explosives sensor based on a CMOS fluorescence lifetime analysis micro-system," *AIP Advances*, vol. 1, no. 3, 2011.

[65] A. Zarowna-Dabrowska, S. L. Neale, D. Massoubre, J. McKendry, B. R. Rae, R. K. Henderson, M. J. Rose, H. Yin, J. M. Cooper, E. Gu, and M. D. Dawson, "Miniaturized optoelectronic tweezers controlled by GaN micro-pixel light emitting diode arrays," *Optics Express*, vol. 19, no. 3, p. 2720, 2011.

[66] B. Guilhabert, D. Massoubre, E. Richardson, J. J. D. McKendry, G. Valentine, R. K. Henderson, I. M. Watson, E. Gu, and M. D. Dawson, "Sub-micron lithog-

raphy using InGaN micro-LEDs: mask-free fabrication of LED arrays," *IEEE Photonics Technology Letters*, vol. 24, no. 24, pp. 2221–2224, 2012.

[67] S. Zhang, S. Watson, J. J. D. McKendry, D. Massoubre, A. Cogman, E. Gu, R. K. Henderson, A. E. Kelly, and M. D. Dawson, "1.5 Gbit/s multi-channel visible light communications using CMOS-controlled GaN-based LEDs," *Journal of Lightwave Technology*, vol. 31, pp. 1211–1216, Apr 2013.

[68] A. D. Griffiths, M. S. Islim, J. Herrnsdorf, J. J. D. McKendry, R. Henderson, H. Haas, and E. Gu, "CMOS-integrated GaN LED array for discrete power level stepping in visible light communications," *Optics Express*, vol. 25, no. 8, pp. A338 – A345, 2017.

[69] B. Rae, *Micro-systems for time-resolved fluorescence analysis using CMOS single-photon avalanche diodes and micro-LEDs.* PhD thesis, University of Edinburgh, 2009.

[70] M. Monavarian, A. Rashidi, A. A. Aragon, S. H. Oh, A. K. Rishinaramangalam, S. P. DenBaars, and D. Feezell, "Impact of crystal orientation on the modulation bandwidth of InGaN/GaN light-emitting diodes," *Applied Physics Letters*, vol. 112, no. 4, p. 041104, 2018.

[71] A. V. Jalajakumari, E. Xie, J. McKendry, E. Gu, M. D. Dawson, H. Haas, and R. K. Henderson, "High-speed integrated digital to light converter for short range visible light communication," *IEEE Photonics Technology Letters*, vol. 29, no. 1, pp. 118–121, 2017.

[72] S. Rajbhandari, H. Chun, G. Faulkner, K. Cameron, A. V. N. Jalajakumari, R. Henderson, D. Tsonev, M. Ijaz, Z. Chen, H. Haas, E. Xie, J. J. D. McKendry, J. Herrnsdorf, E. Gu, M. D. Dawson, and D. O'Brien, "High-speed integrated visible light communication system: device constraints and design considerations,"

Bibliography

IEEE Journal on Selected Areas in Communications, vol. 33, no. 9, pp. 1750–1757, 2015.

Chapter 2

Discrete Multi-Level Communications

In this chapter, a method for generating discrete light levels with the CMOS-controlled micro-LEDs is presented, characterised and applied to visible light communications. The device provides a "digital-to-light" converter, removing the need for a digital-to-analogue converter. First, the nonlinearity issues with using LEDs for VLC are discussed, with particular focus on digitised, multi-level outputs. Operational methods for digital-to-light conversion using the micro-LED arrays are then introduced. The device is then used to perform discrete PAM, as an initial demonstration of multi-level communications. To improve upon spectral efficiency, discrete OFDM is investigated, work performed in collaboration with colleagues from the University of Edinburgh. Finally, the limitations of the current system are discussed, with opportunities for further investigation.

2.1 Multi-level Signals and Transmitter Linearity

As discussed in introductory Section 1.2, VLC can be performed by modulating the intensity of an optical source according to a digital data stream. In most VLC systems

employing LEDs, a binary data stream is converted to an analogue driving signal using a digital-to-analogue converter (DAC) and transconductance amplifier [1]. In the simplest case, this can be used to employ OOK by switching the LED output intensity between a high and low state to represent a high and low logic level, respectively. Modulating in this manner has low spectral efficiency, defined as the data rate that can be transmitted over a given bandwidth. OOK transmission has a spectral efficiency of 1 bits/s/Hz, limiting the achievable data rate for the system's modulation bandwidth. It is therefore desirable to move to higher order modulation schemes with improved spectral efficiencies, in order to maximise data rate.

A straightforward step to increase spectral efficiency is to make use of more than two output power levels from the transmitting LED. This method is pulse amplitude modulation (PAM), as discussed in Section 1.2.2, and allows multiple bits to be transmitted by each symbol, increasing spectral efficiency. The use of $M = 2^N$ power levels allows N bits to be sent with each symbol period. The transmission scheme is then referred to as M-PAM. This is a single carrier scheme, and its performance is therefore degraded by baseline wander and low frequency interference from other light sources. This is of particular importance if the VLC link is targeting a LiFi type application [2]. Multi-carrier modulation schemes such as orthogonal frequency division multiplexing (OFDM) can overcome these problems through use of adaptive bit and energy loading algorithms, allowing subcarriers with low signal-to-noise ratio (SNR) to be skipped. A more detailed description of OFDM can be found in Section 1.2.2.

When transmitting multiple levels in PAM, or signals with high peak to average power ratios (PAPR) in OFDM, a desirable quality for the optical transmitter is a linear response. Nonlinearities in the transmitter will distort the optical signals making it more difficult to accurately receive the data stream. Figure 2.1(a) shows the current-to-luminosity relationship for an example 99×99 µm GaN LED pixel, emitting at 442 nm, driven under DC conditions (array "Example 1" in Table 1.1). The relationship is highly nonlinear, as LED efficiency decreases with increasing current. Furthermore,
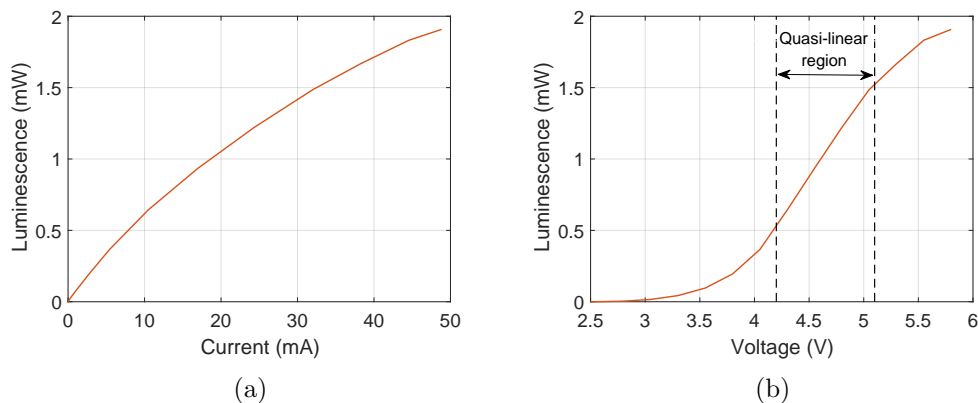
Figure 2.1: Nonlinear response of an example 99×99 µm GaN micro-LED to (a) current and (b) voltage. The non-linearities restrict the useful range to the quasi-linear region.

LEDs are typically driven using a voltage signal, rather than current. The voltage-current relationship adds further non linearities to the voltage-luminosity relationship, which can be seen in Figure 2.1(b). When transmitting higher order modulation scheme waveforms with a single LED care must be taken to operate in the quasi-linear region, indicated by dashed lines, where the response is approximately linear. However, this restricts the dynamic range, of the system significantly, which limits BER performance and channel capacity.

A potentially simple way to generate discrete light levels and avoid the nonlinearity effects is to use groups of LEDs as an optical transmitter, instead of one. There are then two possible approaches to generate and control the discrete output levels. The first is to have a fixed number of LEDs, and control the amount of current supplied to each group [1], adjusting the emitted power to maintain a linear step between each set. The second is to control the number of active LEDs in each group [3]. With driving conditions maintained the same, a group of twice as many LEDs should produce twice as much optical power, allowing linear steps to be built up. Employing multiple LEDs with only *on* and *off* state driving conditions avoids the linearity restrictions of a single LED, provided each element can be equally imaged onto the receiver. In the simplest case, arrays of LEDs can be used to generate multi-level PAM signals. Furthermore,

the series of output power levels can be used to produce discrete OFDM signals [1], potentially providing higher spectral efficiencies than PAM.

2.2 CMOS Controlled Array

Discrete optical signal generation can be performed in a highly compact integrated manner by utilising the CMOS-controlled micro-LEDs discussed in Section 1.3. The device allows input CMOS logic signals to control groups of LEDs in an on-off fashion, which has previously been used to transmit multiple parallel OOK signals [4]. Here, discrete multi-level signals can be generated according to the second method described above. Importantly, as the device directly takes CMOS logic inputs, there is no need for a digital-to-analogue converter (DAC), so it effectively operates as a "digital-to-light" converter [5].

2.2.1 Device Details

Two CMOS-controlled micro-LED array layouts have been used for the following results (devices "MLC array A" and "MLC array B" in Table 1.1). The first consists of uniform $72\,\mu\mathrm{m}$ diameter circular pixels on a $100\,\mu\mathrm{m}$ pitch (array A). A micrograph of array A is shown in Figure 2.2 with 15 enabled pixels. The second array layout consists of varying pixel sizes from $84\,\mu\mathrm{m}$ down to $14\,\mu\mathrm{m}$ (array B), also on the same $100\,\mu\mathrm{m}$ pitch. The arrays are otherwise identical, and both exhibit modulation bandwidths of $\approx 110\,\mathrm{MHz}$ due to the connection to CMOS electronics. The emission wavelength of the devices is centred on 405 nm as early investigations showed devices of this wavelength provided the most promising results in this configuration [5]. This is likely due to the particular on-off scheme used, rather than more common DC-biased AC modulation. Furthermore, such violet-emitting devices are suitable for white light generation when combined with a suitable phosphor or other LED elements with different wavelengths. This enables simultaneous lighting and communications for a "Li-Fi" style network.
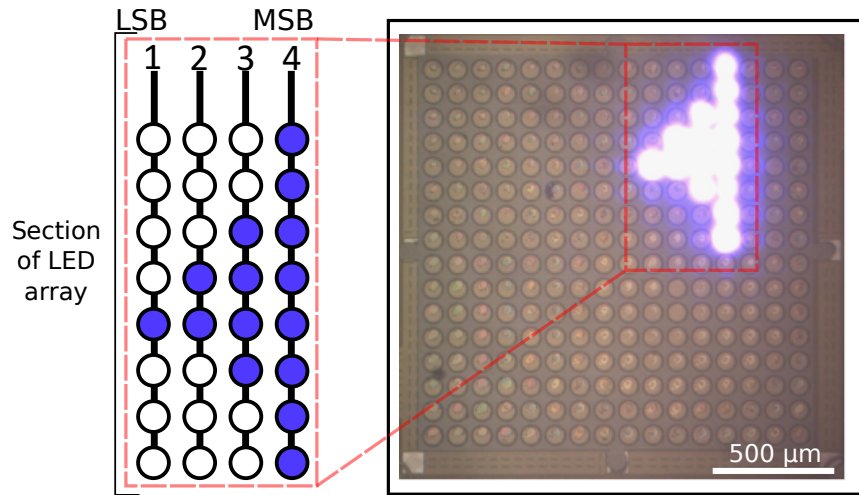
Figure 2.2: Micrograph of array A with an example set of pixels enabled.

The CMOS electronics allow high-speed modulation of each column of micro-LEDs in the array independently through a set of parallel connections, accessible using the VLC board described in Section 1.3.3. The number of active pixels, i.e. pixels that will respond to the modulated input, is specified through a slower set of connections, not suited for communication speeds. By selecting active pixels in binary-weighted columnar groups, as shown in Figure 2.2, the parallel logic inputs can be used to generate levels in a binary fashion. This is shown schematically in Figure 2.3. Here, a 2×2 subsection of the 16×16 array is shown. LEDs in the same column will modulate together according to their logic inputs. Inactive LED elements are indicated in black, and will emit no light regardless of the logic input. Active LED elements are indicated in white when not emitting, and violet when emitting, according to the logic input. As there are twice as many active LEDs, resulting in double the output power in column 2, the 3 active LEDs can be used to generate a 4-level output. This process can then be extended to N columns, yielding $M = 2^N$ discrete levels, suitable for M-PAM.

Generating multi-level signals in a binary fashion makes efficient use of the 16 available columns. However, it was observed experimentally that doing so creates signal distortions at the transitions between levels, as several pixels switch off at the
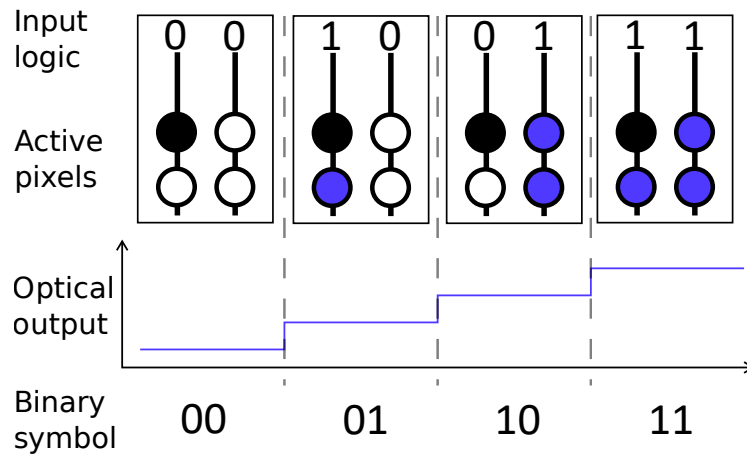
Figure 2.3: Example of binary multi-level generation on a 2×2 subsection of the 16×16 array.

same time as several others switch on. This can cause a sharp dip in signal at the transition, which can be an issue when performing discrete OFDM communications. Alternatively, the micro-LED array can generate multi-level signals in a linear fashion, rather than binary. This is shown schematically in Figure 2.4. To generate higher power levels, more columns are activated, with the same output power per column. While this approach is less efficient in its use of LED columns, it avoids the signal distortions at transitions as fewer LED elements are switched at once. In the following sections, the binary approach was used in most cases, however, for the low-order discrete OFDM signals, the linear method was used. At higher levels of discretisation, a combination of the approaches was used, as it was no longer possible to generate enough levels linearly with the available columns. This requires careful processing of the input data signal into suitable parallel streams.

2.2.2   Linearity of Optical Power

The linearity of the output power levels from array A was assessed by measuring the optical power from the whole array with increasing numbers of emitting pixels. The pixels were modulated with an on-off signal at 50 MHz, with an on-state bias of 6.6 V,
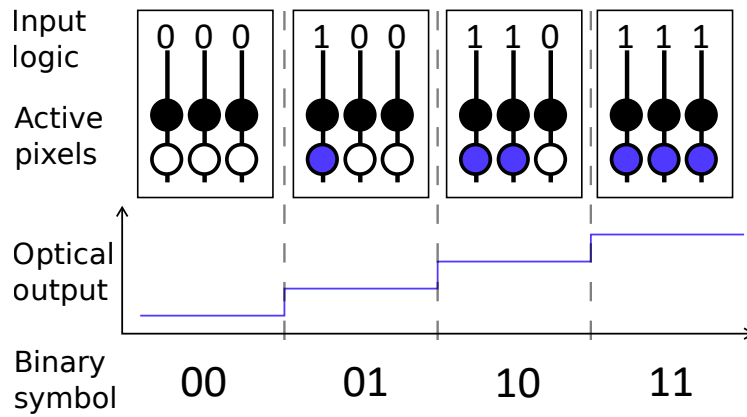
Figure 2.4: Example of linear multi-level generation on a 2×3 subsection of the 16×16 array.
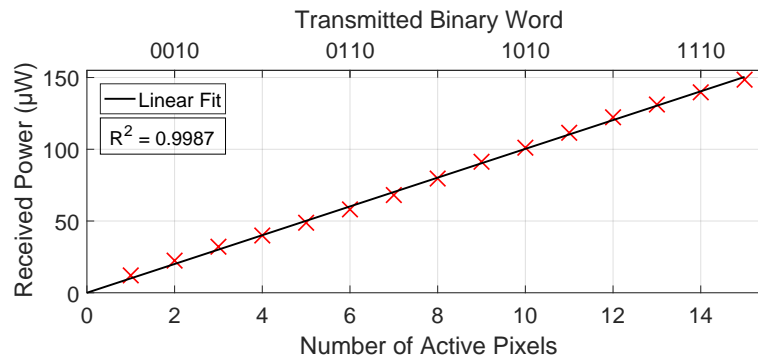
Figure 2.5: Linearity of optical power output at 50% duty cycle as number of active pixels is increased.

consuming 15.7 mA per pixel. Optical power was measured at a distance of 3 cm from the array with a 9.5 mm diameter power meter head. The resulting linearity is shown in Figure 2.5.

The response is very linear, and a significant improvement over the luminosity-to-voltage relationship of a single LED. At higher levels, however, the linearity does begin to degrade. This is attributed to electrical crosstalk and self-heating within the device [6]. As these devices were not specifically designed for this purpose, there is scope for improvement in both the CMOS electronics and LED array designs. Nevertheless, the linearity indicates that at least 16 levels should be available for discrete communications.
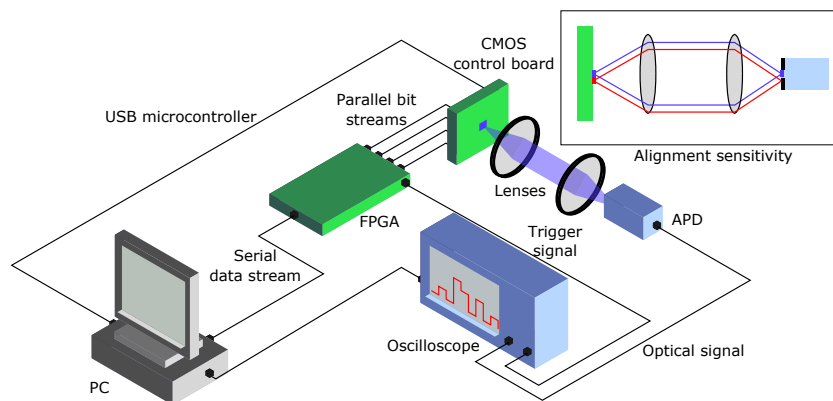
Figure 2.6: Schematic of the experimental setup with alignment sensitivity schematic inset. The lens pair provides a magnification of 0.32 to enable imaging of the LED array onto the APD active area, however, the system is very sensitive to misalignment.

2.2.3 Experimental Setup

The experimental setup for the following communication results is shown schematically in Figure 2.6. A pseudorandom bit sequence (PRBS) is prepared in MATLAB$^{\text{TM}}$ and processed to form suitable parallel data sequences for either PAM or discrete OFDM signals. The data sequence is loaded onto a field programmable gate array (FPGA) board (Opal Kelly XEM3010), which outputs parallel logic streams for controlling the on-off switching of the LED columns. The output from the FPGA repeats indefinitely, with the length of the PRBS limited by the available memory on the board. An extra output sends a trigger signal to the oscilloscope at the start of each data sequence. The parallel data outputs of the FPGA are connected to the VLC control board, which has 16 parallel input channels accessible through SMA connectors, as shown in Figure 2.7. A USB microcontroller on the CMOS control board selects the active pixels in the array, and is controlled through an application on the PC. The control board requires an external 3.3 V supply to power the CMOS electronics and micro-LED array, and the LED ground can be adjusted with respect to global ground to increase LED luminosity [4].

The optical signals from the LED are collected by a pair of lenses (Thorlabs LA1951-
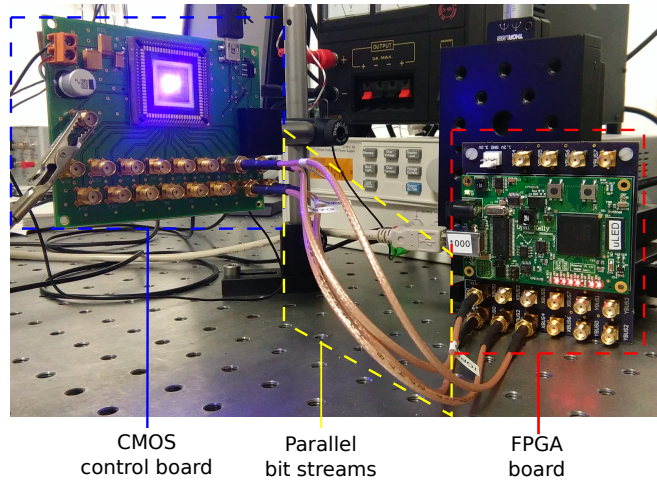
Figure 2.7: Photograph of the micro-LED array in the CMOS control board, with parallel connection to the FPGA.

A and C240TME-A, focal lengths 25.4 mm and 8 mm respectively) onto the active area of an avalanche photodiode (APD) (Hamamatsu C5658 for PAM results, Hamamatsu S8664-05k for OFDM results) at a distance of 70 mm. The lenses provide a magnification of 0.32, enabling the majority of the 1.6 mm LED array to be imaged onto the 0.5 mm diameter active area of the APD. The signal from the APD is collected by the oscilloscope and returned to MATLAB$^{\text{TM}}$ for offline processing of the data.

The current setup is extremely sensitive to optical alignment due to the small active area of the APD. The inset of Figure 2.6 shows the problem schematically in an exaggerated manner. While the LED pixel indicated in blue is imaged onto the active area of the detector, the adjacent pixel in red misses entirely. In the practical system, pixels around the edge of the active selection may not be completely imaged on the APD active area, reducing the received optical power and heavily distorting the signal. Slight changes in the lens arrangement result in significant variations in signal quality. However, it is important to note this is a limitation of the optical arrangement, and not the discrete level micro-LED array approach.

2.3   Communication Results

Data communications using PAM and discrete OFDM were performed using the setup described above. The following subsections detail the results obtained for 4-PAM, 8-PAM and a discussion of higher order limitations. Following this are the results for discrete OFDM, and details on the system limitations and potential for further improvement. The results for PAM were obtained using array A, with uniform pixel sizes. The OFDM results used array B, where the pixel size variation provided a level of flexibility in finding a set of uniform optical power levels.

2.3.1   Discrete 4 level Pulse Amplitude Modulation

Using three active LEDs on array A, one and two pixels on channels 1 and 2, respectively, 4-PAM signals were generated and processed. Figure 2.8 shows an example of a captured trace at 100 MSamples/s, with the transmitted symbol indicated above. With a high frequency cut-off of 1 GHz, the APD response does not limit the communication performance. The optical output, indicated by the blue solid trace, follows the expected 4-level waveform, indicated in red dashed lines, quite closely. The signal was processed offline in MATLAB^{TM} by averaging the central oscilloscope samples for each transmitted symbol and comparing the result to a set of thresholds to determine which symbol was transmitted. The resulting set of symbols can the be converted to a bit stream and compared to the stream that was originally generated on the PC. This method successfully decoded the stream without error, resulting in a data rate of 200 Mb/s, as 2 bits are transmitted per symbol. A PRBS of length 1.64×10^4 was transmitted, limited by the oscilloscope memory, so the BER at this data rate is below 6.10×10^{-5}, which can be corrected for using forward error correction (FEC) [7]. Also shown in Figure 2.8 are eye diagrams at 50 and 100 MSamples/s, 100 and 200 Mb/s respectively. The 4 levels are clear in both eye diagrams, and the eyes are open, indicating a good quality communication link.
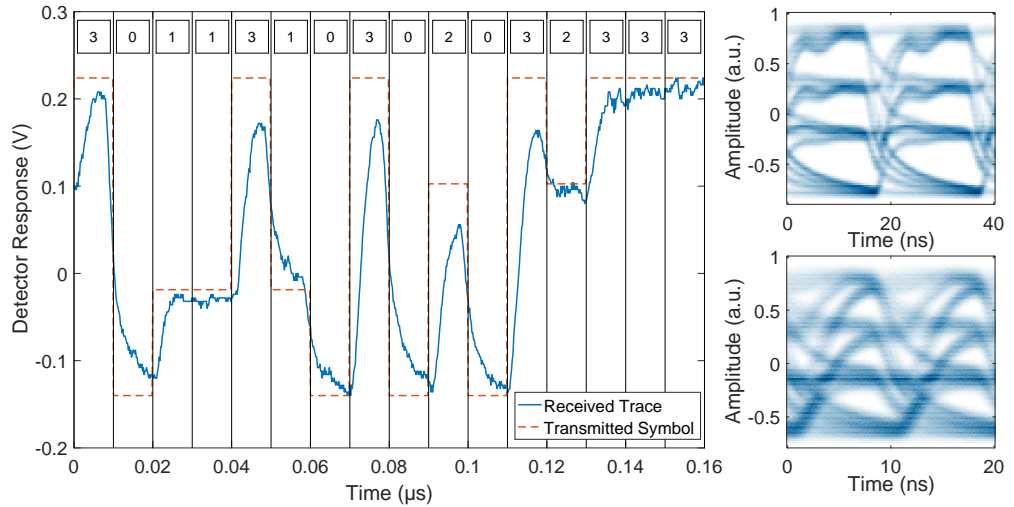
Figure 2.8: Received 4-PAM optical signal at 100 MSamples/s (left), with the transmitted symbol indicated above, and an expected ideal waveform in red. Eye diagrams for 50 MSamples/s (upper right) and 100 MSamples/s (lower right).

The limitation on symbol rate in these results is from the FPGA board, as it cannot produce a stable output at frequencies above 100 MHz. It is likely that slightly higher data rates could be obtained with a faster FPGA, as the modulation bandwidth of the CMOS-controlled micro-LED array is 110 MHz, and the eye diagram at 100 MSamples/s is still widely open. Nevertheless 4-PAM transmission shows an improvement in spectral efficiency over on-off keying, transmitting at 2 bits/s/Hz.

2.3.2   Higher Order Discrete Pulse Amplitude Modulation

Extension of the system to a third channel allows 8-PAM signals to be transmitted. This increases spectral efficiency as more bits are transmitted per symbol. However, with the increased number of optical power levels, baseline wander (BLW) in the system becomes problematic. The APD used (Hamamatsu C5658) is AC coupled, with a low-frequency cutoff at 50 kHz. This causes the received trace on the oscilloscope to drift with the low-frequency components of the signal, making it difficult to decode using thresholds. At 50 MSamples/s a bit error ratio (BER) of 1.18×10^{-2} was recorded.
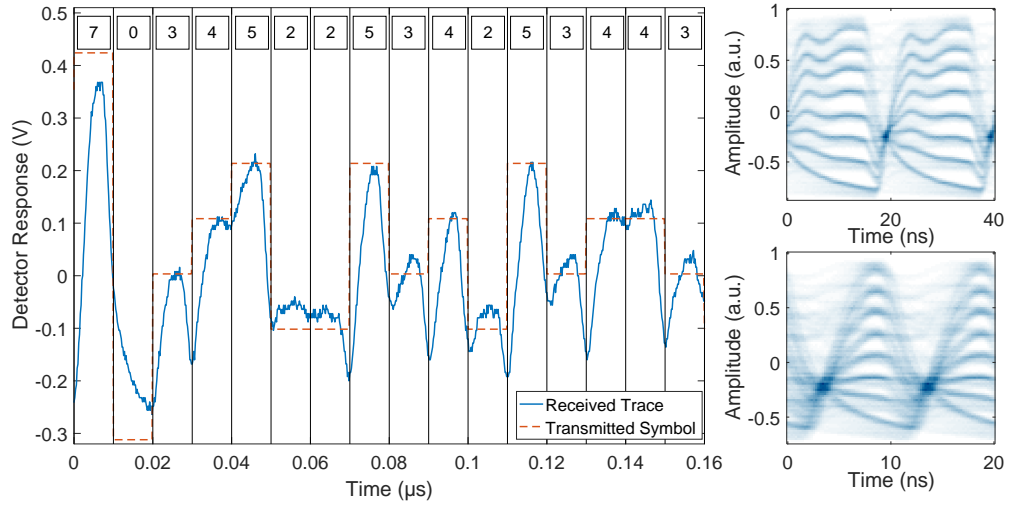
Figure 2.9: Received 8-PAM optical signal at 100 MSamples/s (left). Eye diagrams for 50 MSamples/s (upper right) and 100 MSamples/s (lower right).

In order to improve on this poor BER performance, data streams were encoded to maintain DC balance over every 2 symbols. Each data symbol is followed by its opposite, to balance around the central symbol. For example, a symbol of 7 is followed by 0, 6 followed by 1, and so on. With this encoding method it was possible to transmit at 100 MSamples/s and decode without error. The data stream was 3.28×10^4 bits long, therefore the BER is below 3.05×10^{-5} The example trace and eye diagrams are shown in Figure 2.9. Unfortunately, this encoding method introduces a high overhead cost, as only 50% of the symbols are carrying actual data. Therefore, the resulting data rate is 150 Mb/s; slower than that of 4-PAM transmission. As before, the symbol rate cannot be increased as it is limited by the FPGA.

With an alternative receiver setup, such as a DC coupled photoreceiver with a filter to reject ambient light, no DC balancing would be required. This would allow every symbol to carry useful information, yielding a data rate of 300 Mb/s with a spectral efficiency of 3 bits/s/Hz.

Naturally, the system can be further extended to include additional channels and make use of higher order PAM signals. However, with a 4th channel, 16-PAM trans-

mission yielded a BER of 7.02×10^{-4} at 25 MSamples/s. As the same DC balancing scheme is required to counteract BLW, the data rate is only 50 Mb/s. As there is no gain in data rate, higher orders are of limited usefulness. Furthermore, at 16-PAM and above, nonlinearity in output power levels becomes more significant. Intersymbol interference and multi-level penalty become ever-increasing issues. It is possible that, with an device fabricated specifically for discrete communications and a more suitable receiver, higher order PAM will be feasible.

2.3.3 Discrete Orthogonal Frequency Division Multiplexing

The following results were performed in collaboration with the colleagues from the LiFi Research and Development Centre, University of Edinburgh, utilising their expertise in OFDM transmission. Generation of discrete level OFDM starts with a more conventional analogue OFDM waveform, prepared in MATLAB$^{\text{TM}}$. A general description of OFDM waveform generation can be found in Section 1.2.2. Here, a PRBS is produced and modulated into M-ary quadrature amplitude modulation (M_k-QAM) symbols which are mapped into multiple subcarriers. M_k is the constellation size that is allocated based on the estimated SNR of the system. Hermitian symmetry is imposed on the subcarriers, followed by an inverse fast fourier transform (IFFT) to ensure real-valued OFDM output, as required for optical communications. The number of subcarriers is set as $N_{FFT} = 128$, ensuring statistical significance of multiple frames given that the FPGA has limited memory available. Trial experiments with different cyclic prefix lengths were performed, and it was determined that a length of $N_{CP} = 5$ was sufficient to avoid inter-symbol interference. Finally, the OFDM waveform is filtered using a root-raised cosine pulse shaping filter, and clipped at $|x| \leq 4\sigma_s$, where x_s and σ_s are the OFDM waveform and its standard deviation, respectively [8].

In order to transmit the OFDM waveform using discrete levels from the LED array, the analogue waveform must be digitised. Experiments were performed using 8, 16 and 32 level outputs, corresponding to 3, 4 and 5 bit resolution digitisation of the waveforms.
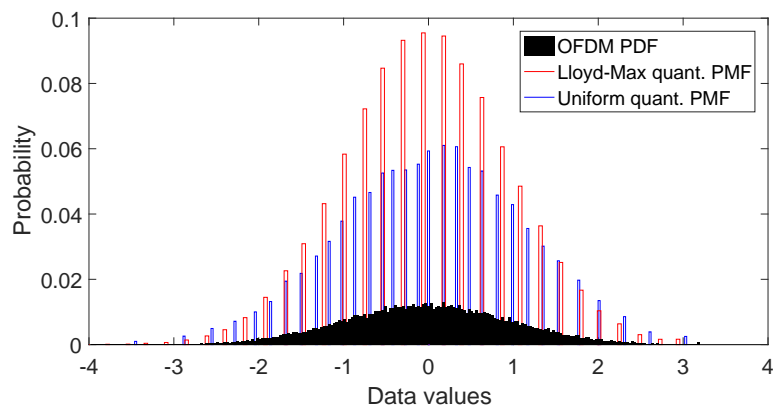
Figure 2.10: Probability distribution function of a typical OFDM waveform, with the probability mass function for 5 bit uniform and Lloyd-Max quantisations.

Two quantisation methods were adopted from source coding literature for this process: uniform quantisation and Lloyd-Max quantisation [9]. Uniform quantisation equally spaces the discrete levels across the expected distribution of the OFDM waveform. However, OFDM waveforms follow a Gaussian distribution, so certain power ranges occur more often than others. Lloyd-Max quantisation puts a higher and lower density of discrete levels in the more and less probable power ranges, respectively [10]. This results in a narrower spacing between discrete levels around the central, high probability waveform values, and wider spacing on the outer, low probability edges. Figure 2.10 shows the probability distribution function (PDF) of the OFDM waveform, with the probability mass functions (PMFs) of uniform quantisation and Lloyd-Max quantisation for 32-level discretisation.

Once the waveform has been digitised, the discrete levels are mapped to optical levels on the CMOS-controlled LED array. Array B was used for flexibility in defining linearly stepped optical levels with varying pixel sizes. Fine tuning the optical outputs was required in order to counterbalance some variations in optical performance of the LED elements. Discrete levels were generated using a combination of the binary and linear methods discussed above. Once the active LED pattern and LED column arrangement was known, the discrete OFDM signal could be mapped to the LEDs
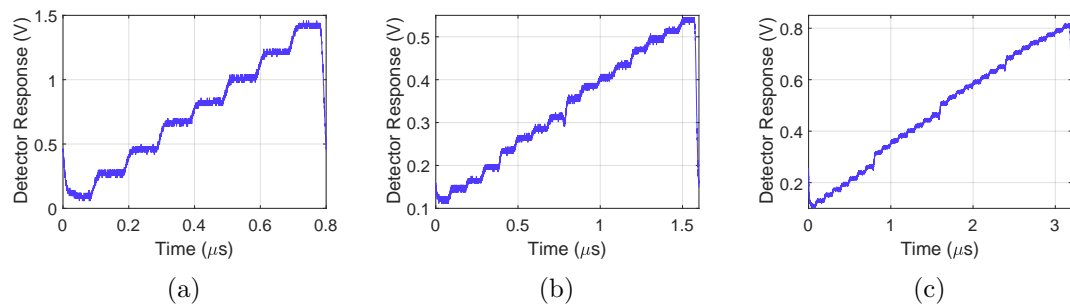
Figure 2.11: (a) 8, (b) 16 and (c) 32 discrete levels generated using array B for OFDM transmission. Note that the detector response here is positive, as the APD used for the OFDM results is not AC coupled. Additionally, the range of voltages varies in each case as the uniformity of levels was prioritised when aligning, rather than maximising dynamic range.

through the parallel outputs of the FPGA. The best performing linear outputs for 8, 16 and 32 discrete levels are shown in Figure 2.11, allowing 3, 4 and 5 bit discretisation. Here the output was set at 10 MHz, transmitting the levels sequentially.

Figure 2.11(a) shows the 8 discrete levels form clear, linear steps. Figure 2.11(b) shows the 16 level output still has good linearity, however, the central transition suffers from a dip in power as several LEDs in the array switch off while others switch on. This has been avoided for most transitions using the linear level generation method, however the availability of columns in the array forces some levels to be generated in a binary fashion. Figure 2.11(c) shows the 32 level output suffers further nonlinearities. Larger jumps at the 8th, 16th and 24th transition are necessary to maintain increasing levels at higher ranges, otherwise the top 8 levels begin to roll over and merge into one.

To transmit data with discrete OFDM the FPGA was operated at its maximum stable output frequency of 100 MHz. With an oversampling of 5 samples per symbol, and the hermitian symmetry requirement of OFDM, this restricts the system bandwidth to 10 MHz. Waveforms are captured by the oscilloscope and processed in MATLAB$^{\text{TM}}$, where parameters such as signal-to-noise ratio (SNR) can be obtained. In principle, higher collected optical power contributes to a higher SNR. However, care must be taken to avoid detector saturation, and excess optical power can increase shot noise in

Table 2.1: Average SNR for uniform and Lloyd-Max quantisation with 3, 4, 5 bit resolution.

Quantisation	Bit resolution		
method	3	4	5
Uniform	13.24 dB	16.11 dB	13.95 dB
Lloyd-Max	16.75 dB	18.93 dB	15.92 dB

the APD. Here, the optical alignment was optimised to maximise the amount of light reaching the detector, while also maintaining the linear discrete power levels desired.

The resulting SNR for each quantisation resolution and method are shown in Table 2.1. Lloyd-Max quantisation shows consistent improvement over the uniform quantisation for all bit resolutions, with a 26%, 17% and 14% improvement for 3, 4 and 5 bit resolution respectively. Furthermore, the average SNR improves with increasing bit resolution, or equivalently, number of discrete levels. This is to be expected, as increasing the number of levels brings the digital output closer to the analogue waveform. However, the 5 bit resolution shows reduced SNR over 4 bit. This is due to the nonlinearity in the 32 level output shown in Figure 2.11(c).

Adaptive bit and energy loading is used for OFDM transmission [11]. As SNR increases, the algorithm can increase bit loading while maintaining the target BER; therefore, higher collected optical power results in a higher data rate. The SNR thresholds can be calculated using the analytical BER model of M-QAM [12]. The target BER is set to be lower than a FEC threshold target. A BER below such a threshold can be corrected through coding methods, incurring a small overhead penalty on the transmitted bits of 7% [7].

The BER performance against varying data rate for both uniform and Lloyd-Max quantisation is shown in Figure 2.12. BER performance generally improves as the bit resolution increases, as expected. Achievable data rates at the FEC threshold can be determined through interpolation. For uniform quantisation, a data rate of 25.2 Mb/s is achieved for 3 bit resolution. This increases to 29 and 35.5 Mb/s for 4 and 5 bit resolutions, respectively. Lloyd-Max quantisation shows a further increase in possible
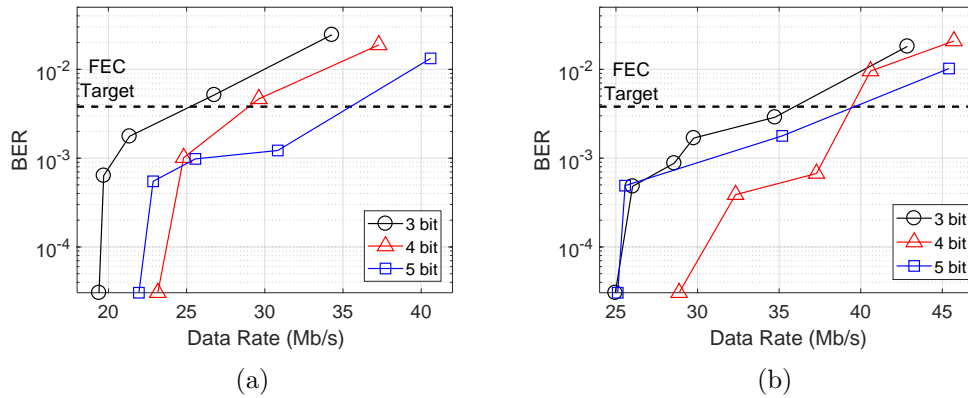
Figure 2.12: BER against data rate for (a) uniform and (b) Lloyd-Max quantisation.

data rates, with 36 and 39.5 Mb/s achieved for 3 and 4 bit resolutions. The performance increase saturates for 5 bit resolution due to the nonlinearity present in the 32 level output. The data rate of 39.5 Mb/s with a bandwidth of 10 MHz, corresponds to a spectral efficiency of 3.95 bits/s/Hz. This indicates that with additional available bandwidth, OFDM transmission would outperform the previous PAM results, where spectral efficiency is 2 and 3 bits/s/Hz for 4 and 8-PAM, respectively.

2.3.4   Limitations and Future Potential

The primary limitation of the current experimental arrangement is the output frequency of the FPGA. With a 100 MHz output, the OFDM transmission can only achieve a total system bandwidth of 10 MHz, limiting the achievable data rates. This limitation could be lifted with a higher frequency FPGA, or custom electronics for producing suitable parallel data streams. Doing so would also allow full exploitation of the bandwidth of the CMOS-controlled micro-LED array, and readily allow data rates in excess of 300 Mb/s. In addition, high overhead encoding schemes were used to overcome issues arising from the low-frequency cutoff of the APD receiver. Moving to a more suitable detector system would help mitigate this limitation.

The CMOS electronics and LED array were not fabricated with the intention of performing discrete communications and, therefore, are not optimised for such an ap-

plication. Issues such as electrical crosstalk and self heating may be improved upon with careful design [6], and use of NMOS transistors can improve device bandwidth [13]. If the linearity of the device at higher output power levels could be improved, higher order PAM or improved bit resolution OFDM could be performed, further increasing data rates and spectral efficiency.

A major issue with the experiments performed was optical alignment. Slight variations in optical paths from the individual LEDs in the array to the APD can result in significant variation in the amount of light collected from each pixel. In this setup, the aim was to have a 1:1 image of the LED array projected on to the active area of the APD over a short range. For a practical system through free space or polymer optical fibre, the optics would have to be carefully implemented to maintain the linearity of the discrete levels.

2.4   Summary

Digital-to-light conversion has been implemented using multiple micro-LED elements with an array. The CMOS-controlled micro-LED array provides a compact, integrated system, operating on a highly miniaturised scale with digital electronic interface. The discrete levels generated show good linearity up to 16 levels, and usable linearity up to at least 32 levels.

4 level PAM has been demonstrated at a symbol rate of 100 MHz, yielding a data rate of 200 Mb/s, limited by the FPGA used. 8-PAM has been demonstrated as feasible, however, BLW adversely affects performance, limiting the data rate to 150 Mb/s. 16-PAM was investigated but suffers strongly under the nonlinearity of the device, inter-symbol interference and multi-level penalty.

Discrete OFDM has been investigated as a method to further improve spectral efficiency over that of PAM. A maximum data rate of 39.5 Mb/s was achieved using Lloyd-Max quantisation and 16 optical levels, corresponding to 4 bit resolution. The

spectral efficiency of the OFDM transmission was 3.95 bits/s/Hz, indicating that with suitable hardware upgrades data rates in excess of 300 Mb/s should be possible.

The CMOS-controlled micro-LED array provides an ideal system for discrete multi-tone generation on a mm-scale device, directly converting digital inputs to optical outputs. With some performance improvements, the LED array approach to generating discrete level signals is scalable to higher orders, and offers optical transmitter technology for communications that is difficult to realise with other optical sources.

The results presented in this chapter were published in reference [14].

Bibliography

[1] T. Fath, C. Heller, and H. Haas, "Optical wireless transmitter employing discrete power level stepping," *Journal of Lightwave Technology*, vol. 31, no. 11, pp. 1734–1743, 2013.

[2] M. S. Islim and H. Haas, "Modulation techniques for Li-Fi," *ZTE Communications*, vol. 14, no. 2, pp. 29–40, 2016.

[3] A. Yang, Y. Wu, M. Kavehrad, and G. Ni, "Grouped modulation scheme for LED array module in a visible light communication system," *IEEE Wireless Communications*, vol. 22, no. 2, pp. 24–28, 2015.

[4] S. Zhang, S. Watson, J. J. D. McKendry, D. Massoubre, A. Cogman, E. Gu, R. K. Henderson, A. E. Kelly, and M. D. Dawson, "1.5 Gbit/s multi-channel visible light communications using CMOS-controlled GaN-based LEDs," *Journal of Lightwave Technology*, vol. 31, pp. 1211–1216, Apr 2013.

[5] J. Herrnsdorf, J. J. D. McKendry, R. Ferreira, R. Henderson, S. Videv, S. Watson, H. Haas, A. E. Kelly, E. Gu, and M. D. Dawson, "Single-chip discrete multitone generation," *2015 IEEE Summer Topicals Meeting Series, SUM 2015*, vol. 2, pp. 47–48, 2015.

[6] J. Herrnsdorf, J. J. D. McKendry, S. Zhang, E. Xie, R. Ferreira, D. Massoubre, A. M. Zuhdi, R. K. Henderson, I. Underwood, S. Watson, A. E. Kelly, E. Gu, and M. D. Dawson, "Active-matrix GaN micro light-emitting diode display with

unprecedented brightness," *IEEE Transactions on Electron Devices*, vol. 62, no. 6, pp. 1918–1925, 2015.

[7] ITU, Geneva, Switzerland, "Recommendation G.975.1: forward error correction for high bit-rate DWDM submarine systems," 2005.

[8] D. Tsonev, S. Sinanović, and H. Haas, "Pulse shaping in unipolar OFDM- based modulation schemes," *2012 IEEE Globecom Workshops*, pp. 1208–1212, 2012.

[9] P. Vary and R. Martin, *Digital speech transmission: enhancement, coding and error concealment.* Chichester: John Wiley & Sons, 2006.

[10] S. Lloyd, "Least squares quantization in PCM," *IEEE Transactions on Information Theory*, vol. 28, pp. 129–137, Mar 1982.

[11] H. E. Levin, "A complete and optimal data allocation method for practical discrete multitone systems," in *Global Telecommunications Conference, 2001. GLOBECOM '01. IEEE*, pp. 369–374, 2001.

[12] F. Xiong, F. Xiong, and F. Xiong, *Digital modulation techniques*, vol. 633. Boston: Artech House, 2nd ed., 2006.

[13] E. Xie, M. Stonehouse, R. Ferreira, J. J. McKendry, J. Herrnsdorf, X. He, S. Rajbhandari, H. Chun, A. V. Jalajakumari, O. Almer, G. Faulkner, I. M. Watson, E. Gu, R. K. Henderson, D. C. O'Brien, and M. D. Dawson, "Design, fabrication and application of GaN-based micro-LED arrays with individual addressing by n-electrodes," *IEEE Photonics Journal*, vol. 9, no. 6, 2017.

[14] A. D. Griffiths, M. S. Islim, J. Herrnsdorf, J. J. D. McKendry, R. Henderson, H. Haas, and E. Gu, "CMOS-integrated GaN LED array for discrete power level stepping in visible light communications," *Optics Express*, vol. 25, no. 8, pp. A338 – A345, 2017.

Chapter 3

Single Photon Communications I: Mathematical Framework

In this chapter, a transmission scheme for low-light optical communications utilising single-photon detectors is introduced. The scheme transmits data by modulating temporal correlation patterns generated by an optical transmitter, in contrast to conventional optical communications which modulate intensity. The mathematical framework for the scheme is described in detail, leading to the conclusion that data can be encoded in the autocorrelation function. Potential data transmission schemes arise that are comparable to conventional on-off keying, pulse position modulation and pulse amplitude modulation. The potential of these schemes is assessed in order to decide upon a suitable implementation, which is the subject of Chapter 4. Acknowledgement goes to Dr. Johannes Herrnsdorf of the Institute of Photonics, and Prof. Robert K. Henderson of the University of Edinburgh for strong contributions to the conceptualisation and mathematical development of this approach.

3.1 Motivation

Conventional optical wireless communications (OWC) is based on modulation of the intensity, frequency, or phase of an optical source, and direct or coherent detection of the output light [1, 2]. When the amount of power incident on the receiver is severely reduced by the properties of the optical channel, or there are other interfering signals, the desired signal will become lost in noise. Under such low-light level conditions, it becomes important to optimise the amount of data that can be transmitted with low received power. Photon efficient optical communications are often characterised by the number of photons required to transmit each bit of information, or photons-per-bit, in addition to the more general data rate and bit error ratio metrics.

There are a number of methods that can be used to operate at very low levels of photons per bit, including error correction with high order modulation schemes [3] and coherent detection [4, 5]. Such schemes are approaching the standard quantum limit (SQL) for optical communications, but make use of complex transmitter and receiver elements such as balanced photodetectors, local oscillators and optical phase-locked loops.

A potentially simpler method for attaining high receiver sensitivities is to use single-photon detection and counting methods [6–11]. High order PPM with forward error correction (FEC) codes can also operate with extremely low photons per bit [6,12], and has been proposed for communication systems to reach Mars orbit [13], and demonstrated for Lunar orbit [14]. However, these systems can be limited by optical noise in the channel [15].

Coincident photon pairs may be used to form communication systems utilising time gating methods to reduce the effects of background noise [16, 17], and transmit data with very low levels of received power [18, 19]. Many similar techniques are also used for quantum key distribution [20–22]. These methods typically require high-efficiency coincident photon pair sources, increasing transmitter complexity and form factor. In

some cases, secondary clock channels are also required.

Here, a transmission scheme suitable for OWC at very low-light levels is introduced. The scheme requires only a single, low photon flux channel and can be implemented using readily available semiconductor components and electronics. Alongside the simple form factor, the major advantage of the proposed scheme is in background signal rejection, as the communication link performs well even in the presence of high power, modulated background signals. While detection of the optical signal could be performed with any photodetector, the scheme has been designed with single-photon detectors in mind for increased sensitivity. This chapter introduces the mathematical basis for the data transmission method, while Chapter 4 discusses a practical implementation. In Chapter 5, the scheme is demonstrated for suitable applications.

3.2 SPAD Receivers

The transmission scheme has been specifically designed with single-photon avalanche diodes (SPADs) in mind as detectors. Other single-photon detection methods could be used, such as photomultiplier tubes or superconducting nanowires. However, SPADs show advantages over these methods such as: spectral response curves that fit well with visible wavelengths, functionality at room temperatures, solid state nature, and small form factors. As there are a number of important characteristics of SPADs that will affect the implementation, this section briefly describes the operating principle and behaviour of such a device.

An avalanche photodiode (APD) produces an analogue response to the optical signal incident on the device. As it is a p-n junction biased close to its breakdown voltage, carrier multiplication provides high gain [23]. Operating an APD beyond breakdown voltage creates an electric field strong enough for a single carrier to generate a self-sustaining avalanche. A device operating in this regime is referred to as being in "Geiger-mode". The self-sustaining avalanche must be quenched to avoid damage to

the device and improve timing resolution, using either a passive or active circuit [24]. If such a device has been engineered so that the avalanche is triggered by a single incident photon then it is referred to as a single-photon avalanche diode.

The spectral response of a SPAD is characterised by the photon detection probability (PDP) or efficiency (PDE). The PDP is defined as the fraction of incident photons which produce an avalanche, and is wavelength-dependent due to the wavelength dependency of photon penetration depth into the device [23]. Typical spectral ranges cover the visible and infrared regions.

With additional suitably designed circuitry, SPADs can provide a digital signal indicating the detection of a single-photon. The rising edge of the digital output will have high timing accuracy, to sub-nanosecond levels [25]. However, the quenching circuit introduces a period of time where the device will be unresponsive, known as the "dead time". The bias across the detector must be reduced to avoid permanent damage, and then brought back above the breakdown voltage so that the device is ready to detect another photon. The timescale of this process will depend on the approach used and parameters of the SPAD and surrounding circuitry. For devices fabricated using CMOS technology, dead times are generally 10s of ns [11, 26, 27]. The dead time limits the maximum count rate of the detector, and its effect must be considered when using the high-speed signals in the following sections.

While the intention of a SPAD is to detect single photons, the avalanche process can be triggered by any charge carriers in the active region, no matter how they are generated [23]. Even with no incident light, there are a number of mechanisms that can lead to unwanted avalanche events from the SPAD, resulting in a dark count rate (DCR). This means no matter how low the background light level is, there will always be a noise component in the output signal.

As the output of a single SPAD is a series of logic pulses indicating a photon detection event, a changing light intensity incident on the device is reflected in a change in the output count rate, as shown schematically in Figure 3.1. An analogue-style signal
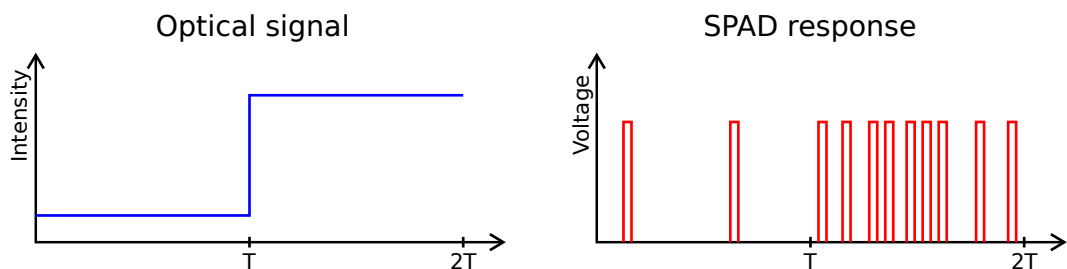
Figure 3.1: Schematic representation of a SPAD output under changing intensity.

could be recovered by taking the sum of photon counts in a given time interval; however, the dynamic range of such an approach will be limited by the dead time.

Whether as a single element or in an arrayed "silicon photomultiplier" format, SPADs have found applications in many scientific and commercial areas. Examples include positron emission tomography [28], fluorescence lifetime imaging [29], ranging applications [30] and quantum key distribution [21]. The application most relevant to the work presented here is in optical wireless communications. Here, SPAD receivers are attractive due to their high sensitivity and directly digital output [31, 32]. SPAD receivers have been demonstrated for use with OOK [9], PPM [12] and OFDM [10] transmission schemes, with sensitivities that bring efficiency levels close to the standard quantum limit [11], a limitation which is discussed in further detail in Section 4.1.5.

The following sections discuss the use of a single SPAD as a receiver for a novel transmission scheme for optical wireless communication. The scheme is inspired by time correlated single-photon counting (TCSPC) techniques used in fluorescence lifetime measurements [33]. By encoding data in the temporal correlation of an optical signal, single-photon level signals should be detectable even in the presence of strong, modulated background signals. Additionally, it is expected that multiple simultaneous data streams will show little interference, simply by operating with different temporal correlations.

68

3.3 Photon Correlations and Signal recovery

This section provides the mathematical basis for recovering a temporally correlated signal, beginning from a probabilistic approach to the output of a single SPAD.

3.3.1 Mathematical Analysis of SPAD Output

The output of a SPAD is probabilistic in nature and the exact timing of an output pulse cannot be predicted. However, the probability (P) of a pulse occurring in a time interval $[t, t + \Delta t]$ will follow:

$$P(t, t + \Delta t) = \int_{t}^{t+\Delta t} f(t)dt, \qquad (3.1)$$

where $f(t)$ is the probability distribution of pulses. This equation, and subsequent analysis, is only valid under short time scales, such that $P \in [0, 1]$. Thus, the valid time scales are comparable to the dead time of the SPAD.

The potential triggers for a pulse can be divided into incident photons and dark counts. Incident photons are detected with photon detection probability η_{PDP} which is wavelength-dependent. Therefore, while the SPAD is primed for photon detection in Geiger mode:

$$f_{Geiger}(t) = \eta_{PDP}\Phi_{ph}(t) + R_{dark}, \qquad (3.2)$$

where $\Phi_{ph}(t)$ is the incident photon flux and R_{dark} is the dark count rate. The dead time of the SPAD, τ_d, must also be taken into account, as during this time period no detection events will occur, meaning:

$$f_{dead} = 0. \qquad (3.3)$$

This means that $f(t)$ depends on the probability $P(t - \tau_d, t)$ that a pulse occurred less than the τ_d before the current time: t. The full expression for $f(t)$ is therefore:

$$f(t) = (\eta_{PDP}\Phi_{ph}(t) + R_{dark})\left(1 - \int_{t-\tau_d}^{t} f(t')dt'\right). \tag{3.4}$$

Equation 3.4 is recursive, so is intractable to solve for a general case. However, it can be solved for various special cases according to the incident photon stream $\Phi_{ph}(t)$. The distribution of photons will consist of a controlled part $\Phi_{signal}(t)$, dictated by the optical transmitter, and a background component Φ_{bg}:

$$\Phi_{ph}(t) = \Phi_{signal}(t) + \Phi_{bg}. \tag{3.5}$$

The optical transmitter can therefore be used to adjust the photon distribution $\Phi_{ph}(t)$ to encode data.

Static solution

In the case where there is no transmitted signal, $\Phi_{signal}(t) = 0$. Solving equation 3.4 results in a constant $f(t)$, which shall be referred to as f_{bg}:

$$f(t) = \frac{\Phi_{bg}\eta_{PDP} + R_{dark}}{1 + \tau_d(\Phi_{bg}\eta_{PDP} + R_{dark})} = f_{bg}. \tag{3.6}$$

As the incident background light increases, the detector eventually saturates. In this situation, the SPAD output pulses occur as soon as the recovery cycle has completed, so the pulse rate is given by the dead time:

$$\lim_{\Phi_{bg}\to\infty} f_{bg} = \frac{1}{\tau_d}. \tag{3.7}$$

Short pulse solution

A useful approximation to consider is an infinitely short optical pulse:

$$\Phi_{signal}(t) = \rho_0\delta(t). \tag{3.8}$$

Here, ρ_0 is the number of photons in the pulse and δ is the Dirac-δ function. If $f(t)$ is then integrated over a time interval $[-t_1, t_1]$ to get a detection probability, we obtain:

$$\int_{-t_1}^{t_1} f(t)dt = \; t_1 f_{bg} + \rho_0 \eta_{PDP}(1 - \tau_d f_{bg})$$
$$+ \int_{0^+}^{t1} (\Phi_{bg}\eta_{PDP} + R_{dark})\left(1 - \int_{t-\tau_d}^{t} f(t')dt'\right)dt. \quad (3.9)$$

By inspecting Equation 3.9, it can be determined that:

$$f(t) = \begin{cases} f_{bg} & , t < 0 \\ \delta(t)\rho_0\eta_{PDP}(1 - \tau_d f_{bg}) & , t = 0 \\ (\Phi_{bg}\eta_{PDP} + R_{dark})\left(1 - \int_{t-\tau_d}^{t} f(t')dt'\right) & , t > 0. \end{cases} \quad (3.10)$$

Low signal, high background solution

If the integral for $t > 0$ in Equation 3.10 is dominated by the constant background photon stream, Φ_{bg}, then a complete solution for $f(t)$ can be determined. This relies on the condition:

$$\rho_0\eta_{PDP}(1 - \tau_d f_{bg}) \ll \tau_d f_{bg}. \quad (3.11)$$

If this holds, then:

$$f(t) = f_{bg} + \delta(t)\rho_0\eta_{PDP}(1 - \tau_d f_{bg}). \quad (3.12)$$

Equation 3.12 is used in the following analysis due to its simplicity. As long as the timescales considered are longer than τ_d the approximation is expected to be reasonable, even if Equation 3.11 is not strictly fulfilled.

If, instead of a single pulse, the optical signal is a set of discrete pulses at times t_i with photon number ρ_i, then Equation 3.12 can be used to express $f(t)$ as:

$$f(t) = f_{bg} + \sum_i \delta(t_i)\rho_i\eta_{PDP}(1 - \tau_d f_{bg}). \tag{3.13}$$

Photon timing statistics

As Equation 3.13 describes the probability distribution for a stream of short pulses, it is natural to consider parallels to conventional pulse position modulation (PPM). Given that a pulse is detected at time t, the probability of detecting a second pulse at time $t + \tau$ can be determined. During the dead time τ_d after the pulse at t, the probability is 0, as no photons can be detected. Afterwards, the probability distribution will relax back to $f(t)$. Therefore, only timescales longer than τ_d will be considered.

While $f(t)dt$ is the probability of a detecting a photon in the interval $[t, t + dt]$, the probability of receiving a second photon in the interval $[t + \tau, t + \tau + dt']$ is $f(t)dt f(t + \tau)dt'$. The total number of recorded photons is then:

$$N = \int_{-t_1}^{t_1} f(t)dt, \tag{3.14}$$

with the number of secondary counts received in a time separation interval $[\tau, \tau + \Delta t']$ after the first is given by:

$$N' = \int_{\tau}^{\tau+\Delta t'} dt' \int_{-t_1}^{t_1} f(t)f(t + t')dt. \tag{3.15}$$

Finally, the count density function $g(\tau)dt'$ of recording two subsequent counts with temporal separation in the interval $[\tau, \tau + dt']$ is given by:

$$g(\tau) = \int_{-t_1}^{t_1} f(t)f(t + \tau)dt. \tag{3.16}$$

This equation allows data transmission through modulation of *photon timing statistics*, rather than the intensity, frequency or phase of an optical transmitter. A periodically repeating signal, as described by Equation 3.13, could have the time between pulses

modulated. This changes the form of $g(\tau)$, which can then be decoded as a data stream. Details of transmission schemes similar to on-off keying, pulse position modulation and pulse amplitude modulation are discussed in Section 3.4. Note that Equation 3.16 is the definition of the autocorrelation of $f(t)$, therefore, data is being encoded in temporal correlations.

3.3.2 Discrete Correlation Function

As the output of a SPAD is often a digital logic signal, determination of $g(\tau), N'$ and a data stream can be done directly with digital electronics. Therefore, it is important to consider a discrete form of Equation 3.16.

Firstly, the receiver samples SPAD counts over the sampling period T_s into time bins t_i, $i = 1, \ldots, N_s$, where N_s is the number of samples. Time bins have a uniform size of $t_{bin} = t_{i+1} - t_i$. Each time bin t_i contains an integer number of photon counts f_i. The time bin width can be deliberately chosen to be shorter than the dead time of the SPAD, $t_{bin} < \tau_d$, meaning f_i takes only binary values. This eases the numerical effort for calculation of discrete $g(\tau)$.

Similarly to the sampled time variable, the correlation time τ is also discretised into correlation time bins τ_j, $j = 1, \ldots, N_\tau$. The correlation time bin size should be chosen as an integer multiple of the time bin, i.e. $\tau_{bin} = k t_{bin}$, $k \in \mathbb{N}^+$. Furthermore, it is useful to define start and stop indices:

$$n_{start} = \frac{\tau_1}{t_{bin}} \tag{3.17}$$

$$n_{stop} = n_{start} + k N_\tau - 1. \tag{3.18}$$

Using this, the discretised form of Equation 3.16 is:

$$g(\tau_j) = \sum_{i=1}^{N_s - n_{stop}} \sum_{l=0}^{k-1} f_i f_{i+n_{start}+(j-1)k+l}. \tag{3.19}$$

As f_i is a binary variable the multiplication can be implemented with if-statements and the summation performed using counters. This vastly simplifies the calculations required for offline processing, and allows $g(\tau_j)$ to be determined using simple logic circuits for a real-time link.

3.4   Single Photon Transmission Schemes

The previous section describes the mathematical method to determine a discrete temporal correlation function from the output of a single SPAD. This function can be exploited for the transmission of data through the optical channel. In this section, potential transmission schemes will be discussed. Each bears significant similarities to conventional forms of on-off keying (OOK), pulse position modulation (PPM) and pulse amplitude modulation (PAM), but with the distinction of relying on temporal correlations rather than intensity variation.

In all cases, a detectable pattern of pulses must be obtained from the transmitter. If two subsequent pulses are sent at times $t = 0$ and $t = T$ with photon numbers ρ_0 and ρ_T, then:

$$\Phi_{signal} = \rho_0 \delta(t) + \rho_T \delta(t - T). \tag{3.20}$$

In parallel to Equation 3.12, this gives:

$$f(t) = f_{bg} + \delta(t)\rho_0 \eta_{PDP}(1 - \tau_d f_{bg}) + \delta(t - T)\rho_T \eta_{PDP}(1 - \tau_d f_{bg}). \tag{3.21}$$

Using this $f(t)$ in Equation 3.16 yields:

$$g(\tau) = 2t_1 f_{bg}^2 + 2f_{bg}\eta_{PDP}(1 - \tau_d f_{bg})(\rho_0 + \rho_T) + \underbrace{\delta(\tau - T)\rho_0\rho_T\eta_{PDP}^2(1 - \tau_d f_{bg})^2}_{\text{Peak at } \tau = T}. \quad (3.22)$$

The time separation T causes a peak in $g(\tau)$ at $\tau = T$, meaning changing the temporal separation of pulses controls the peak location in $g(\tau)$, allowing data to be encoded and transmitted. This naturally leads to a style of transmission similar to conventional PPM, described in Section 1.2.2. However, OOK can also be implemented, as a lowest order version of PPM, and PAM transmission is also possible through control of photon numbers (or equivalently, pulse energy) ρ_0 and ρ_T.

Importantly, to properly implement data transmission the signal will have to be repeated periodically with time period τ_{rep}:

$$\Phi_{signal} = \sum_{n=-\infty}^{\infty} [\rho_0\delta(t - n\tau_{rep}) + \rho_T\delta(t - n\tau_{rep} - T)]. \quad (3.23)$$

This is necessary to build up the peak in $g(\tau)$ at $\tau = T$ to a level where it can be reliably distinguished from the background signal. This cannot be done with a single pulse pair, as a maximum of one photon can be detected per pulse, and there is a significant probability of not detecting one or both pulses. Even if both photons are detected, this results in a single correlation count, which cannot be distinguished from the random probability of noise SPAD counts generating the same signal. In a real application, the summation in Equation 3.23 will not have limits $[-\infty, \infty]$, but finite integers dictated by the bit period, or equivalently data rate, of the transmission system used.

As many pulse repetitions will be required to form distinguishable peaks in $g(\tau)$, transmitting data with this approach is expected to have limited data rates. However, the single-photon nature of the approach should yield low received optical power requirements. Furthermore, it is expected that the data transmission should show ro-
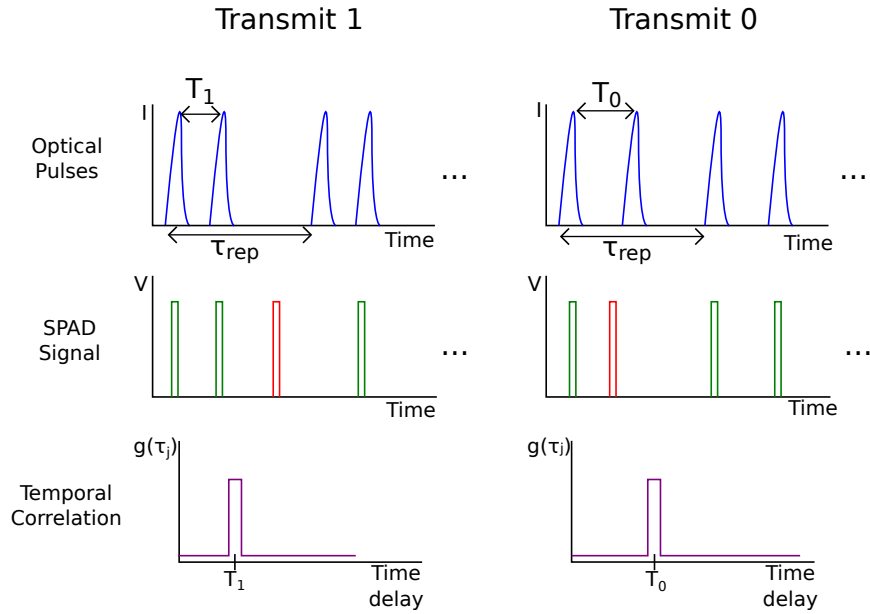
Figure 3.2: Schematics of waveforms for a general OOK-style transmission.

bustness to background signals, as they are very unlikely to show the same temporal correlation.

3.4.1 On-Off Keying

The simplest method of transmitting data with the correlation function $g(\tau_j)$ is to modulate between two different correlation patterns, or temporal separations between pulses. Equation 3.22 indicates pulse pairs separated by time T give a peak in $g(\tau)$ at $\tau = T$. Therefore, binary symbols of "0" and "1" can be represented by pulse pair separations of T_0 and T_1, respectively. When the transmitter switches pulse pair separations, $g(\tau_j)$ (calculated by the receiver) will have a peak that changes position. Thresholds on the histogram of $g(\tau_j)$ can then be used to determine which bit has been transmitted.

A schematic of the expected waveforms for such transmission is shown in Figure 3.2. The transmitter sends pulse pairs periodically with time period τ_{rep}, with the pair separation varying for different bits. The SPAD detects at most one photon from

each transmitted pulse, indicated in green. Additional SPAD pulses occur due to background signals or dark counts, indicated in red. With sufficient repetition of pulse pairs, the temporal correlation $g(\tau_j)$ is built up. The correlation histogram will show a flat background component with a peak at the time lag specified by the pulse separation, as predicted by equation 3.22. Note that each pulse used here has the same photon number, $\rho_0 = \rho_T$, as the intention is to exploit only the correlation peak location, not the peak intensity. A scheme with varying pulse energies may enable PAM-style transmission, as discussed in Section 3.4.3.

The correlation function in Figure 3.2 is somewhat simplified, as in reality there will be additional correlation peaks at larger time intervals. These occur as the pulse pairs correlate with the next, or previous pair. Therefore, additional peaks would appear at $\tau = \tau_{rep}$ and $\tau = \tau_{rep} \pm T_{0/1}$. Care must be taken in the choice of T_0 and T_1 to ensure the correlation peaks are separated, as an overlap will interfere with the accurate determination of the presence of a correlation peak.

Initial experiments in implementing OOK-style transmission revealed two enhancements to the general approach displayed in Figure 3.2. Firstly, a binary symbol could be represented by transmitting no pulses at all, corresponding to $T_0 = \infty$, resulting a flat $g(\tau_j)$ with no peaks. This results in lower received power levels at the receiver, and also simplifies transmitter design and reduces output optical power, so was implemented for the transmission symbol "0". In addition, to decode the scheme now only requires a single threshold to determine if there is a signal in $g(\tau_j)$ or only noise, rather than determining which correlation peak is present.

Secondly, instead of transmitting separate pairs of pulses, it is more efficient to send pulses at a constant repetition rate R_{rep}. Instead of received additional correlation peaks at $\tau = \tau_{rep}$ and $\tau = \tau_{rep} \pm T_1$, all correlations occur at $\tau = T_1 = 1/R_{rep}$, and therefore the correlation peak in $g(\tau_j)$ builds up more rapidly. This also results in lower requirements on received power, while maintaining the same signal distinguishability. A schematic representation of the expected waveforms for this improved version is
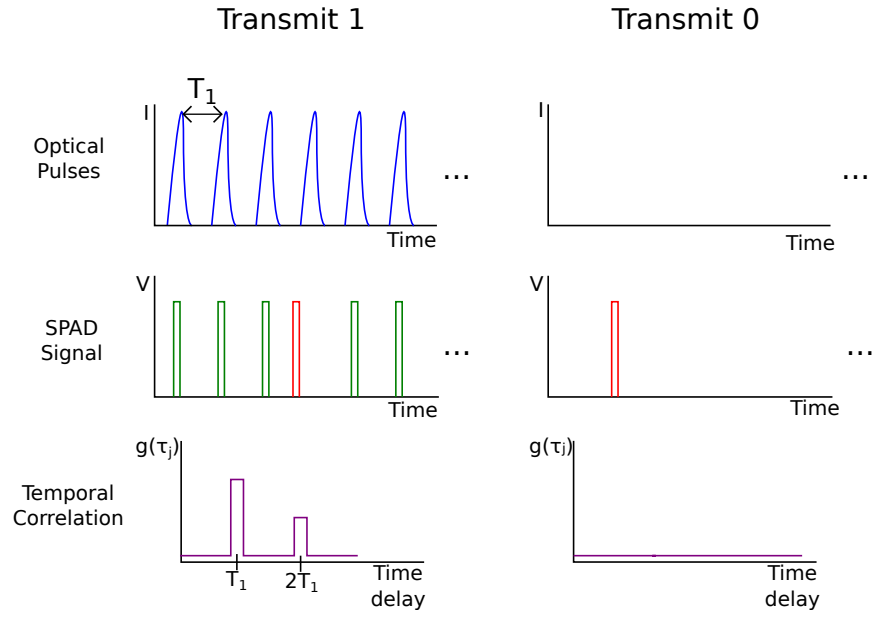
Figure 3.3: Schematics of waveforms for an improved version of OOK-style transmission.

shown in Figure 3.3. Note that there will now be an additional secondary correlation peak at $\tau = 2T_1$, as pulses correlate with their next-nearest pulse, but this can be easily rejected. This style of transmission has been implemented experimentally, and is discussed in Chapter 4.

3.4.2 Pulse Position Modulation

Pulse position modulation can be implemented with additional time separations T_i, $i = 1 \ldots N_{slots}$, where N_{slots} is the total number of PPM time slots used. Two potential approaches arise, in parallel to the general and improved OOK methods, henceforth referred to as PPM-A and PPM-B

PPM-A

The first option for PPM is to transmit initial pulses at a constant repetition rate, and the following pulse is positioned at a set time delay after, as shown in Figure 3.4. This leads to waveforms similar to the general OOK case, but extended to additional time
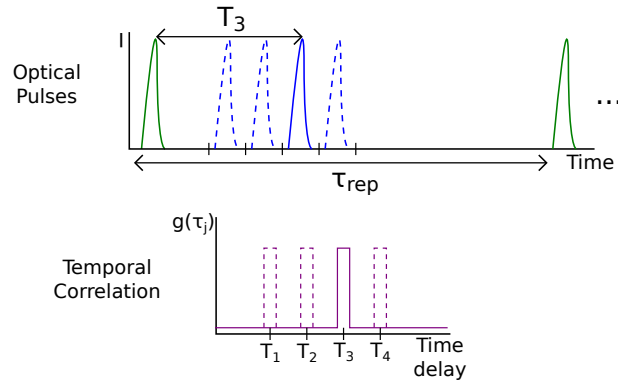
Figure 3.4: Schematics of pulse format and correlation function for PPM-A transmission.

separations and correlation peaks. The green pulses are always present at the start of each repetition, and the blue pulses indicate possible secondary pulse locations in times slots T_1 - T_4. As shown, the next repetition must leave a time length greater than T_4 after the final possible pulse in order to avoid interference. An initial gap after the green pulse is unused, to represent spacing that must be present to account for the dead time of the SPAD, i.e. $T_1 > \tau_d$. In order to avoid interference from correlations between separate pulse pairs, the repetition time τ_{rep} must be extended as N_{slots} increases.

As the number of bits transferred by a pulse position increases according to $N_{bits} = \log_2(N_{slots})$, but the time length needed to send pulses increases linearly in N_{slots}, there is an optimum value of N_{slots} to maximise data rate. As the time scales must be increased, it is unlikely that PPM-A transmission will outperform OOK-style in terms of data rate, however, the strength of a PPM approach lies in improved efficiency. With large N_{slots}, many bits can be transmitted with a single pulse position, meaning fewer photons are required to send information.

PPM-B

Alternatively, similar to the improved OOK-style transmission, pulses could be emitted at a constant rate specific to each symbol, as shown in Figure 3.5. In this case, $\tau_{rep} = T_i$, meaning a different number of pulses will be transmitted for each bit. This results in
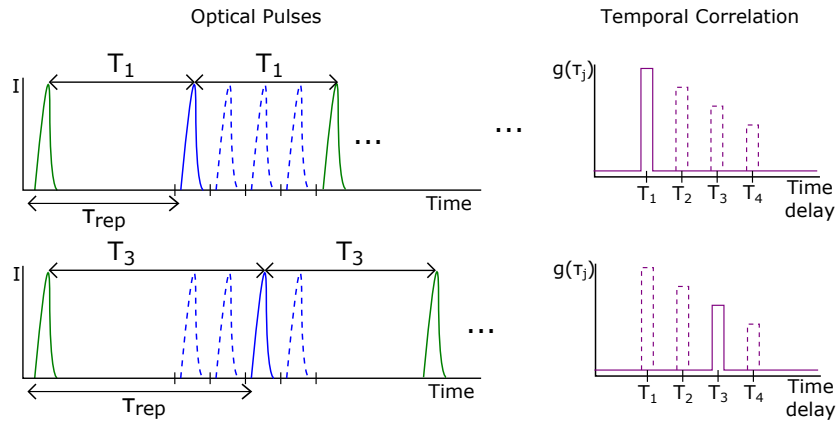
Figure 3.5: Schematics of pulse format and correlation function for PPM-B transmission.

the histograms for shorter time intervals building more rapidly than those for longer intervals. As the additional spacing is no longer required, the histogram will build up at a faster rate. However, the constant repetition of pulses results in additional correlation peaks at $\tau = 2T_i$. In OOK, this is easily rejected as only one peak position is of interest. Here, care must be taken to ensure secondary peaks do not correspond to another value of T_i, introducing an additional constraint $T_{N_{slots}} < 2T_1$ or $N_{slots} = T_1/2t_p$, where t_p is pulse width.

3.4.3 Pulse Amplitude Modulation

An improvement on the data rates attainable with OOK-style transmission may arise from a PAM style of transmission. If ρ_T in Equation 3.20 assumes a number of discrete levels, then the peak at T in $g(\tau_j)$ will do the same. Figure 3.6 shows an example of 4 level PAM transmission, with binary words "01" and "11" transmitted. The secondary pulse takes one of 4 possible levels in order to produce varying heights in $g(\tau)$. This requires an additional level of complexity in the transmitter in order to generate the sequential pairs of pulses. The method could also be combined with PPM-style transmission.
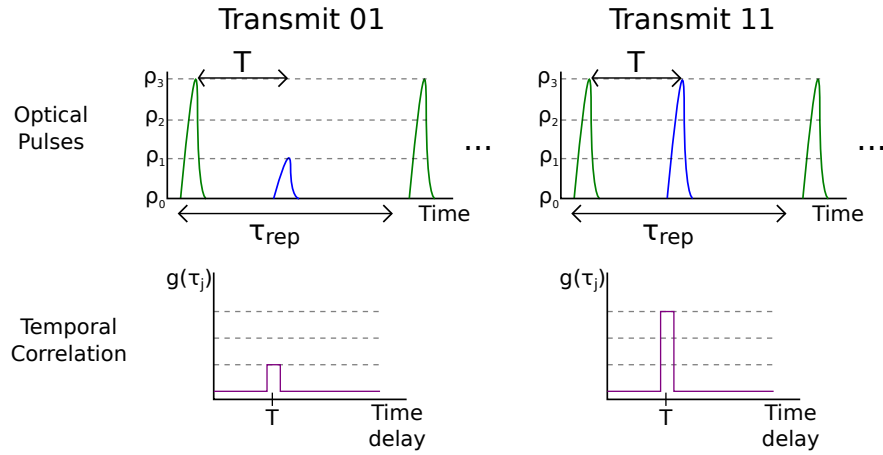
Figure 3.6: Schematic of pulse arrangements for PAM-style transmission with 4 levels.

Figure 3.6 assumes that the discrete levels in $g(\tau_j)$ can be uniformly distributed. In reality, as will be shown in Chapter 4, the peaks in $g(\tau_j)$ follow a Poissonian distribution (see Appenix A). As the variance of a Poissonian variable is equal to its mean, the higher levels in $g(\tau_j)$ will have a wider distribution of values, meaning they will have to be separated further from the previous levels in order to distinguish them. PAM style transmission will therefore require significantly higher levels of transmitter output power and received power, even for the modest data rate increase of 4-level PAM. Furthermore, the complexity of decoding this transmission scheme is significantly increased.

3.4.4   Transmission Scheme Comparison

Each transmission method detailed above has strengths and weaknesses, however, some qualitative comparison is useful in deciding which scheme to implement. It was decided that efforts should focus initially on OOK and PPM-style transmission, as PAM introduces additional complexity on both transmitter and receiver.

To compare the potential performance of OOK and PPM transmission, a "frame" of pulses is considered. The frame is defined as the time window required to transmit equally distinguishable correlation peaks in $g(\tau_j)$. The frame will have a specific time
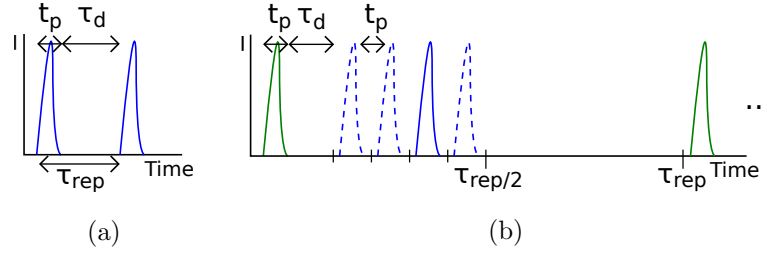
Figure 3.7: Frame timings for (a) OOK and (b) PPM-A style transmission.

window, number of pulses and number of transmitted bits, defined by the transmission method used. These parameters can then be used to qualitatively compare the potential data rates and received power requirements of each method.

Data rate

The data rate can be defined as the number of bits transmitted over the time length of of a single frame. Here, a frame is defined as the period over which the same pulse pattern is repeated. For the case of enhanced OOK-style transmission as shown in Figure 3.3, where a single time separation is used to represent a symbol "1" and no pulses for symbol "0", the number of bits transmitted in a single frame is 1. The frame length is dependent on the pulse width t_p, detector dead time τ_d and the number of pulse repetitions required to form a peak in $g(\tau)$. In order to detect both pulses for a single correlation, they must be separated by $\tau_{rep} = t_p + \tau_d$, otherwise the detector may be blinded by a photon from one pulse and not detect the next. The timings are indicated in Figure 3.7(a). Assuming the probability of detecting each pulse remains the same throughout, the number of repetitions of the time length τ_{rep} can be defined as N_r, and is the same for both OOK and PPM. For OOK, we then have:

$$R_{data,OOK} = \frac{1}{N_r(t_p + \tau_d)}. \tag{3.24}$$

For PPM-A, care must be taken to avoid the repeating pattern from correlating with itself, so all secondary pulses must occur before $\tau_{rep}/2$, as shown in Figure 3.7(b). In

addition, as $g(\tau)$ is the autocorrelation function, if pulse widths of t_p are used correlation peaks will have widths of $2t_p$. Therefore, each secondary peak must be separated by a minimum time window of t_p to avoid overlapping correlation peak locations. These constraints, in addition to the same dead time restrictions from OOK transmission, result in $\tau_{rep} = 2((2N_{slots} + 1)t_p + \tau_d)$. As the number of bits transmitted per frame will be $\log_2(N_{slots})$, and the repetitions required to build up a signal in $g(\tau)$ remains N_r, the data rate is given by:

$$R_{data,PPM-A} = \frac{\log_2(N_{slots})}{2N_r((2N_{slots} + 1)t_p + \tau_d)}. \tag{3.25}$$

In PPM-B, where each symbol is represented by different, constant pulse repetitions, the time interval τ_{rep} is determined by the maximum correlation time used, similar to OOK. However, there are additional constraints introduced by the dead time of the detector and the need to avoid interfering secondary pulses. The number of slots that can be used is related to the minimum time separation T_1 as $N_{slots} = T_1/2t_p$. In addition, T_1 must be greater than $\tau_d + t_p$ in order to resolve the correlation peak. The data rate is therefore given by:

$$R_{data,PPM-B} = \begin{cases} \frac{\log_2(N_{slots})}{N_r(2N_{slots}-1)t_p+\tau_d} & 2N_{slots}t_p < \tau_d \\ \frac{\log_2(N_{slots})}{2N_r(2N_{slots}-1)t_p} & 2N_{slots}t_p > \tau_d. \end{cases} \tag{3.26}$$

Here, the different cases ensure that $T_1 > \tau_d$, and the time slots have been constrained so that $T_{N_{slots}} < 2T_1$.

Equations 3.24, 3.25 and 3.26 allow comparison of expected data rates from each transmission method. The number of repetitions to obtain a useful signal N_r is unknown at this stage, however, it appears in an identical fashion in all equations and, therefore can be factored out. Resulting "scaled" data rate calculations will then be an unattainable maximum ceiling, as real values will be reduced by a factor of N_r. In Chapter 4, the hardware used provided values of $t_p = 5$ ns and $\tau_d = 35$ ns, so the
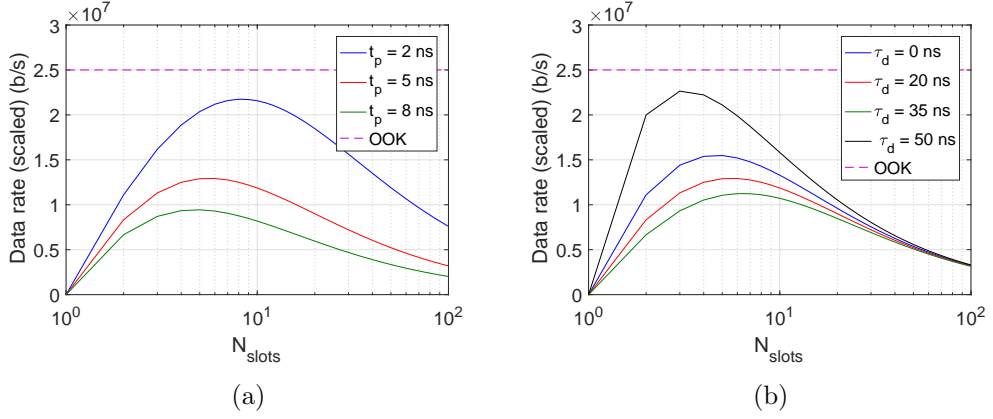
Figure 3.8: Scaled potential data rates for PPM-A with slot number N_{slots}, with (a) $\tau_d = 35$ ns and varying t_p and (b) $t_p = 5$ ns and varying τ_d. Peak values occur due to the logarithmic increase in transmitted bits, but linear increase in time scales required. The OOK-style data rate is included for comparison.

following analysis is done on values in this region.

For OOK, the data rate is limited in an inverse fashion to the timescales required. Both t_p and τ_d contribute in an identical manner, with shorter optical pulses and shorter dead times being desirable for high data rates. For $t_p = 5$ ns and $\tau_d = 35$ ns, the scaled data rate yields 25 Mb/s.

For PPM-A and PPM-B, the relationship is more complex. Figures 3.8 and 3.9 show the variation of expected data rate as the number of pulse position slots is increased for different pulse widths (a) and detector dead times (b). Dead time values around those expected from SPADs have been considered, along with no dead time, as arrayed receivers can mask such effects. Both t_p and τ_d contribute to the performance, but the effect of t_p is much stronger. In all cases, the general trend is the same: as N_{slots} increases bits-per-frame and time lengths differently, there is an optimum value of N_{slots} to maximise data rate, which varies with t_p and τ_d. Note that Figure 3.9(b) does not show a plot for $\tau_d = 0$ ns as the result is identical to $\tau_d = 20$ ns due to the cases detailed in Equation 3.26.

In Figure 3.10 the data rates for PPM-A and PPM-B at the optimum value of N_{slots} is shown for varying t_p and τ_d. Again the stronger dependence on t_p can be seen. As

(a)　　　　　　　　　　　　(b)
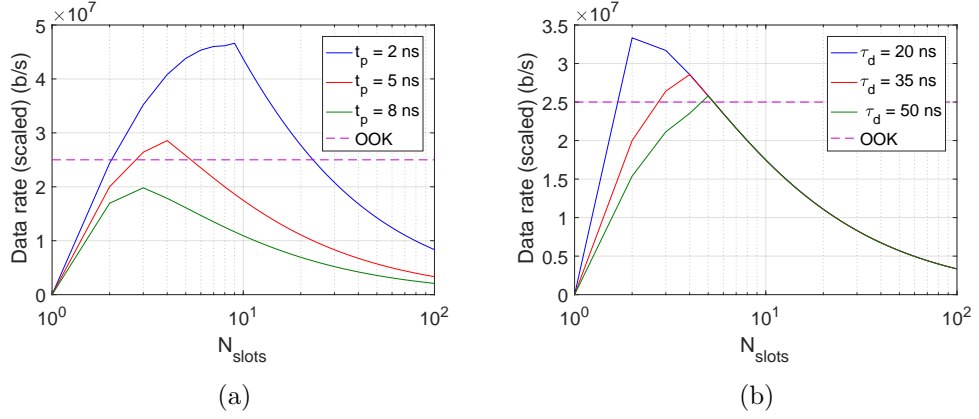
Figure 3.9: Scaled potential data rates for PPM-B with slot number N_{slots}, with (a) $\tau_d = 35$ ns and varying t_p and (b) $t_p = 5$ ns and varying τ_d. Similar trends are observed to the PPM-A case, however, higher data rates are possible.

(a)　　　　　　　　　　　　(b)
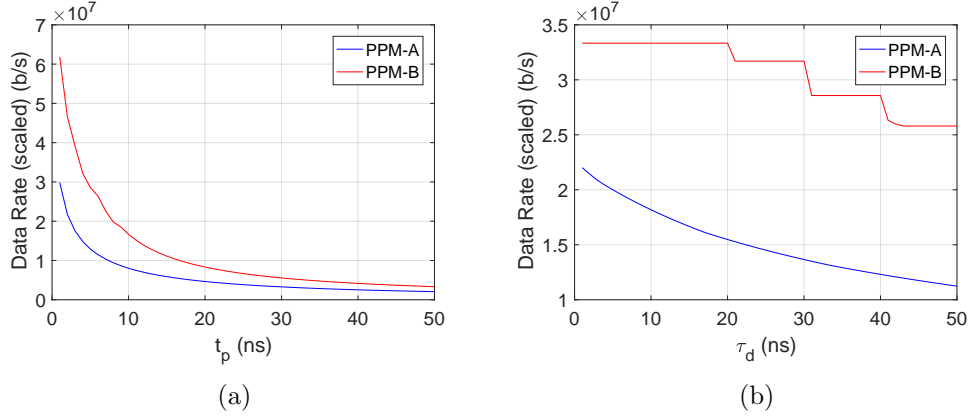
Figure 3.10: Scaled peak potential data rates for PPM-A with (a) $\tau_d = 35$ ns and varying t_p and (b) $t_p = 5$ ns and varying τ_d.

the pulse length becomes narrower, many more pulse slots can fit into the same time window to rapidly increase data rate. However, τ_d only sets constraints on the first time slots, so its contribution is less significant, particularly as N_{slots} increases. As with OOK, minimising both t_p and τ_d provides higher data rates. The stepped behaviour of the PPM-B plot in Figure 3.10(b) occurs as the condition $2N_{slots}t_p < \tau_d$ is progressively shifted as τ_d increases.

While the analysis so far deals with parameter values expected from a link using a micro-LED transmitter and SPAD receiver, the transmission scheme is not dependent
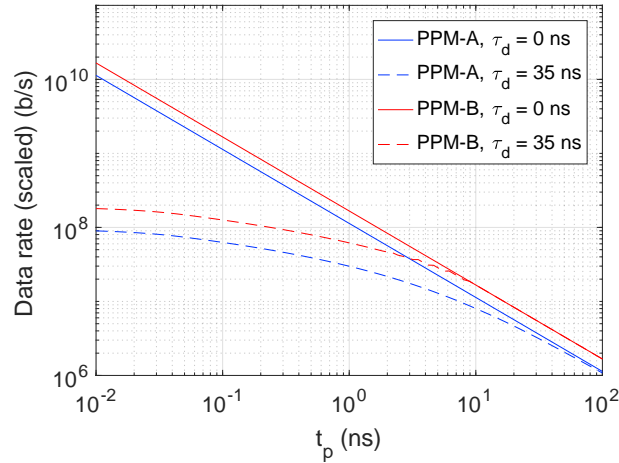
Figure 3.11: Scaled peak potential data rates for PPM-A with shorter optical pulses.

on this particular hardware arrangement. As such, it is useful to consider the use of shorter optical pulses attainable with laser sources. Figure 3.11 shows the expected data rates for PPM-A and PPM-B down to 10 ps width pulses for a detector with a dead time of 35 ns and a detector with no dead time. Data rate rapidly increases as pulses are shortened, as more pulses can fit in a given time window, and the optimum value of N_{slots} increases. For a detector with no dead time, and 10 ps optical pulses, Gb/s data rates may be possible. However, this is under the assumption that a value of $N_{rep} \approx 10$ is reasonable, and that there is no influence of background noise.

Finally, the expected maximum scaled data rates for the hardware used in Chapter 4 ($t_p = 5$ ns and $\tau_d = 35$ ns) can be calculated, and the result is shown in Figure 3.12. The maximum attainable data rate with PPM-A with these parameters does not reach the level achievable with OOK. This is primarily due to the fact that the OOK signals can be built up more rapidly when using a signal with constant repetition rate R_{rep}, as discussed in Section 3.4.1, since there is no need to space out the pulses and avoid interfering correlation peaks. PPM-B does slightly outperform OOK at the optimum number of N_{slots}, however, OOK-style transmission is used in Chapter 4 as it is significantly simpler to implement, with only a minor reduction in potential data
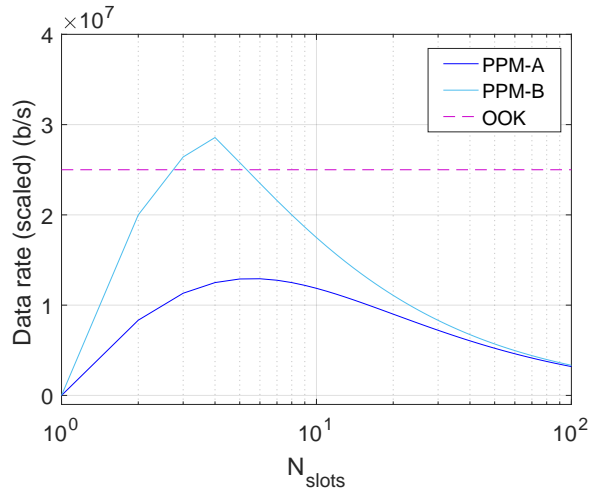
Figure 3.12: Comparison of potential OOK and PPM-A data rates for $t_p = 5$ ns and $\tau_d = 35$ ns.

rates.

Pulse Efficiency

While data rate has been prioritised for the experiments presented in the following chapter, another important factor is the efficiency of data transmission. For a qualitative comparison, efficiency can be defined as the number of bits that can be sent per optical pulse, as the photon number per pulse, ρ_0, and photon detection efficiency, η_{PDP}, will be equal for both OOK and PPM.

In OOK, the number of pulses sent per frame will be $1 \times N_r$: the number of repetitions to obtain a useful signal. As one bit is sent per frame, the resulting pulse efficiency is:

$$\eta_{pulse,OOK} = \frac{1}{N_r}. \tag{3.27}$$

In the case of PPM-A, a secondary pulse is required, so the number of pulses sent per frame is $2 \times N_r$. With $\log_2 N_{slots}$ bits transmitted per frame, the pulse efficiency is then:
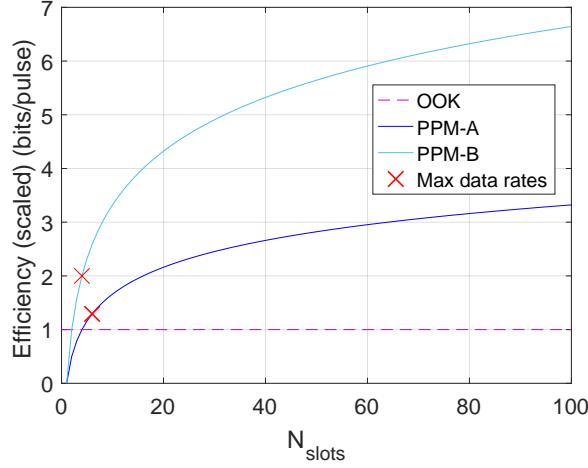
Figure 3.13: Comparison of pulse efficiency for transmitting using OOK or PPM.

$$\eta_{pulse,PPM-A} = \frac{\log_2 N_{slot}}{2N_r}. \tag{3.28}$$

For PPM-B, the number of pulses sent per frame is identical to that of OOK, however, the number of bits transmitted is the same as PPM-A. Therefore, the pulse efficiency is:

$$\eta_{pulse,PPM-B} = \frac{\log_2 N_{slot}}{N_r}. \tag{3.29}$$

As with data rate, N_r is unknown, but appears identically in all equations so can be factored out. The resulting scaled efficiencies are shown in Figure 3.13, with the maximum PPM data rate points indicated in red. PPM transmission provides enhanced pulse efficiency over OOK, suggesting that the overall energy or photon efficiency will be higher, even if data rate is lower. The trend also indicates that efficiency can continue to increase as N_{slots} is increased. However, as shown in Figure 3.8, the data rate will continue to reduce. The choice of transmission scheme can therefore be made based on the priority of the communication system.

The bits-per-photon efficiency of the scheme will be related to the pulse efficiencies

described here, but will be strongly dependent on the receiver performance. Many photons will be present in a single optical pulse, and while the dead time of a single SPAD prevents multiple photon detections per pulse, increased numbers of incident photons increase the probability of a detected event. The exact number of photons required to trigger a detection will depend on the photon detection probability (PDP) of the SPAD. Higher PDP devices will require fewer incident photons and result in a better photons-per-bit performance. The analysis here allows a qualitative comparison between transmission schemes, as the detection of pulses by a SPAD will behave in the same manner for all approaches.

3.4.5 Single Photon Channel Capacity

It is important to consider the proposed data transmission scheme within the framework of information theory, and therefore discuss the capacity of the single-photon counting channel. The capacity is a measure of how much information can theoretically be sent over a noisy channel. The widely successful Shannon-Hartley theorem gives an analytical solution for the capacity of an analogue channel with additive white Gaussian noise (AWGN) [34]:

$$C = f_{BW} \log_2(1 + SNR). \tag{3.30}$$

Here, C is channel capacity, f_{BW} is the bandwidth of the channel and SNR is the signal-to-noise ratio. While this theorem has overwhelming success for classical communication channels, single-photon channels differ significantly from AWGN analogue channel conditions due to the discrete nature of detection events.

Instead of looking for an analytical solution for channel capacity, a numerical solution can be found using the Blahut-Arimoto algorithm [35]. This is a fixed-point iteration method that considers a transmitter and receiver with finite discrete alphabets X and Y respectively, operating at a sample rate R_s. If the conditional probability

$(p(y|x))$ of receiving $y \in Y$ when $x \in X$ was sent is known, then for a given transmitter symbol distribution $p(x)$, an upper and lower bound for the transmitted bits per sample period can be calculated. Then $p(x)$ is updated iteratively until the bounds converge to the capacity per sample period.

For the single SPAD link described in this chapter, with dead time τ_d and photon detection probability η_{PDP}, choosing $R_s > 1/\tau_d$ results in a receiver alphabet of $Y = 0, 1$, with $y = 1$ corresponding to a SPAD rising edge occurring in the sample interval, and $y = 0$ corresponding to no rising edge. The transmitter also has an alphabet of $X = 0, 1$, corresponding to the LED being off or on. To maintain constant average photon flux (desirable to avoid flicker) at the receiver of Φ_s, the LED transmits photon fluxes of Φ_0 and Φ_1 for $x = 0$ and $x = 1$ as:

$$\Phi_0 = 0 \tag{3.31}$$

$$\Phi_1 = \Phi_s/p(x = 1). \tag{3.32}$$

With a constant flux of background photons and dark counts, the average number of photons incident on the SPAD during a sample period n_{av} is given by:

$$n_{av} = \begin{cases} \Phi_{bg}/R_s & , x = 0 \\ (\Phi_{bg} + \Phi_1)/R_s & , x = 1. \end{cases} \tag{3.33}$$

The probability of receiving a photon count P_{count} in the sample period is given by:

$$P_{count}(n_{av}(x)) = \sum_{n=1}^{\inf} P_{n_{av}}(n).P_{count}^{(n)}. \tag{3.34}$$

Here, $P_{n_{av}}$ is the Poissonian distribution (see Appendix A) with mean n_{av}, and $P_{count}^{(n)}$ is the probability of a detector count when n photons are incident on the detector.

If the photons in a pulse are considered as sequentially incident on the detector, the probability of *not* detecting a pulse is $(1 - \eta_{PDP})^n$. Therefore, the probability of a detector count is given by:

$$P_{count}^{(n)} = 1 - (1 - \eta_{PDP})^n. \tag{3.35}$$

The dead time of the SPAD must also be accounted for, and can be expressed as a number of sample intervals n_{dead}:

$$n_{dead} = \tau_d R_s. \tag{3.36}$$

The probability that the SPAD is undergoing recovery and cannot detect a photon is then given by:

$$P_{dead} = \sum_{i=1}^{n_{dead}} (p(x=0)P_0 + p(x=1)P_1) \times (1 - p(x=0)P_0 - p(x=1)P_1)^{i-1}. \tag{3.37}$$

The probabilities of detecting a "1" when a "1" or "0" were transmitted are then:

$$P_0 = P_{count}(n_{av}(x=0))(1 - P_{dead}) \tag{3.38}$$

$$P_1 = P_{count}(n_{av}(x=1))(1 - P_{dead}). \tag{3.39}$$

Equation 3.37 can be solved numerically with a standard zero search in the interval $[0, 1]$. The channel matrix $p(y|x)$ is given by:

$$p(y|x) = \begin{cases} 1 - P_0 & , x = 0, y = 0 \\ P_0 & , x = 0, y = 1 \\ 1 - P_1 & , x = 1, y = 0 \\ P_1 & , x = 1, y = 1. \end{cases} \tag{3.40}$$

This is the input for the Blahut-Arimoto algorithm, and is updated for each iteration as it depends on the transmitter distribution $p(x)$.

Capacity Results

In Chapter 4, a SPAD receiver is used with parameters of $\tau_d = 35$ ns and $\eta_{PDP} = 0.25$ or 0.18, depending on the wavelength used. For low background conditions of $\Phi_{bg} = 619$ Hz, the Blahut-Arimoto algorithm was applied to determine the channel capacity for each value of η_{PDP}. The results are shown in Figure 3.14 for a range of incident signal counts expected for a single SPAD system. Intuitively, as the signal count rate increases, the maximum potential data rates also increase, with higher photon detection probabilities enabling higher capacities. At very high count rates, there is a saturation effect. This is caused by the dead time of the detector, which restricts the maximum number of detection events in a given time window.

3.5 Summary

This chapter has introduced methods and background mathematics for transmission of classical data using a single SPAD as a receiver. By transmitting optical pulses with known temporal separations, data can be encoded in the temporal correlation pattern, rather than intensity as in conventional VLC. The autocorrelation $g(\tau)$ of the signal from temporally spaced pulses will show peaks at the chosen time lags. The presence, absence or position of such peaks can be used to encode data. As the temporally correlated signal must be repeated to obtain a useful correlation signal
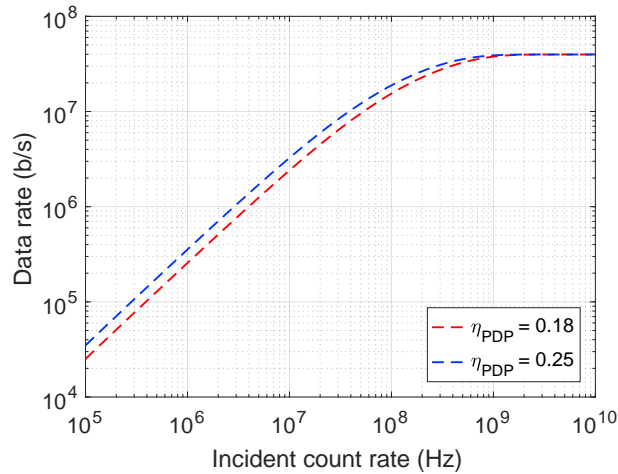
Figure 3.14: Channel capacity for given incident photon flux with photon detection efficiencies of $\eta_{PDP} = 0.18$ and $\eta_{PDP} = 0.25$ under low background conditions.

level, the data rates are expected to be modest, however the single-photon approach with strong potential for background rejection makes this an attractive scheme.

Transmission schemes arise naturally from this approach as parallels of conventional data transmission methods. Forms of on-off keying, pulse position modulation and pulse amplitude modulation are discussed here, with particular focus on OOK and PPM due to their relative simplicity. OOK is expected to be simpler to implement and provide high data rates, while PPM is more energy efficient. As such, the transmission scheme should be chosen based on the requirements of the communication system.

The discrete autocorrelation function $g(\tau_j)$ of the output of a SPAD can be calculated either offline or with simple logic circuits, utilising the digital nature of the SPAD. The optical source does not require any complex driving electronics to generate the correlated pulses, nor does it require high optical power. As such, the hardware requirements on such a scheme are simple. In the following chapter, OOK-style transmission is implemented using a single CMOS controlled micro-LED as a transmitter, and a single commercial SPAD as a receiver.

Bibliography

[1] K. Kikuchi, "Fundamentals of coherent optical fiber communications," *Journal of Lightwave Technology*, vol. 34, no. 1, pp. 157–79, 2015.

[2] S. Rajbhandari, J. J. D. McKendry, J. Herrnsdorf, H. Chun, G. Faulkner, H. Haas, I. M. Watson, D. O'Brien, and M. D. Dawson, "A review of gallium nitride LEDs for multi-gigabit-per-second visible light data communications," *Semiconductor Science and Technology*, vol. 32, no. 2, pp. 1–44, 2017.

[3] D. M. Boroson, "A survey of technology-driven capacity limits for free-space laser communications," *Free-Space Laser Communications VII*, vol. 6709, pp. 18–19, 2007.

[4] M. L. Stevens, D. O. Caplan, B. S. Robinson, D. M. Boroson, and a. L. Kachelmyer, "Optical homodyne PSK demonstration of 1.5 photons per bit at 156 Mbps with rate-(1/2) turbo coding," *Optics Express*, vol. 16, no. 14, pp. 10412–20, 2008.

[5] D. Geisler and T. Yarnall, "Demonstration of 2.1 photon-per-bit sensitivity for BPSK at 9.94-Gb/s with rate- FEC," *Optical Fiber Communication Conference*, pp. 13–15, 2013.

[6] B. S. Robinson, D. O. Caplan, M. L. Stevens, R. J. Barron, E. A. Dauler, and S. A. Hamilton, "1.5-photons/bit photon-counting optical communications using Geiger-mode avalanche photodiodes," *LEOS summer topical meetings*, 2005.

Bibliography

[7] B. S. Robinson, A. J. Kerman, E. A. Dauler, R. J. Barron, D. O. Caplan, M. L. Stevens, J. J. Carney, S. A. Hamilton, J. K. W. Yang, and K. K. Berggren, "781 Mbit/s photon-counting optical communications using a superconducting nanowire detector," *Optics Letters*, vol. 31, no. 4, pp. 444–446, 2006.

[8] M. M. Willis, A. J. Kerman, M. E. Grein, J. Kansky, B. R. Romkey, E. A. Dauler, D. Rosenberg, B. S. Robinson, D. V. Murphy, and D. M. Boroson, "Performance of a multimode photon-counting optical receiver for the NASA lunar laser communications demonstration," *Proc. International Conference on Space Optical Systems and Applications (ICSOS)*, 2012.

[9] D. Chitnis, L. Zhang, H. Chun, S. Rajbhandari, G. Faulkner, D. O'Brien, and S. Collins, "A 200 Mb/s VLC demonstration with a SPAD based receiver," *2015 IEEE Summer Topicals Meeting Series, SUM 2015*, vol. 3, pp. 226–227, 2015.

[10] Y. Li, M. Safari, R. Henderson, and H. Haas, "Optical OFDM with single-photon avalanche diode," *IEEE Photonics Technology Letters*, vol. 27, no. 9, pp. 943–946, 2015.

[11] H. Zimmermann, B. Steindl, M. Hofbauer, and R. Enne, "Integrated fiber optical receiver reducing the gap to the quantum limit," *Scientific Reports*, vol. 7, no. 1, p. 2652, 2017.

[12] I. Alsolami, D. Chitnis, D. C. O'Brien, and S. Collins, "Broadcasting over photon-counting channels via multiresolution PPM: implementation and experimental results," *IEEE Communications Letters*, vol. 16, no. 12, pp. 2072–2074, 2012.

[13] J. A. Mendenhall, L. M. Candell, P. I. Hopman, G. Zogbi, D. M. Boroson, D. O. Caplan, C. J. Digenis, D. R. Hearn, and R. C. Shoup, "Design of an optical photon counting array receiver system for deep-space communications," *Proceedings of the IEEE*, vol. 95, no. 10, pp. 2059–2069, 2007.

Bibliography

[14] D. M. Boroson and B. S. Robinson, "The lunar laser communication demonstration: NASA's first step toward very high data rate support of science and exploration missions," *Space Science Reviews*, vol. 185, no. 1-4, pp. 115–128, 2014.

[15] S.-K. Liao, H.-L. Yong, C. Liu, G.-L. Shentu, D.-D. Li, J. Lin, H. Dai, S.-Q. Zhao, B. Li, J.-Y. Guan, W. Chen, Y.-H. Gong, Y. Li, Z.-H. Lin, G.-S. Pan, J. S. Pelc, M. M. Fejer, W.-Z. Zhang, W.-Y. Liu, J. Yin, J.-G. Ren, X.-B. Wang, Q. Zhang, C.-Z. Peng, and J.-W. Pan, "Long-distance free-space quantum key distribution in daylight towards inter-satellite communication," *Nature Photonics*, vol. 11, no. July, pp. 509–514, 2017.

[16] J. Lekki, Q.-V. Nguyen, T. Bizon, B. Nguyen, J. Kojima, and M. Hizlan, "An extremely low power quantum optical communication link for miniature planetary sensor stations," *Journal of Aerospace Computing, Information, and Communication*, vol. 5, pp. 1–24, 2008.

[17] M. Hizlan, J. D. Lekki, and B. V. Nguyen, "Glenn Research Center quantum communicator receiver design and development," *Optical Engineering*, vol. 48, no. 10, pp. 1050031–8, 2009.

[18] S. Seward, P. Tapster, J. Walker, and J. Rarity, "Daylight demonstration of low-light-level communication system using correlated photon pairs," *Optical and Quantum Electronics*, vol. 3, pp. 201–207, 1991.

[19] C. K. Hong, S. R. Friberg, and L. Mandel, "Optical communication channel based on coincident photon pairs," *Appl. Opt.*, vol. 24, no. 22, pp. 3877–3882, 1985.

[20] R. J. Hughes, W. T. Buttler, P. G. Kwiat, S. K. Lamoreaux, G. L. Morgan, J. E. Nordholt, and C. G. Peterson, "Free-space quantum key distribution in daylight," *Journal of Modern Optics*, vol. 47, no. 2-3, pp. 549–562, 2000.

Bibliography

[21] K. J. Gordon, V. Fernandez, P. D. Townsend, and G. S. Buller, "A short wavelength GigaHertz clocked fiber-optic quantum key distribution system," *IEEE Journal of Quantum Electronics*, vol. 40, no. 7, pp. 900–908, 2004.

[22] H. Takenaka, A. Carrasco-Casado, M. Fujiwara, M. Kitamura, M. Sasaki, and M. Toyoshima, "Satellite-to-ground quantum-limited communication using a 50-kg-class microsatellite," *Nature Photonics*, vol. 11, no. 8, pp. 502–508, 2017.

[23] B. Nabet, *Photodetectors: materials, devices and applications*. Oxford: Elsevier, 2016.

[24] S. Cova, M. Ghioni, A. Lacaita, C. Samori, and F. Zappa, "Avalanche photodiodes and quenching circuits for single-photon detection," *Applied Optics*, vol. 35, no. 12, pp. 1956–1976, 1996.

[25] S. Cova, A. Longoni, and A. Andreoni, "Towards picosecond resolution with single photon avalanche diodes," *Review of Scientific Instruments*, vol. 52, no. 3, pp. 408–412, 1981.

[26] L. Pancheri and D. Stoppa, "Low-noise CMOS single-photon avalanche diodes with 32 ns dead time," *ESSDERC 2007 - Proceedings of the 37th European Solid-State Device Research Conference*, vol. 2007, pp. 362–365, 2008.

[27] J. A. Richardson, E. A. Webster, L. A. Grant, and R. K. Henderson, "Scaleable single-photon avalanche diode structures in nanometer CMOS technology," *IEEE Transactions on Electron Devices*, vol. 58, no. 7, pp. 2028–2035, 2011.

[28] L. H. Braga, L. Pancheri, L. Gasparini, M. Perenzoni, R. Walker, R. K. Henderson, and D. Stoppa, "A CMOS mini-SiPM detector with in-pixel data compression for PET applications," *IEEE Nuclear Science Symposium Conference Record*, pp. 548–552, 2012.

Bibliography

[29] B. R. Rae, K. R. Muir, Z. Gong, J. McKendry, J. M. Girkin, E. Gu, D. Renshaw, M. D. Dawson, and R. K. Henderson, "A CMOS time-resolved fluorescence lifetime analysis micro-system," *Sensors*, vol. 9, no. 11, pp. 9255–9274, 2009.

[30] A. M. Pawlikowska, A. Halimi, R. A. Lamb, and G. S. Buller, "Single-photon three-dimensional imaging at up to 10 kilometers range," *Optics Express*, vol. 25, no. 10, p. 11919, 2017.

[31] E. Fisher, I. Underwood, and R. Henderson, "A reconfigurable single-photon-counting integrating receiver for optical communications," *IEEE Journal of Solid-State Circuits*, vol. 48, no. 7, pp. 1638–1650, 2013.

[32] L. Zhang, D. Chitnis, H. Chun, S. Rajbhandari, G. Faulkner, D. C. O'Brien, and S. Collins, "A comparison of APD and SPAD based receivers for visible light communications," *Journal of Lightwave Technology*, vol. 36, no. 12, pp. 1–1, 2018.

[33] W. Becker, *Advanced time-correlated single photon counting applications*. Cham: Springer, 2015.

[34] H. Yang, *Introduction to digital wireless communications*. Stevenage: The Institution of Engineering and Technology, 2017.

[35] R. Blahut, "Computation of channel capacity and rate-distortion functions," *IEEE transactions on information theory*, vol. 18, pp. 460–473, July 1972.

Chapter 4

Single Photon Communications II: Experimental Implementation

The previous chapter introduced the mathematical basis for a new form of data transmission using temporally correlated optical signals. In this chapter, the experimental implementation of such a scheme is discussed. The hardware used and particular parameters for the transmission protocol are introduced, and the communications link is characterised. As the behaviour is somewhat different to conventional VLC, new parameters are introduced for characterisation. Bit error ratio performance is measured for varying received power. Most importantly, the transmission scheme is assessed under high optical background conditions, both constant and modulated. Finally, a real-time link was developed using FPGAs, to demonstrate the practical functionality of the scheme.

4.1 Current Implementation

In Section 3.4, transmission schemes for the correlated communication method were introduced and compared. The OOK-style of transmission was chosen for implementation in this Chapter, due to its simple requirements and higher potential data rates.
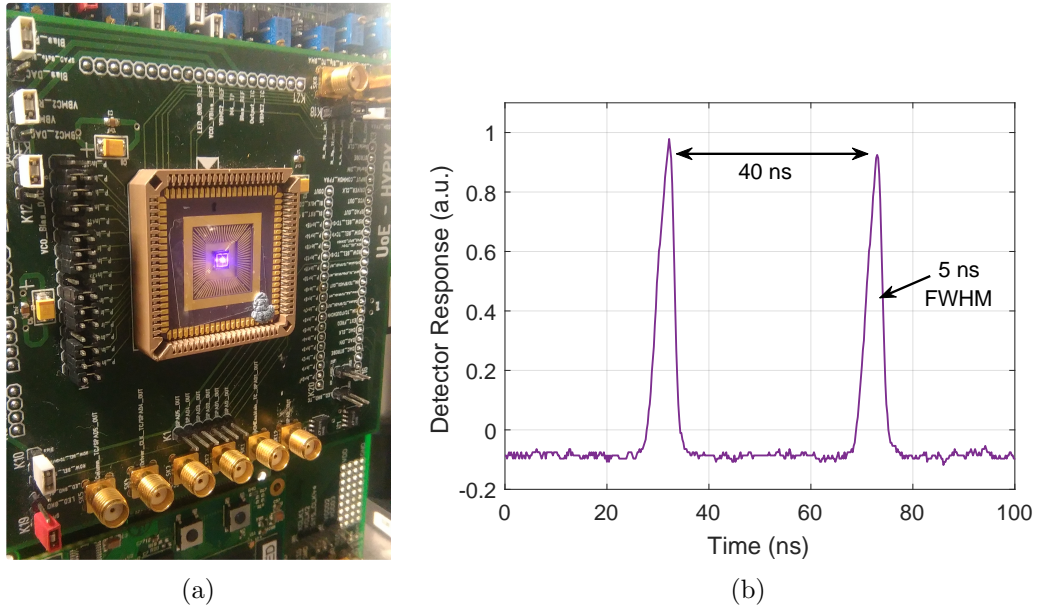
Figure 4.1: (a) The CMOS controlled micro-LED array in the control board. (b) Optical pulses from the micro-LED pixel.

4.1.1 Transmission Protocol and Hardware

The performance of the transmission protocol is dependent on the performance of hardware used for transmitting and receiving the signals; primarily the optical pulse width t_p and SPAD dead time τ_d. A CMOS controlled micro-LED provided the optical pulses and a commercial SPAD was used as a receiver.

The micro-LED array used consists of 16×16 individually addressable LED pixels. For this work, only a single pixel was used; however, pixels could be grouped to increase transmitter output power. A detailed description of the CMOS controlled micro-LED arrays can be found in Section 1.3 in the introduction. The array used here consisted of 99×99 µm square pixels, arranged in a tessellated fashion on a 100 µm pitch. For the majority of the following results, a 405 nm emitting device was used (device "SPC array A" in Table 1.1), and is shown in Figure 4.1(a), housed in the control motherboard. However, for the specific applications in Chapter 5 a 450 nm device has been used ("SPC array B"), which has the same pixel arrangement.

The CMOS electronics allow the micro-LED to be driven in a short pulsed mode
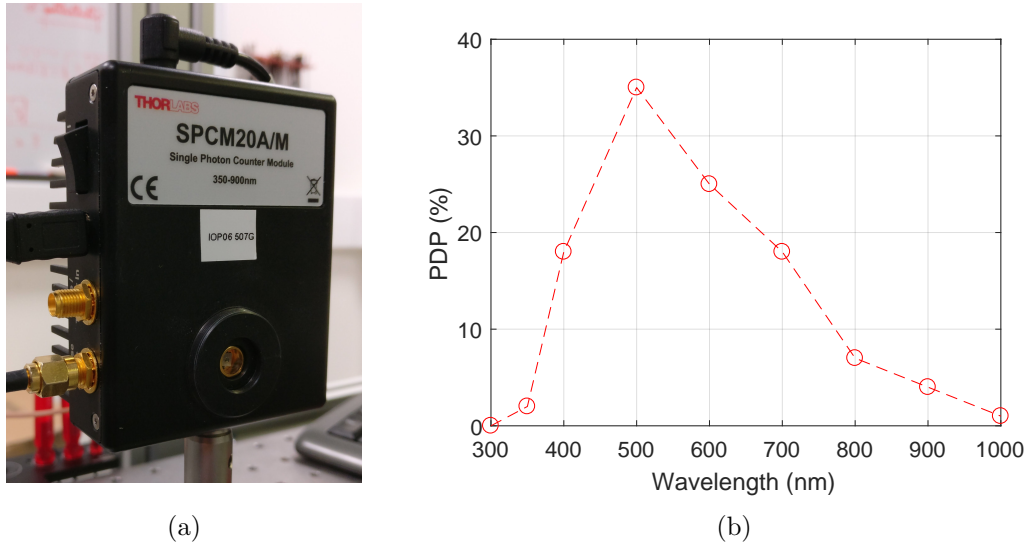
Figure 4.2: (a) Thorlabs SPCM20A. (b) Spectral response of the SPAD.

where the optical output is triggered by the falling edge of an input logic signal. The shortest stable output pulses are shown in Figure 4.1(b), and have a pulse width of 5 ns full width at half maximum (FWHM). Similar devices have been used to produce optical pulses of 300 ps [1]; however, it was observed with this particular device that the pulses became non-uniform and inconsistent when operated below 5 ns. Nevertheless, 5 ns wide pulses fulfil the requirements of the transmission scheme of $t_p < \tau_d$.

The commercial single-photon counting module (Thorlabs SPCM20A) used as a receiver consists of a single SPAD with relevant control and pulse detection electronics in a single package, shown in Figure 4.2(a). The 20 µm diameter SPAD has a dead time of 35 ns and a typical dark count rate of 25 Hz. This is a very low value for a SPAD, and enabled by a Peltier cooling element, which stabilises the SPAD's temperature below ambient temperature. Various photon counting methods are available through a USB interface and logic pulses for detected photons can be read out directly through an SMA connection. The spectral response of the SPAD is shown in Figure 4.2(b), plotted from data supplied with the module. From this, a PDP of 18% is estimated for the 405 nm wavelength used.

In order to produce signals suitable for the OOK-style transmission, the micro-LED was triggered using a field-programmable gate array (FPGA) board and a small additional board of digital electronics. The FPGA was programmed with a pseudorandom bit sequence (PRBS) which could be output at the desired data rate. The output is connected to the digital electronics, which consists of an AND gate and a square-wave oscillator. The data stream therefore controls the presence or absence of the pulse stream, while the oscillator controls the time separation between pulses. The signal from the AND gate is then used to trigger the common input of the CMOS control board, controlling the pulse output of the entire array simultaneously. The pixel is selected using an additional FPGA board housed on the CMOS control board.

The experimental setup is shown schematically in Figure 4.3. The output from the LED is collected and imaged onto the receiver plane with a lens (Thorlabs C220TME-A, focal length of 11 mm) and transmitted through a graded neutral density (ND) filter wheel (Thorlabs NDC-50C-4M-A). A 450 nm shortpass filter is placed in front of the SPAD to reject additional background light. The pixel is imaged onto the 20 μm diameter SPAD active area; however, as the pixel image is approximately a 7 mm square, only a small portion of the light is collected. In a practical system, receiver optics could be used to collect more light on to the active area of the SPAD, allowing higher degrees of loss through the channel. This was not necessary for the experiments here, as more than enough optical power was received with minimal effort on alignment and light collection. A secondary light source is present in the optical setup to allow control over the background light signals. The logic signal from the SPAD was captured by an oscilloscope (Tektronix MDO3104) and transferred to a PC for offline processing in MATLAB$^{\text{TM}}$.

With a pulse width of $t_p = 5$ ns and a SPAD dead time of $\tau_d = 35$ ns, the analysis presented in Chapter 3 indicates that OOK transmission should be performed with a minimum pulse separation of 40 ns. The expected waveforms and timings for transmitting in this way are shown in Figure 4.4. Setting the oscillator in the digital driving
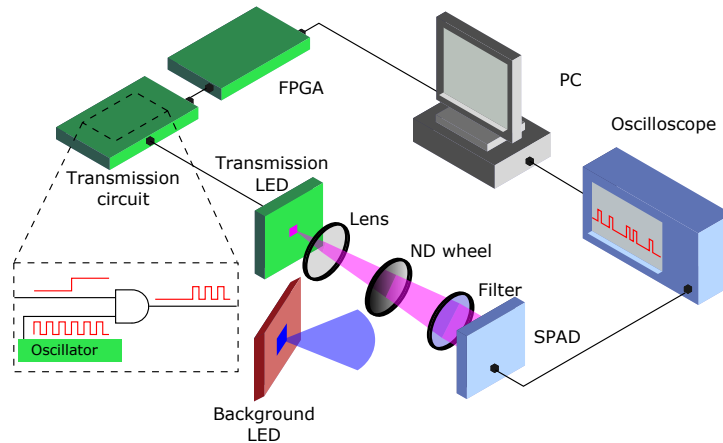
Figure 4.3: Schematic of the experimental setup used.

electronics to 25 MHz gives the desired 40 ns separation between the 5 ns pulses. As correlations are built up, the correlation histogram will show a peak at a time lag of 40 ns. An additional secondary peak will also appear at 80 ns, as pulses can correlate beyond their nearest neighbours, but this can safely be rejected by setting a correlation window around only the 40 ns pulse.

With this experimental setup and transmission method, the communication link was characterised, processing data streams in an offline fashion. This method was used for the coming subsections. Section 4.2 introduces a real-time link, in which the data is processed on the FPGA, which was used for the applications in Chapter 5.

4.1.2 Numerical Calculation of Received Power

While the photon counts from the SPAD will determine the communication link performance, the photon flux incident on the receiver, and received optical power are useful characterisation parameters. As the output of a SPAD is a series of photon counts with a probabilistic nature, the incident photon flux and optical power on the detector can be determined through numerical methods. For the transmission protocol used in the current implementation, it will be necessary to characterise power levels for both constant illumination and received average power under the pulsed repetitive signals.
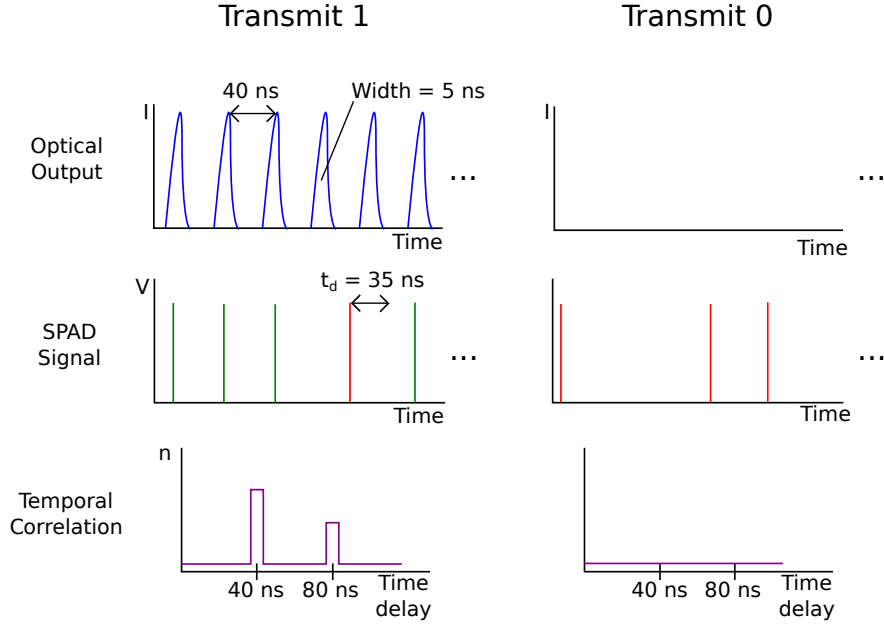
Figure 4.4: Schematic of expected waveforms for the chosen transmission scheme.

Constant illumination

The SPAD used as a receiver has known values for detection probability η_{PDP}, dark count rate R_{dark} and dead time τ_d. If $\Phi(t)$ is the photon flux incident on the active area of the SPAD, in photons per second, the probability $f(t)dt$ of receiving a count in the time interval $[t, t + dt]$ is given by:

$$f(t)dt = (\eta_{PDP}\Phi(t) + R_{dark})(1 - f_d(t))dt. \tag{4.1}$$

Here, $f_d(t)$ is the probability that at time t the SPAD is still undergoing a recovery cycle from a previous photon count, given by:

$$f_d(t) = \int_{t-\tau_d}^{t} f(t')dt'. \tag{4.2}$$

These equations form a set of integral equations that is non-trivial to solve. However, for constant illumination $\Phi(t) = \Phi_c$, and $P(t) = P_c = R_c$, where R_c is the measured count rate from the detector. Equation 4.1 can then be solved for Φ_c as:

$$\Phi_c = \frac{1}{\eta_{PDP}} \left(\frac{R_c}{1 - \tau_d R_c} - R_{dark} \right). \tag{4.3}$$

The dead time correction factor $1 - \tau_d R_c$ is as expected for a discrete event detector which is not paralysed by additional events within its recovery time [2], while η_{PDP} accounts for detection efficiency at the wavelength used. Incident optical power is then given by:

$$L = \frac{hc}{\lambda} \Phi_c, \tag{4.4}$$

where h is Planck's constant, c the speed of light and λ the wavelength of the source.

Pulsed conditions

Under the repeating optical pulses, Equation 4.1 can again be replaced with a simplified approach. The incident pulses of light on the SPAD are continuous with repetition rate R_{rep}. As pulses are deliberately chosen to have width $\tau_p < \tau_d$, and temporal separation $1/R_{rep} > \tau_d$, the average incident photon flux can be calculated numerically as follows.

For one optical pulse, the SPAD will output, at most, one count. A single optical pulse incident on the detector will actually contain $n \in \mathbb{N}$ photons. Therefore, the probability $P_{count}^{(n)}$ of receiving one photon count from this pulse is given by:

$$P_{count}^{(n)} = 1 - (1 - \eta_{PDP})^n. \tag{4.5}$$

Note that this makes use of the identities $\sum_{i=1}^{0} \equiv 0$ and $\prod_{j=1}^{0} \equiv 1$. The probability P_{count} of receiving a photon count for any pulse is then:

$$P_{count}(n_{av}) = \sum_{n=0}^{\infty} P_{n_{av}}(n) \cdot P_{count}^{(n)}. \tag{4.6}$$

Here, $P_{n_{av}}(n)$ is the probability that a given incident pulse contains n photons, which follows a Poisson distribution with average photon number $n_{av} \in \mathbb{R}^+$, described by:

$$P_{n_{av}}(n) = \frac{n_{av}^n}{n!} e^{-n_{av}}. \tag{4.7}$$

P_{count} can also be measured experimentally from the measured signal count rate when transmitting a binary symbol of "1" $R^{(1)}$:

$$P_{count,exp} \approx \frac{R^{(1)} - R_{dark}}{R_{rep}}. \tag{4.8}$$

Here, R_{dark} is the dark count rate of the detector. It is therefore possible to find n_{av} numerically by solving:

$$P_{count}(n_{av}) - P_{count,exp} = 0. \tag{4.9}$$

Average incident flux and incident power are then given by:

$$\Phi_{inc}^{(1)} = R_{rep} n_{av} \tag{4.10}$$

$$L_{inc}^{(1)} = \frac{hc}{\lambda} \Phi_{inc}^{(1)}. \tag{4.11}$$

Note that this is calculated assuming transmission of binary symbol "1". During data transmission, as described in Section 4.1.1, no pulses are transmitted on the binary symbol "0". Assuming that the two binary symbols are equally likely, average incident photon flux and optical power are given by:

$$\Phi_{inc} = \Phi_{inc}^{(1)}/2 \tag{4.12}$$

$$L_{inc} = L_{inc}^{(1)}/2 \tag{4.13}$$

4.1.3 Poissonian Signal-to-Noise Ratio

In conventional OWC, the signal-to-noise ratio (SNR) is often used to characterise the strength of the received signal. In the transmission method investigated here, it is the distinguishability of the correlation peak in $g(\tau)$ that indicates the robustness of classical information recovery to noise. A conventional definition of SNR for this system can be defined as:

$$SNR = 10 \log_{10} \frac{N_{signal}}{N_{noise}}, \tag{4.14}$$

where N_{signal} and N_{noise} are average signal and noise correlation counts. However, as the correlation counting interval increases, N_{signal} and N_{noise} will both increase at linear rates, resulting in a constant SNR. This does not reflect the observed increase in distinguishability of signal correlations with increasing repetitions.

Instead, the statistical distributions of signal and noise correlation counts have been investigated, with the aim of determining a more applicable figure of merit for signal strength. Photon counting experiments were performed using the setup discussed in Section 4.1.1. The transmitter was set to send pulses in a continuous fashion, as though the data stream was a continuous stream of the binary symbol "1". The received average count rate was measured as 1.07×10^7 Hz in a dark lab environment, with an average background count rate of 619 Hz. The temporal correlations of photon detections were binned with a bin width of 10 ns. Figures 4.5(a) and 4.5(b) show average histograms of photon correlations for 1000 experiments after 5 and 100 pulse pair repetitions, respectively.

At 5 repetitions, the histogram peak is very low, and difficult to distinguish from background signals. After 100 repetitions the signal is much easier to distinguish, however, in real data transmission with no averaging, the histogram will follow a distribution. The correlations are discrete independent events, so they follow a Poissonian distribution (see Appendix A). The distributions of signal and noise are plotted in Fig-
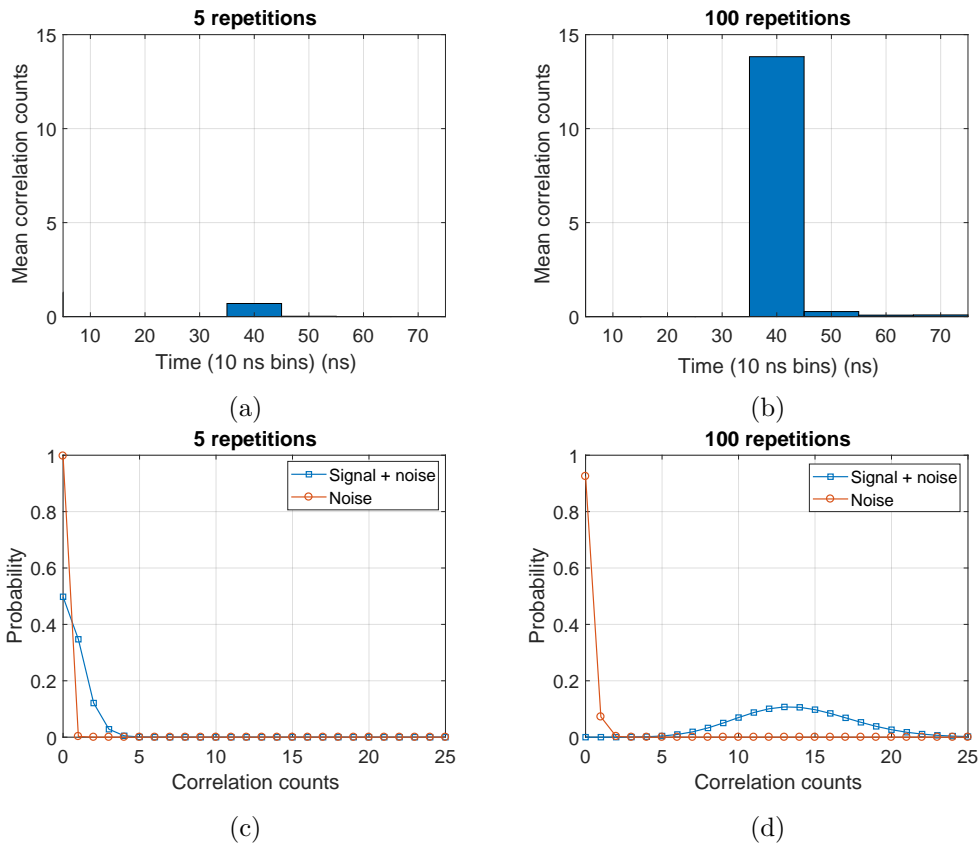
Figure 4.5: Measured correlation histograms for (a) 5 and (b) 100 pulse repetitions. Poissonian distributions of signal and noise for (c) 5 and (d) 100 repetitions. The values were obtained from the average of 1000 experimental repetitions. There is a slight increase in counts in the 50 ns bin for 100 repetitions due to the finite optical pulse widths. While the FWHM is 5 ns, the tail end of the pulses is slightly longer.

(a)   (b)
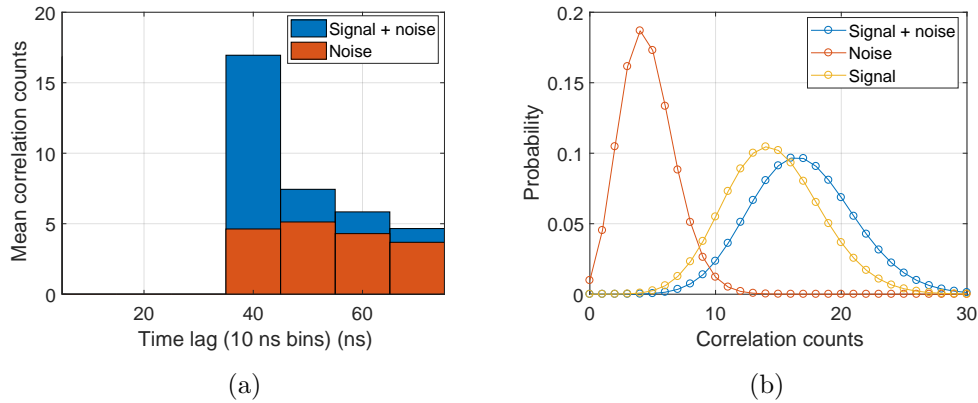
Figure 4.6: (a) Measured correlation histograms for signal with noise, and noise alone. (b) Poissonian distributions for signal, signal with noise and noise.

ures 4.5(c) and 4.5(d) for 5 and 100 repetitions, respectively. Signal has been defined as the number of correlations in the 40 ns bin, and noise defined as the number in the 60 ns bin. In Figure 4.5(c), it can be seen that the signal and noise distributions overlap strongly, so it is difficult to distinguish them. In Figure 4.5(d), the distributions have separated significantly. If a threshold on the histogram is used to determine the presence of a peak, it corresponds to a point along the x-axis of the Poissonian distributions. At 100 repetitions a threshold of around 3 correlation counts would sufficiently distinguish between noise and signal counts. The majority of signal readings would be correctly identified, and noise readings rejected.

An additional factor in the correlation histograms is the increase of background counts. The same experiment was performed with the background count rate deliberately increased to a constant rate of 1×10^7 Hz, to investigate the effect of noise counts. The resulting histogram and distributions are shown in Figure 4.6. The number of background noise correlations has significantly increased. In the distributions, it can be seen that the noise distribution moves further along the x-axis, but also the signal distribution, as noise counts are present in both. The signal distribution with no noise is shown for comparison.

Distinguishability of the signal correlation peak is therefore determined by the over-
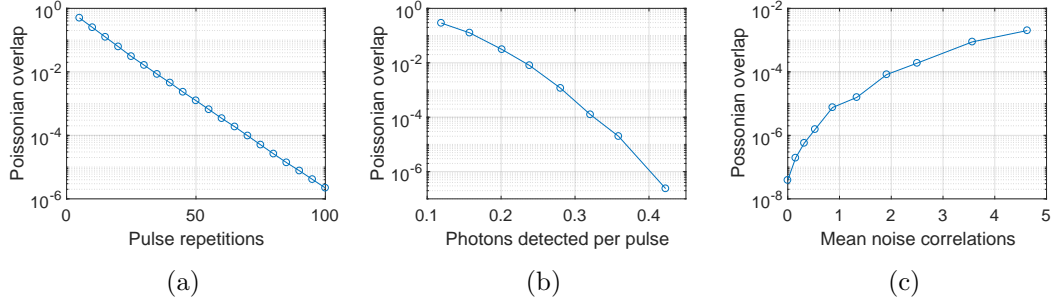
Figure 4.7: Poissonian overlap for changing (a) pulse repetition number, (b) photon detection probability and (c) noise correlations.

lap of the Poissonian distributions for total signal plus noise correlations, $P_T(k)$, and the noise alone $P_n(k)$. $P_n(k)$ is the probability of k correlations occurring due to noise with mean λ_n, given by the Poisson distribution in Equation 4.15. Similarly, the correlations counts with signal alone is given by $P_s(k)$ with mean λ_s. The distribution of correlations counts in the presence of both signal and noise, $P_T(k)$, is given by Equation 4.16. The Poissonian overlap is then given by Equation 4.17.

$$P_{s/n}(k) = \frac{\lambda_{s/n}^k e^{-\lambda_{s/n}}}{k!} \tag{4.15}$$

$$P_T(k) = \sum_{m=0}^{k} P_n(m) P_s(k-m). \tag{4.16}$$

$$Overlap = \sum_{k=0}^{\infty} P_T(k) P_n(k), \tag{4.17}$$

A lower value for the overlap indicates a more distinguishable signal, which will result in a more reliable communication link. There are three major factors that will influence the overlap: number of pulse repetitions (equivalently data rate), photon detection probability (equivalently received power), and noise correlations. Example overlap functions, as each of these parameters change, are shown in Figure 4.7.

The overlap reduces exponentially with increasing pulse repetition number, though the rate of decay will depend on the received signal power. Figure 4.7(a) is valid for a

received power of 38 pW with low background light. Higher received power results in steeper decay, and lower power a more shallow decay. In addition, the overlap depends on the probability of photon detection from each pulse. Figure 4.7(b) shows the overlap for 100 repetitions as the photon probability is changed, and shows the decay is faster than exponential. The different trends can be understood by noting that λ in Equation 4.15 follows $\lambda = p_{ph}^2 N_r$, where p_{ph} is the probability of detecting a photon from a single pulse, and N_r is the number of pulse repetitions sent. This relationship gives rise to the linear appearance of Figure 4.7(a) and the quadratic appearance of Figure 4.7(b). As background correlations increase, the overlap also increases, as shown in Figure 4.7(c). Here, the trend is sub-exponential. It is important to note that the noise model in this transmission scheme is asymmetric, due to the Poissonian nature of photon detections. This is significantly different to noise in conventional optical communications, which is usually treated as Gaussian and symmetric.

Distinguishability of a signal in $g(\tau)$ is characterised well by the Poissonian overlap given in Equation 4.17. This makes it a more useful parameter for link characterisation than conventional SNR.

4.1.4 Data Rates and Bit Error Ratio

As determined in Chapter 3, the data rate of the transmission scheme implemented here is related to dead time (τ_d) and pulse width (t_p) by:

$$R_{data} = \frac{1}{N_{rep}(t_p + \tau_d)}. \tag{4.18}$$

Here N_{rep} is the number of pulse repetitions required to see a distinguishable peak in $g(\tau)$. Another way of looking at this is that the data rate fixes the number of repetitions available and therefore the probability of detecting a photon must be increased to maintain the $g(\tau)$ peak. As photon detection probability is directly related to received power, this leads to characterisation of the communication link in a conventional OWC
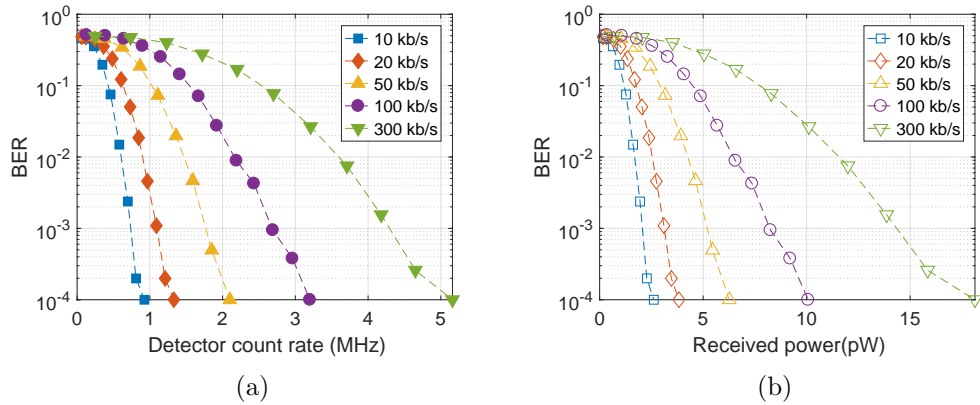
Figure 4.8: BER against (a) detector count rate and (b) received power for data rates of 10, 20, 50, 100 and 300 kb/s. In all cases, the LED pulse rate is 25 MHz, causing pulse separations of 40 ns.

manner: by bit error ratio (BER) against received power.

A PRBS of 1×10^4 bits is prepared on the FPGA, the length of which is limited by the data processing capabilities of the oscilloscope and PC components in the measurement setup. The ND filter wheel allows control over the received power and, therefore, photon detection probability. The received photon count streams are processed offline into a data stream, which can then be compared to the original stream sent to the FPGA. The resulting BER curves are shown in Figure 4.8 in terms of both detector count rate (a) and received power (b). While the curves in Figure 4.8(a) and (b) appear almost identical, the relationship between detector count rate and received power is not strictly linear, as detailed in the power calculations in Section 4.1.2. These results were taken for very low background conditions, with an average background count rate of 619 Hz.

The received power measurements for the BER results are the amount of power incident on the active area of the SPAD, calculated using the numerical methods detailed in Section 4.1.2. The detector count rate is the parameter which governs the BER performance; however, the optical power required to attain the required counts is influenced by the properties of the SPAD. The detection efficiency of the SPAD at

405 nm is 18% (see Figure 4.2(b)), meaning the incident photon flux on the active area is significantly higher than the detector count rate. More efficient photon detection would yield improved BER performance in terms of received power, though performance for count rate would remain the same.

As shown in the Poissonian distributions in the previous section, the probability of detecting a noise correlation under low background conditions is very low. The threshold for determining the presence of a peak can therefore be set at very low levels. For this experiment a threshold of 2 correlation counts was used. This means the bit errors arise almost exclusively from missed correlation counts when transmitting a symbol of "1".

Figure 4.8(b) shows that with 15 pW of received power, a BER of less than 1×10^{-3} can be achieved for a 300 kb/s link. The same BER can be achieved with 2 pW for a 10 kb/s link. As expected, these data rates are modest, however, the trade off between data rate and received power can extend in both directions. Data can be transmitted at almost arbitrarily low received power levels, at the expense of data rate. Similarly, if more received power is available, the data rate can be increased. The relationship between data rate and count rate is expected to be governed by $R_{data} \propto (ph/s)^2$, as the number of correlations depends on the square of received power. Figure 4.9(a) shows data rate for given count rates at a BER of 1×10^{-3}, with experimental data in circular points and a fitted curve. The $R_{data} \propto (ph/s)^2$ relationship is a good fit, indicating it can be used to estimate achievable data rates for given detector count rates.

Figure 4.9(b) uses a logarithmic scale to compare the same results to the channel capacity, which was calculated in Section 3.4.5. Evidently, the correlation approach falls significantly short of the channel capacity for this SPAD and operational wavelength. The primary reason for this is that the process of receiving correlations inherently requires a photon from each of two adjacent pulses to be detected. As this occurrence is unlikely, the pulses are repeated many times to build a histogram. This can be thought of as a channel coding approach, to correct for erroneous detections through
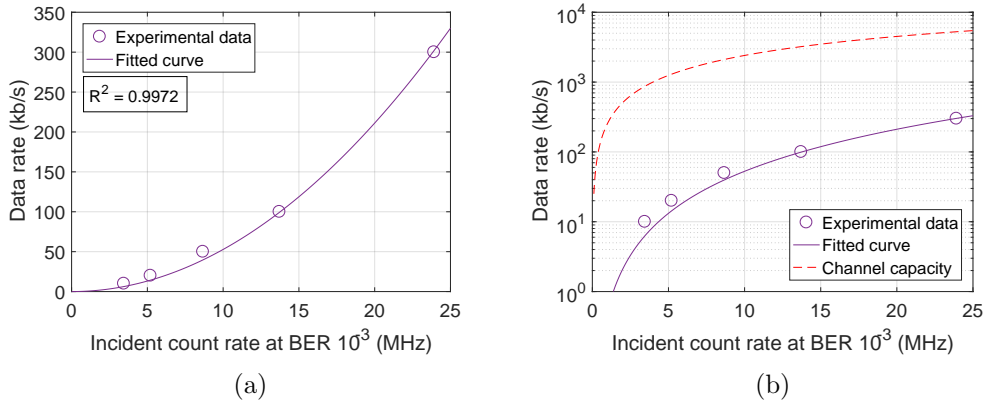
Figure 4.9: (a) Data rate against count rate for a BER of 1×10^{-3}, fitted with $y = ax^2$ using a non-linear least squares method in MATLAB$^{\text{TM}}$, resulting in $a = 0.528$. (b) Logarithmic scale plot to show comparison to channel capacity.

repetition. Such repeat code methods are inefficient compared to modern forward error correction methods, so the correlation approach is far from achieving capacity.

While there is significant loss in performance compared to channel capacity, the advantage from repeated, correlated pulses is expected to be in background rejection capabilities. Incident photons from background sources are unlikely to be correlated on the same time-scales used for data transmission and, therefore, should not show significant interference. These effects are investigated in Sections 4.1.6 and 4.1.7.

4.1.5 Photons Per Bit Cost and the Quantum Limit

A metric for characterising the efficiency (or cost) performance of the link is the number of received photons per bit. If n_{av} is the average number of photons per pulse incident on the detector, then for a given R_{data}, the number of incident photons per bit n_{inc} is given by:

$$n_{inc} = \frac{n_{av} R_{rep}}{2 R_{data}}. \tag{4.19}$$

Here, R_{rep} is the pulse repetition rate, and the factor of 2 accounts for half the transmitted bits being "0". However, the number of photons *received* per bit is found

experimentally according to:

$$n_{rec} \approx \frac{R_{sig}^{(1)} - R_{dark}}{2R_{data}}, \qquad (4.20)$$

and related approximately to n_{inc} by:

$$n_{rec} \approx \eta_{PDP} n_{inc}. \qquad (4.21)$$

The standard quantum limit (SQL) for optical communications will apply to the number of received photons per bit n_{rec}, as it is defined for an ideal photodiode with 100% efficiency [3]. The SQL is the minimum number of photons per bit required to maintain a certain BER for a given transmission scheme, set by the Poissonian nature of photon detection. If an average number of photons n_{rec} is incident on a detector for transmission of a binary "1", electron hole pairs are formed with a Poissonian probability distribution with mean n_{rec}. For a binary symbol of "0" it is assumed that no electron hole pairs are generated. The probability distribution of the response under n_{rec} incident photons has a non-zero probability of recording no counts and, therefore, being indistinguishable from transmission of a "0", leading to a bit error. The BER can be expressed in terms of n_{rec} by rearranging the equation for a Poissonian distribution at $k = 0$ (see Appendix A) as:

$$BER = \frac{1}{2}e^{-n_{rec}}. \qquad (4.22)$$

Alternatively, the minimum number of photons that are required to maintain a set BER is given by rearranging Equation 4.22 into:

$$n_{rec} > -\log(2 \times BER) \quad n_{rec} \in \mathbb{N}. \qquad (4.23)$$

Note that n_{rec} is the number of photons received for transmission of a binary "1", and it is assumed that the transmission scheme has equal probability of transmitting each
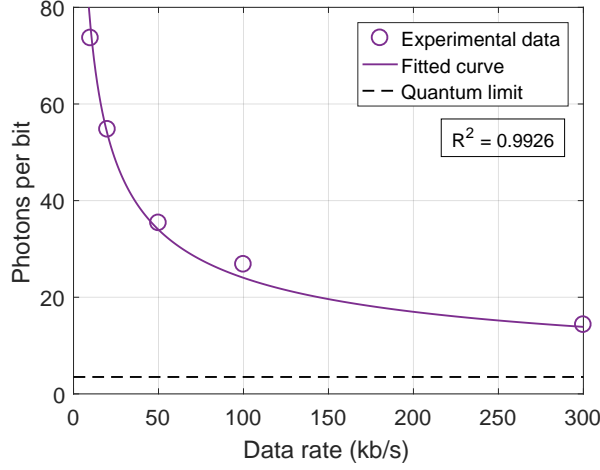
Figure 4.10: Received photons per bit for data rates to maintain a BER of less than 1×10^{-3}.

symbol. Therefore, the standard quantum limit in photons per bit for OOK is given by:

$$SQL = \frac{n_{rec}}{2}.$$ (4.24)

For the case considered here, a target BER of 1×10^{-3} is set, resulting in an SQL of 3.5 photons per bit.

The photons per bit for each data rate investigated is plotted in Figure 4.10, with the SQL for comparison. The fitted curve is calculated from the relationship between correlation counts, received power and data rate. The number of signal correlations depends on the square of received power, and is inversely proportional to data rate R_{data}. In order to maintain a target BER, a constant number of correlation counts must be reached, meaning $(ph/s)^2 \propto R_{data}$. As photons per bit is then the required photons per second over data rate, the following relationship is obtained:

$$ph/bit \propto \frac{1}{\sqrt{R_{data}}}.$$ (4.25)

Therefore, the data in Figure 4.10 is fitted with a $y = a/\sqrt{x}$ relationship, resulting in

a value of $a = 240$ with an R^2 value of 0.9926.

At 300 kb/s, the communication link is transmitting each bit with an average of 14.3 detected photons. This is relatively close to the SQL, as described above. While the trend of the curve suggests higher data rates will move closer, the correlation scheme will be ultimately unable to reach the SQL. Two photons must be detected for each correlation count, increasing the cost of data transmission. Furthermore, the correlation counts themselves follow a Poissonian distribution, which must reach a high enough level to be distinguished from background noise.

It is important to note that no FEC has been implemented for these experiments, so there is potential for improved efficiency by using powerful error correction codes [4–6]. Furthermore, only OOK-style transmission has been implemented here. As discussed earlier in Section 3.4.4, PPM-style transmission has potential for much more efficient data transfer, though at an increased level of complexity and at the cost of data rate.

After correcting for detector efficiency, 14.3 detected photons corresponds to 79.6 incident photons. At a wavelength of 405 nm, this equates to 3.91×10^{-17} J incident on the detector per bit. This extremely low energy demonstrates the suitability of the transmission scheme for low emitted power or high channel loss environments.

4.1.6 Influence of Constant Background Signals

A major strength of this transmission method is that it is expected to be robust to background noise counts. Ambient light, such as sunlight or interior lighting, is approximately constant, and does not show temporal correlations on the time scales of 10s of ns. To verify the minimal interference, BER data was taken with increasing levels of background light generated with a secondary LED. The background LED (OSRAM LD CQ7P) emitted at 450 nm, and was placed within a few centimetres of the SPAD, with no additional optics. The filter in front of the SPAD was removed to allow strong background signals for testing.

As background light levels increase, the number of counts detected by the SPAD

(a) (b)
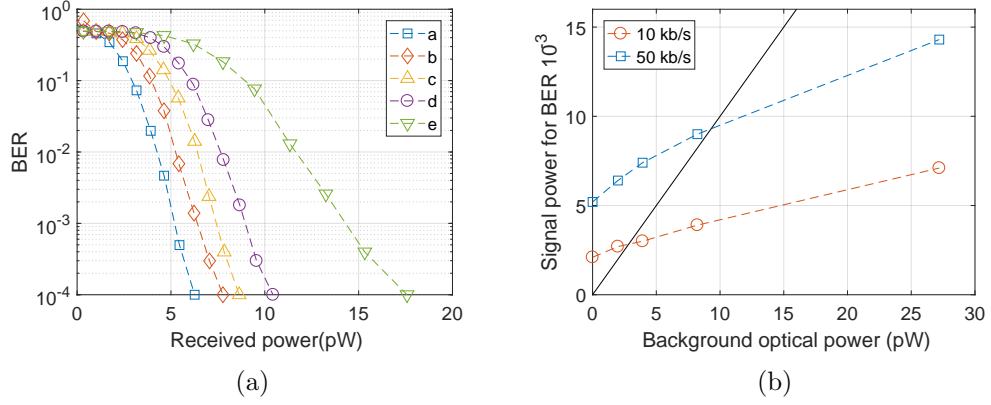
Figure 4.11: (a)BER curves for a 50 kb/s link under varying background conditions. Legend values correspond to table 4.1, with increasing levels of background counts. (b) Comparison of required signal power to background power.

Table 4.1: Table of conditions for BER curves in Figure 4.11(a). Detector count rate (R), incident photon flux (Φ) and optical power (P) are shown for background conditions (subscript bg) and for the signal at a BER of 10^{-3} (subscript s/inc).

Curve	R_{bg} (s^{-1})	Φ_{bg} (ph/s)	P_{bg} (pW)	$R_{s}ig$ (s^{-1})	Φ_{inc} (ph/s)	P_{inc} (pW)
a	619	2.48×10^3	1.09×10^{-3}	2.04×10^6	1.06×10^7	5.2
b	1.08×10^6	4.49×10^6	1.98	2.46×10^6	1.30×10^7	6.4
c	2.06×10^6	8.88×10^6	3.92	2.80×10^6	1.51×10^7	7.4
d	4.00×10^6	1.86×10^7	8.22	3.29×10^6	1.81×10^7	8.9
e	1.00×10^7	6.15×10^7	27.20	4.84×10^6	2.91×10^7	14.3

from background signals also increases. The probability of unwanted correlations also increases, so the threshold for rejecting noise and accepting signal correlations in $g(\tau_j)$ must be increased accordingly. This results in higher requirement on received power, as shown in the BER curves in Figure 4.11(a) for a 50 kb/s link. Each curve represents a different level of background light, with the conditions detailed in Table 4.1. Light levels corresponding to values of 0, 1×10^6, 2×10^6, 4×10^6, and 1×10^7 Hz for detector count rate R_{bg} were targeted, resulting in the incident photon flux and optical power values indicated by Φ_{bg} and P_{bg}, respectively. Table 4.1 also shows the detector count rate, photon flux and power values for a the signal at a BER of 1×10^{-3}.

There is an increase in the required power levels to maintain the same BER perfor-

mance; however, the 50 kb/s link still retains a BER of 1×10^{-3} for a received power of 14.3 pW, while under background conditions of $R_{bg} = 1 \times 10^7$ Hz, or 27.20 pW. This condition is somewhat extreme, as the detector will saturate at a count rate of 1.4×10^7, and normal room lighting with this setup gives a count rate of 2.33×10^5. To better visualise the background rejection, Figure 4.11(b) shows the required signal power to maintain a BER of 1×10^{-3} plotted against the power of the background signal. Data has been taken for both 50 kb/s and 10 kb/s. The solid black line indicates where the power levels are equal. As background power levels increase, the required signal power increases only a comparatively small amount. At very high background light levels, data is being transmitted with signal power at a fraction of the background level.

The constant background light rejection detailed here shows the transmission scheme is capable of operating even under extreme levels of illumination. High intensity background light only requires a minor increase in signal power to maintain the same link performance. The system should therefore easily be capable of operating in conditions where direct sunlight, room lighting, or other constant background lights are present, even if no filter was implemented.

4.1.7 Influence of Modulated Background Signals

As the transmission scheme depends on variations in temporal correlation, it can also be expected to be robust to modulated background signals. While modulated signals will have some level of temporal correlation, dependent on the modulation frequency, in general it will not show significant variation in the correlation window that is being exploited and, therefore, should not cause strong interference.

As the number of correlation counts depends on the square of received power, a high modulation rate background signal should interfere in the same manner as a constant signal at the root mean square (RMS) of its count rate. For this reason, background signals were prepared with modulated intensity and RMS photon count

(a)   (b)
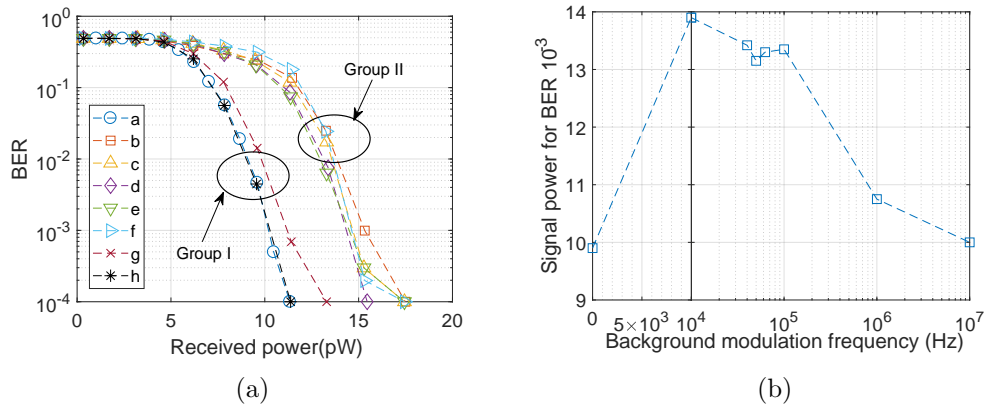
Figure 4.12: (a) BER curves for a 50 kb/s link with modulated background signals. Legend values correspond to Table 4.2, with increasing modulation frequency for the background signal. (b) Signal power required to maintain constant BER for varying background modulation rate.

rates maintained at approximately 5 MHz, resulting in average background power levels of 11 pW. A secondary LED (OSRAM LERTDUW S2W, 450 nm) was modulated with a transistor to generate pseudorandom OOK signals, similar to what would be expected from a conventional OWC link. A number of background modulation rates were investigated, from around the same symbol rate as the correlation link, up to 10 MHz. The resulting BER curves for a data rate of 50 kb/s are shown in Figure 4.12(a), with the corresponding background conditions listed in Table 4.2.

The BER curves show two distinct groups of results, labelled as Group I and II. Group I consists of the results under unmodulated and high modulation rate background signals. Group II consists of the results under background signals with modulation rates comparable to the data rate of the correlation link. When the background signal has a modulation rate similar to the data rate of the desired signal, it causes stronger interference, increasing the required signal power to maintain the same BER. This is shown clearly in Figure 4.12(b), where the signal power to reach a BER of 1×10^{-3} is plotted against background signal frequency. Note the scale changes from linear to logarithmic at 1×10^{4} Hz. High frequency background signals interfere in the same manner as unmodulated signals of the same RMS power, while frequencies

Table 4.2: Table of modulated background conditions for results in Figure 4.12. Optical power P_{bg} and modulation rate of the background interference, detector signal count rate (R_sig), incident signal photon flux (Φ_{inc}) and signal optical power (P_{inc}) are shown.

Curve	Background Modulation Rate	P_{bg} (pW)	R_sig (s^{-1})	Φ_{inc} (ph/s)	P_{inc} (pW)
a	DC	11.35	3.60×10^6	2.02×10^7	9.9
b	10 kHz	12.26	4.74×10^6	2.83×10^7	13.9
c	40 kHz	11.75	4.60×10^6	2.73×10^7	13.4
d	50 kHz	11.39	4.55×10^6	2.69×10^7	13.2
e	62.5 kHz	11.45	4.57×10^6	2.71×10^7	13.3
f	100 kHz	11.36	4.60×10^6	2.73×10^7	13.4
g	1 MHz	11.36	3.84×10^6	2.18×10^7	10.7
h	10 MHz	11.47	3.63×10^6	2.04×10^7	10

close to the correlation link data rate require approximately 40% more received power. This is in contrast to conventional OWC, where it would be very difficult to decode an intensity modulated signal when the background light is also modulated at the same rate.

The lack of interference at higher background frequencies can be attributed to two factors. Firstly, the background signal completes many cycles within a single bit period of the correlation link, making its modulation less significant and it appears closer to an unmodulated signal. Secondly, the dead time of the SPAD restricts the number of photons that can be detected per background cycle, reducing the difference between a high and low level. This reduction in modulation depth also makes the background signal appear more like an unmodulated signal.

When the background signal modulates close to the correlation link data rate, the changes in intensity have greater effect. The background signal is now generating different levels of noise correlations from one bit period to the next, making threshold decisions more difficult. However, under all conditions, a BER of 1×10^{-3} is achieved with less than 14 pW of received power.

The correlation link is robust to modulated background signals as it operates on two time scales simultaneously, namely the correlation time and the bit period. As

conventionally modulated signals tend to operate on a single time scale set by the modulation frequency, they are unlikely to cause significant interference. This means the correlation link could potentially be used in the presence of other modulated optical signals, making it suitable for applications such as the "Internet of Things", where many devices may be communicating simultaneously, or as a secondary link in an OWC network. Furthermore, multiple correlation links can operate in parallel simply by adjusting the correlation time used, enabling parallel scaling of data rates, or multiple simultaneous data streams to different devices.

4.2 Real-Time Link

The previous results relied upon offline processing of SPAD counts and decoding of data streams. A trigger signal from the FPGA sent to the oscilloscope bypassed any issue of synchronisation. As this is far from a practical communications link, a system for decoding data streams in real-time on an FPGA was developed. An embedded clock word allows the data stream to be synchronised on both a symbol and frame level.

4.2.1 Clock Synchronisation

For the sent and received data streams to synchronise, data is divided into frames. Each frame of length N_{frame} is sent with a clock word of length n_{clk} and data packet of length n_{data}. Frame level synchronisation can then be obtained by searching for the clock word in the data stream. Synchronisation can only be correctly achieved if the clock word is not replicated in part of the data packet. Therefore, n_{clk}, n_{data} and the clock word should be carefully chosen in order to minimise the probability of this occurring. Assuming there are no errors during transmission, and M frames are sent to obtain synchronisation, the probability of incorrect synchronisation can be calculated as:

$$P_{err}(n_{clk}, n_{data}, M) = \frac{p(n_{clk}, n_{data}, M)}{1 + p(n_{clk}, n_{data}, M)}. \tag{4.26}$$

Here, $p(n_{clk}, n_{data}, M)$ is the average number of times the clock word is replicated in the data stream, and can be calculated recursively:

$$p(n_{clk}, n_{data} < n_{clk}, M) = 0 \tag{4.27}$$

$$p(n_{clk}, n_{data} = n_{clk}, M) = \frac{1}{2^{n_{clk}M}} \tag{4.28}$$

$$p(n_{clk}, n_{data} > n_{clk}, M) = \frac{1}{2^{n_{clk}M}}(1 + p(n_{clk}, n_{data}, M))$$
$$+ \left(1 - \frac{1}{2^{n_{clk}M}}\right)p(n_{clk}, n_{data}, M). \tag{4.29}$$

Importantly, the clock word should be chosen so that it cannot be replicated by adding matching bits before or after the sequence. For example, a clock word of "010101" would yield higher values of $p(n_{clk}, n_{data}, M)$ than calculated in Equations 4.27 - 4.29 as the sequence "01" preceding or following the clock would lead to incorrect synchronisation.

If the clock word, n_{clk} and n_{data} are chosen according to the above conditions, then the probability of the clock word appearing in the data stream can be extremely low. Here, values of $n_{clk} = 6$ and $n_{data} = 32$ are used, with $M = 6$ frames used for synchronisation. This results in $P_{err} = 3.9 \times 10^{-10}$. A clock word of "001101" is used, which satisfies the requirements detailed above.

The clocks of the transmitter and receiver must also be synchronised on a symbol level, in order to correctly allocate correlation counts to their bit periods. In addition to frame-level synchronisation, the clock word also permits calculation of the phase offset between transmitter and receiver by comparing correlation counts for each bit. By optimising the offset to maximise correlations for "1" and minimising for "0", symbol level synchronisation is achieved.

The clock word can also be used to determine a suitable threshold level between
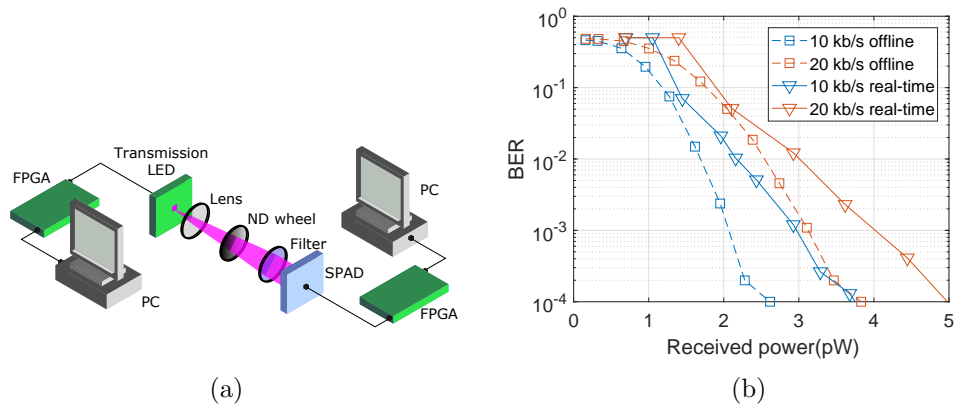
Figure 4.13: (a) Schematic of the real-time experimental setup. (b) BER performance of the real-time link.

noise and signal correlations. As the clock is sent at the beginning of every frame, the threshold can be continuously adapted as count rates vary.

All synchronisation and threshold definition can be done in real-time on an FPGA using these methods, permitting characterisation of a more realistic application scenario.

4.2.2 Bit Error Ratio Performance

In addition to the clock synchronisation methods for decoding, the driving method previously performed through an FPGA and additional digital electronics was combined into the pixel selection FPGA on the CMOS control board. The experimental setup is therefore simplified as shown in Figure 4.13(a). Now the communication link is between separate PCs, with no forced synchronisation.

The BER performance of the real-time link was assessed by transmitting data from one PC to another and comparing the data streams. Due to operational frequency limitations on the receiver FPGA, only data rates up to 20 kb/s are possible. The BER curves are shown in Figure 4.13(b), with the offline processed results also shown for comparison. It can be seen that the performance of the real-time link is slightly reduced compared to offline processing. This is attributed to the offline system having

forced perfect synchronisation, where the real-time system may not be able to reach this standard. It should also be noted that the data rates quoted here include the clock word. The overhead of 18.75% from the clock word reduces useful data transfer rates to 8.42 and 16.84 kb/s for 10 and 20 kb/s links respectively. This real-time setup was used to demonstrate the systems suitability for various applications in Chapter 5.

4.3 Summary

This chapter has discussed the experimental implementation of the correlation-based transmission scheme introduced in Chapter 3. The current setup utilises a CMOS controlled micro-LED array as a transmitter, with a commercial SPAD module as a receiver. Electronic control of the transmitter system is achieved through an FPGA.

As conventional SNR does not give meaningful information on the signal distinguishability, a new figure of merit, the Poissonian overlap, has been discussed. Furthermore, the system has been characterised in conventional BER performance with received power, indicating a data rate of 300 kb/s is possible with 15 pW of power, for a BER of less than 1×10^{-3}.

The key strength of the correlation approach is in background rejection. Both constant and modulated signals cause little interference with the signal, and data can be sent with signal power at a fraction of the background optical power. This capability allows the scheme to operate in the presence of other modulated signals, such as a conventional OWC link.

A real-time system has been developed and implemented using FPGAs for both transmitter control and signal decoding. The system uses a clock word to achieve frame-level and symbol-level synchronisation, and can operate at data rates up to 20 kb/s. This system is used to demonstrate application scenarios in Chapter 5.

A full comparison of the proposed data transmission scheme to conventional optical communications has not been performed here. However, it is expected that the per-

formance in terms of data rates and photons-per-bit will not outperform conventional schemes. This is due to the increased number of optical pulses, and therefore optical power, required to detect correlations. Additionally, the probability of detecting correlations is related to the square of the probability of detecting a single pulse, further reducing correlation count rates. Nevertheless, the potnetial background rejection performance and simple hardware requirements make this an attractive data transmission method.

Bibliography

[1] J. J. D. McKendry, B. R. Rae, Z. Gong, K. R. Muir, B. Guilhabert, D. Massoubre, E. Gu, D. Renshaw, M. D. Dawson, and R. K. Henderson, "Individually addressable AlInGaN micro-LED arrays with CMOS control and subnanosecond output pulses," *IEEE Photonics Technology Letters*, vol. 21, pp. 811–813, Jun 2009.

[2] G. Knoll, *Radiation detection and measurement*. New York: John Wiley & Sons, 1989.

[3] W. Shieh and I. Djordjevic, *OFDM for optical communications*. London: Elsevier, 2010.

[4] B. S. Robinson, A. J. Kerman, E. A. Dauler, R. J. Barron, D. O. Caplan, M. L. Stevens, J. J. Carney, S. A. Hamilton, J. K. W. Yang, and K. K. Berggren, "781 Mbit/s photon-counting optical communications using a superconducting nanowire detector," *Optics Letters*, vol. 31, no. 4, pp. 444–446, 2006.

[5] M. L. Stevens, D. O. Caplan, B. S. Robinson, D. M. Boroson, and a. L. Kachelmyer, "Optical homodyne PSK demonstration of 1.5 photons per bit at 156 Mbps with rate-(1/2) turbo coding," *Optics Express*, vol. 16, no. 14, pp. 10412–20, 2008.

[6] D. Geisler and T. Yarnall, "Demonstration of 2.1 photon-per-bit sensitivity for BPSK at 9.94-Gb/s with rate- FEC," *Optical Fiber Communication Conference*, pp. 13–15, 2013.

Chapter 5

Single Photon Communications III: Applications

In the previous chapter, a real-time link was developed to demonstrate the practicality of employing the correlation-based single-photon transmission link. In this chapter, experimental applications of this link are presented.

The first application is an underwater channel, where optical signals are attenuated by scattering and absorption effects. The single-photon nature of the scheme allows functional data transmission even under high degrees of optical loss. Following this, the link was tested under power from a nanosatellite simulation testbed, indicating suitability for use on CubeSat systems for inter-satellite communication links. Finally, an extension to a 2D array of SPADs as a receiver is discussed, as a means of increasing dynamic range and data rates, with scope for parallel channel transmission for "Internet of Things" applications.

5.1 Underwater Transmission

A potential application for the correlation-based transmission scheme is in underwater communications. Recently, underwater optical wireless communications (UOWC)

has arisen as an alternative to the widely used acoustic communications for underwater scenarios [1]. Communication links need to be made between underwater vehicles (manned or un-manned), sensors, divers or structures. Currently, data is sent using either acoustic or radio frequency (RF) methods, though both have limitations. Acoustic communications are limited in data rate, and RF signals are heavily attenuated by seawater, particularly at high frequencies. Optical communications are less limited in range, and potentially offer data rates up to Gb/s [2].

A major difficulty in UOWC is that absorption and scattering within the turbid media can cause high degrees of loss in the optical channel. However, the light absorption spectra show lower levels of attenuation in the blue-green region, shifting to slightly higher wavelengths with additional scattering particles [3]. This presents an opportunity for lasers [4–6], GaN based LEDs [7–9] and micro-LEDs [10] to be used as transmitters. Furthermore, SPADs have been considered as receivers for their high sensitivities [8,11].

As shown in the previous sections, the correlation scheme requires only picowatt levels of received power to transmit data streams at 100s of kb/s. While the data rate is unlikely to compete with other optical approaches, the low received power requirements are a potential strength when transmitting in high-loss conditions. In addition, the simple hardware and low power consumption are appealing for use in remote vehicles or diving equipment.

5.1.1 Scattering Media and Attenuation Length

Optical signals transmitted through water undergo two main power loss processes: absorption and scattering. Some of the transmitted photons are absorbed and converted to heat, and some will be scattered by particulates in the water [1]. The optical attenuation can be characterised by the attenuation length $c(\lambda) = a(\lambda) + b(\lambda)$, which is the sum of the loss due to to absorption $a(\lambda)$ and scattering $b(\lambda)$. All parameters are dependent on wavelength λ and also vary significantly with the type of water in
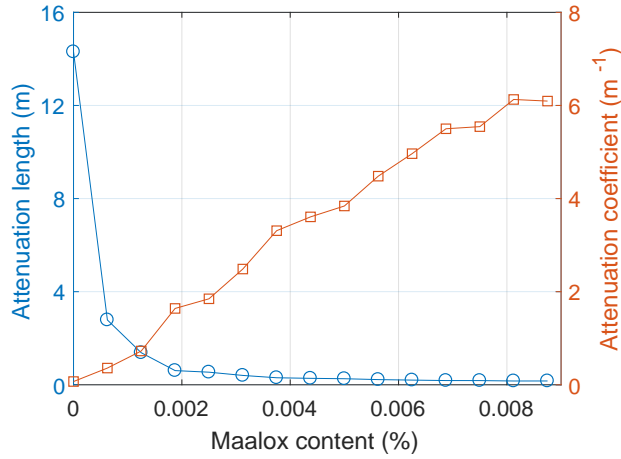
Figure 5.1: Attenuation characteristics at 450 nm for the 1.5 m water tank under increasing Maalox content, expressed in attenuation coefficient, or its inverse, attenuation length.

question, as different materials and substances will be present. Typically, $c(\lambda)$ can vary from $0.1514\,\mathrm{m}^{-1}$ for clear ocean waters, through $0.399\,\mathrm{m}^{-1}$ for coastal ocean, to $2.195\,\mathrm{m}^{-1}$ for harbour water [4]. Propagation loss L_P is dependent on $c(\lambda)$ according to:

$$L_P(\lambda, z) = e^{-c(\lambda)z}. \tag{5.1}$$

Where z is the distance through the media. To simulate high-loss environments such as harbour water, it is common practice to add Maalox antacid, a mix of magnesium hydroxide and aluminium hydroxide, to water [4, 5, 12]. The scattering albedo $\omega_0 = b(\lambda)/c(\lambda) = 0.95$ of Maalox is very high, and can be used to produce similar spectral attenuation properties to real-world water samples.

To test the correlation-based communication scheme in an underwater environment, a 1.5 m long, 180 l water tank was used as the optical channel. The tank is filled with tap water, and Maalox added to increase the attenuation coefficient. A 450 nm laser diode was used to characterise the attenuation coefficient and attenuation length through the tank; the resulting data is displayed in Figure 5.1.

130
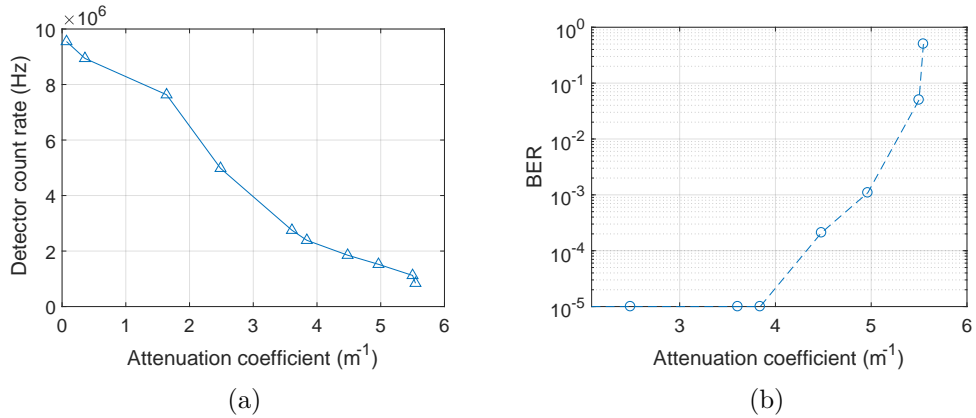
Figure 5.2: (a) Detector count rate changes with attenuation coefficient. (b) BER of a 20 kb/s link with changing attenuation coefficient.

At 450 nm, $c(\lambda)$ scales roughly linearly with Maalox percentage. The data here allows characterisation of the performance of the communication link for varying attenuation situations by adjusting the Maalox content.

5.1.2   Communication Link Performance

The real-time link described in Section 4.2 was installed at either end of the water tank. In place of the 405 nm device used previously, a 450 nm device, with identical layout, was used to fit better with the attenuation window for underwater communications (device "SPC array B" in Table 1.1). A lens (Thorlabs C220TME-A) was used to collimate the light from the LED through the tank. A collection lens (Thorlabs ACL4532U) was used to increase light collection on to the active area of the SPAD at the receiver end. The link was set to send a PRBS of 1×10^5 bits at 20 kb/s. The resulting detector count rate and BER are shown in Figure 5.2.

As expected, increasing the attenuation coefficient decreases the number of counts reaching the receiver, as more light is scattered through the tank. As a consequence, more bit errors are recorded as the correlation counts do not reach the required thresholds. Figure 5.2(b) shows a BER of less than 1×10^{-3} is achievable with an attenuation coefficient of $5\,\mathrm{m}^{-1}$. With a tank length of 1.5 m, this corresponds to a loss factor of

5.53×10^{-4}, meaning over 99.94% of the light sent into the tank is lost. The single photon nature of the transmission scheme enables data transmission with this large degree of loss, without the need for a high power optical transmitter.

In this particular experiment, the BER performance for the detector count rates are identical to that of Figure 4.13, however, multi-path scattering is likely to affect communication performance at higher data rates or longer ranges. As photons can be scattered many times through the media, they can take paths of significantly different lengths to reach the receiver. This delay can result in detection events occurring in later bit periods than intended and causing bit errors due to inter-symbol interference. With higher data rates the time delays experienced are more likely to move photon detections into the wrong bit period, while longer ranges will increase the number of scattering events and potential path lengths. Here, the data rate and communication range are low, 20 kb/s and 1.5 m respectively, reducing such effects.

While the data rate here was specified as 20 kb/s, the detector count rate can be used to estimate achievable data rates through the tank. Figure 5.3 shows potential data rates calculated based on the detector count rate and the fitted curve for data rate against photon counts in Figure 4.9. This curve is valid for the 1.5 m tank used in the experiment. In a highly turbid harbour environment with an attenuation coefficient of $2.195\,\text{m}^{-1}$ [4], the transmission link would be able to maintain a data rate of ≈ 600 kb/s over 1.5 m with the current optical arrangement. This range and attenuation corresponds to a propagation loss factor of 0.0372, meaning the vast majority ($¿$ 96%) of the light transmitted into the tank is lost. Equivalently, the range could be extended at the expense of data rate, assuming suitable levels of light collection are achieved.

As the LED transmitter is a divergent source, and the channel scatters the emitted light, a significant amount of optical power is lost in the area surrounding the receiver. While this will adversely affect the performance, resulting in lower data rates, it can also be thought of as a degree of coverage, or relaxation of alignment requirements.

The experiments shown here are a proof-of-concept demonstration for the correla-
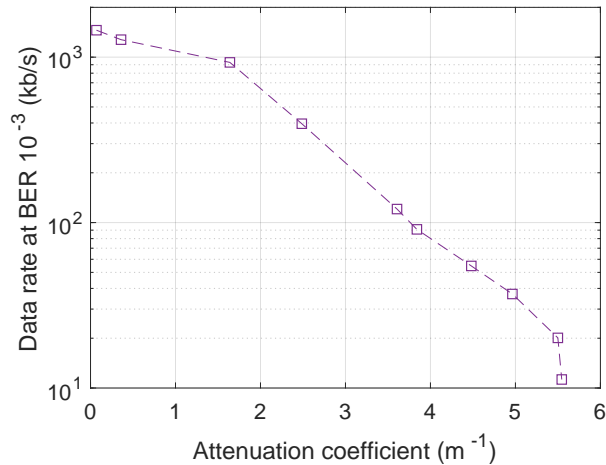
Figure 5.3: Achievable data rates for given attenuation coefficients over a 1.5 m range.

tion link in an underwater environment. Evidently, the system can cope with channel loss associated with highly scattering environments, and there is potential for further improvements by increasing light collection with different optics, or increasing the power output from the LED.

5.2   Solar Powered Satellite Demonstration

The communication system is particularly attractive for inter-satellite links. The hardware used is extremely compact, with low power consumption and integrated control electronics. This combination fits well with cube-satellites (CubeSats), where power budgets and form factor are limited. The robustness to background signals and low received power may relax the high-accuracy pointing requirements and telescope optics of current optical satellite systems. In addition, LED based VLC has shown potential for this application area [13].

5.2.1   CubeSats

CubeSats are small-scale satellites, classified as nanosatellites, constructed in increments of $10 \times 10 \times 10$ cm cubes [14]. Each cube is referred to as 1U (one unit), with

each cube usually associated with around 1 kg of mass. The most common size is a 3U satellite, though 1U up to 6U systems are often used. These small-scale satellites are often constructed using commercial off-the-shelf components, and are launched into orbit by ride-sharing on larger payloads, or deployed from the International Space Station [15]. This significantly reduces the cost of development and sending the satellites into orbit, making space missions much more accessible, and no longer exclusive to large countries and corporations.

A large proportion of the mass and volume available within a CubeSat chassis is taken up by platform systems, including power generation and storage, communication systems, attitude control, and an on-board computer. The remaining space is available for the satellite's payload. Electrical power is generated using deployable solar panels, and stored in lithium ion batteries. The solar panels can generate approximately 2 W per 1U (10×10 cm) panel, with systems deployed on 3U CubeSats able to generate up to 30 W [15]. During eclipse, the satellite relies on the power stored in the battery.

CubeSat Optical Communications

Optical communications using CubeSats has been demonstrated by NASA with the AeroCube optical communication and sensor demonstration (OCSD) [16,17]. This 1.5U CubeSat has demonstrated low-earth orbit (LEO) to ground communications using a diode laser and ytterbium doped fibre amplifier (YDFA). This system was designed to demonstrate 10s of Mb/s downlink rates, though consumes 55 W when operational, and hence can only operate under battery power.

An additional LEO to ground system under development is the nanosatellite optical downlink experiment (NODE) from Massachusetts Institute of Technology [18]. NODE is a 1U CubeSat module to be operated as part of a 3U satellite. As with AeroCube, the optical source is a laser diode and fibre amplifier. Though it has not yet been launched, it is expected to achieve 10 Mb/s data rate with a power consumption of 15 W. For inter-satellite links a similar system is under development, the free-space lasercom and

radiation experiment (FLARE) [19]. FLARE is also a 1U module with laser diode and fibre amplifier, designed to provide 5-20 Mb/s over a range of 20-500 km.

The above examples are communication systems which take up large amounts of the available volume, mass and power in a CubeSat. The advantage of the LED and SPAD based system described in Chapter 4 for CubeSats is that the dimensions and power consumption required should allow it to be integrated as part of the CubeSats platform systems and still allow additional payloads. Achievable range may be reduced when compared to laser based systems, however the link may be useful in formation flying of CubeSats, where inter-satellite distances will be lower.

5.2.2   NANOBED System

To highlight the capability of the system to work with satellite systems, the communication link was tested in the nanosatellite mission test environment, NANOBED, which can seen in Figure 5.4. The NANOBED is a nanosatellite hardware and software test-bed, with CubeSat systems laid out individually, described as a "FlatSat" configuration. Systems included are an electrical power system (EPS), batteries, on-board computer (OBC), and radio communication systems (VUTRX, STC, USRP). A software design tool offers mission design, simulation and analysis, including a link to the hardware for in-loop simulation and testing. A software-defined radio link enables ground software validation and operational testing, over which command and control of the system components can be invoked.

The experimental setup is shown schematically in Figure 5.5. The LED transmission system was integrated with one NANOBED system, and the receiver with a second. The NANOBED power sources emulate the performance of solar panels supplying the nanosatellite and provide power through the EPS. No power is supplied from the PCs to the FPGAs, only a data signal. All power is provided through the NANOBED systems. Figure 5.6 shows a photograph of the micro-LED board under power from the NANOBED system. The communication system is the real-time link described in
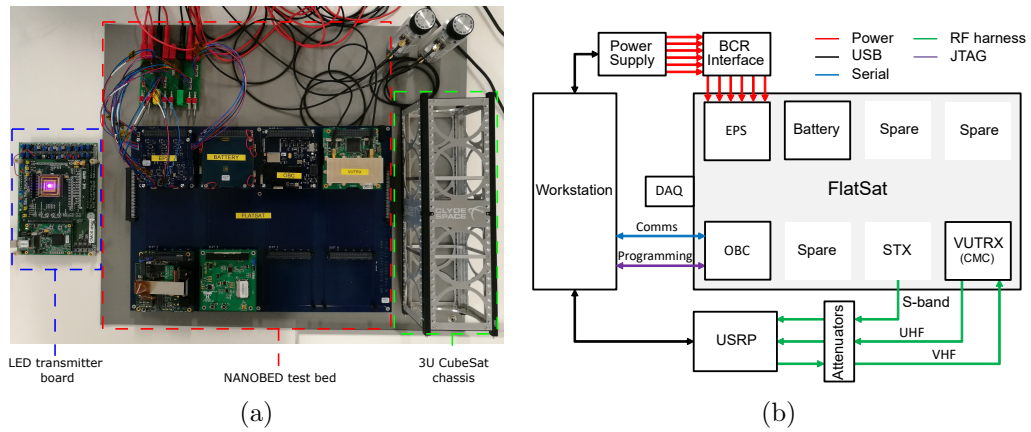
Figure 5.4: (a) Photograph of the NANOBED test environment, with LED transmitter board and 3U cubesat chassis. (b) Schematic of the NANOBED environment.
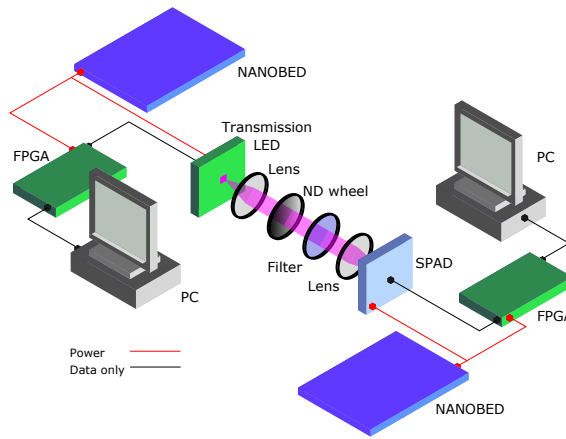
Figure 5.5: Schematic of the experimental setup for the NANOBED experiments.

Section 4.2; however, a 450 nm LED array has been used, with identical pixel layout. The transmitter and receiver are placed 4 m apart, with a transmitter lens to image the pixel at the receiver (Thorlabs C220TME-A), and collection lens (Thorlabs ACL4532U) to increase the amount of light incident on the active area of the SPAD.

5.2.3 Power Requirements and Performance

The electrical power requirements of the communication system are summarised in Table 5.1. The majority of the power consumption comes from the commercial SPAD
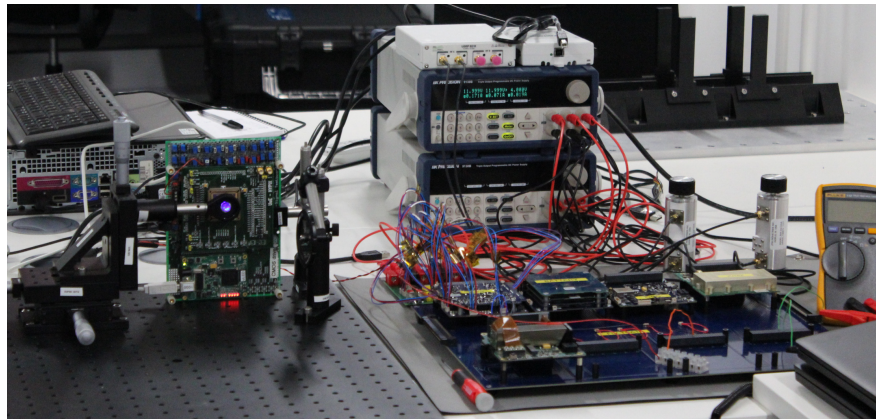
Figure 5.6: Photograph of the micro-LED control board (left) under power from the NANOBED system (right).

module, consuming 3.570 W. The majority of this requirement is likely due to the active cooling system within the module, used to reduce the dark count rate. The NANOBED EPS provides a 5 V bus suitable for powering the FPGA boards directly. Note that the LED and CMOS chip are powered through the transmitter FPGA board. The unregulated battery bus was used with a voltage regulator to provide the 6 V required for the SPAD. So long as the batteries remained suitably charged, the NANOBED system was capable of powering the communication link throughout all experiments. Importantly, this setup had not been optimised to minimise power consumption. There is significant potential for power saving with a suitably designed SPAD receiver, and application-specific integrated circuits (ASICs) in place of FPGA boards. Therefore, this demonstration should be thought of as an upper limit on power requirements. Nevertheless, these values fall well within the expected available power levels from a suitably designed 3U CubeSat [15]. Based on the power consumption of other SPAD based receivers [20, 21], an ideal SPAD receiver for this application may show power requirements of 10-100 mW. This would put the receiver power requirements below 1 W, with the FPGA boards consuming the majority of the power. It is important to note that such a receiver would not have any active cooling systems, which will result in a higher dark count rate than the experimental results shown here. However,

Table 5.1: Typical power requirements of the communication system. The large 6 V power requirements come from the SPAD modules cooling system.

	Voltage (V)	Current (mA)	Power (W)
Transmitter	5	181	0.905
Receiver	5	122	0.610
	6	595	3.570
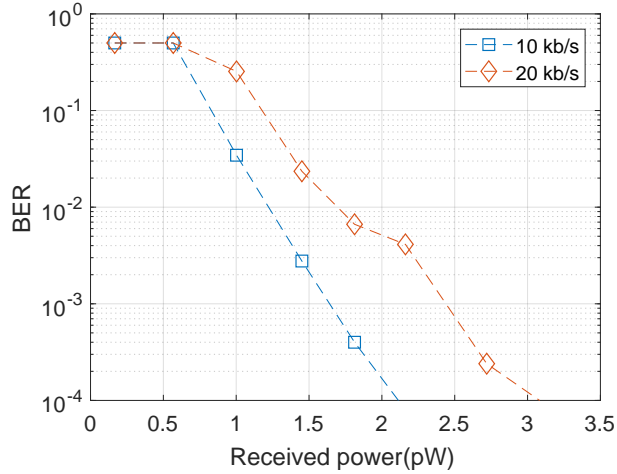
Figure 5.7: BER performance of the communication link in the NANOBED experiments.

as demonstrated in Section 4.1.6, the scheme is robust to constant background count rates, and should only show minimal changes in performance.

The BER experiments performed in Section 4.2 were redone under power from the NANOBED supply. The results are shown in Figure 5.7 in terms of received power. The resulting BER curves were almost identical to previous experiments as shown in Figure 4.13(b) in terms of detector count rate, though show reduced recieved power requirements due to the lower energy photons and increased PDP of the SPAD at 450 nm.

The 4 m arrangement and transmitter lens resulted in the micro-LED pixel projecting a 4 cm wide square image on to the receiver plane. As shown in Figure 5.7, the receiver requires over 2.5 pW of received power to maintain a BER of 1×10^{-3} at 20 kb/s. On a 20 µm diameter SPAD, 3 pW corresponds to an intensity of $9.5\,\mathrm{mW\,m^{-2}}$.

To provide this over the projected 4 cm wide square, the micro-LED must emit an average power of only $15.3\,\mu W$, assuming perfect coupling through the lens.

In an example inter-satellite scenario using CubeSats, a 10 mm receiver aperture could be used. To achieve the 3 pW required for 20 kb/s transmission, an intensity of $30\,nW\,m^{-2}$ would be required at the receiver. An LED with an average output power of 1 mW can provide this intensity over a 180×180 m area. At an example inter-satellite link range of 40 km, this requires a half-angle source divergence of 0.13 degrees, which represents a significant relaxation on the alignment of current laser based systems in which pointing requirements are often less than 1 mrad (0.057 degrees) [22–24]. Furthermore, GaN LEDs at low current densities show higher wall-plug efficiencies than their laser diode counterparts [25], further motivating the use of LEDs to reduce the power consumption characteristics of this system.

5.3 SPAD Receiver Arrays

The results detailed above and in Chapter 4 were taken with a single SPAD as a receiver. A natural progression to increase the number of recorded signal counts is to move to an array of receiver SPADs. In contrast to camera-style arrays of interest for imaging, here, a more useful format for a SPAD array is as a digital silicon photomultiplier (dSiPM) [26]. In a dSiPM, the signal from all SPADs in the array are combined, forming a single detector. Efficient pulse combining methods in digital electronics, combined with high fill factor designs allows fully digital optical detectors with high detection rates [27–29]. Such devices have been demonstrated for use in conventional optical communications [20, 30].

5.3.1 Photon Torrent Receiver

The SPAD receiver array used here is a "Photon Torrent" chip, supplied by the University of Edinburgh, and pictured in Figure 5.8. The detector array consists of 64 rows of
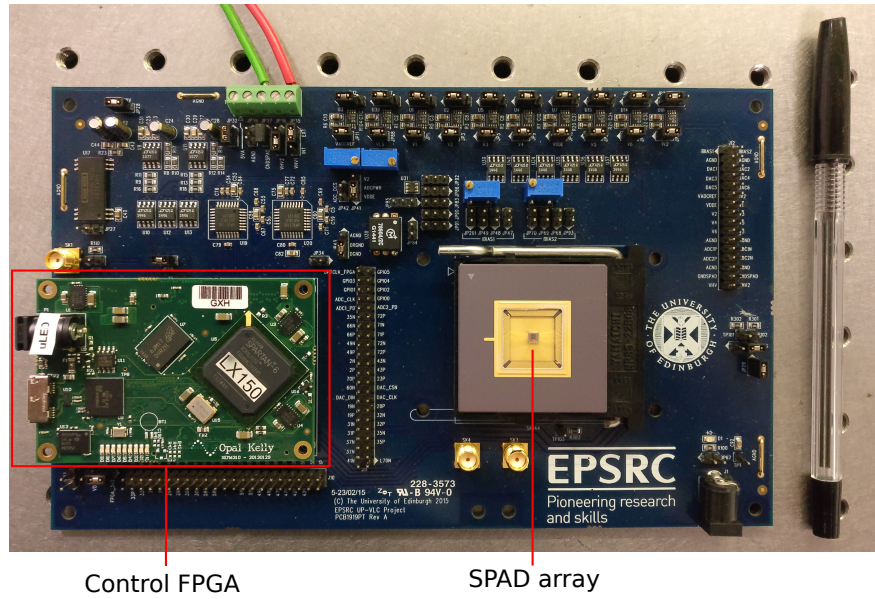
Figure 5.8: Photograph of the Photon Torrent chip and control board.

64 pixels fabricated in 130 nm CMOS [31], giving 4096 SPADs on a 21 µm pitch, with a fill factor of 43% and a measured dark count rate of 350 Hz. This fill factor (F_{fill}) effectively reduces the photon detection efficiency (PDE) of the array, as photons which are incident on the non-active areas will not be detected. Combined with the photon detection probability of each SPAD in the array (η_{PDP}), the PDE is given by:

$$\eta_{PDE} = \eta_{PDP}F_{fill}. \tag{5.2}$$

Including the surround electronics, the receiver chip is 2.6×2.8 mm, and packaged to interface with a control board. The block diagram of the chip layout is shown in Figure 5.9. The array is divided into two areas, in which the output of each row of 32 pixels is combined with an XOR tree and ripple counter [28, 32]. An adder tree combines the output of the ripple counters, and externally controlled multiplexer allows selection of the number of output levels in powers of 2. Low-voltage differential signalling output pads display the signal from the digital-to-analogue converter (DAC) at up to 800 MHz.

The FPGA on the motherboard in Figure 5.8 allows control of the board through
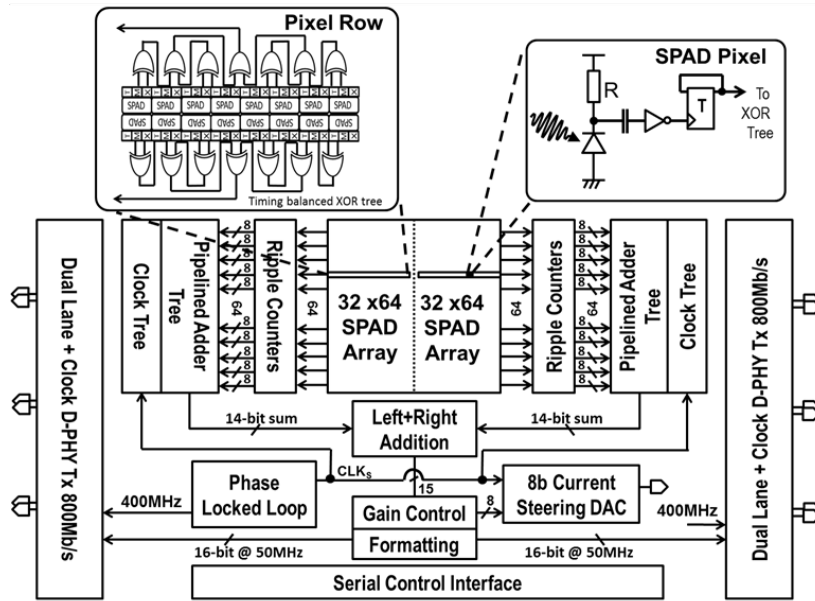
Figure 5.9: Block diagram of Photon Torrent electronics.

a MATLAB$^{\text{TM}}$ interface. The output can be set to sampling frequencies of 100, 200, 400 and 800 MHz. Output photon count ranges can be set from 0-1 up to 0-255 in powers of 2. The output differential signal then consists of voltage levels across a range of around 1 V, discretised into the number of output levels and sampling at the chosen frequency.

As the array of SPADs is combined in an XOR and adder tree, selecting a lower photon count range does not deactivate SPADs in the array, but clips the signal to the specified level. If the array detects more photons than the selected output can display, the output will begin to roll-over back to low counts, so care must be taken not to saturate the device.

The signal from the Photon Torrent chip is captured using a 1 GHz bandwidth active differential probe and high-speed oscilloscope. The oscilloscope is operated at a higher sampling frequency than the SPAD array output in order to accurately recover the signal. The captured traces are exported to MATLAB$^{\text{TM}}$for processing.

For this application, a digital signal showing the number of photons detected in
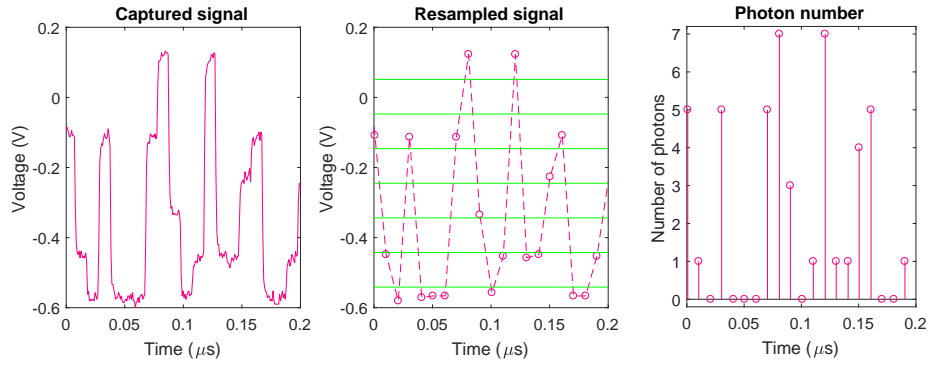
Figure 5.10: Signal processing for Photon Torrent output. (Left to right) Initial 1.25 GHz differential signal, resampled to 100 MHz with thresholds indicated, and final photon number output.

a particular time window is desired, therefore, the analogue voltage signal must be re-digitised. The process is shown in Figure 5.10 for an example output of 0-7 counts at 100 MHz. The 1.25 GHz oscilloscope trace is first resampled to match the output sample rate of the Photon Torrent receiver. The resampled voltage levels are compared to a set of thresholds, which have been pre-determined based on the output voltage ranges and number of discrete levels. This comparison allows conversion of the analogue voltage signal to a digital photon count stream.

The signal processing method applied has limitations for the purposes of determining a photon detection number. The output voltage is always over a range of approximately 1 V, regardless of the count range selected. This means at higher ranges, it becomes increasingly difficult to distinguish the discrete levels. Additionally, higher output frequencies of the Photon Torrent chip begin to approach the bandwidth of the oscilloscope probe, resulting in distorted waveforms which are more difficult to digitise. These effects limit the reliably decoded output mode selections to 200 MHz and an 8 level (0-7 photons) range. Improvements could be made using digital electronics decoding the stream directly from the digital outputs, rather than through the analogue voltage pins.

With the photon number signal in Figure 5.10, the correlation signal $g(\tau_j)$ can be

measured by a sum of element-wise multiplication of the photon sample trace with itself at a sample offset corresponding to the correlation time:

$$g(\tau_j) = \sum_t \sum_{i=-w}^{w} Y(t)Y(t + \tau_j + i). \tag{5.3}$$

Here, $Y(t)$ is the photon number signal varying with the discrete time variable $t = 0, \Delta t, 2\Delta t \dots N\Delta t$, with Δt set by the sample rate of the Photon Torrent chip. The variable w describes the half-width of the correlation window as an integer of the time intervals.

5.3.2 Performance

The Photon Torrent receiver was used to perform optical communications experiments in the same manner as discussed previously. The transmitter was the same CMOS controlled micro-LED used throughout this chapter (device "SPC array 2" in Table 1.1), emitting at 450 nm with 5 ns wide pulses. The OOK-style transmission scheme was implemented with a correlation time of 40 ns on transmission of a binary "1" and no pulses on transmission of a "0". Bit error ratio measurements were taken for varying received average count rates to characterise the performance of the link under different receiver configurations.

Due to the large number of SPADs in the chip (4096) background light, even in a dark lab, gives a high count rate, making the low photon number and low frequency outputs unusable. By using a ND filter of optical density 2.0, the background count rate was minimised, allowing the low photon number modes to be used.

Incident Power Calculation

Photon counts at the receiver are readily measured from the signal processing method above, as a photon number is determined for each sample. While the photon counts determine the BER performance of the receiver, the incident photon flux or power is

an important measure of system performance. For a single SPAD, incident flux and power were calculated using numerical methods, and the same can be applied here.

As shown in Section 4.1.2, the probability P_{count} of receiving a photon count from a pulse incident on single SPAD can be found experimentally by:

$$P_{count,exp} = \frac{R^{(1)}_{single} - R_{dark}}{R_{rep}}.$$

(5.4)

Here, $R^{(1)}_{single}$ is the count rate of a single SPAD when transmitting the binary symbol "1", R_{dark} is the dark count rate, and R_{rep} is the pulse repetition rate. The Photon Torrent chip is 2.6×2.8 mm, and can therefore be assumed to be under uniform illumination across all SPAD pixels in the current experimental setup. With this assumption, $R^{(1)}_{single}$ and R_{dark} can be determined as:

$$R^{(1)}_{single} = \frac{R^{(1)}_{total}}{N_{SPADs}}$$

(5.5)

$$R_{dark} = \frac{R_{dark,total}}{N_{SPADs}}.$$

(5.6)

Here, N_{SPADs} is the number of SPADs in the array, which is 4096, $R^{(1)}_{total}$ and $R_{dark,total}$ are the total count rate and dark count rate from the array, respectively. From here, the numerical method follows that of Section 4.1.2 to calculate the average number of photons per pulse incident on one SPAD, n_{av}. This value can then be converted to incident photon flux and power on the whole SPAD array by:

$$\Phi^{(1)}_{inc} = R_{rep} n_{av} N_{SPADs}$$

(5.7)

$$L^{(1)}_{inc} = \frac{hc}{\lambda} \Phi^{(1)}_{inc}.$$

(5.8)

Note that the numerical method contains the photon detection probability η_{PDP} in the expression for P_{count}, and this value differs from that of the commercial single SPAD
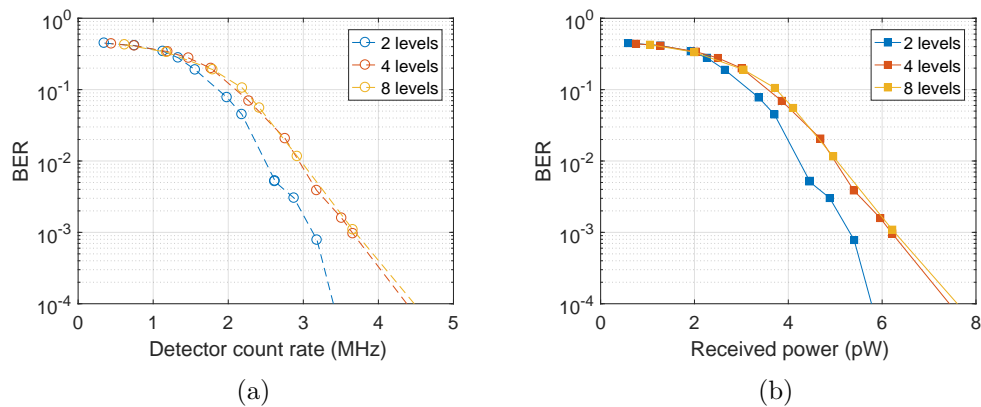
Figure 5.11: BER against (a) photon count rate and (b) received power for 2, 3 and 8 level outputs at 50 kb/s.

used in the previous experiments. The spectral response of the SPADs in the Photon Torrent chip is found in reference [31], from which the 450 nm PDP is taken to be 26%. Furthermore, the photon flux and power levels calculated here are for the signal incident on the active area of the SPAD array only. If the intensity at the receiver is required, the fill factor of the device will have to be considered.

Photon Count Range

The BER experiments were performed first with varying photon count ranges from the Photon Torrent receiver. As mentioned above, only ranges up to 8 levels are available due to the signal processing limitations. Therefore, the BER measurements were performed at a sample rate of 100 MHz with 2, 4 and 8 level outputs, corresponding to 1, 3 and 7 photon counts per sample, respectively. The data rate was set to 50 kb/s initially, to fit with previous results. The BER curves are shown in Figure 5.11. Count rates are determined by summing all photon counts while transmitting, and subtracting background counts.

The 2-level output shows a slight improvement over the other outputs, however, this is likely due to the photon counts being clipped, so the received count rate is artificially lower than it should be. The 4 and 8-level outputs show identical performance, as
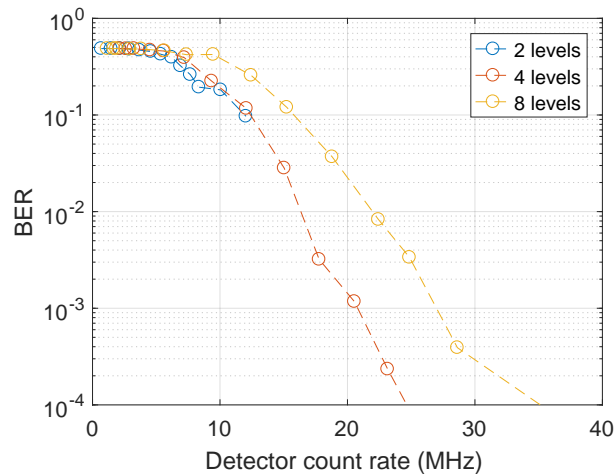
Figure 5.12: BER against photon count rate for 2, 3 and 8 level outputs at 1 Mb/s.

expected, since the choice of output levels sets the upper ceiling of photon counts. It can be assumed that further increasing the output level range would continue to raise the count rate ceiling, rather than improve performance.

The Photon Torrent receiver requires a higher count rate for 50 kb/s than the single SPAD experiments shown previously in Figure 4.8(a). This is attributed to the higher DCR and background counts from 4096 parallel connected SPADs, increasing the number of noise correlations and therefore the required threshold. The results in terms of received power should not be directly compared to previous experiments, as the properties of the receiver and operational wavelength used are different. However, the picowatt power ranges shown here continue to justify the low received power nature of this scheme, with the 50 kb/s link attaining a BER of 1×10^{-3} for less than 7 pW in all cases.

Moving to higher data rates, and therefore count rates, shows the ceiling on photon counts more clearly. Figure 5.12 shows the BER performance in terms of photon counts at 1 Mb/s. At this higher data rate, with a 40 ns pulse separation, there are only 25 pulses per bit period that can produce correlations. As the receiver is sampling at 100 MHz, each optical pulse occurs in only one sample. Therefore, for a

2-level output, only 1 photon can be detected per pulse, setting a maximum number of signal correlations of 25. As shown in the figure, this limits the possible BER, as no more signal photons can be detected. A 4-level output lifts this restriction, as now up to 3 photons can be detected per pulse, permitting a maximum of $3^2 \times 25 = 225$ correlations. This allows a lower BER to be reached, or equivalently, a higher data rate. Increasing the number of photons that can be detected per sample effectively increases the dynamic range of the system. An 8-level output further increases dynamic range, with a maximum of $7^2 \times 25 = 1225$ correlations; however, the BER in Figure 5.12 does not improve. This is attributed to the method used to determine thresholds on the correlation counts. Currently, the threshold is defined to identify all "0" transmissions correctly, while "1" transmissions must surpass the threshold to be correctly identified. With an 8-level output, the "0" level correlations can reach a higher level, as more dark counts and background counts are recorded. This pushes the threshold higher and requires additional signal counts to attain the same BER.

Sampling Frequency

The sampling frequency of the Photon Torrent chip can also be used to increase dynamic range. If the temporal width over which correlations are counted remains 10 ns, then a 200 MHz sample rate results in two samples per correlation event, increasing the number of photons and therefore correlation counts that are detected.

Figure 5.13 shows the BER performance for 100 and 200 MHz sampling frequencies at a data transmission rate of 1 Mb/s. In both cases, the number of output levels was set to 8. The curves show very similar behaviour, diverging slightly at higher count rates. This may be due to the roll-over effects coming into play as the 100 MHz output begins to saturate.
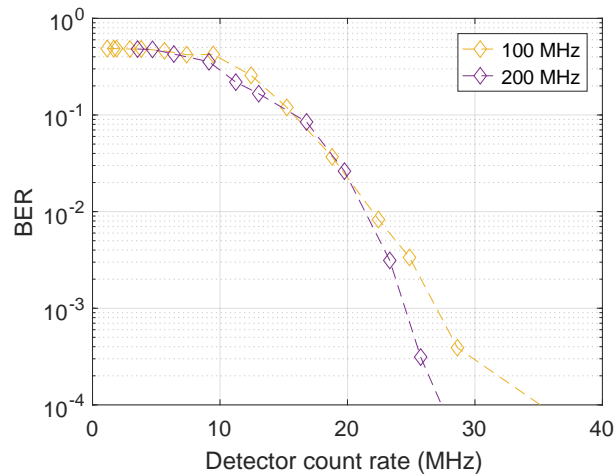
Figure 5.13: BER against photon count rate for a 1 Mb/s link with the Photon Torrent receiver sampling at 100 and 200 MHz.

Correlation Time

A limitation of the single SPAD system is that the correlation time must be longer than the dead time of the SPAD, limiting the pulse frequency and therefore the data rate. The arrayed nature of the Photon Torrent receiver masks the dead time of individual SPADs, giving flexibility in correlation time. The oscillator used to control the output pulse frequency of the LED can be tuned to change the correlation time of the pulses.

Figure 5.14 shows BER performance for correlation times of 20 and 40 ns at a data rate of 1 Mb/s. In both cases, the number of output levels was set to 8, and the sampling frequency to 200 MHz. The shorter correlation time exhibits significantly poorer performance in terms of photon count rate, or equivalently, received power. This is perhaps counter-intuitive, as a 20 ns pulse separation yields 50 pulses per bit period (2450 possible correlations), an increase over the 40 ns separation which only provides 25 (1225 possible correlations). The reduced performance is due to the multiplicative nature of counting correlations. The average number of correlations detected N_{corrs} follows:
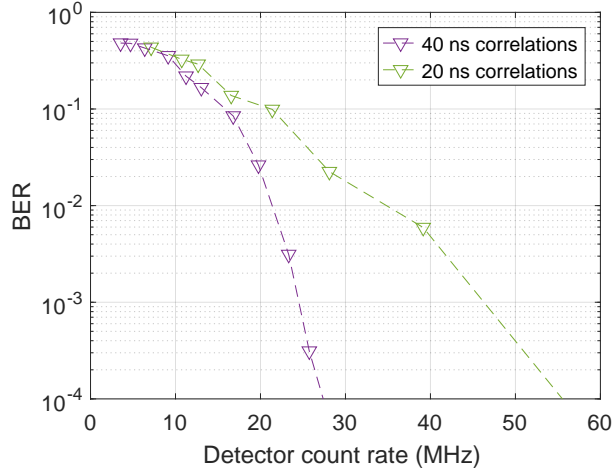
Figure 5.14: BER against photon count rate for 20 and 40 ns correlation times at 1 Mb/s.

$$N_{corrs} = n_{ph}^2 N_{rep}. \tag{5.9}$$

Here, n_{ph} is the average photons per pulse, and N_{rep} is the number of pulse repetitions. With half the pulses per bit period, and the same total count rate, the 40 ns data has twice the detected photons per pulse, but half the repetitions, therefore, n_{ph} is doubled, and N_{rep} is halved. As n_{ph} dominates Equation 5.9 this results in higher correlation counts and lower BER.

This result leads to the assumption that the best performing system would utilise only two high-intensity pulses per bit period to maximise correlation detection. However, this will be limited by saturation of the receiver, restricting the maximum count rate and correlation counts that can be detected. Using shorter correlation times with greater numbers of pulses will allow a larger number of correlations to be detected, and therefore increase the dynamic range of the system. Thus, there is a trade off between optimum BER against optical power performance, and dynamic range.

5.3.3   Surpassing Previous Data Rates

The single SPAD system was fundamentally limited to ≈ 3.57 Mb/s for a BER of 10^{-3}. This limit arises as the Poissonian nature of the signal requires 7 detected photons per transmitted "1". As a maximum of one photon can be detected per pulse, 7 pulses must be transmitted per bit. The dead time of the SPAD requires that pulses are separated by 40 ns, resulting in a minimum bit period of 280 ns, and therefore a data rate of 3.57 Mb/s. The results in the previous section show that the Photon Torrent array provides an increase in the number of photons that can be detected, improving the dynamic range of the system. As multiple photons can be detected at once, the correlation histograms will build up more rapidly in the same time window, as the restriction of less than one detected photon per pulse is lifted. This will permit higher data rates.

By using a 20 ns correlation time, with the Photon Torrent receiver set to a 200 MHz sample rate and 8-level output, the best dynamic range possible with the current setup is attained. The Photon Torrent settings are limited by the re-digitisation of the output voltage. The correlation time is limited by the performance of the oscillator used to control the pulsed output of the LED. These limitations may be overcome in future experiments with different hardware choices.

To verify that higher data rates are possible, the system was set to 5 Mb/s with the above receiver settings. Figure 5.15 shows the performance, where a BER of 10^{-5} is achievable, thereby significantly outperforming the best case scenario with a single SPAD. No saturation effect was observed at a received power of 230 pW, corresponding to a count rate of 12×10^7, indicating this is not yet the limit of performance. Either improved BER or higher data rates should still be possible.
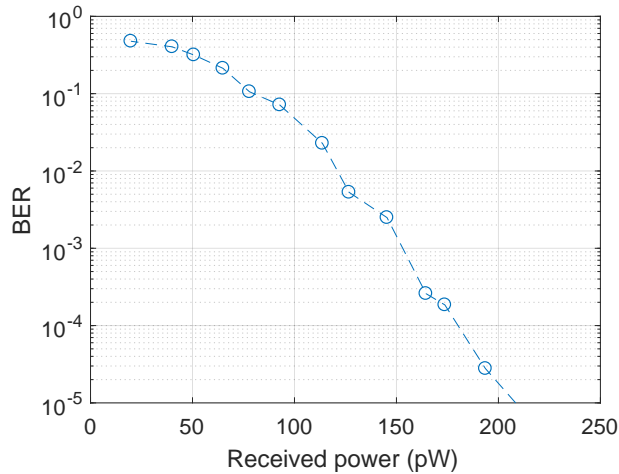
Figure 5.15: BER against photon count rate for 5 Mb/s.

5.3.4 Multiple Correlation Time Communications

With the dead time of the individual SPADs masked in the array, it is possible to send multiple data streams simultaneously, with different correlation times. While this could be done with a single SPAD, the dead time severely restricts the correlation times that can be used, and combined with the limit of 1 photon per pulse, significantly limits the data rate.

Here, 2 data streams were transmitted using different LED pixels in the array. The VLC board, used in Chapter 2 and described in Section 1.3.3, allows modulation of each column of LEDs in the array separately through SMA connections. As this board does not have short pulsing capabilities, the pulse widths are limited by the FPGA sampling rate, which is 100 MHz. This gives optical pulses of approximately 15 ns.

A pair of lenses (Thorlabs C220TME and LA1951-A) were used to focus the light from both LEDs on the Photon Torrent chip. Both data streams are operated at 500 kb/s, giving a total data rate of 1 Mb/s. Stream 1 is sent with pulses at a correlation time of 80 ns, and stream 2 at 120 ns, in the same manner as the previous OOK-style experiments, with constant repetition rate. These correlation times are not as short as in the previous experiments, as the wider optical pulses produce wide correlation
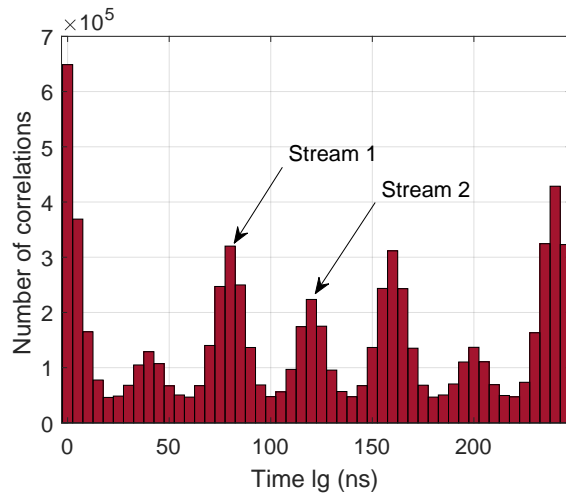
Figure 5.16: Correlation function $g(\tau_j)$ of a multi-stream system with both LEDs pulsing.

peaks. If the correlation peaks overlap, there is significant interference between the data streams.

Figure 5.16 shows the correlation histogram of the received signal while both LEDs are pulsing continuously, with a bin width of 5 ns. This displays the need for highly separated correlation peaks. The correlation peaks for stream 1 and 2 can be observed at 80 and 120 ns, respectively. Other peaks occur at 40 ns, 160 ns, 200 ns and beyond due to inter-correlations between the two streams. As the pulses are synchronised, when both data streams are transmitting '1', there is a correlation peak at 40 ns, which is the difference in correlation times. A peak occurs at 160 ns as it is the secondary correlation peak from the 80 ns correlations. The signal peaks must be positioned carefully to avoid extra correlations interfering with data streams. The problem of correlation interference becomes increasingly difficult with increasing numbers of data streams, though improvements can be made with shorter optical pulses, reducing correlation pulse width.

Additionally, Figure 5.16 shows that the peak for stream 2 has a lower number of counts than that of stream 1. This is because both streams are running at the same data rate, but with different correlation times. Therefore, stream 2 has less pulses per bit
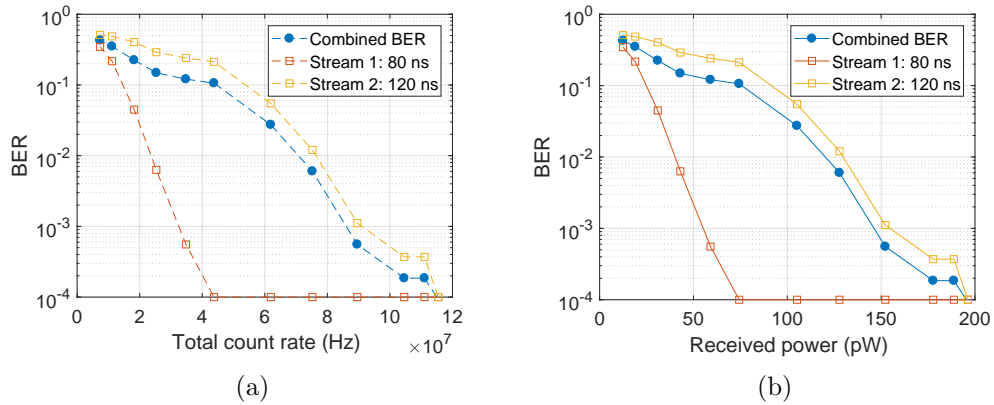
Figure 5.17: BER against (a) photon count rate and (b) received power for 2 simultaneous 500 kb/s data streams with different correlation times.

period, reducing the received power from that stream, and the number of correlations. The imbalance in received power could be dealt with by having each data stream run at a different data rate, chosen so that all streams have the same number of pulses per bit (e.g. with 80 ns at 500 kb/s and 120 ns at 333 kb/s both produce 25 pulses per bit); however, this is an additional layer of complexity that was not investigated here.

Figure 5.17 shows the BER performance of the multi-stream link, as individual streams and an aggregate BER. Evidently stream 2 performs worse than stream 1. The first detail to note is that the total count rate is not equally divided between the streams. Pulses from stream 1 occur 1.5 times more frequently, and as all pulses have the same energy, the total count rate is divided between stream 1 and 2 at 60 and 40% respectively. Additionally, the rate of correlation counts depends on the square of photon count rate. The combination of these factors causes the vastly different BER performance that appears in Figure 5.17. Nevertheless, it was possible to independently decode the two data streams.

Comparing Figure 5.17(a) to Figure 5.14(b), which has the same data rate but for a single stream, it can be seen that a single data stream at 1 Mb/s performs much better than multiple streams with different correlation times. The number of received counts required for a parallel link is significantly higher. This is attributed to two

factors. The first is due to the $\lambda = p_{ph}^2 N_r$ relation, where λ is mean correlations, p_{ph} is the probability of photon detection and N_r is the number of pair repetitions. If the data rate is halved (therefore N_r doubled), the probability of detecting a photon can decrease by a factor of $\sqrt{2}$ to maintain the same mean correlations. Therefore, splitting the 1 Mb/s stream into 2×500 kb/s requires $2/\sqrt{2} = \sqrt{2}$ times as much optical power for the same BER. The second reason for the reduced performance is that even when care is taken to separate the correlation peaks, the number of background correlations is still increased, as a significant number of photons emitted by the LEDs will follow many paths throughout the environment and result in additional correlations at many correlation times. As demonstrated previously, an increase in background light causes a small increase in requirements on received power.

Nevertheless, the results in Figure 5.17 show proof-of-concept for multi-stream parallel communications with varying temporal correlations, and further improvements to hardware may significantly improve performance. This approach could be thought of as temporal correlation division multiplexing, in comparison to time or wavelength division multiplexing. The principle extends to multiple transmitter locations sending data to a single receiver system, which is potentially attractive for low power networks such as in an "Internet of Things" environment.

5.4   Summary

The correlation-based single-photon communication link implemented in Chapter 4 has potential for a number of application areas, some of which have been investigated in this chapter.

The system has been demonstrated for an underwater channel, where the low received power requirements fit well with a high-loss channel. Additionally, the setup was demonstrated under power from a nanosatellite simulation test bed. The low electrical power consumption from the simple, small form factor electronics make this an

attractive method for inter-satellite communications on CubeSats.

The final part of this chapter discussed use of a multiplexed receiver. The Photon Torrent chip is a digital silicon photomultiplier, which lifts previous restrictions caused by detector dead time, and less than one photon detected per pulse. This increases the dynamic range of the system significantly, allowing higher data rates to be achieved. A data rate of 5 Mb/s has been demonstrated, significantly surpassing the maximum attainable with the single SPAD arrangement. Furthermore, multi-stream transmission has been demonstrated, with two data streams transmitting with different correlation times. This has potential for application in low-power networks, such as in an "Internet of Things" environment.

Bibliography

[1] H. Kaushal and G. Kaddoum, "Underwater optical wireless communication," *IEEE Access*, vol. 4, pp. 1518–1547, 2016.

[2] J. Muth, "Free-space optical communications: Building a'deeper'understanding of underwater optical communications," *Laser Focus World*, Oct 2017.

[3] B. Wozniak and J. Dera, *Light absorption in sea water*. New York: Springer, 2007.

[4] F. Hanson and S. Radic, "High bandwidth underwater optical communication," *Applied Optics*, vol. 47, no. 2, p. 277, 2008.

[5] A. Al-halafi, H. M. Oubei, B. S. Ooi, and B. Shihada, "Real-time video transmission over different underwater wireless optical channels using a directly modulated 520 nm laser diode," *IEEE/OSA Journal of Optical Communications and Networking*, vol. 9, no. 10, pp. 826–832, 2017.

[6] T. C. Wu, Y. C. Chi, H. Y. Wang, C. T. Tsai, and G. R. Lin, "Blue laser diode enables underwater communication at 12.4 Gbps," *Scientific Reports*, vol. 7, pp. 1–10, 2017.

[7] M.-A. Khalighi, T. Hamza, S. Bourennane, P. Leon, and J. Opderbecke, "Underwater wireless optical communications using silicon photo-multipliers," *IEEE Photonics Journal*, vol. 9, no. 4, pp. 1–10, 2017.

Bibliography

[8] C. Wang, H.-Y. Yu, and Y.-J. Zhu, "A long distance underwater visible light communication system with single photon avalanche diode," *IEEE Photonics Journal*, vol. 8, no. 5, pp. 1–11, 2016.

[9] S. Fasham and S. Dunn, "Developments in subsea wireless communications," in *2015 IEEE Underwater Technology (UT)*, pp. 1–5, 2015.

[10] P. Tian, X. Liu, S. Yi, Y. Huang, S. Zhang, X. Zhou, L. Hu, L. Zheng, and R. Liu, "High - speed underwater optical wireless communication using a blue GaN - based micro - LED," *Optics Express*, vol. 25, no. 2, pp. 1193–1200, 2017.

[11] T. Shafiqu, O. Amin, M. Abdallah, I. S. Ansari, M. S. Alouini, and K. Qaraqe, "Performance analysis of single photon avalanche diode underwater VLC system Using ARQ," *IEEE Photonics Journal*, vol. 9, no. 5, 2017.

[12] A. Maccarone, *Single-photon detection techniques for underwater imaging*. PhD thesis, Heriot-Watt University, 2016.

[13] Y. Kawamura and T. Tanaka, "Transmission of the LED light from the space to the ground," *AIP Advances*, vol. 3, no. 102110, 2013.

[14] A. Carrasco-casado, A. Biswas, R. Fields, B. Grefenstette, F. Harrison, S. Sburlan, and M. Toyoshima, "Optical Communication on CubeSats - Enabling the Next Era in Space Science -," *ICSOS*, pp. 46–52, 2017.

[15] D. K. Oi, A. Ling, J. A. Grieve, T. Jennewein, A. N. Dinkelaker, and M. Krutzik, "Nanosatellites for quantum science and technology," *Contemporary Physics*, vol. 58, no. 1, pp. 25–52, 2017.

[16] S. W. Janson and R. P. Welle, "The NASA Optical Communication and Sensor Demonstration Program," *27th Annual AIAA/USU Conference on Small Satellites*, pp. 1–10, 2013.

Bibliography

[17] S. Janson, R. Welle, T. Rose, D. Rowen, B. Hardy, R. Dolphus, P. Doyle, A. Faler, D. Chien, A. Chin, G. Maul, C. Coffman, S. D. L. Lumondiere, I. Nicolette, and D. Hinkley, "The NASA Optical Communications and Sensor Demonstration Program : Initial Flight Results," *29th Annual AIAA/USU Conference on Small Satellites*, pp. SSC16–III–03, 2015.

[18] E. Clements, R. Aniceto, D. Barnes, D. Caplan, J. Clark, I. del Portillo, C. Haughwout, M. Khatsenko, R. Kingsbury, M. Lee, R. Morgan, J. Twichell, K. Riesing, H. Yoon, C. Ziegler, and K. Cahoy, "Nanosatellite optical downlink experiment: design, simulation, and prototyping," *Optical Engineering*, vol. 55, no. 11, p. 111610, 2016.

[19] R. Morgan and K. Cahoy, "Nanosatellite lasercom system," *AIAA/USU Conference on Small Satellites*, 2017.

[20] E. Fisher, I. Underwood, and R. Henderson, "A reconfigurable single-photon-counting integrating receiver for optical communications," *IEEE Journal of Solid-State Circuits*, vol. 48, no. 7, pp. 1638–1650, 2013.

[21] H. Zimmermann, B. Steindl, M. Hofbauer, and R. Enne, "Integrated fiber optical receiver reducing the gap to the quantum limit," *Scientific Reports*, vol. 7, no. 1, p. 2652, 2017.

[22] I. I. Kim, R. Stieger, J. Koontz, C. Moursund, M. Barclay, P. Adhikari, J. Schuster, E. Korevaar, R. Ruigrok, and C. De Cusatis, "Wireless optical transmission of fast ethernet, FDDI, ATM, and ESCON protocol data using the TerraLink laser communication system," *Optical Engineering*, vol. 37, no. 12, p. 3143, 1998.

[23] M. Guelman, A. Kogan, A. Kazarian, A. Livne, M. Orenstein, H. Michalik, and S. Arnon, "Acquisition and pointing control for inter-satellite laser communications," *IEEE Transactions on Aerospace and Electronic Systems*, vol. 40, no. 4, pp. 1239–1248, 2004.

Bibliography

[24] Y. Koyama, M. Toyoshima, Y. Takayama, H. Takenaka, K. Shiratama, I. Mase, and O. Kawamoto, "SOTA: small optical transponder for micro-satellite," *2011 International Conference on Space Optical Systems and Applications, ICSOS'11*, pp. 97–101, 2011.

[25] J. Piprek, "Comparative efficiency analysis of GaN-based light-emitting diodes and laser diodes," *Applied Physics Letters*, vol. 109, no. 2, pp. 2–6, 2016.

[26] T. Frach, G. Prescher, C. Degenhardt, R. De Gruyter, A. Schmitz, and R. Ballizany, "The digital silicon photomultiplier - principle of operation and intrinsic detector performance," *IEEE Nuclear Science Symposium Conference Record*, pp. 1959–1965, 2009.

[27] R. J. Walker, E. A. G. Webster, J. Li, N. Massari, and R. K. Henderson, "High fill factor digital silicon photomultiplier structures in 130nm CMOS imaging technology," *IEEE Nuclear Science Symposium Conference Record*, pp. 1945–1948, 2012.

[28] S. Gnecchi, N. A. Dutton, L. Parmesan, B. R. Rae, S. Pellegrini, S. J. McLeod, L. A. Grant, and R. K. Henderson, "Digital silicon photomultipliers with OR/XOR pulse combining techniques," *IEEE Transactions on Electron Devices*, vol. 63, no. 3, pp. 1105–1110, 2016.

[29] S. Gnecchi, R. Bruce, N. A. W. Dutton, L. Parmesan, S. Pellegrini, S. J. Mcleod, L. A. Grant, R. K. Henderson, B. Rae, S. Pellegrini, S. J. Mcleod, L. A. Grant, and R. K. Henderson, "Analysis of photon detection efficiency and dynamic range in SPAD based visible light receivers," *Journal of lightwave technology*, vol. 8724, no. 1, pp. 1–7, 2016.

[30] Y. Li, M. Safari, R. Henderson, and H. Haas, "Optical OFDM With Single-Photon Avalanche Diode," *IEEE Photonics Technology Letters*, vol. 27, no. 9, pp. 943–946, 2015.

Bibliography

[31] J. A. Richardson, L. A. Grant, and R. K. Henderson, "Low dark count single-photon avalanche diode structure compatible with standard nanometer scale CMOS technology," *IEEE Photonics Technology Letters*, vol. 21, no. 14, pp. 1020–1022, 2009.

[32] T. A. Abbas, N. A. W. Dutton, O. Almer, N. Finlayson, F. M. D. Rocca, and R. Henderson, "A CMOS SPAD sensor with a multi-event folded flash time-to-digital converter for ultra-fast optical transient capture," *IEEE Sensors Journal*, vol. 1748, no. c, pp. 1–1, 2018.

Chapter 6

Single Photon Correlations for Colour Imaging

Chapter 3 set out the mathematics for transmitting data using temporal correlations and a single-photon detector. As seen in the experimental implementation in Chapter 4, the magnitude of correlation peaks is strongly dependent on the received power. As sources can be distinguished through the temporal correlation pattern of their emission, relative measurements of received power can be made.

This chapter presents experimental work on colour imaging with correlations, in which multiplexing of both transmitter and receiver will be required. Commercial LEDs are used with varying correlation patterns to discriminate between different coloured targets. Relative reflectance measurements can be made, and the principle extends to hyperspectral imaging with a wide spectral range. Here, the principle is introduced with only a single SPAD as a receiver, however, it should be a straightforward extension to implement the approach with a receiver array to perform imaging.

6.1 Low-light-level and photon efficient imaging

The most widespread technologies used for optical imaging are charged couple device (CCD) and complementary metal-oxide-semiconductor (CMOS) image sensors. In both cases, incident photons are converted into electrical signals by excitation of electrons and holes in silicon [1]. This provides an analogue electrical signal proportional to the amount of light incident on each pixel in an array. When incident light levels are low, the performance of such detectors can be severely limited by noise, occurring either within the photodetector or the electronics used to read the signal.

The sensitivity of CCD image sensors can be enhanced using an imaging intensifier (ICCD) or electron multiplication methods (EMCCD) [2]. In an ICCD, a photocathode, microchannel plate and phosphor screen are placed in front of the CCD sensor. An incident photon generates a large number of electrons, which are converted back to photons again by the phosphor to be detected by the CCD. An ICCD is primarily shot noise limited, as noise from the readout process and dark currents are negligible. In an EMCCD, an in-built electron multiplying structure is used during the read out process of the CCD, providing gain in the collected charge rather than photons [3]. While the quantum efficiency of these devices is higher than that of ICCDs, they require cooling to low temperatures ($< -70°$C) as dark currents are also amplified by the electron multiplication process.

Single-photon level imaging can be achieved using arrays of single-photon avalanche diodes (SPADs). As discussed in Chapter 3, SPADs provide digital logic pulses indicating the arrival of a single photon, with high timing accuracy. In comparison to CCD systems, SPAD arrays are advantageous due to single-photon sensitivity, high frame rates, and fully digital processing, which avoids issues with readout noise [4]. In addition, the high resolution of photon arrival times allows time-of-flight measurements to be combined with imaging to construct 3D images [5], perform fluorescence lifetime imaging [6] and observe light-in-flight [7].

Colour imaging is usually achieved by utilising multiple detection elements with different optical filters. With three detectors filtered to allow only red, green, or blue light, colour information can be reconstructed based on the relative intensity on each pixel [8]. Often, the filtered pixels are arranged according to the Bayer pattern, with two elements responding to green light for every one responding to blue and red, as the human eye is more responsive to these wavelengths. The disadvantage of this approach is that four sub-pixels are required for each pixel on an image, reducing the resolution of images and increasing the form factor of the device, however, interpolation can be used to recover the full resolution.

In this chapter, an alternative method for distinguishing different incident wavelength photons is presented, based on temporally structured light sources and single-photon detector arrays. The approach can be used to distinguish signals from any wavelength source within the detectors spectral response range, without a filter, enabling the full resolution of a single-photon detector array to be used for colour imaging. Additionally, the method is not limited to three colours, and can be readily extended to enable hyperspectral imaging across the full spectral range of the receiver.

6.2 Analysis of Correlation Histograms

The previous communications results exploited the autocorrelation patterns of pairs of optical pulses. A single LED was used, changing between pulse separations and therefore correlation patterns. Here, additional LED sources are used and multiple signals are detected simultaneously, with careful arrangement of correlation patterns for each transmitter. By setting each transmitter to output pulse pairs with different temporal separations, the resulting correlation histogram at the SPAD will have a distinguishable peak associated with each LED. Even though the output of a SPAD does not give wavelength information, the temporal structure of the light sources provides a way to associate particular photon counts with a particular source, and therefore

163
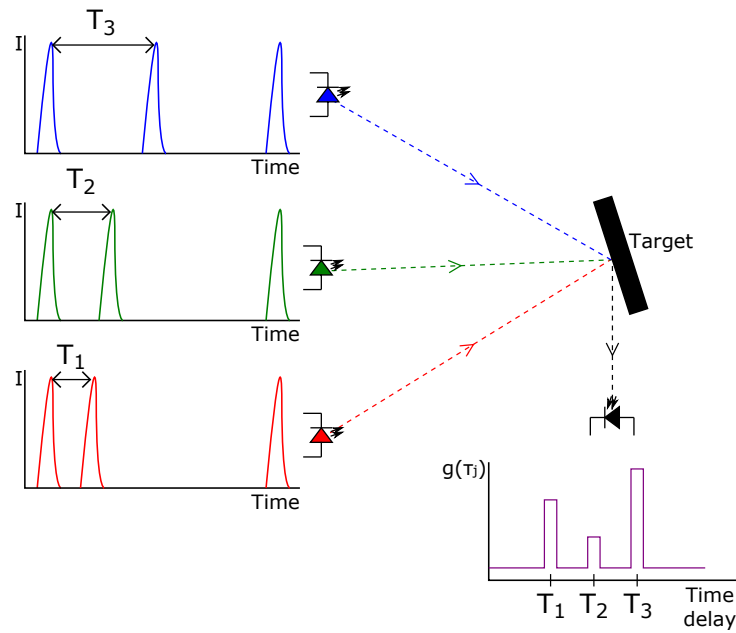
Figure 6.1: Schematic example of LED output waveforms and received correlation pattern for reflectance measurement.

wavelength.

Figure 6.1 shows a schematic example where three LED sources can be used to measure the relative reflectance of a target. A red, green and blue LED are pulsed with different temporal separations, T_1, T_2, and T_3, with enough separation before the next pair to avoid extra correlation peaks. The emission from the LEDs is incident on a target, and the reflected light collected onto a SPAD. By performing the same autocorrelation methods as for the communications work, correlation peaks appear at time lags T_1, T_2, and T_3, which are associated only with one LED. While the schematic is shown for the reflectance case, the principle also applies to measure absorption, with a suitably implemented setup.

The magnitude of each correlation peak will depend on the incident power on the SPAD from the associated LED, and the spectral response of the SPAD at the wavelength used. As the spectral response and implemented wavelengths will be known, a measurement of the received power from each LED can be made using numerical

methods detailed below. With relative received power, and the known emission spectra of each LED, the received spectra can be calculated. Furthermore, as the relative emitted power spectrum from the LED transmitters is also known, the reflectance of the intermediate target can be measured. Importantly only relative measurements of reflectance can be made, as even though emitted power and received power can be measured, a large amount of the emitted power will be lost due to the divergent nature of LED emission and scattering of light from the target.

If suitable wavelength sources are used, the reflectance measurement can be used to determine the perceived colour of a target, taking into account the response of the human eye. While the example in Figure 6.1 is for a single SPAD, a detector array with suitable optics would allow colour imaging to be performed, without the need for filtering.

As the emission spectra of an LED has finite linewidth, usually on the order of 10s of nanometres, the correlation peak height is a measure of received power averaged over the LED emission spectrum. Therefore, any reflectance measurement calculated from this will also only provide an average over the spectral range of the LED. The example shown in Figure 6.1 would provide three data points of reflectance, broadly averaged across the visible spectrum, which should be sufficient for colour imaging based on a red, green and blue (RGB) system. In order to optimise the resolution of the reflectance measurement, many sources with narrow linewidths are required, with tightly packed emission spectra. The temporal arrangement of pulses would have to be considered carefully to avoid interfering correlation peaks. This method allows higher resolution measurements, and potentially allows hyperspectral imaging, extending into the ultraviolet and infrared spectra.

6.2.1 Numerical Calculation of Received Power

It is necessary to calculate the received power incident on the SPAD, L_i, for each LED wavelength λ_i. This is done using numerical methods very similar to those for the

communications work. The probability of a correlation count per transmitted pulse, can be found experimentally ($P_{corr,exp}$) and defined mathematically ($P_{corr}(n_{av})$), so a numerical solution of Equation 6.1 will allow the number of photons per pulse incident on the detector n_{av}.

$$P_{corr}(n_{av}) - P_{corr,exp} = 0. \tag{6.1}$$

The probability of a correlation $P_{corr}(n_{av})$ is directly related to the probability of detecting a photon count $P_{count}(n_{av})$ by:

$$P_{corr}(n_{av}) = (P_{count}(n_{av}))^2. \tag{6.2}$$

Section 4.1.2 already introduced the mathematical derivation for $P_{count}(n_{av})$, so by using Equation 4.6, $P_{corr}(n_{av})$ is given by:

$$P_{corr}(n_{av}) = \left(\sum_{n=0}^{\infty} P_{n_{av}}(n) \cdot P_{count}^{(n)} \right)^2, \tag{6.3}$$

where $P_{n_{av}}(n)$ is the probability that a given incident pulse contains n photons, which follows a Poisson distribution with average photon number $n_{av} \in \mathbb{R}^+$. $P_{count}^{(n)}$ is the probability of receiving one photon count in a single pulse with $n \in \mathbb{N}$ photons, given by:

$$P_{count}^{(n)} = 1 - (1 - \eta_{PDP})^n. \tag{6.4}$$

Here, η_{PDP} is the photon detection probability, which will vary depending on the wavelength used. The spectral response of the SPAD therefore affects the number of correlations recorded for a given incident power.

Once n_{av} has been determined, the incident optical power can be calculated as the emitted pulses per second N_p and emission wavelength λ_i are known:

$$L_i = N_p n_{av} \frac{hc}{\lambda_i}. \tag{6.5}$$

Here, h is Plancks constant and c is the speed of light.

6.2.2   Recovery of Received and Reflectance Spectra

If the received power L_i is known for each wavelength λ_i, the incident spectra on the SPAD can be determined. Each LED emitter will have a known, normalised emission spectrum $\sigma_i(\lambda)$, showing the power distribution across wavelength. The total received spectra can be determined by summation of each LED spectrum, scaled by the respective received power:

$$\sigma_{Rec}(\lambda) = \sum_{i=1}^{N_{LED}} L_i \frac{\sigma_i(\lambda)}{\int \sigma_i(\lambda) d\lambda}. \tag{6.6}$$

The received spectrum σ_{Rec} is dependent on the spectra of the light sources. To determine the spectral properties of the object or channel being illuminated, the emission spectrum at the transmitter $\sigma_{Tr}(\lambda)$ must also be known. This spectrum must be a calibrated relative power measurement, to contain the relative power contributions from each LED. With σ_{Tr}, the relative reflectance of a target $R(\lambda)$ can be determined by:

$$R(\lambda) = \frac{\sigma_{Rec}(\lambda)}{\sigma_{Tr}(\lambda)}. \tag{6.7}$$

This equation works under the assumption that the reflectance profile of the target is a smoothly varying function. While this is a significant simplification, the approach may still be useful in determining low resolution spectral reflectance information. The targets used in Section 6.3.2 do have smoothly varying reflectance profiles, however this is not the general case for all materials.
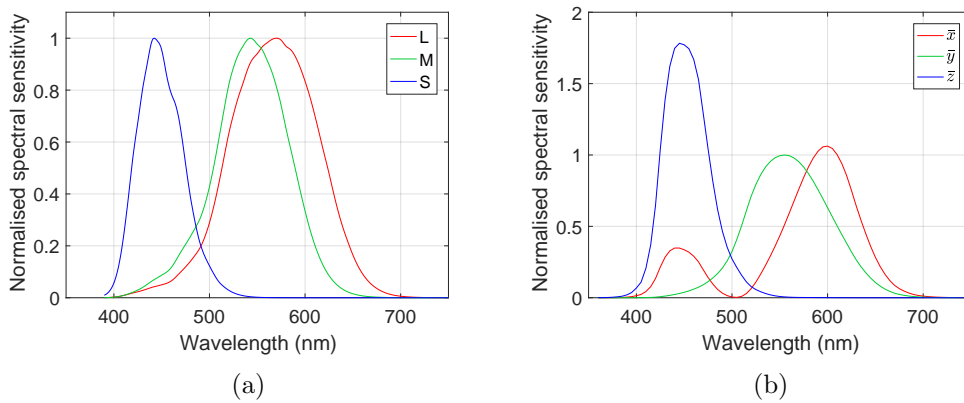
Figure 6.2: (a) Spectral response of the three human cone cells, named L, M and S for their long, medium and short wavelength sensitivities. (b) CIE colour matching functions $\bar{x}$, $\bar{y}$ and $\bar{z}$.

6.2.3 Colour Interpretation

To perform colour imaging, the radiometric result for reflectance in Equation 6.7 must be converted to a photometric result, taking into account the response of the human eye. Colour vision in humans is enabled by three kinds of photoreceptive cone cells within the eye [8]. Each responds to different spectral ranges of light, and so are designated as S, M, and L cones as they respond to short, medium and long wavelengths. The normalised spectral response for the tristimulus values of S, M and L cones are shown in Figure 6.2(a). Given these responses, it is intuitive that a perceived colour should only require three numbers to describe.

As the observers field of view affects the tristimulus values, a colour mapping function for a standard observer is required. The International Commission on Illumination (CIE) defines the CIE 1931 chromaticity coordinates [9], which are commonly used to characterise the colour of light sources [10, 11]. In order to determine the coordinates, colour matching functions $\bar{x}$, $\bar{y}$ and $\bar{z}$ are used, which can be regarded as a linear combination of the cone response functions. The CIE colour matching functions are shown in Figure 6.2(b).

With spectral radiance $L(\lambda)$, CIE xy chromaticity coordinates can be derived using:
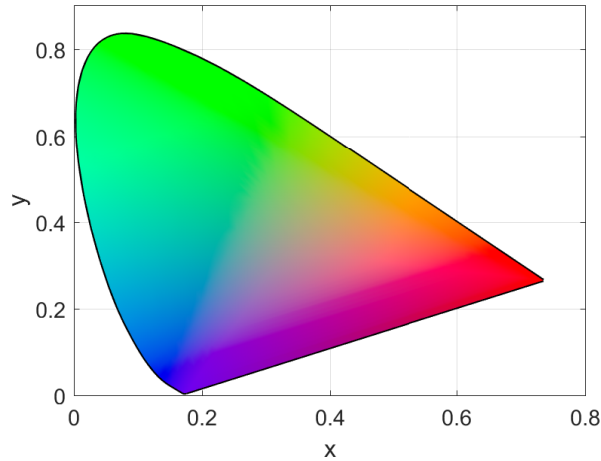
Figure 6.3: CIE 1931 colour space chromaticity diagram.

$$X = \int_\lambda L(\lambda)\bar{x}(\lambda)d\lambda \tag{6.8}$$

$$Y = \int_\lambda L(\lambda)\bar{y}(\lambda)d\lambda \tag{6.9}$$

$$Z = \int_\lambda L(\lambda)\bar{z}(\lambda)d\lambda \tag{6.10}$$

$$x = \frac{X}{X + Y + Z} \tag{6.11}$$

$$y = \frac{Y}{X + Y + Z}. \tag{6.12}$$

The resulting values x and y fall within the CIE 1931 colour space, shown in Figure 6.3. The outer curved boundary in this figure shows monochromatic wavelengths, and the area covers all chromaticities visible to the average person. It is important to note that the colours shown in the CIE diagram will be affected by both screen output capabilities and printing methods. Therefore, the colours seen by the reader in the CIE plot here, and results later in this chapter may not be accurate reproductions.

For the experiments performed here, the focus is on the reflective case, rather than direct spectral radiance $L(\lambda)$. In this case, X, Y and Z are calculated according to:

$$X = \frac{K}{N} \int_\lambda R(\lambda)I(\lambda)\bar{x}(\lambda)d\lambda \tag{6.13}$$

$$Y = \frac{K}{N} \int_\lambda R(\lambda)I(\lambda)\bar{y}(\lambda)d\lambda \tag{6.14}$$

$$Z = \frac{K}{N} \int_\lambda R(\lambda)I(\lambda)\bar{z}(\lambda)d\lambda \tag{6.15}$$

$$N = \int_\lambda I(\lambda)\bar{y}(\lambda)d\lambda. \tag{6.16}$$

Where $R(\lambda)$ is the reflectance spectrum, $I(\lambda)$ is the spectrum of the illuminant and K is a scaling factor. Relative measurements of $R(\lambda)$ can be performed using the correlation approach as detailed above. As only relative measurements of $R(\lambda)$ can be made using the approach here, the scaling and normalisation factors are ignored. The choice of illuminant $I(\lambda)$ will then yield x and y coordinates that correspond to the colour of the target when under that spectral illumination. For the following experiments, the CIE standard illuminant D65 was used, which approximates daylight. Calculation of x and y values can therefore be made for a target yielding $R(\lambda)$ from the correlation approach.

Limitations

Colour science is a complex field, and the model presented here for reproducing colour values on the CIE colour space is a very simplistic approximation. In an imaging system, the intention is to reproduce the colour of an object such that a human observer will see no difference between the original and the reproduction. In order to do this, it must satisfy the Luther-Ives condition [8]. This condition requires that the spectral response functions of the imaging system are a linear transformation of the CIE colour matching functions $\bar{x}$, $\bar{y}$ and $\bar{z}$, shown in Figure 6.2(b).

In general, CCD and CMOS cameras do not satisfy the Luther-Ives condition, as producing the required filters is difficult and expensive, and often incompatible with the

finished camera product [8]. The approach presented here relies on the LED emission spectra σ_i, which will also not satisfy the Luther-Ives condition. In fact, this approach is a very simple and crude approximation at this stage. A future system may come closer to the required conditions with very careful choice of illumination sources, closer to either the colour matching functions or the S, M and L response curves of the human cone cells.

As a consequence of these limitations, this approach is unlikely to faithfully reproduce colours of an object to match the perception of a human observer. Additionally, it is likely to suffer from metamerism, where different coloured objects will be perceived as the same. However, it can still be expected to give approximate information about the colour of an object. Given that the approach utilises single photon detection, a degree of colour discrimination, however limited, may still be useful for imaging under very low illumination conditions.

6.3   RGB LED Pulsing System

For proof-of-principle, three LED wavelengths have been used. The commercially available LED chip OSRAM LERTDUWS2W provides a single chip device with red (632 nm), green (520 nm) and blue (449 nm) LEDs. The emission spectrum of each LED is shown in Figure 6.4(a), and the relative power spectrum of total emission from the transmitter is shown in Figure 6.4(b). These emission spectra were taken under the pulsed driving conditions described below, and measured with a fibre-coupled spectrometer (Avantes AvaSpec-2048L) calibrated with a halogen light source (Ocean Optics HL-2000-FHSA). A transmitter board, shown in Figure 6.4(c), provides electronic components to drive the LEDs in a pulsed fashion. The green LED has noticeably poorer performance in the relative power spectrum, which is a result of the common "green gap" efficiency problem in LED fabrication.

Each LED is driven independently with the driving circuit shown in Figure 6.5. An

171
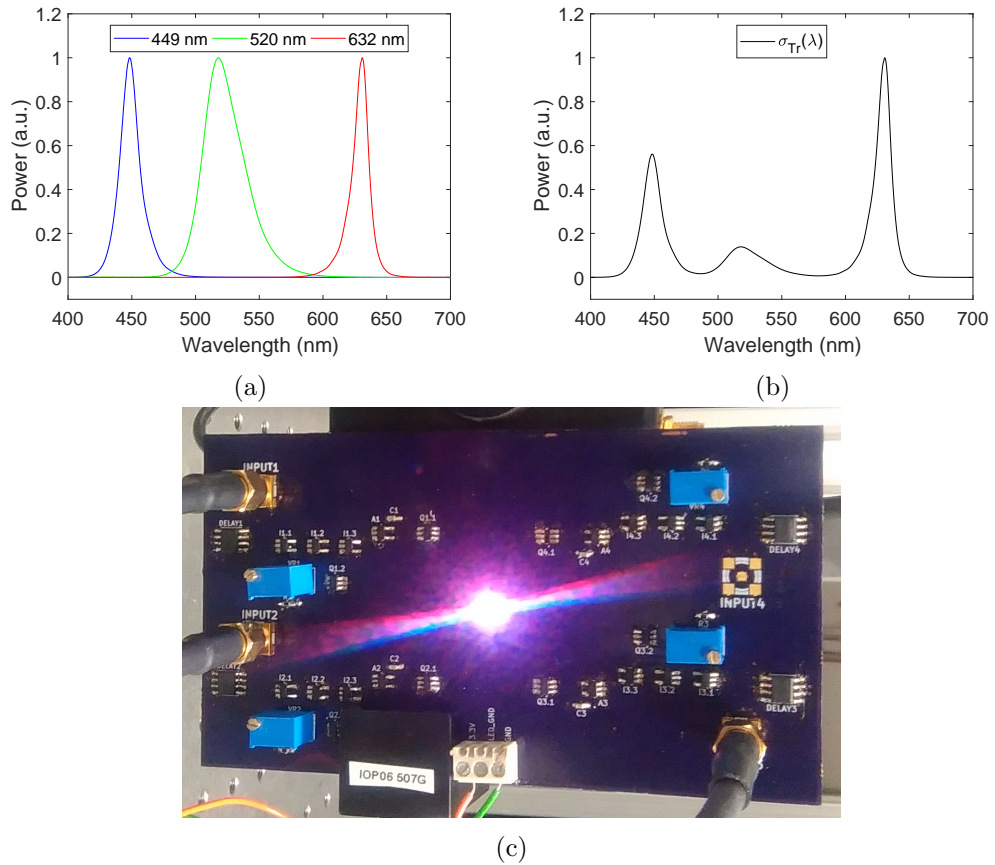
Figure 6.4: (a) Emission spectra of each LED in the commercial chip, (b) relative emission spectrum of the transmitter, (c) photograph of the transmitter board in operation.
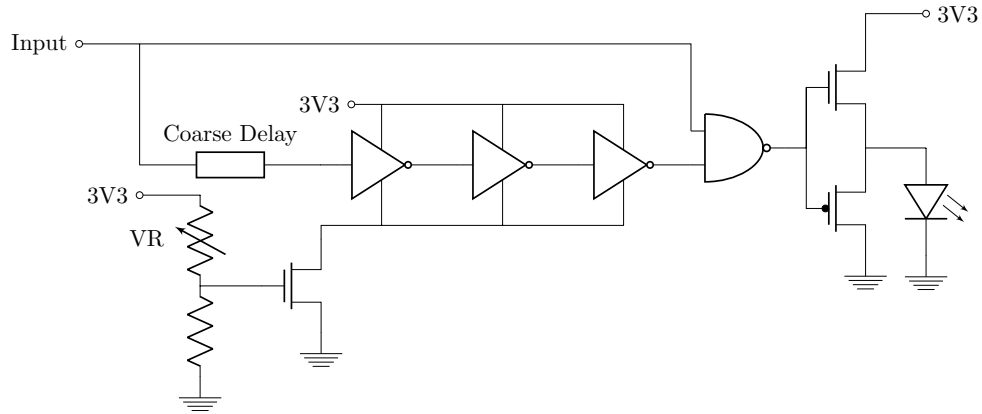
Figure 6.5: Circuit diagram of the driver electronics for RGB LED pulsing system.

input logic signal, provided by an FPGA, is sent to a NAND gate, both directly and through a delay line. The delay is generated using a coarse delay line chip, a chain of inverters and a current starving transistor, utilising the same principle as the short-pulse circuitry of the CMOS devices described in Section 1.3.3 and reference [12]. The coarse delay line chip allows selection of delays with 5 ns spacing, and the variable resistor VR controls the current starving transistor, allowing fine control of the delay through the inverter chain. The resulting output from the NAND gate is a short electrical pulse on the falling edge of the input logic signal. This pulse then drives the NMOS and PMOS transistors controlling the 3.3 V supply to the LED. Driving in this way allows high current driving of the LED, without sourcing through the digital electronics.

Electrical pulse conditions were tuned to obtain the shortest useful pulse from each LED, with a temporal spacing of 300 ns. The optical signals measured with an APD (Hamamatsu C5658) are shown in Figure 6.6. The FWHM pulse widths were 8.5 ns, 22.2 ns and 15.8 ns for blue, green and red, respectively. It is desirable to have the pulse widths shorter than the dead time of the SPAD $\tau_d = 35$ ns to avoid additional photon detections which increase the time the detector spends in a recovery state. While the FWHM pulse widths all fulfil this requirement, the green pulses show a longer tail of emission which extends beyond 35 ns. The poor performance of the green devices, both in relative power in Figure 6.4(b), and optical pulses in Figure 6.6(b), are attributed

173
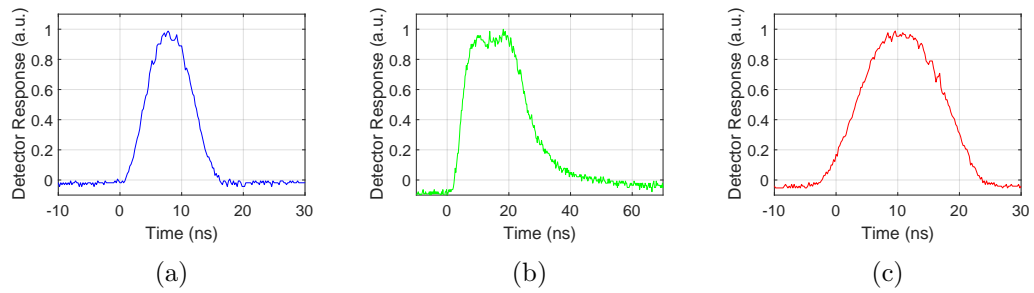
Figure 6.6: Optical pulses from the (a) blue, (b) green and (c) red LEDs. The green LED shows much poorer performance, with a long tail of emission.

to the higher forward voltage of the device at 3.6 V, which is slightly higher than the driving voltage of 3.3 V. In comparison, the blue and red LEDs have forward voltages of 3.45 V and 2.5 V, respectively.

6.3.1 Direct LED Spectra Measurement

To verify that relative received power can be reconstructed with the correlation method, the LEDs were first aligned directly with the SPAD (Thorlabs SPCM20A), with no intermediate target or focussing optics, so the calculated spectra should match exactly the emission spectra in Figure 6.4(b). The SPAD was positioned 10 cm away from the transmitter, and aligned to maximise count rate from each LED in turn. A neutral density filter was used on the receiver side to avoid saturation. Each LED was measured separately, with pulsed conditions as detailed above. In each case, 11×10^3 pulse pairs were transmitted. The output of the SPAD was collected with an oscilloscope and processed offline in MATLAB$^{\text{TM}}$. The correlation histograms for each LED are shown in Figure 6.7, where peaks of different heights are identifiable for each wavelength at a time lag of 300 ns.

The correlation peaks show finite widths, approximately equal to twice the FWHM of the optical signals as expected from the autocorrelation process. Importantly, the received power is dependent on the total number of correlations from a single LED, regardless of specific time lag, so correlation counts should be summed over the entire
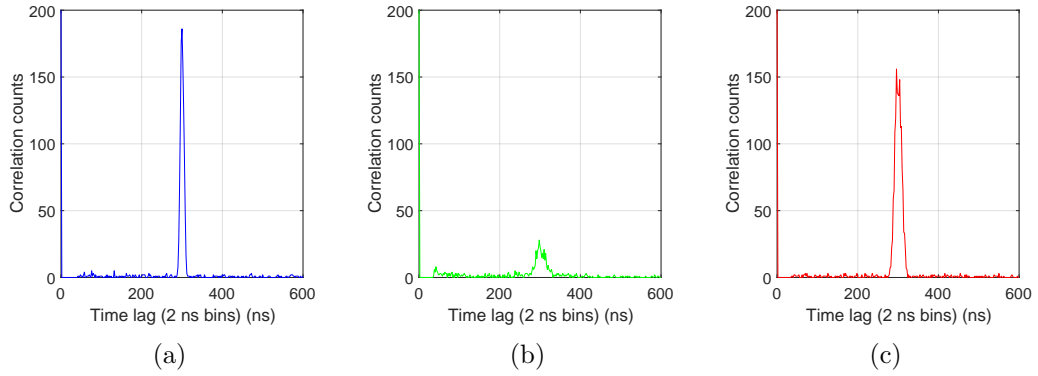
Figure 6.7: Correlation histograms received for (a) blue, (b) green and (c) red LEDs directly incident on the SPAD.

Table 6.1: Parameters and measurements for direct LED colour correlation measurement.

LED	Correlation width (ns)	Counts	Received Power L_i (pW)
Blue	26	1030	7.72×10^{-2}
Green	162	398	3.29×10^{-2}
Red	50	1595	9.51×10^{-2}

interval associated with a particular LED. In this experiment, where each measurement was taken independently, this is relatively simple. However, when all LEDs are used simultaneously with different time lags, care must be taken to fully separate the correlation peaks so each time bin is associated with only one LED.

To account for additional noise correlation counts, a background reading was taken over the same number of repetitions as the measurement with the LEDs switched off. The mean number of background correlations is then subtracted from the measurement before further analysis. By inspecting figure 6.7, we can estimate correlation peak widths and sum all counts within that range. This is more difficult for the green pulses due to the extended tail of the optical pulse. From the sum of counts the received power L_i can be calculated. The correlation peak widths, number of correlation counts and received power are summarised in Table 6.1. These values, along with the known spectra σ_i in Figure 6.4(a), can then be used with Equation 6.6 to reconstruct
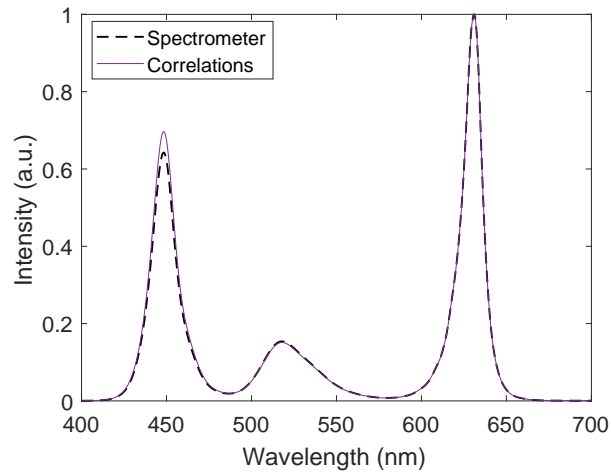
Figure 6.8: Calculated spectrum from correlations and individual LED spectra (solid) compared to measurement from a spectrometer (dashed).

the spectrum incident on the SPAD. The result is shown in Figure 6.8, with the spectrometer measurement for comparison. The two measurements show strong agreement, indicating the correlation counting approach does accurately measure relative power from each LED source.

Sources of Error

There is generally good agreement between the two spectra in Figure 6.8, however, minor differences have occurred as there are some sources of error that are inherent to the approach used.

Firstly, the recorded correlation counts is a Poissonian variable, as was discussed in detail in the communications work and described in Appendix A. A Poissonian distribution has variance equal to its mean, putting a fundamental physical limit on the accuracy of the correlation count measurement.

Secondly, the LED spectra are 10s of nm wide; however, we have accounted for detector efficiency only at the peak wavelength. Slight variations in spectral response around the peak may influence the detection rate of correlations.

Finally, the pulses from the green LED are much wider than red or blue. This means

(a)
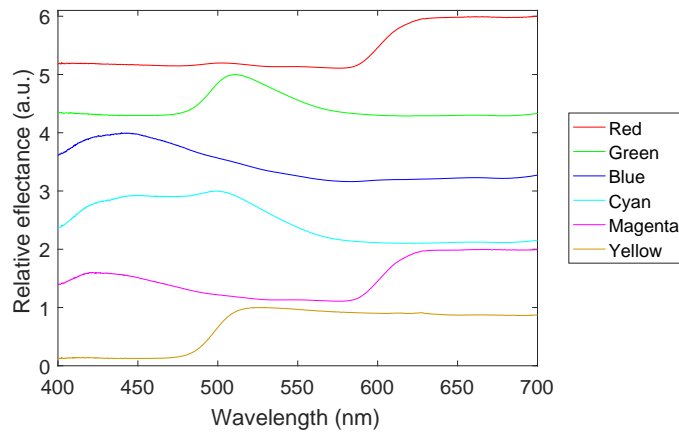
(b)

Figure 6.9: Photograph (a) and relative reflectance measured with a spectrometer (b) of the colour targets used to verify colour imaging.

correlations are counted over a wider range of time lags, increasing the number of noise correlations that may be recorded. Shorter, more intense optical pulses should provide improved results as noise correlations from background counts will have reduced effect on the correlation counts. Shorter pulses may be obtained by moving to a system using micro-LEDs, to exploit their high bandwidth, and fast pulsing properties [12].

6.3.2 Single Colour Target and Single SPAD

To show reflectance and colour interpretation can be determined using the correlation approach, the system was used to measure the properties of paper targets, printed with a coloured area. The targets used are shown in Figure 6.9(a), and are henceforth referred to as red, green, blue, cyan, magenta and yellow. The relative reflectance spectra measured with a halogen light source (Ocean Optics HL-2000-FHSA) and spectrometer

(Avantes AvaSpec-2048L) are shown in Figure 6.9(b). The reflectance of these targets is smooth, which fits well with the assumptions of the analysis in Sections 6.2.2.

The LED transmitter was positioned 20 cm away from a target board. No optics were used on the transmitter, so that the target is approximately equally illuminated by all three LEDs. The SPAD was fitted with camera optics (Navitar DOZ-11110) in order to image only the target and avoid light from the background scene. As the detector has only one pixel, it is extremely difficult to properly focus the lens arrangement. As an approximation, the receiver was placed at the minimum working distance of the optics (1.3 m), aligned to the target and adjusted to maximise the detected count rate.

For all three LEDs to be operated simultaneously, the temporal pulse separations must be different for each wavelength. Correlation times of 300 ns, 600 ns and 900 ns have been used for red, green and blue, respectively. This long time separation is required primarily due to the wide optical pulses from the green LED, which must be separated to avoid additional unwanted correlations. Pulse pairs are sent sequentially, i.e. two red pulses, followed by two green and two blue, with a delay of $1.8\,\mu s$ between each pair to avoid correlations between different wavelengths. Large temporal separations are required due to the wide pulses of the green LED. Pulse pairs were repeated 1.389×10^6 times to produce useful correlation histograms. This high number of repetitions is required as a large amount of light is lost over the 1.5 m round trip, as no focussing optics were used on the transmitter. Currently, the data from the SPAD is captured by an oscilloscope and processed offline, making image capture a lengthy process. However, in a practical system the processing could be done live, where 1.389×10^6 repetitions would take approximately 10 s. With an improved LED system utilising shorter pulses, the temporal separations could be reduced, improving the pulse rate and reducing the acquisition times.

Figure 6.10 shows the received correlation histograms for all coloured targets. Each target produces a distinct histogram, as a different amount of light is reflected from each LED. These histograms do not account for variation in detector efficiency and emitted
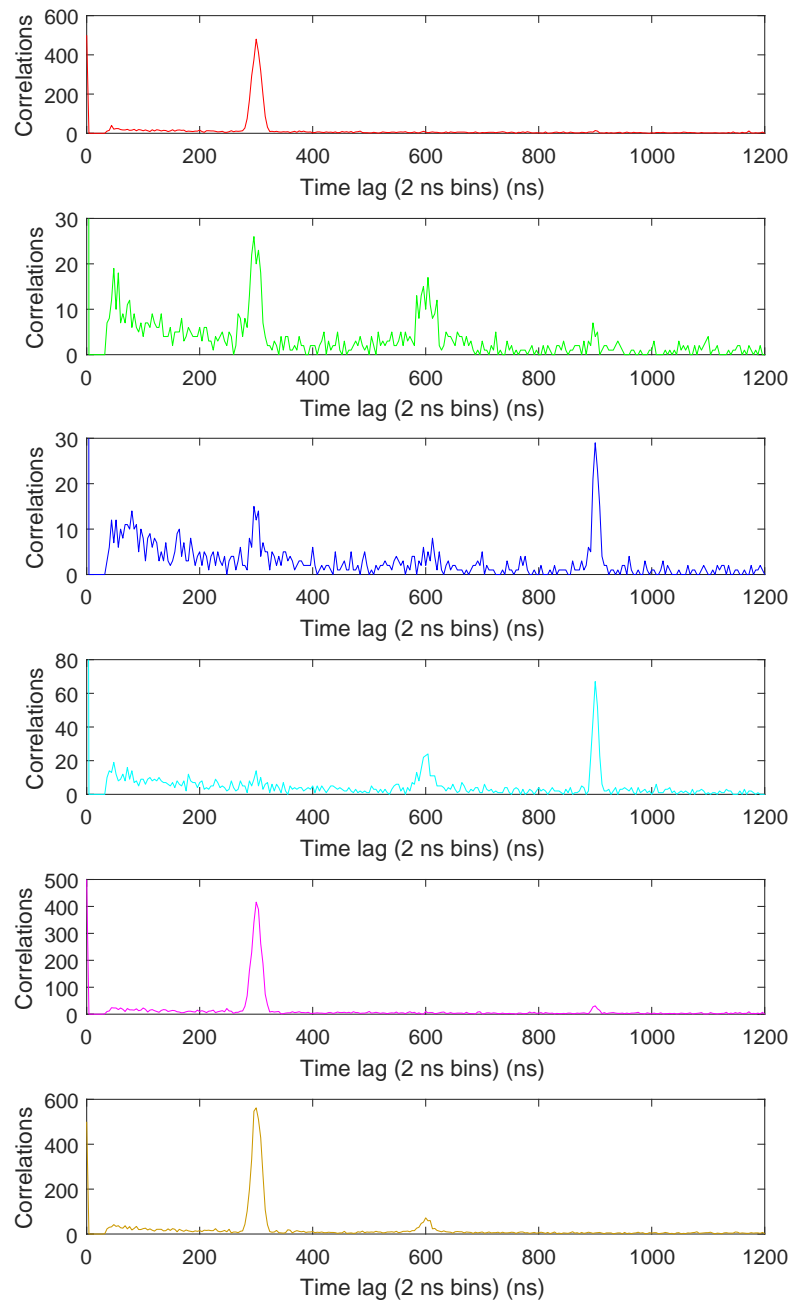
Figure 6.10: Received correlation histograms for (top to bottom) red, green, blue, cyan, magenta and yellow targets.

power at each wavelength, which results in a greater number of correlation counts for red light (300 ns) and reduced for green (600 ns). It is also noted that the background noise level in these histograms is significantly higher than those in Figure 6.7. This is attributed to the large number of photons emitted by the LEDs and scattering around the room before being incident on the detector. As these photons will have additional time delays introduced by travel around the room they will increase the number of correlations at all time delays.

By counting the correlations associated with each transmitter LED wavelength in the histograms of Figure 6.10, the received power L_i can be calculated. Equation 6.6 then allows calculation of the received spectrum incident on the SPAD, and Equation 6.7 gives the reflectance spectrum of the target. The resulting spectra are shown in Figure 6.11 for all colour targets. Each received spectra is identifiably different, and follows expected trends in terms of quantities of light from each LED reflected by the target. It is important to note that the received spectra includes the variation in output power from each LED as shown in Figure 6.4(b), which skews the data in favour of red light and against green. As an example, the cyan data shows large amounts of blue light, significant levels of red light, and very little green in the received spectra, despite green showing the highest reflectivity in the reflectance spectra.

Each reflectance plot shows the characteristic trends that are expected of each colour target. Comparing to the measurement with the spectrometer (dashed lines), it can be seen that the general reflectance properties are captured, though at a very low resolution. The results here only made use of three LED wavelengths, so the reflectance show plateaus around the peak wavelengths. In effect, the measured reflectance values are averages across the total emission spectra of each LED, giving very low resolution data.

Using the method described in Section 6.2.1, CIE xy coordinates were calculated for each target, based on the reflectance spectra in Figure 6.11. The resulting coordinates on the colour space diagrams are shown in Figure 6.12, indicated with triangular mark-

Received Spectra **Relative Reflectance Spectra**
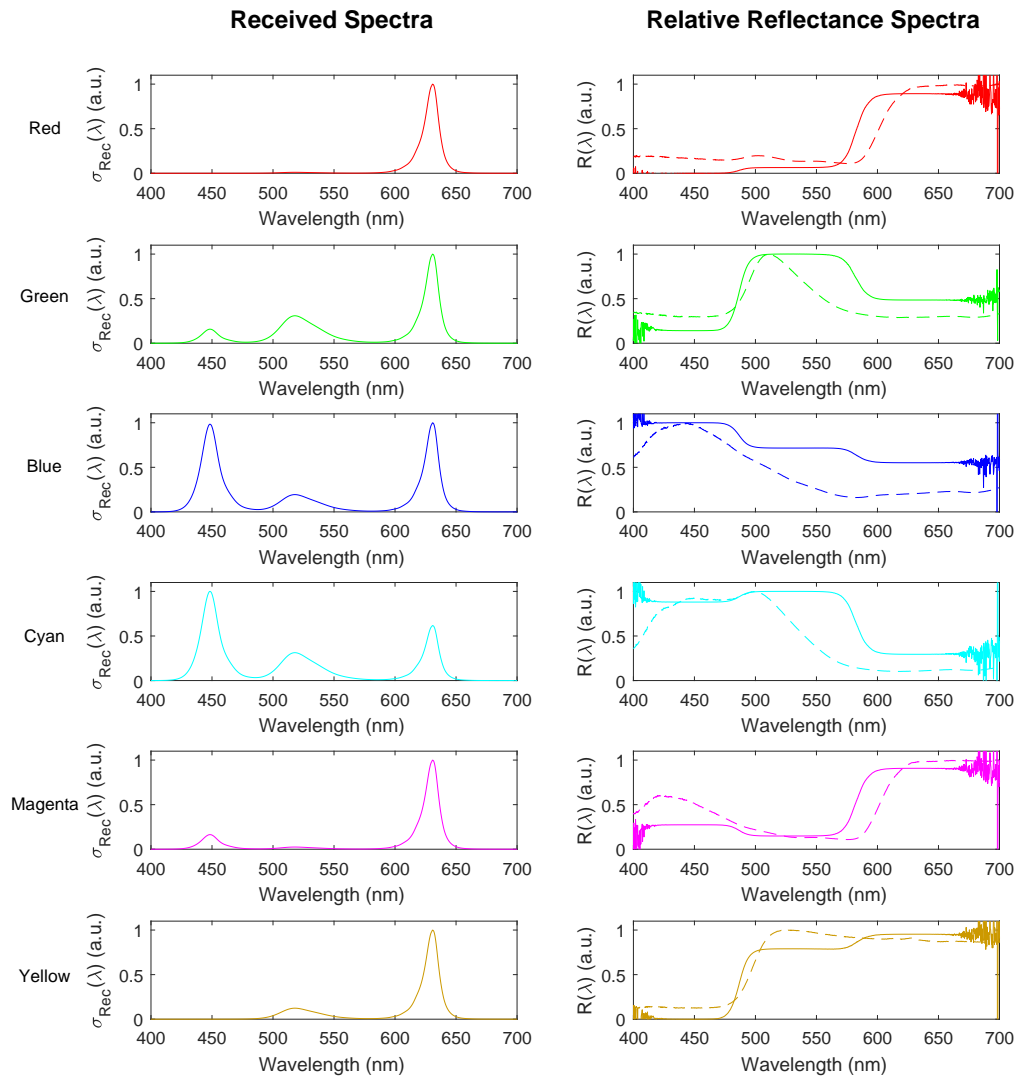
Figure 6.11: Received and reflectance spectra for each colour target for the 3-LED system. The dashed lines represent the reflectance measured with a spectrometer, for comparison.
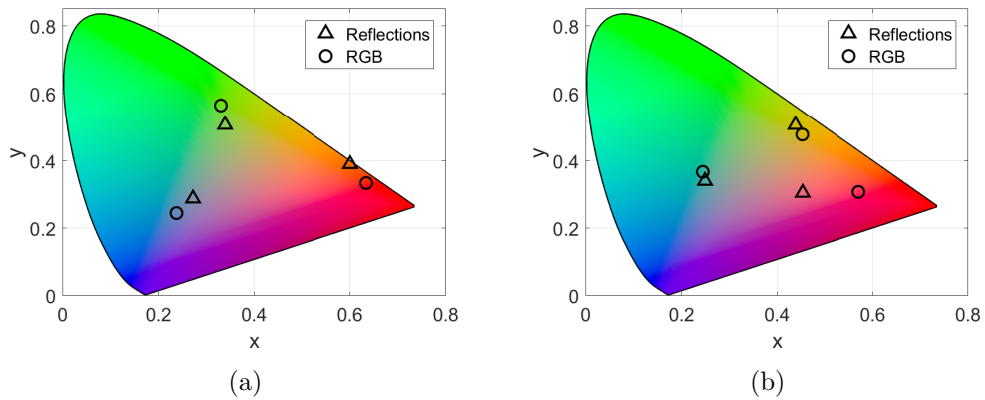
Figure 6.12: Calculated xy coordinates for (a) red, green, blue, (b) cyan, yellow and magenta targets. Triangles indicate full reflectance data, circles indicate RGB approximation.

ers. Each colour target appears in approximately the correct region of the CIE colour space, however, green and blue targets are calculated as whiter, or more "washed out" than expected, and the red target is calculated as slightly orange. Both these effects are attributed to the low-resolution aspect of the approach, where the reflectance is averaged over the full emission range of each LED. As a result, some wavelengths are overrepresented in the reflectance spectra, causing a change in the calculated colour. Using multiple sources with narrower emission peaks would avoid this effect.

As the transmitter consists of red, green and blue LEDs, an RGB colour model is a logical alternative to describe target colours. Instead of using the full reflectance spectra, the reflectance values at the peak LED wavelengths (449, 520 and 632 nm) can be rescaled to the range 0-255 (or 0-1) to produce a corresponding colour on the RGB colour space. Doing so gives the values in Table 6.2. The table also shows coloured blocks defined by the RGB parameters. The final column consists of coloured blocks defined by converting the reflectance CIE coordinates to RGB values. In addition, Figure 6.12 also shows the RGB interpreted colours on the CIE diagrams, indicated in circles. In general, the RGB approximation appears to give purer colours, moving away from the white region of the CIE colour space. This is likely because the reflectance

Table 6.2: RGB values from reflectance data for each target.

Target colour	R	G	B	RGB Colour	Reflectance Colour
Red	255	24	0		
Green	123	255	55		
Blue	141	186	255		
Cyan	75	255	224		
Magenta	255	41	77		
Yellow	255	211	0		

averaging effect has been avoided.

While the CIE coordinates and representative squares in table 6.2 may not accurately reproduce the target colours as shown in Figure 6.9, a level of colour discrimination has been achieved. There are a number of factors which influence the interpretation of colour, and therefore colour comparisons, that may not be accurately represented in the images shown in this section. Firstly, the calculation of CIE coordinates requires a choice of illuminant, which may not be representative of the lighting used in Figure 6.9. Secondly, printing and display effects will influence the appearance of colours shown on screen or on paper. Thirdly, the reflectance spectra suffers under the low-resolution nature of the 3-LED approach. Finally, the RGB approach is an approximation, which has assumed the three LED wavelengths used are representative of the red, green and blue components of the RGB system.

6.4 Hyperspectral Imaging

The above results show proof-of-concept experiments for correlation-based imaging for three wavelengths, with red, green and blue LEDs potentially enabling colour imaging. The approach can be readily extended to more wavelengths of light to enable hyperspectral imaging. LEDs across the full visible range, and extending into ultraviolet and infrared, are available due to the band gap ranges of III-V semiconductors [10]. This potentially enables low-cost hyperspectral imaging to be implemented using the cor-

Table 6.3: Summary of emission wavelength (λ), detection efficiency at λ (η_{PDP}), FWHM pulse width (t_p) and applied correlation time (τ_{corr}) for the LEDs used in the 10-LED board.

Label	λ (nm)	η_{PDP} (%)	t_p (ns)	τ_{corr} (ns)
Deep Red	660	21	11.12	60
Red	630	23	12.00	100
Red-Orange	615	24	11.85	140
Amber	590	26	13.87	200
Green	530	33	9.02	240
Cyan	500	34	9.89	260
Blue	470	30	11.68	300
Royal Blue	450	26	8.13	340
Violet	420	21	8.13	380
Ultra Violet	415	21	7.51	420

relation approach, a suitably chosen set of LED elements and a SPAD based receiver. The following sections discuss a 10-LED transmitter, covering a wide wavelength range, used to characterise the same coloured paper targets as the previous sections.

6.4.1 10-LED Pulsing System

A new driving board was designed for pulsed operation of ten commercial LEDs simultaneously. The LEDs used were Lumileds Luxeon Z series, as a range of wavelengths across the visible and near UV were available, all with the same packaging footprint. The PCB was designed to keep all LED elements close together in a circular arrangement, in order to illuminate a target in an approximately equal manner across each wavelength. The final board is shown in Figure 6.13(a), with all LEDs active. The details of the LEDs used and important parameters are summarised in Table 6.3.

The pulsing circuitry used in the 3-LED system was simplified, as the FPGA is capable of generating a 10 ns pulse without the need for the delay line shortening approach. This is sufficient to generate pulses with shorter lengths than the dead time of the SPAD. Therefore the driver for each LED consists of a double inverter, as shown in Figure 6.13(b). The inverters and transistors were chosen to have operating voltages ranging from at least 3.3 V to 5 V, to allow a range of LED driving voltages without

(a)   (b)
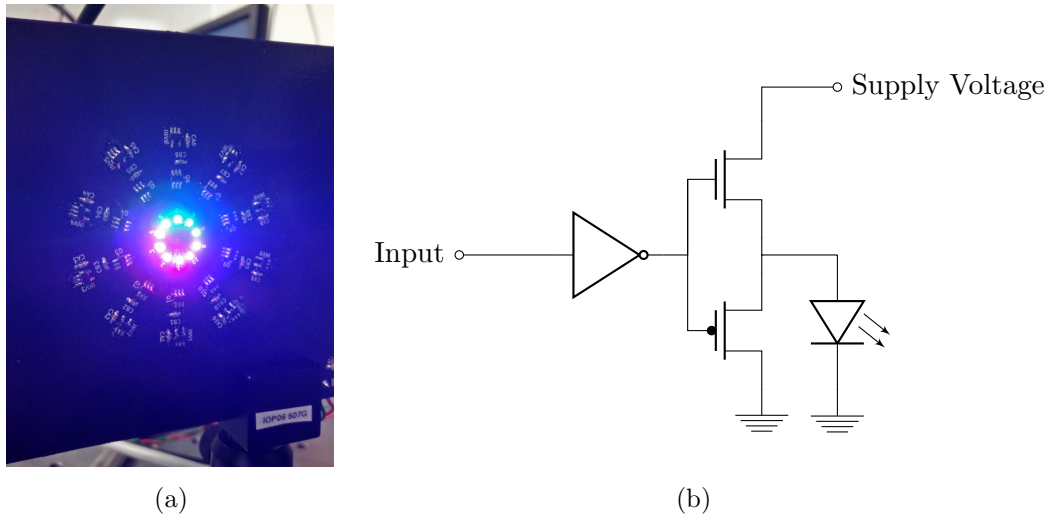
Figure 6.13: (a) Photograph of the 10-LED driver board. (b) Circuit diagram of an individual driving element.

the need for multiple power lines. For all the following results, a driving voltage of 5 V was used. Even though this is significantly above the recommended DC driving voltages for some of the commercial LEDs used, the low repetition rate pulsed approach avoids damaging the LEDs, and the higher voltage allows higher intensity pulses to be generated.

The LEDs were pulsed with 10 ns logic pulses from an FPGA input into the circuit diagram in Figure 6.13(b). Each LED emits a pair of pulses sequentially, with pulse separations as shown in Table 6.3, with spacing between each pair to avoid inter-correlations. The optical pulses are shown in Figure 6.14, measured with an APD (Hamamatsu C5658), and the FWHM pulsewidths are detailed in Table 6.3. Importantly, all LED emission occurs within a 35 ns window, meaning every pulse is less than the dead time of the SPAD $\tau_d = 35$ ns.

The emission spectra from the transmitting LEDs was measured while in pulsed operation using the fibre-coupled spectrometer aligned to each LED in turn. The spectra are shown in Figure 6.15, both individually normalised and in relative emitted power. The normalised plots show that this set of LEDs covers the visible range reasonably
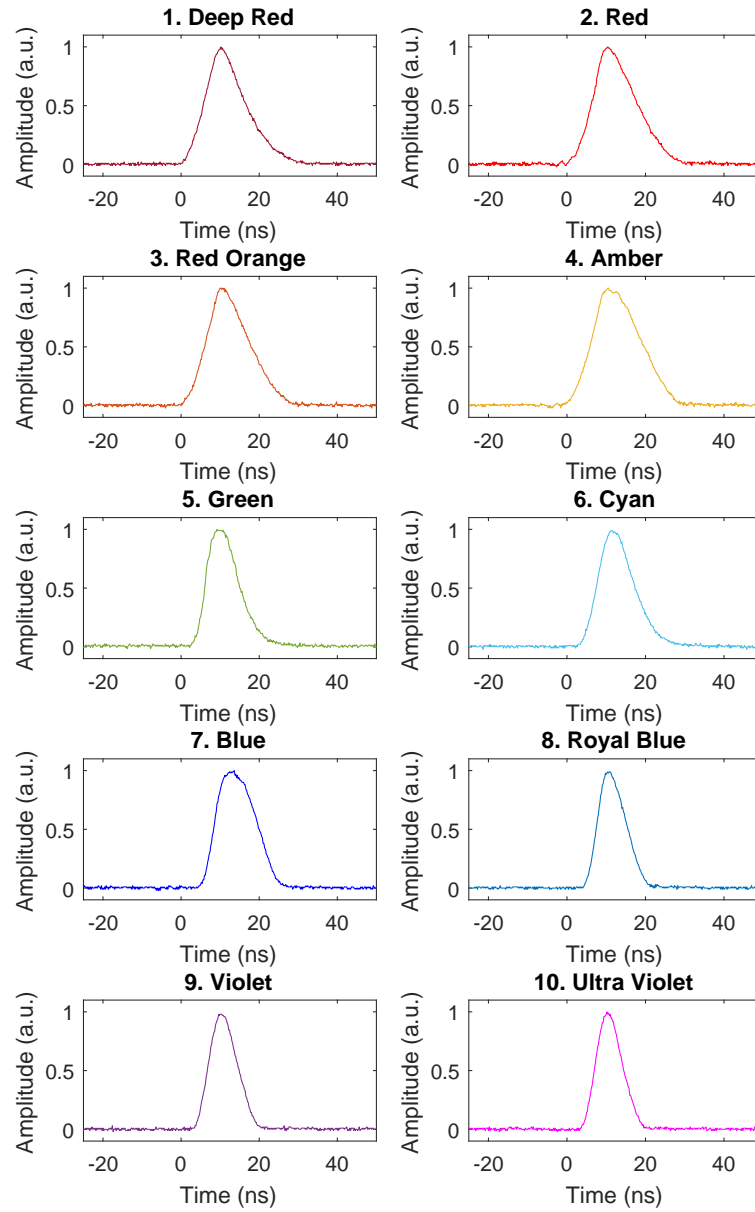
Figure 6.14: Optical pulses of the 10 LEDs when a 10 ns logic pulse is applied.
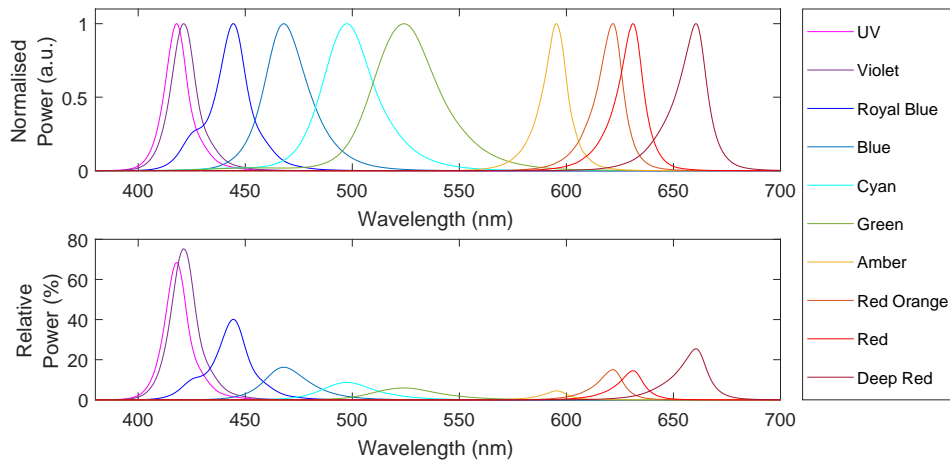
Figure 6.15: Normalised (upper) and relative (lower) emission spectra of the LEDs used in the 10-LED board.

well, though there is a significant gap around 570 nm. The relative emitted power spectra shows that the UV, deep blue and red wavelengths have much higher emitted power than the green and amber. Both these effects are due to the green gap problem in semiconductor materials, where neither InGaN nor AlGaInP based LEDs can currently obtain high efficiency for the green-yellow region [13].

6.4.2 Measurement of Single Colour Targets

With the relative emission spectra and correlated pulse outputs from the 10-LED system, reflectance measurements and colour interpretation can be performed using the methods detailed in Section 6.2.1. The experimental setup was identical to that for the 3-LED setup, with the transmitter positioned 20 cm away from the target, and the SPAD with camera optics 1.3 m away.

The received and reflectance spectra for each target are shown in Figure 6.16. Comparing the results to those in Figure 6.11, it can be seen that the 10-LED system essentially provides a higher resolution result than that of the 3-LED, as expected. The plateau effect of the LED emission widths is less significant, though is still particularly strong in the central green-yellow regions, which is not as well represented in the LED

Table 6.4: Colour of targets from the 10-LED system.

Target colour	Measured colour
Red	■
Green	■
Blue	■
Cyan	■
Magenta	■
Yellow	■

wavelengths. As in the previous results, it is quite clear that each target reflects more light in the expected wavelength ranges. Comparison to the spectrometer measurement (dashed lines) reveals that the approach produces reasonable approximations to the actual spectra for red, blue and magenta targets. The discrepancy is much larger for green, cyan and yellow results. The common factor here is the green portion of the spectrum. As this region is represented poorly by the LED system, the reflectance results are less accurate.

As before, the reflectance spectra can be converted into a colour interpretation. The resulting CIE coordinates are shown in Figure 6.17, with the individual colours, converted to RGB, shown in Table 6.4. These show significant changes over the 3-LED system results in Figure 6.12, most notably a general shift towards the blue region. This may be related to the transmitter emission spectra now being dominated by short wavelength LEDs, rather than in the 3-LED case where red is dominant. If the relative emitted power spectra are not fully accurate, certain wavelengths may be over-represented. A more accurate set of relative power spectra may be determined by collecting all power from each LED in an integrating sphere, rather than aligning a fibre-coupled spectrometer to each LED emission area.

The reflectance spectra of the targets given in Figure 6.16 has a contribution from the emission profile of the transmitter LEDs, which results in the reflectance of a wavelength region spreading out over the emission width. It may be more useful to only show the reflectance measurement at the peak wavelength of emission. The reflectance
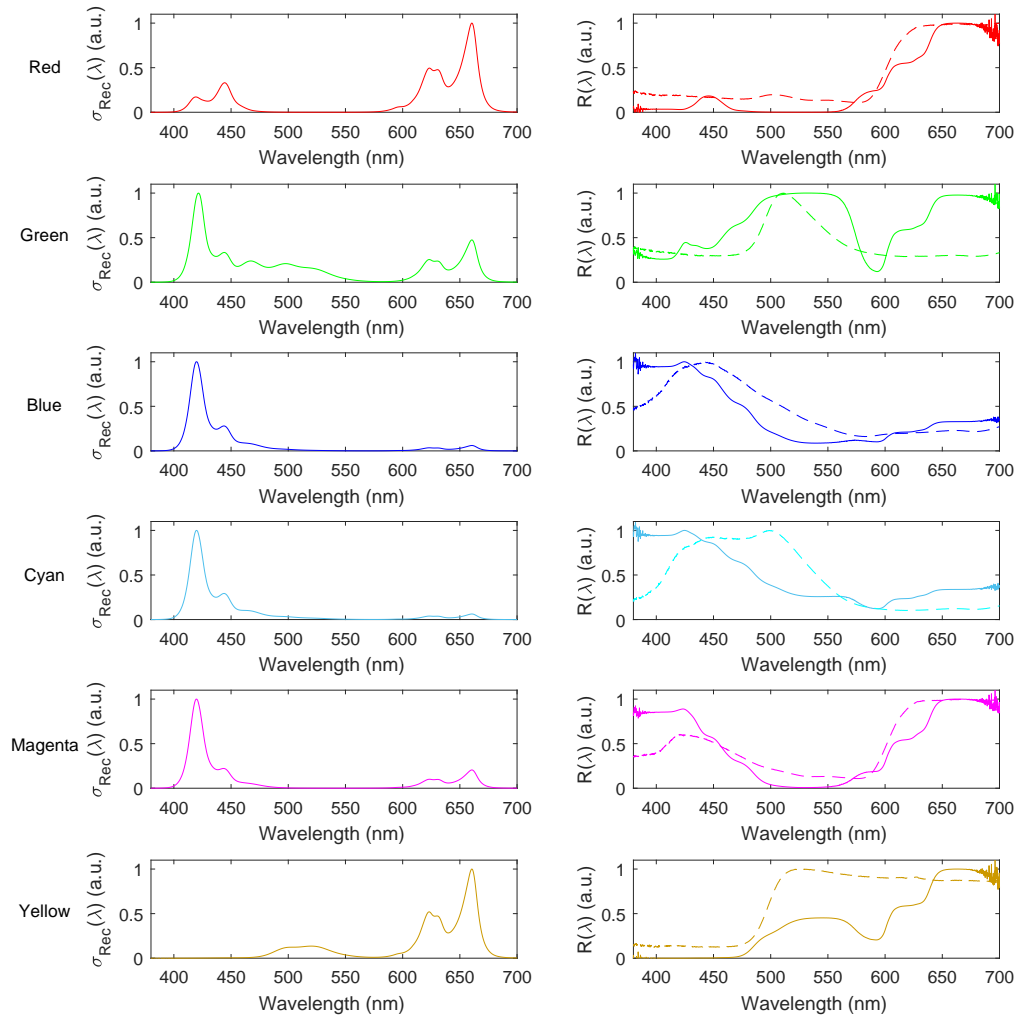
Figure 6.16: Received and reflectance spectra for each colour target for the 10-LED system. The dashed lines represent the reflectance measured with a spectrometer, for comparison.
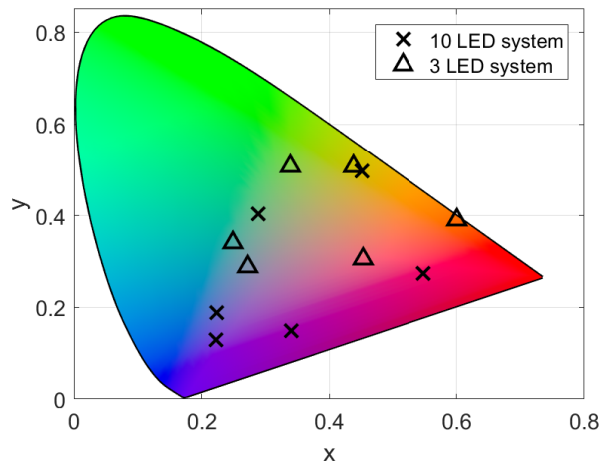
Figure 6.17: CIE colour space with the measured colour of each target using the 10-LED system. The reflection based RGB system results are included for comparison.

spectra displayed in this way are shown in Figure 6.18 with the spectreometer measurement included for comparison. Here it is clear how adding more emitters with different wavelengths improves the spectral resolution of the imaging system. Provided suitable emitters are available, and a detector sensitive to the correct regions, the principle can extend into the infrared or ultraviolet and potentially beyond.

6.5   Further Potential

While a level of colour discrimination and spectral reflectance measurement has been demonstrated here, the system shown is not capable of imaging a scene, as it is limited to a single pixel. There are two potential routes to full 2-dimensional images: arrayed receivers or arrayed transmitters.

The simpler of the two methods is to use a 2D array of SPADs as a receiver [14]. Such devices often have timing electronics dedicated to each individual pixel [15, 16], and have been demonstrated for applications such as fluorescence lifetime imaging microscopy [6], 3D imaging [5], light-in-flight imaging [7] and object tracking around corners [17]. A similar receiver could be implemented here to achieve colour or hy-
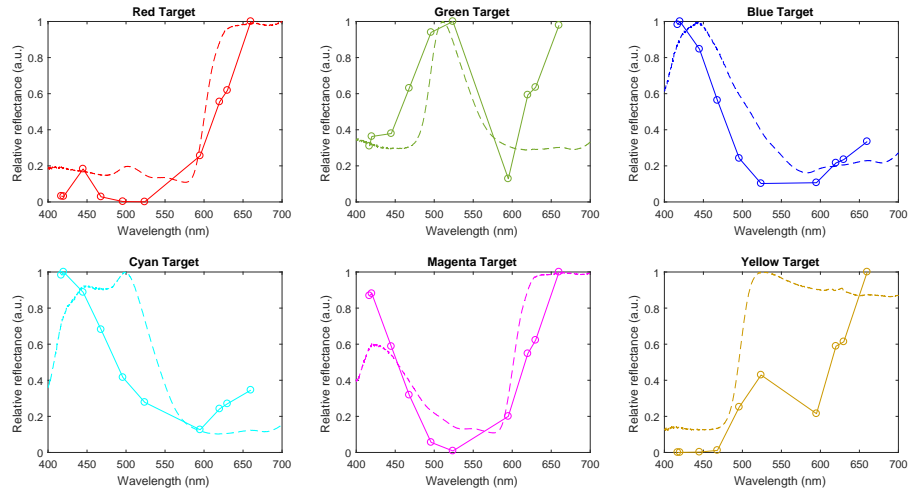
Figure 6.18: Reflectance spectra of the coloured targets at the peak emission wavelengths for the LEDs. The dashed lines represent the reflectance measured with a spectrometer, for comparison.

perspectral imaging, where each receiver pixel is capable of discriminating wavelengths by the temporal structure from the source. Essentially, each pixel would perform the operations described in previous sections. allowing an image to be reconstructed.

An alternative, more computationally complex method is to use an array of transmitters, and perform computational imaging based on a spatially structured light source [18–20]. A CMOS controlled micro-LED array, as discussed in much of this thesis, could be used to project structured light patterns. The known spatial patterns incident on the target can be correlated with the intensity received on the single SPAD, and used to computationally reconstruct a 2D colour image.

6.6   Summary

This Chapter has discussed further developments in applying the temporal correlation methods described in Chapter 3 in a multiplexed format. The first part discussed a method to perform colour discrimination based on temporally structured light sources of different wavelengths. The correlation function $g(\tau_j)$ can be used to determine the

relative received power of multiple sources.

By using a red, green and blue LED, simple colour targets could be discriminated, and relative measurements of reflectance made. In the current implementation, this is sufficient to make an estimate of the colour of the target, either through the reflectance spectrum or an RGB approximation.

By extending the system to 10 LED wavelengths, spanning the visible spectrum, a higher resolution can be obtained in the reflectance spectra. This technique enables hyperspectral imaging of a target, and potentially more accurate colour measurements.

While the current demonstrations only show single-pixel images, as the receiver is a single SPAD, it should be relatively straightforward to extend the principle to a 2D array of SPAD detectors. Doing so would readily enable colour imaging at the full resolution of the detector, without the need for optical filters. If sources and detectors are available with suitable emission spectra and response, imaging in the ultraviolet and/or infrared can also be performed using the same techniques.

Bibliography

[1] D. Durini, *High performance silicon imaging.* Cambridge: Elsevier, 2014.

[2] D. Dussault and P. Hoess, "Noise performance comparison of ICCD with CCD and EMCCD cameras," *Proc. SPIE 5563, Infrared Systems and Photoelectronic Technology*, p. 195, 2004.

[3] P. Jerram, P. J. Pool, R. Bell, D. J. Burt, S. Bowring, S. Spencer, M. Hazelwood, I. Moody, N. Catlett, and P. S. Heyes, "The LLCCD: low-light imaging without the need for an intensifier," *Proc. SPIE 4306, Sensors and Camera Systems for Scientific, Industrial, and Digital Photography Applications II*, p. 178, 2001.

[4] F. Guerrieri, S. Tisa, A. Tosi, and F. Zappa, "Two-dimensional SPAD imaging camera for photon counting," *IEEE Photonics Journal*, vol. 2, no. 5, pp. 759–774, 2010.

[5] D. Shin, F. Xu, D. Venkatraman, R. Lussana, F. Villa, F. Zappa, V. K. Goyal, F. N. Wong, and J. H. Shapiro, "Photon-efficient imaging with a single-photon camera," *Nature Communications*, vol. 7, no. May, pp. 1–8, 2016.

[6] D.-U. Li, J. Arlt, J. Richardson, R. Walker, A. Buts, D. Stoppa, E. Charbon, and R. Henderson, "Real-time fluorescence lifetime imaging system with a 32 × 32 0.13μm CMOS low dark-count single-photon avalanche diode array," *Optics Express*, vol. 18, no. 10, p. 10257, 2010.

Bibliography

[7] G. Gariepy, N. Krstajić, R. Henderson, C. Li, R. R. Thomson, G. S. Buller, B. Heshmat, R. Raskar, J. Leach, and D. Faccio, "Single-photon sensitive light-in-fight imaging," *Nature Communications*, vol. 6, p. 6021, 2015.

[8] H. Lee, *Introduction to color imaging science.* Cambridge: Cambridge University Press, 2005.

[9] P. Alessi, E. Carter, M. Fairchild, R. Hunt, C. McCamy, B. Kranicz, J. Moore, L. Morren, J. Nobbs, Y. Ohno, M. Pointer, D. Rich, A. Robertson, J. Schanda, R. Seve, P. Trezona, K. Witt, and H. Yaguchi, "Colorimetry, 3rd edition," Tech. Rep. CIE 015:2004, International Commission on Illumination (CIE), 2004.

[10] E. F. Schubert, *Light emitting diodes.* Cambridge: Cambridge University Press, 2006.

[11] T. Seong, J. Han, H. Amano, and H. Morkoç, *III-Nitride based light emitting diodes and applications.* Singapore: Springer, 2013.

[12] J. J. D. McKendry, B. R. Rae, Z. Gong, K. R. Muir, B. Guilhabert, D. Massoubre, E. Gu, D. Renshaw, M. D. Dawson, and R. K. Henderson, "Individually address-able AlInGaN micro-LED arrays with CMOS control and subnanosecond output pulses," *IEEE Photonics Technology Letters*, vol. 21, pp. 811–813, Jun 2009.

[13] M. H. Crawford, "LEDs for solid-state lighting: performance challenges and recent advances," *IEEE Journal on Selected Topics in Quantum Electronics*, vol. 15, no. 4, pp. 1028–1040, 2009.

[14] A. Rochas, M. Gosch, A. Serov, P. A. Besse, R. S. Popovic, T. Lasser, and R. Rigler, "First fully integrated 2-D array of single-photon detectors in standard CMOS technology," *IEEE Photonics Technology Letters*, vol. 15, no. 7, pp. 963–965, 2003.

Bibliography

[15] J. Richardson, R. Walker, L. Grant, D. Stoppa, F. Borghetti, E. Charbon, M. Gersbach, and R. K. Henderson, "A 32×32 50ps resolution 10 bit time to digital converter array in 130nm CMOS for time correlated imaging," *Proceedings of the Custom Integrated Circuits Conference*, no. 029217, pp. 77–80, 2009.

[16] F. Villa, R. Lussana, D. Bronzi, S. Tisa, A. Tosi, F. Zappa, A. Dalla Mora, D. Contini, D. Durini, S. Weyers, and W. Brockherde, "CMOS imager with 1024 SPADs and TDCS for single-photon timing and 3-D time-of-flight," *IEEE Journal on Selected Topics in Quantum Electronics*, vol. 20, no. 6, pp. 364–373, 2014.

[17] G. Gariepy, F. Tonolini, R. Henderson, J. Leach, and D. Faccio, "Detection and tracking of moving objects hidden from view," *Nature Photonics*, vol. 10, no. 1, pp. 23–26, 2016.

[18] Y. Bromberg, O. Katz, and Y. Silberberg, "Ghost imaging with a single detector," *Physical Review A - Atomic, Molecular, and Optical Physics*, vol. 79, no. 5, pp. 1–4, 2009.

[19] B. Sun, M. P. Edgar, R. Bowman, L. E. Vittert, S. Welsh, A. Bowman, and M. J. Padgett, "3D computational imaging with single-pixel detectors," *Science*, vol. 340, no. 6134, pp. 844–847, 2013.

[20] S. S. Welsh, M. P. Edgar, R. Bowman, P. Jonathan, B. Sun, and M. J. Padgett, "Fast full-color computational imaging with single-pixel detectors," *Optics Express*, vol. 21, no. 20, p. 23068, 2013.

Chapter 7

Conclusions

This thesis has described the application of CMOS controlled micro-LED arrays for optical communications and imaging. The high-frequency modulation characteristics of micro-LED arrays, combined with the control systems implemented in CMOS technology, provides devices capable of generating temporally and spatially structured optical signals on nanosecond time scales. This has been shown to provide enhancements to intensity modulated communication schemes, and also to enable novel transmission methods which extend into imaging systems.

Chapter 2 presented experimental results using a CMOS controlled micro-LED as a "digital-to-light" converter. Multi-level schemes such as pulse amplitude modulation improve on the spectral efficiency of low complexity on-off keying, however, the non-linearity of LEDs is problematic for reliably reproducing discrete signals. The micro-LED arrays can provide improved linearity by transmitting discrete levels with increasing numbers of active elements. The integrated nature of the device allows optical signals to be directly generated from input electronic logic signals, removing the need for a digital-to-analogue converter. Pulse amplitude modulation was performed with 4 and 8 levels, producing a maximum data rate of 200 Mb/s. Furthermore, discrete level orthogonal frequency division multiplexing (OFDM) was implemented. This further improves spectral efficiency over pulse amplitude modulation, and avoids issues

such as baseline wander. Discrete OFDM was shown to provide a maximum spectral efficiency of 3.95 bits/s/Hz, and high data rates can be expected with hardware improvements.

A new form of optical communications was introduced mathematically in Chapter 3, and developed experimentally in Chapter 4. Using a single-photon avalanche diode (SPAD) and short optical pulses from a micro-LED array, data can be encoded in the temporal correlation of an optical signal. This is in contrast to conventional optical communications which encodes data in the intensity of a signal. By using single-photon detection, the transmission scheme operates on a low power level, with data rates of 300 kb/s achieved at a BER of 1×10^{-3} and received power of 15 pW. Furthermore, received power requirements can be reduced almost arbitrarily by reducing the data rate. Equivalently, if more received power is available, data rates can be increased. The primary strength of this transmission scheme is in background signal rejection. Data can be transmitted in the presence of not only constant background illumination, but also modulated signals. If the background signal frequency is close to the data rate of the link, only a modest increase in received power is required to maintain the same BER performance.

A secondary advantage of the implemented scheme is in the simplicity of the components and low electrical power consumption. This advantage is demonstrated in Chapter 5 by operating the communication link under power from a nanosatellite simulation testbed. The consumed power of approximately 5 W can be readily supplied by the solar panels and battery systems of a CubeSat, making the communication system attractive for inter-satellite links. Replacing the single SPAD receiver with an arrayed digital silicon photomultiplier (dSiPM) system allows a dramatic increase in the dynamic range of the transmission system. In addition, limitations from detector dead time are lifted. Using a dSiPM, a data rate of 5 Mb/s has been demonstrated, greater than that possible with a single SPAD. Furthermore, it is possible to transmit multiple simultaneous data streams by encoding each with a different temporal pattern.

The correlation approach to optical communications also has potential in imaging applications, which has been investigated in Chapter 6. Here, commercial LEDs were employed for proof-of-concept experiments, providing a wide range of emission spectra. By applying different temporal correlation patterns to each wavelength of LED, relative measurements of received power can be made using a single SPAD by comparing the amplitude of the correlation patterns. As the relative emission spectrum from the transmitter is known, the data at the receiver can be used to determine the relative reflectance or transmittance of an object in the channel. This has been exploited to perform simple colour measurements of targets, with potential application in low-light colour imaging. Utilising additional LED sources, hyperspectral imaging can be performed using the same methods. This has been demonstrated for 10 visible LED wavelengths, and the principle extends to the infrared and ultraviolet spectra.

7.1 Future Work

As the correlated pulse methods presented in this thesis are novel, there is significant scope for further work in both correlated communications and imaging.

An initial extension of the communications work is to determine the maximum data rate achievable with the current receiver array. While 5 Mb/s was demonstrated here, higher data rates should be possible, as detector saturation was not reached and data rate can be traded off with received power. It will be possible to do this with the current micro-LED transmitter setup, however, a number of improvements can be made. Firstly, the oscillator used to produce the pulse trigger signal can be replaced with a higher frequency model, to enable the short pulses with correlation times shorter than 20 ns. Shorter time intervals effectively increases the dynamic range of the system, as more pulses can be detected per bit period. Secondly, improvements to the receiver sampling approach should be made in order to use higher frequency outputs with greater numbers of photon counts. Alternatively, more direct access to
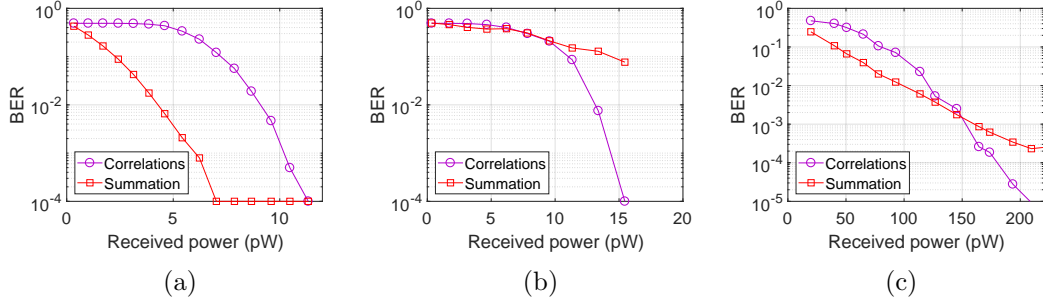
Figure 7.1: Comparison between correlation and summation decoding for (a) 50 kb/s in the presence of constant background with single SPAD, (b) 50 kb/s in the presence of 50 kHz background with single SPAD and (c) 5 Mb/s with no background with SPAD array.

the digital outputs from the chip would facilitate directly digital decoding. In an ideal setup, the receiver would be running at 0-255 photon counts at 800 MHz, enabling detection of extremely short correlation times, large numbers of photons per pulse, and a maximum photon count rate of 2.04×10^5 MHz. The optical pulse performance and modulation rate of the micro-LED transmitter may also be improved upon by replacing it with a laser diode, with the correlated patterns generated with a pair of electro-optic modulators. Alternatively, resonant cavity LEDs can also provide high modulation bandwidths.

The current implementation of the correlation communication scheme involves transmission of repeating pulses for one binary symbol, and no transmission for the other. Therefore, the data stream can also be decoded by simply summing the photon counts in a data interval, as in a conventional intensity modulated signal. This results in an interesting comparison of approaches, which warrants further investigation. Figure 7.1 shows BER curves for both the correlation and summation decoding. Figure 7.1(a) is a 50 kb/s link with constant background illumination of 15 pW. Evidently, summation of photon counts outperforms the correlation method. However, in the presence of modulated signals, as shown in Figure 7.1(b), the summation approach suffers heavily. Furthermore, the arrayed receiver shows correlation decoding to outperform summation for high photon counts. Figure 7.1(c) shows the BER performance at 5 Mb/s with

the arrayed receiver. The improvement of correlations at high powers can be explained by its multiplicative nature. For example, if 4 photons are detected per pulse, a pair of pulses produces 16 correlations, however, the summation will only count 8 photons. Therefore, the signal builds more rapidly for correlations. The results shown here are preliminary; a detailed investigation is required to justify correlated communications over intensity modulation. It should also be noted that the summation approach only works here due to the particular implementation of the communication scheme. Alternate approaches such as the PPM-style transmission could not be decoded in this manner.

An additional direction worth investigating is in multiple data stream communications using the arrayed receiver. Preliminary results indicate simultaneous data streams can be sent with little interference. However, it is more efficient to transmit a single high data rate stream, limiting the potential data rate improvements from parallelism. Nevertheless, there is still potential for using multiple streams in a networked situation. Such an approach may have use for "Internet of Things" applications, where multiple devices are simultaneously communicating with each other. The distinction of data streams by correlation pattern could be thought of as a multiple access technique.

As the data transmission method is probabilistic in nature, it is likely that a much more sophisticated model could be developed to help with signal recovery and decoding. In particular, it would be interesting to pursue a Bayesian approach to signal recovery. This appears to be appropriate as the scheme depends on repeating pulses, the detection (or absence) of which could be used to update a conditional probability related to the presence of a signal.

The satellite simulator experiments demonstrated that the communication system can be powered by CubeSat systems, however, the current system is not optimised for such an application. Initially, the form factor would need to be altered to fit the 10×10 cm dimensions of CubeSats. This should be relatively straightforward, as many of the elements on the control boards for the CMOS devices are for testing, or

unnecessary for this application. Additionally, it would be advantageous to modify the system to produce a transceiver to allow bi-directional communications. This would require the SPAD receiver, micro-LED array, and all relevant electronics to be housed on the same PCB. A replacement for the commercial SPAD should be found, as the power consumption of the module is high. The initial work with the SPAD array suggests such a format is beneficial for dynamic range and data rate, so could be employed here. With a suitable form factor developed, the system could be put through a full set of simulations for CubeSat components, verifying suitability for potential use in a real satellite environment.

An additional application area of interest for the communication link is in neural data collection. In vivo experiments on mice using neural probes collect large amounts of data which must be transmitted to other systems. While a cable link is possible, it is desirable to allow the mouse to move freely within an area. As animal testing regulations limit the size and mass of equipment that can be mounted on a mouse's head or body, the data transmission must be small, lightweight and low power consumption. This fits well with the performance of the optical link described in Chapters 4 and 5. Additionally, the LED wavelength can be chosen such that it is invisible to the mouse, and the background rejection properties of the correlation-based link should allow reliable data transmission in a variety of laboratory conditions.

The imaging work presented in Chapter 6 is mostly at a proof-of-concept level, as only single-pixel "images" have been taken. As such, the priority for this work is to extend the principle to a 2-dimensional system. The natural approach is to use an array of SPAD receivers. However, in contrast to the array used in communications, the output of each pixel must be separated. The correlation approach can then be used to determine the spectrum incident on each SPAD individually, and therefore produce a colour or hyperspectral image. Extensive characterisation of the system will be needed to justify the correlation approach and its potential advantages over other imaging and spectroscopic methods.

Further operational improvements are possible for the imaging system by moving to the CMOS-controlled micro-LED arrays. The time required to take an image is limited by the pulse performance of the transmission system. The current setup uses commercial LEDs, with fairly wide pulse widths and limiting control over driving conditions. The micro-LED arrays allow much shorter pulses at higher rates, which will enable faster image acquisition. However, developing a system of CMOS driven micro-LEDs with as many wavelengths as used in these preliminary experiments would be challenging.

The arrayed nature of the CMOS-controlled micro-LEDs may also permit advantages for correlation-based imaging. Projection of patterns may allow colour or hyperspectral images to be taken using computational single-pixel imaging. A set of different wavelength LED arrays could project patterns, with each array transmitting using a different correlation signal. The signal detected with a single SPAD could then produce an image for each wavelength to be combined into a colour or hyperspectral image.

Appendix A

Poisson Distributions

Due to the discrete nature of photon counting events, the Poisson distribution is a recurring feature in this thesis. A brief description of such distributions is presented here, for reference.

The Poisson distribution describes the probability of a number of discrete events occurring within a fixed interval. The distribution is valid only if the events occur with a constant rate and are independent of one another. The probability, P, of k events occurring within a given interval is given by:

$$P(k) = \frac{e^{-\lambda}\lambda^k}{k!}. \tag{A.1}$$

Here, λ is the average number of events that occur within the interval. For a Poissonian distribution, the variance is equal to the mean λ. Distributions for $\lambda = 1, 5$ and 7 are shown in Figure A.1. Importantly, the distribution is only defined for $k \in \mathbb{Z}$. Poisson distributions with low values of λ vary significantly from Gaussian distributions, particularly due to strong asymmetry as k cannot be negative. This causes single photon based communications experiments to exhibit different signal-to-noise behaviours to classical, analogue detection methods, which will be influenced by additive white Gaussian noise.

Appendix A. Poisson Distributions
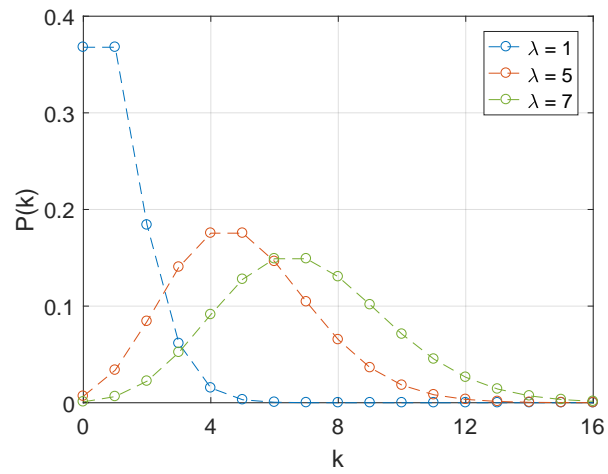
Figure A.1: Poisson distributions for mean values of 1, 5 and 7.

Appendix B

Publications

B.1   Journal Publications

A. D. Griffiths, J. Herrnsdorf, R. Henderson, M. J. Strain, and M. D. Dawson, "Temporal encoding to mitigate background signals in photon counting communication links," *In preparation*, 2018.

A. D. Griffiths, J. Herrnsdorf, C. Lowe, M. MacDonald, R. Henderson, M. J. Strain, and M. D. Dawson, "Poissonian communications: free space optical data transfer at the few-photon level," *arXiv*, arXiv:1801.07994 [physics.optics], 2018.

A. D. Griffiths, M. S. Islim, J. Herrnsdorf, J. J. D. McKendry, R. Henderson, H. Haas, E. Gu and M. D. Dawson, "CMOS-integrated GaN LED array for discrete power level stepping in visible light communications," *Optics Express*, vol. 25, no. 8, pp. A338 - A345, 2017.

B.2 Conference Submissions

A. D. Griffiths, J. Herrnsdorf, R. Henderson, M. J. Strain, and M. D. Dawson, "Few-photon visible light communications using nitride LEDs," *UK Nitrides Consortium* Manchester, 2018. (Oral presentation).

R. Bian, S. Videv, A. D. Griffiths, J. J. D. McKendry, E. Xie, E. Gu, M. D. Dawson and H. Haas, "Experimental demonstration of generalised space shift keying for visible light communication," *IEEE International Black Sea Conference on Communications and Networking* Istanbul, 2017.

A. D. Griffiths, J. Herrnsdorf, J. J. D. McKendry, R. Henderson, H. Haas, E. Gu, and M. D. Dawson, "Spatially Superposed Pulse Amplitude Modulation Using a Chip-Scale CMOS-Integrated GaN LED Array," *Light, Energy and the Environment, Optical Society of America*, SSM2C.2, Leipzig, 2016. (Oral presentation).

A. D. Griffiths, J. Herrnsdorf, J. J. D. McKendry, E. Xie, E. Gu, M. J. Strain and M. D. Dawson, "Picosecond pulses with high peak optical power from GaN LEDs," *Photon16*, Leeds, 2016. (Poster presentation).

R. Bian, S. Videv, A. D. Griffiths, J. J. D. McKendry, E. Xie, K. Cameron, E. Gu, S. Rajbhandari, G. Faulkner, D. O'Brien, M. D. Dawson, R. Henderson and H. Haas, "A high speed generalised space shift keying link with micro-LEDs and CMOS APD receiver," *IEEE Society Summer Topical Meeting Series*, Newport Beach CA, 2016.

J. J. D. McKendry, D. Tsonev, R. Ferreira, S. Videv, A. D. Griffiths, S. Watson, E. Gu, A. E. Kelly, and M. D. Dawson, "Gb/s single-LED OFDM-based VLC using violet and UV Gallium nitride μLEDs," *IEEE Summer Topicals Meeting Series*, Nassau, 2015.

Poissonian communications: free space optical data transfer at the few-photon level

Alexander D. Griffiths[1], Johannes Herrnsdorf[1], Christopher Lowe[2], Malcolm Macdonald[2], Robert Henderson[3], Michael J. Strain[1,*], and Martin D. Dawson[1]

[1]Institute of Photonics, University of Strathclyde, Glasgow
[2]Department of Mechanical & Aerospace Engineering, University of Strathclyde, Glasgow
[3]CMOS Sensors & Systems Group, University of Edinburgh, Edinburgh
[*]Corresponding author: michael.strain@strath.ac.uk

January 25, 2018

Abstract

Communicating information at the few photon level typically requires some complexity in the transmitter or receiver in order to operate in the presence of noise. This in turn incurs expense in the necessary spatial volume and power consumption of the system. In this work we present a self-synchronised free-space optical communications system based on simple, compact and low power consumption semiconductor devices. A temporal encoding method, implemented using a gallium nitride micro-LED source and a silicon single photon avalanche photo-detector (SPAD) demonstrates data transmission at rates up to 100 kb/s for 8.25 pW received power, corresponding to 27 photons per bit. Furthermore, the signals can be decoded in the presence of both constant and modulated background noise at levels significantly exceeding the signal power. The systems low power consumption and modest electronics requirements are demonstrated employing it as a communications channel between two nano-satellite simulator systems.

1   Introduction

Conventional optical wireless communications (OWC) involves the modulation of the optical intensity of a light source, such as a light-emitting diode (LED) or laser, and direct detection of the output light [1]. When transmitting over long distances, or through high loss media, received power can become greatly reduced. Ul-timately, the modulated signal can become lost in noise, arising from background light in the optical channel or within the receiver electronic components themselves. A number of schemes have been developed to operate using an exceptionally low number of received photons per bit, including error correction coding and higher order modulation schemes [2], coherent detection at Mb/s [3] and Gb/s [4] data rates, phase shift

keying (PSK) and rate-1/2 forward error correction (FEC) codes. Such schemes are approaching the standard quantum limit (SQL) for sensitivity, and make use of complex components such as balanced photodetectors, local oscillators and optical phase-locked loops. It should also be noted that the SQL is not the fundamental quantum limit for optical communications, and can be surpassed by employing quantum receivers [5–7].

A potentially simpler way to attain high receiver sensitivity is to make use of single photon detection and counting [8–12]. With the use of FEC codes and high order pulse position modulation (PPM) [13], photon counting systems can also operate with extremely low numbers of photons per bit [2]. However, these systems are critically dependent on temporal synchronisation of the transmitter and receiver. The high sensitivity of single photon counting techniques, combined with PPM and arrayed receivers has potential for deep-space communication links, operating at megabit rates. Such systems have been proposed for communications to Mars orbit [14], and demonstrated for Lunar range optical communications [15]. These detection schemes are however limited by the optical noise in the channel and the dark count rate of the detector [16].

Transmitters that generate coincident photon pairs may be used in time gating schemes that can reduce the effects of noise in the system [17, 18]. Counting coincidences allows data to be sent with extremely low levels of received power over long distances [19, 20], and can be used for quantum key distribution [21–23]. These methods typically require high efficiency photon pair sources with large form factor requirements on the internal and transceiver optics, and in some cases, secondary clock channels.

Here we demonstrate a novel optical transmission scheme, suitable for OWC at ultra-low light levels, requiring only a single, low photon flux channel. Compared with existing methods, this scheme is implemented with simple and widely available semiconductor components and electronics in a compact format and with low power consumption. Importantly, the method operates under the presence of both constant and modulated background noise, which is enabled by the encoding of data in the timing statistics of the received photons.

The data is formatted as temporally correlated optical pulses, in this case from an LED, transmitted over a single optical channel. The signal is detected with a single photon avalanche diode (SPAD), the output of which is a series of photon detection events including both data and noise sources. By calculating the autocorrelation of the SPAD output, discretised in a histogram, peaks can be observed corresponding to the specified temporal correlation of the received pulses. Data can therefore be encoded in the presence or absence of correlation peaks at predetermined time intervals. This allows undesired background signals to be rejected efficiently, unless they coincide with the data signal simultaneously on two separate timescales, namely the correlation time and the symbol rate. At data rates of a few kb/s, data can be transmitted with received signal power at a fraction of the background signal power. By trading off the data rate, the scheme can in principle adapt to arbitrarily low signal to noise ratio (SNR) as the link fidelity is governed by the Poissonian count statistics rather than conventional SNR. Furthermore, the experiments were performed using a simple optical and electronic setup comprising a GaN micro-LED transmitter and a single silicon SPAD receiver interfaced with field-programmable gate arrays (FPGAs). The scheme is also scalable to arrayed sources and receivers and can thus be extended to a multiple

input multiple output configuration [1]. All this opens up potential for application in areas such as the internet of things, where a network of individual elements will need to communicate under low power, potentially powered through energy harvesting, with modest data rates. In this light, we demonstrate the suitability of the scheme for nano-satellite communications at such low power levels that transmission distances in the 10's of km range are feasible using a single LED emitter.

The following sections discuss the details of the transmission scheme, its current implementation, data transmission results and a demonstration of the system's suitability for inter-satellite communications, such as shown in Figure 1a.

2 Results

2.1 Time correlation encoding scheme

The transmission scheme presented here, inspired by time-correlated single photon counting (TCSPC) techniques often used for fluorescence lifetime imaging [24], involves the use of a single SPAD to receive time correlated signals at a single photon level. Analysis of the SPAD response to incoming light over an interval $[-t_1, t_1]$ shows that the correlation count density function $g(\tau)\mathrm{d}t'$ of recording two subsequent SPAD counts with temporal separation in the interval $[\tau, \tau + \mathrm{d}t']$ is given by:

$$g(\tau) = \int_{-t_1}^{t_1} \mathrm{d}t \; f(t)f(t + \tau). \tag{1}$$

Here $f(t)$ is the temporal probability distribution of received SPAD pulses, which is determined by the optical signal from the transmitter. Full analysis is given in the supplementary material. If a suitable optical source transmits pulses with a time separation of T, $g(\tau)$ will show a peak

at $\tau = T$, as the probability of observing SPAD pulses separated by T is increased. Equation 1 is the autocorrelation of $f(t)$, so it is expected that peaks in $g(\tau)$ would have a width of $2t_{pulse}$, where t_{pulse} is the width of the optical pulse. It is important that $T > \tau_d$, the dead time of the SPAD, as otherwise the SPAD would not recover from the first pulse in time to see the second. This restriction can be lifted by making use of a SPAD array [25,26], however here we consider the use of only a single SPAD. The presence and/or temporal position of peaks in $g(\tau)$ directly depends on the sequence of optical pulses from the transmitter, and therefore can be used as a means of transmitting data.

In reality, the SPAD output is not a continuous probability distribution, but a series of discrete photon detection events. These events can occur due to the optical pulses from the transmitter, background photons, or dark counts. The SPAD output signal will be sampled over a time period, into time bins t_i, $i = 1, \ldots, N_s$, where N_s is the total number of time bins. Each bin contains a number of counts f_i. If these bins are chosen to be smaller than τ_d, f_i will only have values of 0 or 1. Correlation time will also be discretised into τ_j, $j = 1, \ldots, N_\tau$. For a single pair of pulses a correlation either is or is not detected. This single correlation is indistinguishable from a random correlation of counts, so the optical signal must be repeated many times to produce a usable histogram of correlation counts. If correlation time bin size is chosen as an integer multiple of sampling bin size, $\tau_{bin} = kt_{bin}$, we can define start and stop indices for correlating across i as:

$$n_{start} = \frac{\tau_1}{t_{bin}}, \tag{2}$$

$$n_{stop} = n_{start} + kN_\tau - 1. \tag{3}$$

With this, the discrete form of Equation 1 is:

$$g(\tau_j) = \sum_{i=1}^{N_s - n_{stop}} \sum_{l=0}^{k-1} f_i f_{i+n_{start}+(j-1)k+l}. \quad (4)$$

As f_i is a binary value, and the output from the SPAD is a transistor-transistor logic (TTL) signal, the summation could be implemented with simple logic circuits.

Encoding data in $g(\tau_j)$ has the potential to allow data transfer at exceptionally low light levels, and in the presence of significant background illumination. In order to detect correlations, the receiver requires the detection of a single photon from each optical pulse. Such conditions allow average received power to be extremely low, in the range of pW. The trade-off in this transmission scheme is that the data rate is expected to be relatively modest, as the optical signal must be repeated several times in order to generate a distinguishable signal in $g(\tau_j)$.

There are several potential ways to encode data in $g(\tau_j)$. Forms of pulse position modulation (PPM) or pulse amplitude modulation (PAM) are discussed in the supplementary material. Here we consider the simplest form of encoding, on-off keying (OOK), where data can be encoded using a single pulse time separation. On transmission of the symbol '1', pulses of width t_{pulse} are transmitted continuously with a fixed time separation T, so $g(\tau_j)$ will show a peak at $\tau = T$. On transmission of the symbol '0' no pulses are transmitted, producing only background peaks in $g(\tau_j)$.

A schematic of the expected waveforms is shown in Figure 1b. In this example, optical pulses are sent with time separation of $T = 40$ ns. If we choose $t_{pulse} = 5$ ns, deliberately less than τ_d, then only one photon can possibly be detected from each pulse, indicated by the blue SPAD signals in Figure 1b. In reality the detection rate will be less than one per pulse, and pulses can also be missed if received during the dead time after a noise pulse, indicated in red. Time correlation of the measured events from the SPAD is performed over a data interval, producing a histogram with peaks at 40 ns intervals for transmission of a '1', and a background correlation level for transmission of a '0', with the noise floor determined by ambient background light and detector dark count rate. Simply applying a threshold to the histogram bin generated for each symbol at a delay 40 ns allows decoding of a binary stream. This threshold will have to be sufficient to reject correlation counts from background and dark count correlations.

Finally, a crucial feature of this method is that it is robust to temporal jitter between the transmitter and receiver, unlike other forms of photon counting schemes. Synchronisation of the system can be easily achieved by using an embedded clock in the transmitted data, as discussed in the supplementary material.

2.2 Experimental demonstration

The scheme detailed above was realised using a GaN violet emitting (405 nm), micro-LED device as the transmitter and a silicon Single Photon Avalanche Detector (SPAD) as the receiver. The LED chip was bonded to a custom CMOS driver allowing short pulse operation, with durations of 5 ns. Data signal modulation was applied as a slower on-off keying of the short pulse train. Figure 1c shows a measured pair of pulses from the micro-LED of 5 ns duration and with a relative delay of 40 ns. A variable neutral density filter was placed between the emitter and detector to control the received power at the SPAD.

4
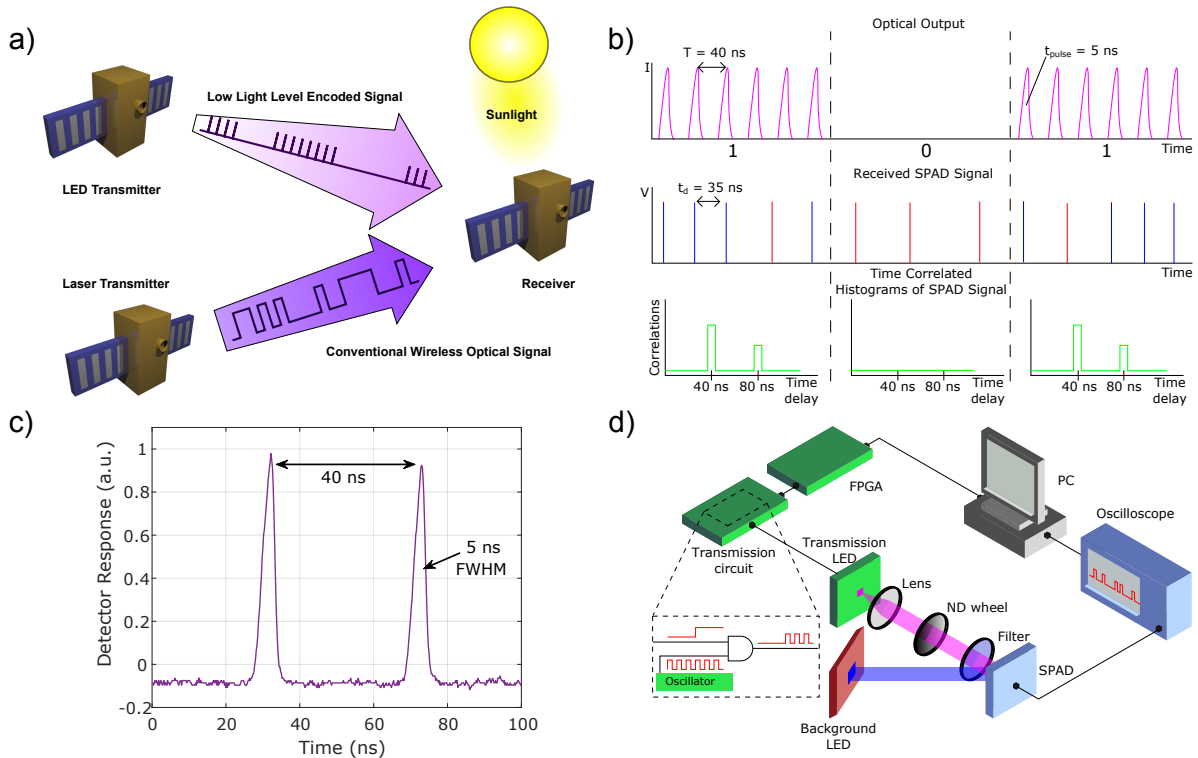
Figure 1: a) Application scenario for inter-satellite communications: The low light level signal encodes data in trains of time-correlated optical pulses and is compatible for use with low power and divergent LED emitters. It is resilient against DC background such as sunlight and also insensitive to most kinds of AC background such as conventional wireless optical signals. b) Schematic of the transmission scheme used. The upper plot shows the LED output on transmission of '0' and '1'. The middle plot shows the SPAD response to the LED signal. The lower plots show the calculated correlation histograms for each data interval. c) Measured pulse pair from a micro-LED source. d) Schematic of the experimental setup.

A schematic of the measurement setup is shown in Figure 1D. Full details of the devices and electronic drivers are given in the methods section.

2.3 Signal-to-noise ratio

To set an operation threshold for the system, a figure of merit similar to the classical signal to noise ratio must be defined. In this method, it is the distinguishability of the correlation peak in the $g(\tau)$ function that indicates the robustness of the classical information recovery to noise. Conventional SNR can be defined as in Equation 5, where N_{signal} is average signal correlation counts and N_{noise} is average noise correlation counts:

$$SNR = 10 \log_{10} \frac{N_{signal}}{N_{noise}}. \qquad (5)$$

As the number of pulse repetitions increases, the correlation counting interval increases, causing both N_{signal} and N_{noise} to increase at linear rates. This results in a constant SNR, which does not reflect the observed increase in distinguishability of signal correlations with increasing pulse repetitions.

Instead, it is more useful to consider the statistical distribution of correlation counts for signal and noise. Photon counting experiments were undertaken using the experimental setup described above, with a received power at the detector of 38 pW, corresponding to a detector count rate of 1.07×10^7 Hz, in a dark lab environment with an average background count rate of 619 Hz. Note that this count rate contains both dark counts within the detector and counts from the small amount of ambient light. The delay correlations of detected photons were binned with a resolution of 10 ns, where the transmitted pulse delay was set at 40 ns. Figure 2a and b show average histograms of received photon correlations for 5 and 100 pulse pair repetitions, respectively. Figure 2c shows the histogram for 100 pulse pair repetitions under high background conditions, displaying the correlation histogram due to background noise alone, and signal with noise. The background count rate for this measurement was 10^7 Hz.

In Figure 2a and b, the signal is defined as the number of correlations in the 40 ns delay time bin, and the noise correlation count is taken from the 60 ns delay bin. Correlation counts should follow a Poissonian distribution, as they are discrete independent events. Figure 2d and e are the measured Poissonian distributions for signal with noise and noise alone correlation counts at 5 and 100 repetitions of the dual pulse cycle, respectively, taken from 1500 independent measurements of each case.

At 5 repetitions, the probability distributions for signal and noise are strongly overlapped. Thus a correlation count peak due to signal transmission is difficult to distinguish from a correlation count peak due to random background and dark counts. At 100 repetitions, the overlap of signal and noise distributions is significantly reduced, making distinction much easier. A histogram threshold equates to a point along the x-axis of the distribution plots. Evidently a threshold point of 2 at 5 repetitions would result in many signal correlation peaks being rejected as noise, whereas at 100 repetitions the majority of signal correlation peaks would be correctly identified, and noise correlation peaks rejected.

Under high background noise conditions, the number of correlations from noise is increased. Figure 2f shows the Poissonian distributions for the background noise, signal alone (identical to Figure 2e) and the combined signal and noise. To properly decode received signals, the threshold must distinguish between the correlations due to noise, from those due to the signal, as both will
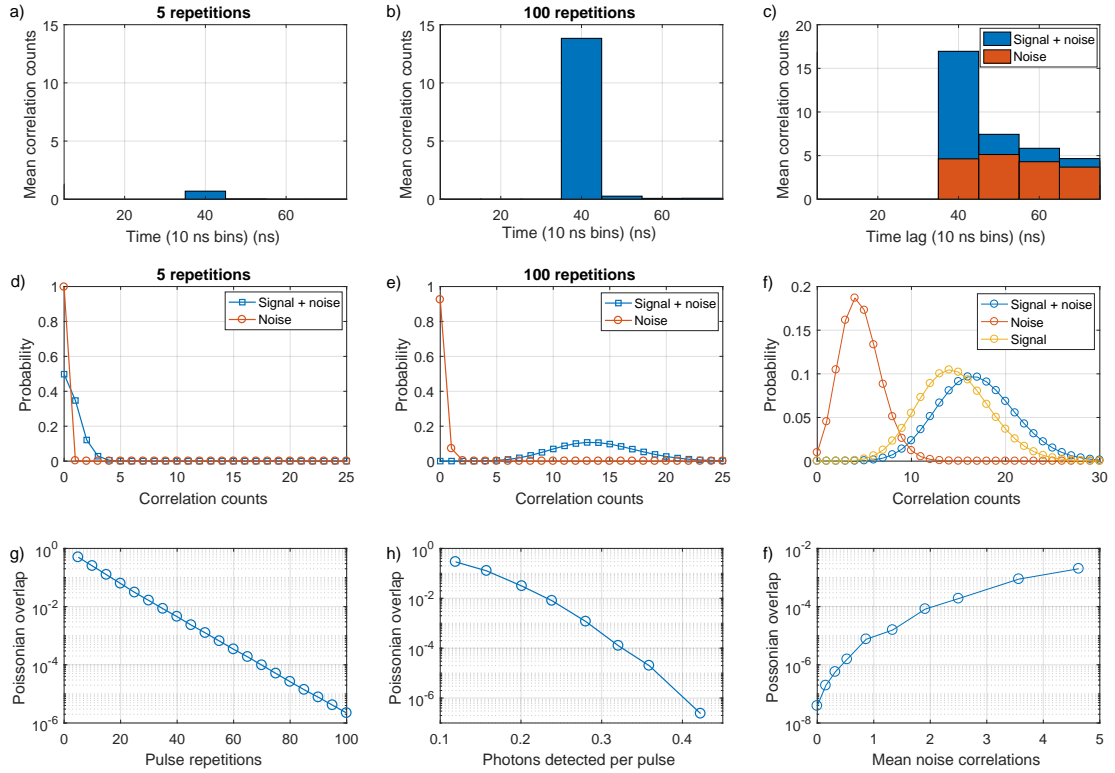
Figure 2: Measured correlation histograms for a) 5, b) 100 pulse pair cycle repetitions and c) 100 repetitions with background noise. Poissonian distributions for the signal and noise correlation counts for d) 5, e) 100 pulse repetitions and f) 100 repetitions with background noise. g–i) Poissonian overlap according to Equation 6 as a function of g) number of pulse repetitions, h) average number of photons detected per pulse, and i) average number of background noise correlations.

be present on transmission of '1'.

Distinguishability is therefore determined by the overlap of the Poisson distributions for (i) the total signal and noise contributions, $P_T(k)$, and (ii) the noise alone $P_n(k)$. Here, $P_n(k)$ is the the probability of k correlation counts occurring due to noise with mean λ, given by Equation 7. Similarly, the distribution of correlation counts $P_s(k)$ when a signal is present without noise is also given by Equation 7. The distribution of correlation counts in the presence of both signal and noise, $P_T(k)$ is related to $P_s(k)$ and $P_n(k)$ via Equation 8. Figures 2g–i show the calculated overlap of these distributions as defined in Equation 6:

$$Overlap = \sum_{k=0}^{\infty} P_T(k)P_n(k), \qquad (6)$$

$$P(k) = \frac{\lambda^k e^{-\lambda}}{k!} \qquad (7)$$

$$P_T(k) = \sum_{m=0}^{k} P_n(m)P_s(k-m). \qquad (8)$$

The overlap of the probability distributions reduces exponentially with increasing pulse repetitions. The rate of decay of the overlap will depend on the received signal power. Figure 2g is valid for a received power of $38\,\mathrm{pW}$. Higher received power would result in a steeper decay, and lower power in a more shallow decay.

In addition to the number of repetitions, the Poisson distribution overlap will depend on the number of photons detected from each pulse. As the pulses used are shorter than the dead time of the SPAD, the maximum number of photons that can be detected is one. Figure 2h shows the overlap for 100 pulse repetitions as a function of received photons per pulse. It can be seen that

the overlap reduces faster than exponential. This is understood by noting that λ in Equation 7 follows $\lambda = p_{ph}^2 N_{rep}$, where p_{ph} is the probability of detecting a photon from a single pulse, and N_{rep} is the number of pulse repetitions. This relationship gives rise to the linear appearance of Figure 2g and the quadratic appearance of Figure 2h.

The rate of random correlation counts due to the background noise will also affect the overlap of Poisson distributions, as increased noise correlations changes the distribution P_n. Figure 2i shows the calculated overlap as background correlation counts increases. Larger numbers of noise correlations increase the overlap between P_n and P_T with a sub-exponential trend.

Therefore, the distinguishability of binary 0 and 1 is governed by the Poissonian overlap, Equation 6, and in turn depends on the number of sampled pulse repetitions, the received signal power, and the background intensity, with the first two parameters dominating.

2.4 Data rates

The achievable data rate of this system is determined by the number of pulse repetitions required to distinguish the signal, and hence the received power and the time separation between pulses. The SPAD response imposes a lower limit on this separation, due to the dead time τ_d and pulse width, τ_{pulse}, giving an achievable data rate of:

$$R_{data} = \frac{1}{N_{rep}(\tau_{pulse} + \tau_d)}. \qquad (9)$$

Where N_{rep} is the number of pulse repetitions required to see a distinguishable peak in the correlation histogram. Use of a SPAD array could lift the restrictions imposed by dead time through pulse combining techniques [26]. To demonstrate

8

the system performance as a function of received power and data rate, bit error ratio (BER) measurements were made over these parameters. A pseudo-random bit sequence (PRBS) of 10^4 bits was used, limited by the data processing capabilities of the oscilloscope and PC components in the measurement setup. The ND filter wheel allowed control of received power, or equivalently, photon detection probability. Figure 3a shows BER curves for varying data transmission rates, taken with minimal background light.

As detailed above, detection of a noise correlation is extremely unlikely. On transmission of a '0', no pulses are sent, meaning only noise correlations will be present. Bit errors arise almost exclusively from missed correlation counts on transmission of a '1' rather than noise correlations on transmission of '0'. Therefore, a decision threshold of 2 counts applied to the correlation histograms provides the lowest BER values. At 8.25 pW of average power, a data rate of 100 kb/s was possible with a BER of less than 10^{-3}. Received optical power can be reduced at the expense of data rate. A data rate of 10 kb/s can be achieved at the same BER with 2 pW.

The power measurements quoted here and used in Figure 3 are the incident optical power on the active area of the SPAD. This value has been calculated through numerical methods from the average count rate detected by the SPAD, details of the method can be found in the supplementary material. Detector count rate is the parameter which governs BER performance, however the optical power to attain the required counts will be influenced by the performance of the SPAD. Most importantly, the detection efficiency of the SPAD at 405 nm is 18%, meaning the incident photon flux is higher than the detector count rate. More efficient photon detection would improve BER performance in terms of required power.

The system performance can also be described in terms of the number of received photons per bit. Figure 3b shows detected photons per bit for each data rate, at the level required for a BER of less than 10^{-3}. The fitted curve is calculated from the relationship between correlation counts, received power and data rate. The number of signal correlations depends on the square of received power and is inversely proportional to the data rate R_{data}. In order to reach a given target BER, a certain constant number of signal correlation counts must be reached, meaning $(ph/s)^2 \propto R_{data}$. As photons per bit is simply the required photons per second divided by data rate, we obtain Equation 10:

$$ph/bit \propto \frac{1}{\sqrt{R_{data}}}. \qquad (10)$$

The 100 kb/s link is transmitting each bit with an average of 27 detected photons. This is relatively close to the standard quantum limit (SQL) for uncoded OOK, set by Poissonian photon statistics [27]. The SQL for a given BER is defined by the minimum number of photons required to distinguish a signal from noise. For a BER of 10^{-3}, a minimum of 7 photons is required, to detect a '1'. Therefore an average of 3.5 photons per bit is required, assuming the probability of transmitting '0' or '1' is equal. The implemented scheme will be unable to reach the SQL, due to the correlation approach. Two photons are required for a single correlation detection, which itself has a Poissonian distribution that must be distinguished from noise.

Note that no FEC has been implemented here, so there is potential for improved efficiency. Furthermore only OOK style signalling has been implemented. Further efficiency improvements will be possible through use of PPM style transmission, to transmit multiple bits per correlation
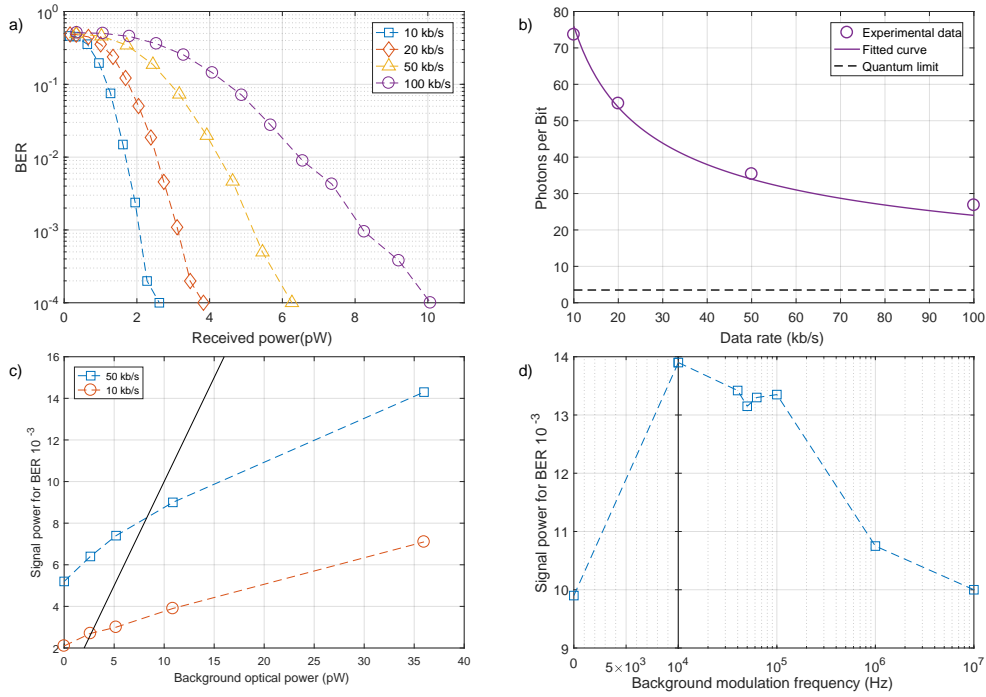
Figure 3: a) BER as a function of received signal power for varying data rates. b) Received photons per bit required to achieve a BER of less than 10^{-3} for varying data rates, fitted with a $x^{-\frac{1}{2}}$ relationship. The standard quantum limit for uncoded OOK at this BER is also shown. c) Required signal power to attain a BER of 10^{-3} under constant background power for 50 and 10 kb/s. Detailed conditions are shown in Table 1. Equal signal and background power is indicated by the solid line. d) Required signal power to attain a BER of 10^{-3} under modulated background conditions. Required power increases when background modulation rates are comparable to the signal data rate.

peak.

After correcting for detector efficiency, 27 detected photons equates to 7.37×10^{-17} J incident on the detector per bit. This exceptionally low energy demonstrates the suitability of the transmission scheme in low power or high loss systems. As mentioned above, more efficient photon detection would allow further reductions in energy received per bit.

2.5 Robustness to noise

A major advantage of this transmission scheme is that it is expected to be robust against background counts, as ambient light is generally uncorrelated on the time scale of 10s of ns. To verify this, BER curves were taken for increasing levels of background light using a secondary light source, as shown in Figure 1d. As background counts increase, the probability of detecting noise correlations increases. The threshold applied to the correlation histogram must then be increased to avoid erroneous detection of '0' symbols. This means higher received average power is required to obtain error-free transmission.

The results for varying background at data rates of 50 and 10 kb/s are shown in Figure 3c, with the background conditions detailed in Table 1. Full BER curves can be found in the supplementary material. R_{bg} is the detector count rate from the background light alone, before the signal is sent. Background incident photon flux (Φ_{bg}) is the number of photons incident on the detector, calculated using numerical methods described in the supplementary material. Optical power (P_{bg}) is then simply the photon flux multiplied by photon energy. Table 1 also shows the detector count rate (R_s), incident photon flux (Φ_{inc}) and optical power (P_{inc}) of the signal required to obtain a BER of 10^{-3} at 50 kb/s.

Figure 3c shows increasing levels of background optical power increases the signal power required to obtain a BER of less than 10^{-3}. However, the power requirements are still very low. At high background levels, the required signal power is significantly lower than the power received from background illumination. With a background count rate of 10^7, corresponding to an optical power of 35.98 pW, less than 15 pW of signal power is required for a 50 kb/s link, and less than 8 pW for 10 kb/s. This background illumination level is somewhat extreme, as the detector will saturate at 1.4×10^7, and normal room lighting in this setup gives a background count rate of 2.33×10^5 In a practical system, background counts can be minimised using suitable optical filters.

The system was also measured under modulated background illumination. Since the number of detected correlation counts depends on the square of received power, a high modulation rate background should interfere in the same manner as a DC signal at the root-mean-squared (RMS) of its count rate. For this reason, background signals used in the following experiments maintain similar RMS photon count rates for comparison to DC measurements. The power required to maintain a BER of 10^{-3} is shown in Figure 3d, with the background conditions and full BER curves shown in the supplementary material. The RMS background optical power was approximately 15 pW for all measurements.

Figure 3d shows two distinct groups of results. The high background modulation rates of 1 and 10 MHz show similar required signal power to constant background conditions. This can be attributed to 2 factors. Firstly, the background signal completes many cycles within a single bit period of the correlation link, making its modulation less significant. Secondly, the dead time

11

Table 1: Table of conditions for BER curves in Figure 3c. Detector count rate (R), incident photon flux (Φ) and optical power (P) are shown for background conditions (subscript bg) and for the signal at a BER of 10^{-3} (subscript s/inc).

Curve	R_{bg} (s^{-1})	Φ_{bg} (ph/s)	P_{bg} (pW)	R_s (s^{-1})	Φ_{inc} (ph/s)	P_{inc} (pW)
a	619	2.95×10^3	1.45×10^{-3}	2.04×10^6	1.06×10^7	5.2
b	1.08×10^6	5.34×10^6	2.62	2.46×10^6	1.30×10^7	6.4
c	2.06×10^6	1.06×10^7	5.19	2.80×10^6	1.51×10^7	7.4
d	4.00×10^6	2.21×10^7	10.87	3.29×10^6	1.81×10^7	8.9
e	1.00×10^7	7.33×10^7	35.98	4.84×10^6	2.91×10^7	14.3

of the SPAD restricts the number of photons that can be detected per background cycle, reducing the difference between a high and low level, further making the background signal act like constant interference. When the background modulation rate is close to the correlation link data rate, the BER performance is degraded, requiring approximately 40% more received power. However, all conditions still reach a BER of less than 10^{-3} for less than 14 pW of received signal power. This reduction in performance occurs as the background signal is now generating different levels of noise correlations from one bit period to the next. This makes it more difficult to choose a suitable correlation threshold, and increases the BER.

Under all background conditions, the signal is transmitted with a lower photon count rate than the background signal, demonstrating low power performance even with high power modulated background interference.

2.6 Satellite systems demonstration

The communications system presented here is applicable in many scenarios, but is particularly attractive for inter-satellite links. The semiconductor devices are extremely compact, low power

consumption and readily integrated with control electronics. LED based visible light communications shows potential for use with cube satellites [28]. The robustness of the signal to background noise and operation at ultra-low power levels, means that it could be implemented without the high accuracy pointing requirements and telescope optics of current satellite systems.

To highlight this capability the system was tested in the nano-satellite mission development environment, NANOBED, shown in Figure 4a. The NANOBED is a nano-satellite hardware and software test-bed, with mission planning facilities, details of which are given in the methods section. A block diagram of the NANOBED setup is presented in Figure 4b. Furthermore, to demonstrate that the full system functionality was able to be powered by the NANOBED, a real time decoder, incorporating embedded clock signal recovery, was implemented on a FPGA platform to replace the oscilloscope and PC components in the characterisation setup. Details of this setup, shown in Figure 4c, are given in the methods section. Details of the integrated clock recovery are given in the supplementary material.

The LED transmission system was integrated with one NANOBED system, while the SPAD
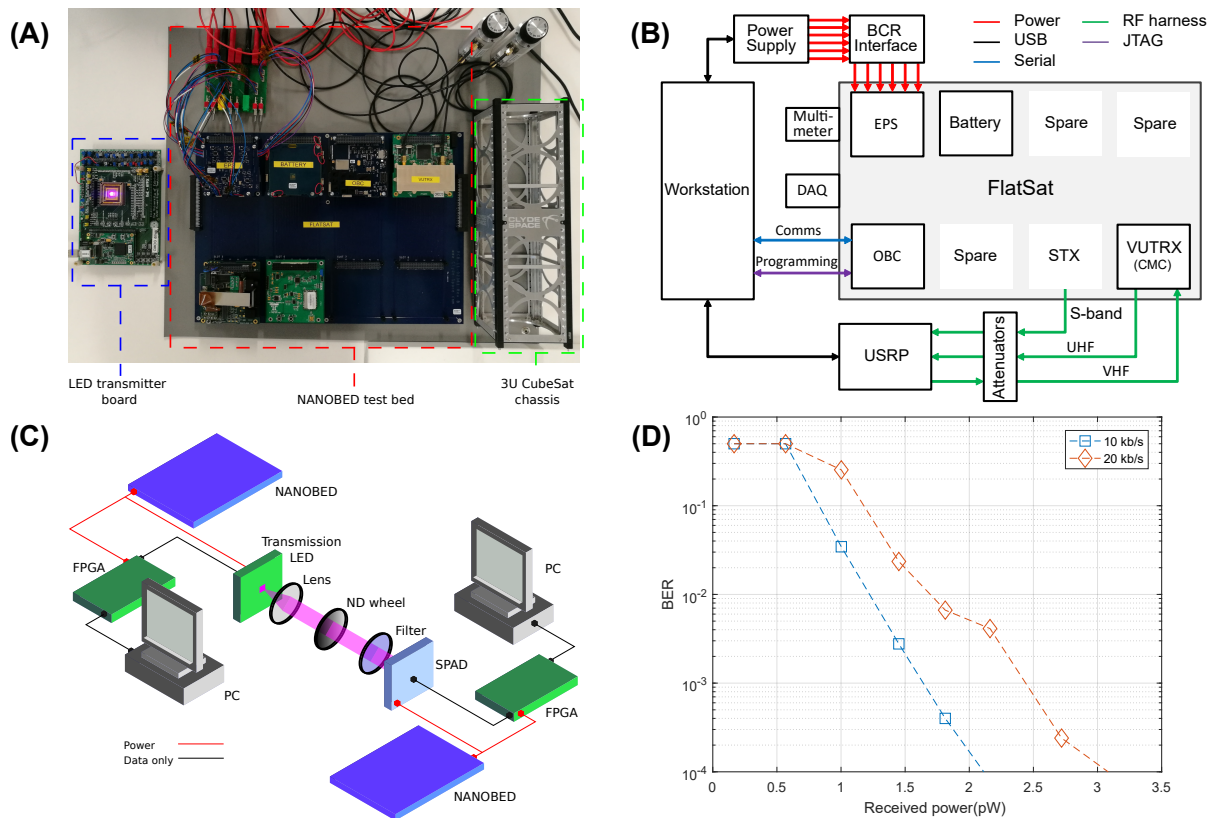
Figure 4: a) Photograph of the micro-LED transmitter board (left), NANOBED "Flatsat" test bed (centre) and a standard 3U CubeSat chassis (right). b) Schematic of the NANOBED architecture. The configuration allows access to individual components of the CubeSat, including the on-board computer (OBC) and electrical power supply (EPS). Radio links are provided by an S-band transmitter (STX) and VHF/UHF Transceiver (VUTRX) connected to a universal software radio peripheral (USRP). c) Schematic of the experimental setup for real time data transmission. d) BER performance of the communication link under power from the NANOBED system.

receiver system was integrated with a second. In this work, the NANOBED solar panel emulating power sources are used to supply the transmitter and receiver devices via the nano-satellite electrical power supply (EPS) and battery units, simulating an in-orbit scenario. The transmitter side of the real time link requires a single FPGA board, from which the CMOS micro-LED array is powered and controlled. On the receiver side, the commercial SPAD module requires a 6 V DC supply, and a second FPGA is used to process the received signals. A summary of typical power consumption is shown in Table 2.

For the laboratory demonstration the transmitter and receiver were placed 4 m apart with the micro-LED pixel projecting the light across a 4 cm wide square with received power controlled using a neutral density filter. A micro-LED emitter at 450 nm was used to improve the Photon Detection Probability (PDP) to 25 %. As shown in Figure 4d, the live link requires 2.5 pW of received power to maintain a BER of 10^{-3} at 20 kb/s. On a 20 µm diameter SPAD, 3 pW corresponds to an intensity of $9.5\,\mathrm{mW\,m^{-2}}$. To provide this over the projected 4 cm wide square, the micro-LED must emit an average power of only 15.3 µW.

3   Discussion

We have demonstrated a transmission scheme suitable for ultra-low light level optical wireless communications. By transmitting temporally correlated signals, data communications can be performed at extremely low light levels, with received power on the order of pico-Watts. Signals can be transmitted using an LED, and received with a single SPAD. A 100 kb/s link has been achieved with a BER of less than 10^{-3} at a re-

ceived power of 8.25 pW, close to the standard quantum limit for uncoded OOK, while received power can be reduced at the expense of data rate.

The scheme is robust to background light, with only a minor increase in required power for very high background conditions. Modulated background signals appear to have little additional influence over that of continuous background, suggesting the scheme could be used in parallel with other optical communications with minimal interference. Furthermore, multiple transmission systems using this scheme could operate without interfering with each other, simply by using different pulse time separations.

A real time transmission setup has been demonstrated, showing a method for clock synchronisation and determination of a threshold level. The current, unoptimised implementation allows a data rate up to 20 kb/s, with only a minor reduction in performance when compared to offline processed transmission. In addition, the real time transmission link has been demonstrated in a simulated satellite environment, at a received power density of 9.5 mW/m2. For an example inter-satellite link distance of 40 km, an LED average power emission of 1 mW and a detector optical aperture of 10 mm, the required pointing accuracy corresponding at this power density, or half angle divergence of the source, would be ≈ 0.1 degree, which represents a significant relaxation in orientation tolerance with respect to current laser based systems. Additionally, GaN LEDs at low current densities show higher wallplug efficiencies than laser diode counterparts [29], further enhancing the power consumption characteristics of the system.

The modest data rates presented in this work are dominated by two key factors, firstly the requirement of this protocol for correlating many repetitions of a pulse pattern, and secondly, the

14

Table 2: Typical power requirements of the communication system

	Voltage (V)	Current (mA)	Power (W)
Transmitter	5	181	0.905
Receiver	5	122	0.610
	6	595	3.570

dead time of the SPAD detector itself. We also demonstrated the simplest transmission protocol case of on-off keying, with no error correction codes applied.

Data rate and photons per bit efficiency can both be improved through relatively straightforward modifications to the system. By using a SPAD array as a receiver rather than a single device, the dead time limitation can be overcome and therefore higher data rates achieved. In addition by implementing a form of pulse position modulation, and implementing powerful FEC codes, the photons per bit transmission efficiency can be improved. Finally, data rates may be enhanced by using a form of pulse amplitude modulation, however the received power requirement would also increase.

This transmission protocol has clear applications in communications systems for long range or high loss environments, but is also equally applicable in microscopy or low light level imaging systems when coupled with a SPAD imaging array, and can be implemented using a wide range of pulsed optical sources dependent on the application.

4 Methods

4.1 Optical transmitter and receiver realisation

The transmitter used for the results presented here is a complementary metal oxide semiconductor (CMOS) integrated gallium nitride micro-LED pixel. Details and fabrication of comparable devices can be found in [30]. The micro-LED pixel is a square 100×100 µm in size, and part of a 16×16 array with a 405 nm emission wavelength.

The micro-LED array is fabricated in flip chip format, and bump-bonded onto CMOS control electronics. The CMOS electronics allow the LEDs to be modulated in a pulsed mode, triggered by the falling edge of an input logic signal. The shortest stable optical pulses t_{pulse} that could be generated with this device and control system were 5 ns.

In order to produce pulses for the OOK transmission, a data signal produced by a field programmable gate array (FPGA) is sent to a simple transmission circuit. Here the data signal is combined with an oscillator producing a signal of square waves with a period of 40 ns, through an AND gate, as shown in Figure 1d.

The SPAD receiver is a commercial module (Thorlabs SPCM20A), with a detector active area diameter of 20 µm. The dead time of the detector is 35 ns, and the typical dark count rate is 25 Hz. At 405 nm and 450 nm the photon detection prob-

15

ability (PDP) is 18% and 25% respectively. The module outputs 3 V logic signals indicating photon counts. This signal is sent to an oscilloscope, and collected by the PC for offline processing of $g(\tau_j)$. In a practical system, this processing could be performed by digital logic circuits

The LED output is collimated with a lens (Thorlabs C220TME-A) and transmitted through a graded neutral density (ND) wheel (Thorlabs NDC-50C-4M-A). A 450 nm shortpass filter is used in front of the SPAD to reject additional background light. This filter is removed for the experiments assessing performance under high background conditions. The pixel is imaged onto the SPAD active area. As the pixel image is approximately a 7 mm square, only a small portion of the light is imaged on to the SPAD circular active area of diameter 20 μm. In a practical system, receiver optics could be used to collect more light on to the active area of the SPAD, allowing higher degrees of loss through the channel.

Received optical power is calculated numerically from the average number of photon counts detected. This method accounts for detector dead time, and photon detection probability at the operational wavelength. Details of the calculation can be found in the supplementary material.

To assess the effects of DC background illumination a commercial 450 nm LED (OSRAM LD CQ7P) was placed within a few centimetres of the transmitter LED, directed towards the SPAD, as shown in the setup schematic in Figure 1d. By increasing the driving current for the commercial LED, the background counts could be controlled.

The modulated background optical signal was generated using a commercial 450 nm LED (OSRAM LERTDUW S2W) modulated with a transistor. This commercial LED had a modulation bandwidth of 15.9 MHz, and was placed within a few centimetres of the transmitting LED. Modulating this LED with a PRBS effectively simulates operation of the correlation link in an environment with conventional optical wireless communication links.

4.2 Real Time Link

The results presented in the first part of the manuscript are all obtained with offline decoding. The output from the SPAD was collected with an oscilloscope, and the traces repeated many times to build a data sequence long enough for BER analysis. In addition, the oscilloscope was triggered from the transmitting FPGA, bypassing the issue of transmitter and receiver synchronisation. To demonstrate a more practical system, a real-time transmitter and receiver have been developed using FPGAs.

A synchronisation system has been implemented, involving data transmission in frames consisting of a 6 bit clock word and 32 data bits. The carefully chosen clock word, '001101', allows both frame level and symbol level synchronisation of data streams. Details on choice of clock work and synchronisation methods can be found in the supplementary material. A block diagram of the experimental setup for real-time transmission is shown in Figure 4c. On the transmitter side, the FPGA is used to generate a data stream in frames, with the 6 bit clock word. In contrast to the offline setup in Figure 1d, the FPGA now directly supplies the falling edge trigger for the LED board, without the need for extra logic circuitry. The receiver FPGA is connected to a separate PC, and clock synchronisation removes the need for a trigger from the transmitter. However, due to limitations from the FPGA boards, the achievable data rates with the real-time setup are limited to 20 kb/s. It should also be noted that the data rates quoted here include transmission

16

of the clock word. This 18.75% overhead reduces useful data transfer to 8.42 and 16.84 kb/s for 10 and 20 kb/s links respectively.

4.3 NANOBED Satellite Simulator Experiments

The LED transmitter and SPAD receiver systems were independently powered by separate NANOBED systems, positioned approximately 4 m apart. A 450 nm micro-LED was used, focussed on the receiver plane using an 8 mm focal length lens (Thorlabs C240TME-A), giving a pixel image size at of approximately 4 cm. To increase received power on the 20 μm diameter SPAD, a 35 mm focal length collection lens (Thorlabs ACL4532U-A) was used.

The satellite simulator test bed is a FlatSat-configured CubeSat system, which includes an electrical power system, batteries, an on-board computer and communication systems. A software design tool offers mission design, simulation and analysis, including a link to the hardware for in-loop simulation and testing. A software defined radio link to NANOBED enables ground software validation and operational testing, over which command and control of the system components can be invoked.

The NANOBED EPS provides a 5 V bus suitable for powering the transmitter and receiver FPGA boards directly. For the SPAD supply, the unregulated battery bus was used with a voltage regulator to fix the voltage to 6 V. The total receiver power requirements were 5.37 W, while the transmitter requires 0.905 W. The SPAD consumes the most power in the system, however the commercial module has not been designed with power conservation in mind. Bespoke electronics in place of FPGA boards may also permit lower power consumption, therefore this demonstration should be thought of as an upper limit on power requirements.

References

[1] Rajbhandari, S. *et al.* A review of Gallium Nitride LEDs for multi-gigabit-per-second visible light data communications. *Semicond. Sci. Technol.* **32**, 1–44 (2017).

[2] Boroson, D. M. A survey of technology-driven capacity limits for free-space laser communications. *Free-Space Laser Communications VII* **6709**, 670918–19 (2007).

[3] Stevens, M. L., Caplan, D. O., Robinson, B. S., Boroson, D. M. & Kachelmyer, A. L. Optical homodyne PSK demonstration of 1.5

17

photons per bit at 156 Mbps with rate-(1/2) turbo coding. *Opt. Express* **16**, 10412–10420 (2008).

[4] Geisler, D. & Yarnall, T. Demonstration of 2.1 Photon-Per-Bit Sensitivity for BPSK at 9.94-Gb/s with Rate- FEC. *2013 Optical Fiber Communication Conference and Exposition and the National Fiber Optic Engineers Conference (OFC/NFOEC)* 1–3 (2013).

[5] Chen, J., Habif, J. L., Dutton, Z., Lazarus, R. & Guha, S. Optical codeword demodulation with error rates below standard quantum limit using a conditional nulling receiver. *Nat. Photon.* **6**, 2–7 (2011).

[6] Tsujino, K. *et al.* Quantum receiver beyond the standard quantum limit of coherent optical communication. *Phys. Rev. Lett.* **106**, 1–4 (2011).

[7] Becerra, F. E. *et al.* Experimental demonstration of a receiver beating the standard quantum limit for multiple nonorthogonal state discrimination. *Nat. Photon.* **7**, 147–152 (2013).

[8] Robinson, B. S. *et al.* 781 Mbit/s photon-counting optical communications using a superconducting nanowire detector. *Opt. Lett.* **31**, 444–446 (2006).

[9] Willis, M. M. *et al.* Performance of a Multimode Photon-Counting Optical Receiver for the NASA Lunar Laser Communications Demonstration. *Proc. International Conference on Space Optical Systems and Applications (ICSOS)* (2012).

[10] Chitnis, D. *et al.* A 200 Mb/s VLC demonstration with a SPAD based receiver.

2015 IEEE Summer Topicals Meeting Series, SUM 2015 **3**, 226–227 (2015).

[11] Li, Y., Safari, M., Henderson, R. & Haas, H. Optical OFDM With Single-Photon Avalanche Diode. *IEEE Photon. Technol. Lett.* **27**, 943–946 (2015).

[12] Zimmerman, H., Steindl, B., Hofbauer, M. & Enne, R.. Integrated fiber optical receiver reducing the gap to the quantum limit. *Sci. Rep.* **7**, 2652 (2017).

[13] Alsolami, I., Chitnis, D., O'Brien, D. C. & Collins, S. Broadcasting over photon-counting channels via multiresolution PPM: Implementation and experimental results. *IEEE Commun. Lett.* **16**, 2072–2074 (2012).

[14] Mendenhall, J. A. *et al.* Design of an optical photon counting array receiver system for deep-space communications. *Proc. IEEE* **95**, 2059–2069 (2007).

[15] Boroson, D. M. & Robinson, B. S. The Lunar Laser Communication Demonstration: NASA's First Step Toward Very High Data Rate Support of Science and Exploration Missions. *Space Sci. Rev.* **185**, 115–128 (2014).

[16] Liao, S. *et al.* Long-distance free-space quantum key distribution in daylight towards inter-satellite communication. *Nat. Photon.* **11**, 509–514 (2017)

[17] Lekki, J. *et al.* An Extremely Low Power Quantum Optical Communication Link for Miniature Planetary Sensor Stations. *J. Aeros. Comp. Inf. Com.* **5**, 1–24 (2008).

[18] Hizlan, M., Lekki, J. D. & Nguyen, B. V. Glenn Research Center quantum communicator receiver design and development. *Opt. Eng.* **48**, 105003 (2009).

[19] Seward, S., Tapster, P., Walker, J. & Rarity, J. Daylight demonstration of low-light-level communication system using correlated photon pairs. *Optical and Quantum Electronics* **3**, 201–207 (1991).

[20] Hong, C. K., Friberg, S. R. & Mandel, L. Optical communication channel based on coincident photon pairs. *Appl. Opt.* **24**, 3877–3882 (1985).

[21] Hughes, R. J. *et al.* Free-space quantum key distribution in daylight. *J. Mod. Opt.* **47**, 549–562 (2000).

[22] Gordon, K. J., Fernandez, V., Townsend, P. D. & Buller, G. S. A short wavelength GigaHertz clocked fiber-optic quantum key distribution system. *IEEE J. Quantum Electron.* **40**, 900–908 (2004).

[23] Takenaka, H. *et al.* Satellite-to-ground quantum communication using a 50-kg-class micro-satellite. *Nat. Photon.* **11**, 502–508 (2017).

[24] Becker, W. *Advanced Time-Correlated Single Photon Counting Applications*, vol. 111 (Springer, 2015).

[25] Fisher, E., Underwood, I. & Henderson, R. A reconfigurable single-photon-counting integrating receiver for optical communications. *IEEE J. Solid-State Circuits* **48**, 1638–1650 (2013).

[26] Gnecchi, S. *et al.* Digital Silicon Photomultipliers With OR/XOR Pulse Combining Techniques. *IEEE Trans. Electron Devices* **63**, 1105–1110 (2016).

[27] W.Shieh & I.Djordjevic. *OFDM for optical communications.* (Academic Press, 2010).

[28] Kawamura, Y., Tanaka, T. Transmission of the LED light from the space to the ground. *AIP Adv.* **3**, 102110 (2013).

[29] Piprek, J. Comparative efficiency analysis of GaN-based light-emitting diodes and laser diodes. *Appl. Phys. Lett.* **109**, 021104–021104-4 (2016).

[30] Zhang, S. *et al.* 1.5 Gbit/s multi-channel visible light communications using CMOS-controlled GaN-based LEDs. *J. Lightw. Technol.* **31**, 1211–1216 (2013).

CMOS-integrated GaN LED array for discrete power level stepping in visible light communications

ALEXANDER D. GRIFFITHS,[1,*] MOHAMED SUFYAN ISLIM,[2]
JOHANNES HERRNSDORF,[1] JONATHAN J. D. MCKENDRY,[1]
ROBERT HENDERSON,[3] HARALD HAAS,[2] ERDAN GU,[1]
AND MARTIN D. DAWSON[1]

[1]Insititute of Photonics, Department of Physics, SUPA, University of Strathclyde, Glasgow G1 1RD, UK
[2]Li-Fi Research and Development Centre, Institute for Digital Communications, The University of Edinburgh, King's Buildings, Mayfield Road, Edinburgh, EH9 3JL, UK
[3]CMOS Sensors & Systems Group, The University of Edinburgh, Edinburgh, EH9 3JL, UK
*alex.griffiths@strath.ac.uk

Abstract: We report a CMOS integrated micro-LED array capable of generating discrete optical output power levels. A 16×16 array of individually addressable pixels are on-off controlled through parallel logic signals. With carefully selected groups of LEDs driven together, signals suitable for discrete transmission schemes are produced. The linearity of the device is assessed, and data transmission using pulse amplitude modulation (PAM) and orthogonal frequency division multiplexing (OFDM) is performed. Error-free transmission at a symbol rate of 100 MSamples/s is demonstrated with 4-PAM, yielding a data rate of 200 Mb/s. For 8-PAM, encoding is required to overcome the baseline wander from the receiver, reducing the data rate to 150 Mb/s. We also present an experimental proof-of-concept demonstration of discrete-level OFDM, achieving a spectral efficiency of 3.96 bits/s/Hz.

References and links

1. S. Rajbhandari, J. J. D. Mckendry, J. Herrnsdorf, H. Chun, G. Faulkner, H. Haas, I. M. Watson, D. O. Brien, and M. D. Dawson, "A review of Gallium Nitride LEDs for multi-gigabit-per-second visible light data communications," Semicond. Sci. Technol. **32**, 1–44 (2017).
2. T. Fath, C. Heller, and H. Haas, "Optical wireless transmitter employing discrete power level stepping," J. Lightwave Technol. **31**, 1734–1743 (2013).
3. J. F. Li, Z. T. Huang, R. Q. Zhang, F. X. Zeng, M. Jiang, and Y. F. Ji, "Superposed pulse amplitude modulation for visible light communication," Opt. Express **21**, 31006–31011 (2013).
4. M. S. Islim and H. Haas, "Modulation Techniques for Li-Fi," ZTE Commun. **14**, 29–40 (2016).
5. A. Yang, Y. Wu, M. Kavehrad, and G. Ni, "Grouped modulation scheme for LED array module in a visible light communication system," IEEE Wirel. Commun. **22**, 24–28 (2015).
6. J. J. D. McKendry, D. Massoubre, S. Zhang, B. R. Rae, R. P. Green, E. Gu, R. K. Henderson, A. E. Kelly, and M. D. Dawson, "Visible-Light Communications Using a CMOS-Controlled Micro-Light- Emitting-Diode Array," J. Lightwave Technol. **30**, 61–67 (2012).
7. A. V. N. Jalajakumari, E. Xie, J. McKendry, E. Gu, M. D. Dawson, H. Haas, and R. K. Henderson, "High-speed integrated digital to light converter for short range visible light communication," IEEE Photon. Technol. Lett. **29**, 118–121 (2017).
8. S. Rajbhandari, H. Chun, G. Faulkner, K. Cameron, A. V. N. Jalajakumari, R. Henderson, D. Tsonev, M. Ijaz, Z. Chen, H. Haas, E. Xie, J. J. D. McKendry, J. Herrnsdorf, E. Gu, M. D. Dawson, and D. O'Brien, "High-Speed Integrated Visible Light Communication System: Device Constraints and Design Considerations," IEEE J. Sel. Areas Commun. **33**, 1750–1757 (2015).
9. J. Herrnsdorf, J. J. D. McKendry, R. Ferreira, R. Henderson, S. Videv, S. Watson, H. Haas, A. E. Kelly, E. Gu, and M. D. Dawson, "Single-chip discrete multitone generation," in 2015 IEEE Summer Topicals Meeting Series, SUM 2015 **2**, 47–48 (2015).

10. S. Pimputkar, J. S. Speck, S. P. DenBaars, and S. Nakamura, "Prospects for LED lighting," Nat. Photon. **3**, 180–182 (2009).
11. S. Zhang, S. Watson, J. J. D. McKendry, D. Massoubre, A. Cogman, E. Gu, R. K. Henderson, A. E. Kelly, and M. D. Dawson, "1.5 Gbit/s multi-channel visible light communications using CMOS-controlled GaN-based LEDs," J. Lightwave Technol. **31**, 1211–1216 (2013).
12. J. Herrnsdorf, J. J. D. McKendry, S. Zhang, E. Xie, R. Ferreira, D. Massoubre, A. M. Zuhdi, R. K. Henderson, I. Underwood, S. Watson, A. E. Kelly, E. Gu, and M. D. Dawson, "Active-matrix GaN micro light-emitting diode display with unprecedented brightness," IEEE Trans. Electron. Dev. **62**, 1918–1925 (2015).
13. D. Tsonev, S. Sinanovic, and H. Haas, "Pulse shaping in unipolar OFDM-based modulation schemes," in "2012 IEEE Globecom Workshops," (2012), pp. 1208–1212.
14. P. Vary and R. Martin, *Digital speech transmission: enhancement, coding and error concealment* (John Wiley & Sons, 2006).
15. S. Lloyd, "Least squares quantization in PCM," IEEE Trans. Inf. Theory **28**, 129–137 (1982).
16. H. E. Levin, "A complete and optimal data allocation method for practical discrete multitone systems," in "Global Telecommunications Conference, 2001. GLOBECOM '01. IEEE," , vol. 1 (2001), vol. 1, pp. 369–374 Vol.1.
17. F. Xiong, F. Xiong, and F. Xiong, *Digital modulation techniques*, Vol. 633 (Artech House Boston, 2006), 2nd ed.

1. Introduction

Demand for wireless data communications is constantly increasing, putting further strain on the limited radio frequency (RF) spectrum. A potential complementary technology to RF communications is visible light communication (VLC). Expanding transmission to the visible spectrum has several advantages, including THz of license-free frequencies, low cost components and potential for integration with solid state lighting.

Transmitters for VLC are commonly light-emitting diodes (LEDs) [1] due to their low cost, high efficiency and increasingly ubiquitous use as illumination sources. A digital data stream is transmitted through modulation of the optical output from an LED. In most VLC systems to date, the binary data stream is converted into an analogue driving signal using a digital to analogue converter (DAC) and a transconductance amplifier [2]. The simplest modulation scheme that can be performed in this way is on-off keying (OOK), where the LED brightness is modulated between a high and low state to represent a high or low logic level, respectively. This modulation method has low spectral efficiency, so it is desirable to move to a higher order modulation scheme.

A straightforward method to increase spectral efficiency is to use pulse amplitude modulation (PAM), making use of multiple output power levels [3]. Using $M = 2^N$ levels allows N bits to be sent with each optical pulse, referred to as a symbol. The transmission scheme is then known as M-PAM. A desirable quality in the transmitters for such a scheme is linearity, in order for the output signal to faithfully replicate the input signal. LEDs have highly non-linear current to luminosity relationships, so have to be driven only within a short range of currents where the response is quasi-linear, restricting the dynamic range of the communication system.

The performance of single carrier schemes such as M-PAM degrades in the presence of baseline wander and low frequency flickering interference from background lights. Multi carrier modulation schemes such as orthogonal frequency division multiplexing (OFDM) overcome these problems by adapting the channel loading to channel capacity using adaptive bit and energy loading algorithms. This allows OFDM to skip subcarriers where the signal to noise ratio (SNR) is low. OFDM is a promising candidate for VLC thanks to the cost-effective single-tap equalizers and the inherent support of multiuser access [4].

A potentially simple way to generate discrete levels and avoid non-linearity effects is to use groups of LEDs. By controlling the driving current of each group [2] or the number of active LEDs in each group [5], discrete sets of optical power levels can be generated without the linearity restrictions of a single LED. Levels generated by grouped LED elements can also be used to produce discrete OFDM signals [2], potentially providing higher spectral efficiencies than PAM.

Here we present a highly compact integrated approach to discrete optical signal generation: an array of micro-LED pixels integrated with complementary metal-oxide semiconductor (CMOS) driving electronics. This provides a mm scale device capable of using CMOS logic signals to control groups of LEDs in an on-off fashion, and generate discrete output levels without the need for a DAC. By driving selected numbers of LEDs together, discrete multi-level signals can be generated such as discrete PAM and OFDM waveforms. We demonstrate data rates up to 200 Mb/s and spectral efficiencies up to 3.96 bits/s/Hz. In principle, this "digital-to-light" transmitter can be scaled to provide higher output power or a higher number of discrete output power levels.
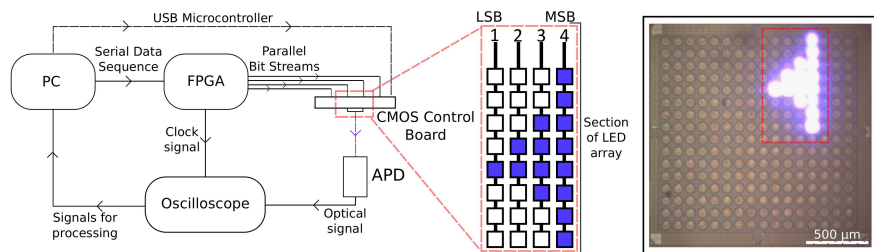
2. Device and experimental setup

Fig. 1. Block diagram of the system (left), with an example LED grouping for binary weighted signals. A micrograph image of LED array A (right) is shown with 15 active pixels.

The LED arrays used for this work consist of 16×16 individually addressable gallium nitride (GaN) LED elements fabricated in flip-chip configuration. Details of comparable device fabrication and performance have been reported previously in [6]. Two different pixel arrangements have been used. The first consists of uniform 72 μm pixels on a 100 μm pitch (array A). The second consists of varying pixel sizes from 84 μm to 14 μm (array B). The arrays are otherwise identical. A micrograph image of array A is shown in Fig. 1, taken from the sapphire side with 15 LED pixels switched on. The flip-chip format of the LED array allows it to be bump bonded to CMOS control electronics with matching bond-pad pitch. The CMOS driver provides on-off control of each pixel by addressing individual p-contacts, with a common n-contact for the array. This matches best with standard LED array fabrication, relying on a PMOS transistor as the LED driver. The -3 dB modulation bandwidth of each individual pixel is 110 MHz, limited by the connection to the CMOS electronics [6]. Higher modulation bandwidths would be possible with the faster switching speeds of NMOS transistors [7], however the LEDs would have to be contacted through individual n-contact pads, requiring a more complex LED fabrication method [8]. The emission wavelength of the device is 405 nm, as early investigations showed devices of this wavelength provided the most promising results in this configuration [9]. This is likely due to improved frequency response at low current densities, combined with the on-off control rather than common DC-biased AC modulation. Violet emitting devices are also suitable for white light generation for combined communications and lighting, using colour converting materials or colour mixing with several LED elements [10].

A CMOS driving board, reported in [11], is used to provide connections allowing independent control of all 16 columns of LEDs on the array. A USB microcontroller allows selection of active pixels from the PC. Fig. 1 shows an example of how the parallel logic channels can be used to group LED pixels and generate discrete signals. With a uniform set of pixels, N bits per symbol

can be mapped on to M discrete output states, and therefore implement M-PAM. This requires N parallel logic channels, where $M = 2^N$. Each parallel logic channel, m, is weighted with 2^{m-1} active LEDs, where m is an integer between 1 and n. Using the array with varying pixel sizes requires more careful planning of active pixels, but permits greater flexibility in discrete level generation. A digitally sampled OFDM signal can be transmitted in a similar manner.

A block diagram of the system used for data transmission is shown in Fig. 1. Signals are prepared in MATLAB$^{\text{TM}}$ and loaded onto the on-chip memory of a field-programmable gate array (FPGA) board (Opal Kelly XEM3010). The FPGA outputs parallel logic streams, with a length of 2^{15} bits, at a programmed symbol rate. Each bit stream is sent in parallel to a different column on the CMOS control board, modulating the LEDs. Modulation of each LED is therefore synchronised and produces a spatially superposed multi-level output. The light output is imaged on to an avalanche photodiode (APD) with a 1 GHz bandwidth (Hamamatsu C5658) using a pair of lenses. The APD response is captured by an oscilloscope, and processed in MATLAB$^{\text{TM}}$.

The maximum symbol rate achievable with this FPGA configuration is 100 MHz, placing a hard limit on the communication link data rate. OOK transmission is therefore limited to 100 Mb/s, despite the 110 MHz bandwidth of an individual LED. Previous experiments show OOK data rates with similar devices up to to 512 Mb/s [6], however the setup used in this earlier work is unable to support the multiplexing functionality presented here.

3. Results

3.1. Discrete pulse amplitude modulation

To produce PAM signals a pseudorandom bit sequence (PRBS) is mapped to M-PAM symbols using MATLAB$^{\text{TM}}$. Parallel bit streams are transmitted to the columns of array A, with pixels selected to form binary weighted groups on each column, as shown in Fig. 1. Fig. 2 shows the linearity of sequential output levels, with pixels driven by a repeating on-off signal at 50 MHz. Optical power was measured at a distance of 3 cm from the array with a 9.5 mm diameter power meter head. The on state bias of the LEDs is 6.6 V, consuming 15.7 mA for a single pixel. At higher levels, the linearity begins to degrade. This is attributed to electrical crosstalk and self-heating within the device [12]. These devices were not specifically designed for discrete signal generation, so there is scope for improvement with custom CMOS and LED array designs.
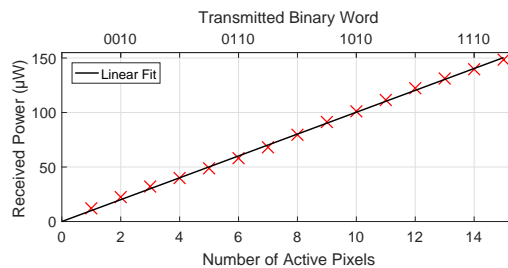

Fig. 2. Linearity of optical power output at 50% duty cycle for increasing numbers of pixels with array A.

Using a total of 3 LEDs on the first 2 channels, one and two on channels 1 and 2 respectively, 4-PAM sequences were transmitted. An example of the captured trace from the 3 LEDs modulated at a 100 MSamples/s is shown in Fig. 3. The LED output follows the 4 level scheme closely, and can be decoded without error, resulting in a data rate of 200 Mb/s. Also shown in Fig. 3 are eye diagrams for 4-PAM at 50 and 100 MSamples/s, showing the 4 distinguishable levels. The symbol rate here is limited by the FPGA, not the LED array.
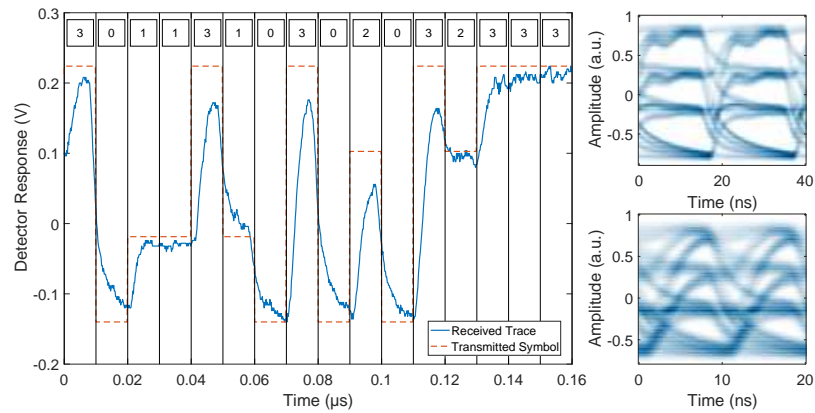
Fig. 3. Received 4-PAM optical signal at 100 MSamples/s, with the transmitted symbol. To the right are the eye diagrams for 50 MSamples/s (upper) and 100 MSamples/s (lower) symbol rates.

Extending the system to a third channel allows 8-PAM signals to be generated, increasing spectral efficiency. With an increased number of levels, baseline wander (BLW) in the system becomes problematic. The APD used is AC coupled with a low-frequency cut-off of 50 kHz. This causes the received trace to drift with the low-frequency components of the signal, and become difficult to decode. At 50 MSamples/s a bit error ratio (BER) of 1.18×10^{-2} was recorded. In order to improve upon this, data streams have been encoded to maintain DC balance over every 2 symbols. Using this method it was possible to transmit at 100 MSamples/s, and decode without error. However, due to the high DC-balancing overhead the resulting data rate is 150 Mb/s; slower than that of 4-PAM. An example of the received trace is shown in Fig. 4 with eye diagrams at 50 and 100 MSamples/s symbol rates. Using an alternative photoreceiver, the full 100 MSamples/s could be used, yielding a data rate of 300 Mb/s.
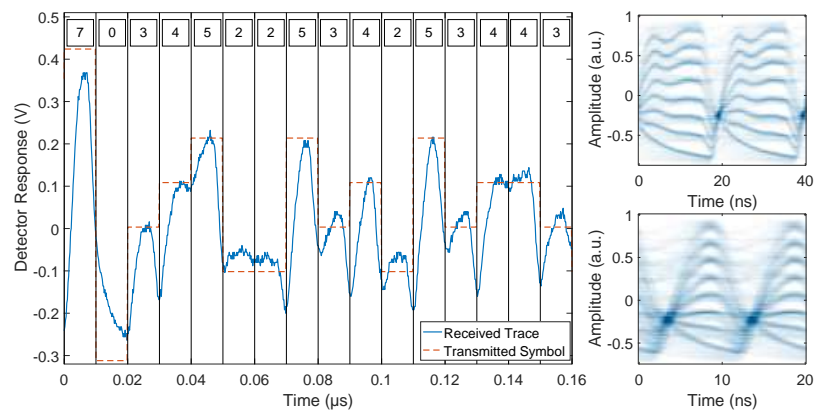

Fig. 4. Received 8-PAM optical signal at 100 MSamples/s symbol rate, with eye diagrams for 50 MSamples/s (upper) and 100 MSamples/s (lower) symbol rates.

With a 4th channel, 16-PAM transmission can be performed. At a 25 MSamples/s the data

stream was decoded with a BER of 7.02×10^{-4}. The encoding method used for 8-PAM is still required to maintain DC-balance, yielding a data rate of 50 Mb/s. At higher PAM levels the received signals become degraded by the increasingly non-linear array output, inter-symbol interference and multilevel penalty.

3.2. Discrete orthogonal frequency division multiplexing

The generation of discrete-levels OFDM starts with an 'analogue' OFDM waveform generation in MATLAB^{TM}. A binary stream of bits is modulated into M-ary quadrature amplitude modulation (M_k-QAM) symbols which are mapped into multiple subcarriers, where M_k is the constellation size that is allocated based on the estimated SNR. Hermitian symmetry is imposed on the subcarriers before the inverse fast Fourier transformation (IFFT) to ensure a real-valued OFDM output. The number of sub-carriers is chosen as $N_{FFT} = 128$, to ensure statistical significance of multiple frames given the limitation of the FPGA output length. A cyclic prefix of $N_{CP} = 5$ was found by exhaustive experiments to be adequate in avoiding any inter-symbol-interference. The OFDM waveform is then filtered using a root-raised cosine pulse shaping filter and clipped at, $|x_s| \leq 4\sigma_s$, where σ_s is the standard deviation of the OFDM waveform, x_s [13].

The analogue OFDM waveform is quantised into (3, 4, 5) bit resolutions corresponding to (8, 16, 32) discrete levels respectively. Two quantisation methods are adopted from source coding literature to convert the analogue waveform into discrete-level OFDM: uniform quantisation and Lloyd-Max quantisation [14]. While uniform quantization uses equally spaced discrete levels, Lloyd-Max uses a narrower level-spacing in the power range that is predominantly used by the OFDM waveform, and wider spacing in the less frequently used power ranges [15]. This is desirable for OFDM as the waveform follows a Gaussian distribution. The probability distribution function (PDF) of the OFDM waveform and the probability mass function (PMF) of the two quantisation methods for 5 bit quantisation are shown in Fig. 5. The quantisation step of Lloyd-Max is smaller at the higher probability densities and vice versa.
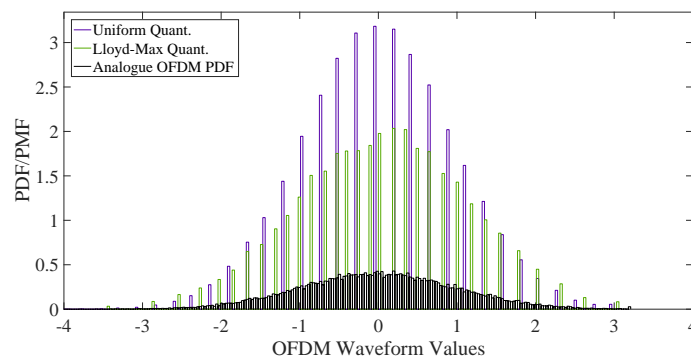

Fig. 5. Probability distribution function of a typical analogue OFDM waveform, with the probability mass function of the uniform and Lloyd-Max 5 bit quantisations.

The discrete levels are mapped onto the CMOS array using the aforementioned FPGA. Array B was used and the mapping is performed by choosing the best-possible candidate columns of the array that would produce a linear output for the considered (8,16,32) discrete levels as shown in Fig. 6. The sampling frequency limit of the FPGA is used at 100 MS/s with an oversampling of 5 samples per symbol. This restricts the overall system bandwidth to 10 MHz due to the Hermitian symmetry requirement of OFDM. The discrete levels are superimposed in the optical domain and the light is collimated and focused into an APD (Hamamatsu, S8664-05k) using two lenses (Thorlabs, LA1951-A and C240TME-A) with a distance of 70 mm between the CMOS chip and the APD. The received signal was processed and demodulated in MATLAB^{TM}.
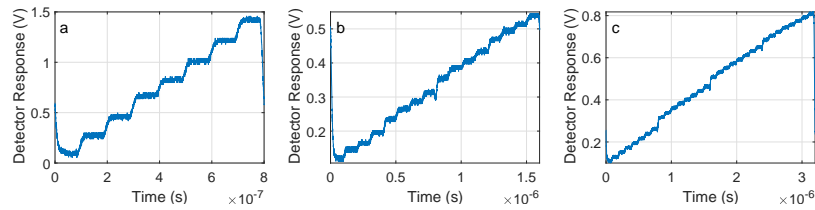
Fig. 6. Levels used for generating OFDM signals with a) 3, b) 4 and c) 5 bit resolution using array B. Symbols were transmitted sequentially at a rate of 10 MHz.

Table 1. Average SNR for uniform and Lloyd-Max quantisation with 3, 4, 5 bit resolution.

Bit resolution	3	4	5
Uniform	13.24 dB	16.11 dB	13.95 dB
Lloyd-Max	16.75 dB	18.93 dB	15.92 dB

The average SNR for the Lloyd-Max quantisation method for all bit resolutions considered is higher than those for the uniform quantisation as shown in table 1. An improvement of 3.51 dB is achieved for the 8 discrete levels case. In addition, the average SNR improves as the number of discrete levels increases. However, this was not shown for 5 bit resolution due to the incurred non-linearity in the 32 discrete levels generation as shown in Fig. 6, where significant steps in output power are seen at the 8th, 16th and 24th level transitions.

In principle, higher collected optical power contributes to a higher SNR, as long as the APD does not saturate. However, excess optical power can also increase shot noise in the APD which may decrease the SNR. In this experiment, the objective was to collect the maximum optical power possible through optimizing optical alignment. This ensured that most of the emitted light from all the deployed LEDs is collected so that the discrete levels can be constructed in the optical domain.

In addition, adaptive bit and energy loading is used for OFDM as described in [16]. With higher SNR, the algorithm can increase bit loading while maintaining a target BER. In this sense, higher collected optical power results in higher data rates. The target BER is usually set to be lower than the FEC threshold target, and the SNR thresholds can be calculated using the analytical BER model of M-QAM [17].

The BER versus data rate for uniform and Lloyd-Max quantisation is shown in Fig. 7 for 3, 4, 5 bit resolutions. It is shown clearly that the BER performance improves as the number of total discrete levels increases. For uniform quantisation, a data rate of 25.2 Mb/s is achieved below the forward error correction (FEC) target for 3 bit resolution. This increases to 29 Mb/s and 35.5 Mb/s for 4 and 5 bit resolutions, respectively. The performance improves for the Lloyd-Max quantisation where data rates of 36 Mb/s, 39.5 Mb/s are achieved for 3 and 4 bit resolutions. The performance saturates for the 5 bit resolution case due to the increased nonlinearity.

4. Conclusion

Pulse amplitude modulation has been implemented using discrete levels generated by multiple LEDs within an array. 4 level PAM is easily performed at error-free levels up to 100 MSamples/s, allowing a 200 Mb/s link. 8-PAM is also possible at 100 MSamples/s, however the baseline wander introduced by the receiver limits the effective data rate to 150 Mb/s. 16-PAM has been investigated, though suffers under the non-linearity of the system, along with decoding difficulty due to the increased number of potential transitions. Discrete OFDM has been shown as feasible, with significant scope for improvement by upgrading the FPGA interface. A maximum of
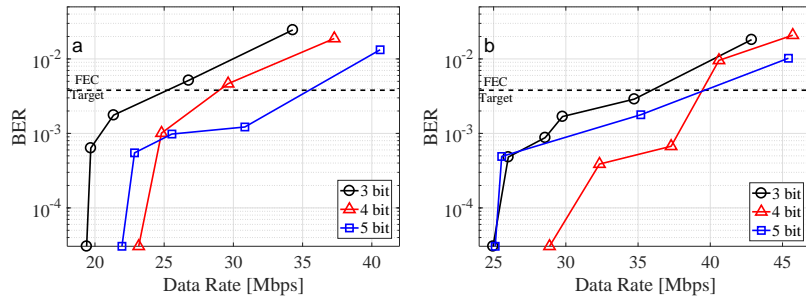
Fig. 7. BER versus data rate for a) uniform and b) Lloyd-Max quantisation.

39.6 Mb/s is achieved using 16-level discrete OFDM with Lloyd-Max quantisation, corresponding to spectral efficiency of 3.96 bits/s/Hz. We have shown that a CMOS integrated micro-LED array provides a compact system for digital-to-light conversion, and is suitable for discrete multi-tone generation on a highly miniaturised scale with digital electronic interface.

Funding

Acknowledgments